Leibniz Universität Hannover

Magnetic and Electric Response of Gold Nanoparticles for Low Frequency Applications in Biological Cells

Von der Leibniz-Forschungsschule für Optik und Photonik
der Gottfried Wilhelm Leibniz Universität Hannover

zur Erlangung des akademischen Grades
Doktorin der Naturwissenschaften
Dr. rer. nat.

vorgelegte Dissertation von

M.Sc. Saba Harke

2024

Referent:	Prof. Dr. Boris Chichkov
Korreferenten:	Prof. Dr. Antonio Calà Lesina,
	Prof. Dr. Anatoly Zayats
Tag der Promotion:	06.05.2024

Saba Harke: *Magnetic and Electric Response of Gold Nanoparticles for Low Frequency Applications in Biological Cells*, Leibniz Universität Hannover, May 2024

Preface

This thesis was carried out during my time as a research associate at the Institute of Quantum Optics (IQ), Leibniz University Hannover (LUH). Some of my research work for this thesis was conducted at the Institute of Microwave and Wireless Systems (IMW), LUH. My research focus there was on a joint project between IMW, the Medizinische Hochschule Hannover and the Institute of Cell Biology and Biophysics, LUH. The scope of this joint research project was to improve the investigation of mechanisms of action between electromagnetic (EM) fields (with focus on the electric field component) and biological cells in the frame of an established therapeutic method called *Tumor Treating Fields*. At the IMW I contributed to a joint publication in the peer reviewed journal *Scientific Reports* [1]. Furthermore, during my research at IMW I was lead author of a publication in a peer reviewed international journal [2]. I led and I was part of several international conference contributions [3–5], and I mentored two Bachelor theses [6, 7].

My research work at IQ resulted from a side research project during my time at IMW. The research group *nanoengineering* of IQ which I became part of worked in the frame of the REBIRTH DFG Excellence Cluster on the differentiation and reprogramming of adult stem cells with application of EM fields and gold nanoparticles (AuNPs). The scope of my work at the IQ was to investigate physical mechanisms of action between EM fields (with focus on the magnetic field component), cells and AuNPs. During my work at the IQ I became part of the Hannover Centre for Optical Technologies (LUH), research group Computational Photonics, which is part of the Exzellenzcluster PhoenixD. I was lead author of one peer reviewed article in the journal *Scientific Reports* [8] and led an additional conference contribution [9].

Acknowledgements

I thank everyone who supported me in the formation process of this thesis and especially in the valuable gain of knowledge and experience during my time as a doctoral candidate. While it is impossible to mention every institution, cooperate partner and person in name, I like to acknowledge some special contributions in the following.

This work is co-supervised by Dr. Atefeh Habibpourmoghadam. My deep appreciation goes to her, who provided constant valuable scientific feedback on my research work and thesis and discussed ideas and results with me.

My special thanks go to Prof. Dr. Boris Chichkov and Prof. Dr. Antonio Calà Lesina for the supervision of this work and for being my examiners. Furthermore, I like to thank Prof. Anatoly Zayats for being my external examiner and I like to thank Prof. Dr. Michael Kues for accepting the chairmanship in the examination process.

I like to thank the whole Computational Photonics group of the Hannover Centre for Optical Technologies for the great reception into their team. Prof. Dr. Antonio Calà Lesina, Dr. Atefeh Habibpourmoghadam, Johannes Gedeon, Dr. Izzatjon Allayarov, Sadeq Bahmani, Chris Staufenbiel, Abhishek Nanda and Emanuel Pegler. It was a pleasure working with you, discussing ideas, learning from you, and sometimes just having a fun coffee break with you. Very special thanks go to Prof. Dr. Antonio Calà Lesina, who invited me into his research group and mentored and supervised me during a critical final phase of my thesis. Special thanks also go to Dr. Andrey Evlyukhin from the Institute of Quantum Optics for sharing his expertise in the mathematical modelling of Micro and Nano Photonics and providing valuable scientific feedback. I would also like to thank Dr. Annette Hoffmeister, formally from the Institute of Quantum Optics, for her guidance concerning the preparation and biological use of nanoparticles.

I like to thank Siqi Lin from the Institute for Drive Systems and Power Electronics for custom-design of Helmholtz coils and I like to thank the Institute of Technical Chemistry for their

custom designed electrodes which I needed for experimental setups. With your close collaborations you enabled big progress in short time.

I like to thank my colleagues from the Institute of Microwave and Wireless Systems: Special thanks go to Lukas Grundmann with whom I shared an office, discussed a lot of ideas and who always had an open ear and asked the right questions. I also like to thank my colleagues Leonardo Jonathan Mörlein, Dr. Nikolai Peitzmeier, Steffen Seewald, Axel Hoffmann, Bernard Lüers, Dr. Markus Grimm, Timo Martinelli, Henning Hartmann and Steffen Probst. I like to thank my former students Sebastian Frankl and Hendrik Jäschke who supported me in my work at the Institute and subsequently became colleagues.

Finally, I like to thank all my family and friends. Special thanks go to my sister Dr. Neda Meshksar for bringing extra fun and joy into my life and always providing the moral support of an older sister, and I thank my mother Susan Mortazavi for her tireless love and support, and for her deep trust in me. She provides me with roots and with wings. I thank Franz Harke, my dedicated husband for providing me continuous encouragement, and Lia Harke, our daughter who brings the most beautiful moments and the deepest love into my life.

Kurzfassung

In der Biomedizin werden elektromagnetische Felder (EMFs) vielfältig eingesetzt. Bei Frequenzen unterhalb des Mikrowellen-Spektrums können elektrische und magnetische Felder häufig als entkoppelt betrachtet werden. Die Reprogrammierung ist ein Beispiel in dem biologische Zellen (und Gold Nanopartikel) einem Magnetfeld ausgesetzt werden. Bei Tumor Treating Fields (TTFields) hingegen werden elektrische Felder angewandt.
Die Reprogrammierung von Zellen ist ein wichtiger Bestandteil der regenerativen Medizin und eine vielversprechende Behandlungsstrategie für degenerative Krankheiten wie Parkinson. *In vitro* und *in vivo* Studien haben gezeigt, dass eine Magnetfeld-Exposition von Zellen in Kombination mit Gold Nanopartikeln (AuNPs) zu einer Verbesserung der Umwandlungsrate führen kann. Dabei ist die initiale Wirkung zwischen Magnetfeldern und Zellen unter Einbezug physikalischer Gesetzmäßigkeiten noch nicht geklärt. TTFields sind seit 2015 in Deutschland für die klinische Anwendung von Glioblastomen zugelassen und stellen somit eine relativ neue Bahandslungsmethode für diese hoch malignen Tumore dar. Wirkungen der Felder auf die Tumorzellen sind unter Einbezug physikalischer Gesetze auch hier nicht abschließend geklärt.
Diese Arbeit trägt zur Aufklärung der initialen Wirkung von EMFs auf Zellen und Zellen mit AuNPs bei. Es werden elektromagnetische Parameter betrachtet, die bei TTFields und der Reprogrammierung üblich sind. Analytische und numerische Berechnungsverfahren, die die Berechnung von Feldverteilungen ermöglichen, werden evaluiert und angewandt. Diese Berechnungen sind Grundlage für die Bewertung möglicher Wirkmechanismen. Weiterhin wird ein elektrisches Ersatzschaltbild-Modell für eine Zelle entwickelt, das im Vergleich zu anderen Modellen, sowie analytischen und numerischen Berechnungen, die Näherung der elektrischen Feldverteilung in verschiedenen Zellschichten vereinfacht. Zusätzlich wird ein kapazitiver Messaufbau mit Platinschwarzelektroden vorgeschlagen, der die Bestimmung der Leitfähigkeit von Ionenlösungen auch bei vergleichsweise niedrigen Frequenzen von einem Kilohertz ermöglicht. Dieser ermöglicht die zukünftige Berücksichtigung der elektrischen Eigenschaften von Nährmedien in Berechnungen. *In vitro* Zellversuche dienen u.a. der Validierung theoretischer Ergebnisse. Dafür wird ein verbesserter Aufbau vorgeschlagen, der es ermöglicht, Zellen mehreren Polarisationsrichtungen von elektrischen Feldern auszusetzen, während gleichzeitig eine höhere Homogenität der elektrischen Felder erzielt wird. Zusammenfassend leistet diese Arbeit einen wichtigen Beitrag im Bereich der Bioelektromagnetik

Abstract

In the context of biomedicine, electromagnetic fields are utilized in a variety of applications, such as cellular reprogramming. At frequencies below the microwave spectrum, electric and magnetic fields can often be considered as decoupled. Controlled reprogramming is an example in which biological cells (and gold nanoparticles) are exposed to an external magnetic field. In contrast, tumor treating fields (TTFields) subject tumor cells to an external electric field.

The controlled reprogramming of cells is an important part of regenerative medicine and a promising treatment strategy for degenerative diseases like Parkinson's. In biological *in vitro* experiments with cell cultures and in some *in vivo* studies, it has been shown that exposure of cells in combination with gold nanoparticles (AuNPs) to magnetic fields can lead to a significant improvement in cell conversion rates. However, the initial interaction between magnetic fields and cells involving physical laws is still not fully understood. TTFields have been approved for clinical use in Germany for the treatment of glioblastoma since 2015, resulting in a relatively new treatment method for these highly malignant tumors. The effects of TTFields on tumor cells have been extensively studied in association with physical laws, but are not yet fully resolved.

In this thesis, I contribute to the understanding of the initial effect of electric and magnetic fields on cells and cells with gold nanoparticles. In particular, electromagnetic parameters are examined that are typical for TTFields and cellular reprogramming. I evaluate and apply analytical and numerical methods to calculate electromagnetic field distributions. These calculations serve as the basis for the assessment of possible mechanisms of action. Furthermore, an electric lumped element model for a cell is developed which compared to other models, analytical calculations and numerical electromagnetic simulations, simplifies the approximation of the relative electric field distribution in different cell layers. Additionally, to allow future consideration of electrical properties of nutrient media in calculations a capacitive measurement setup with platinum black electrodes is tested and proposed. This setup allows the determination of ion solution conductivity reliably even at relatively low frequencies around one kilohertz. *In vitro* cell experiments are important for the validation of theoretical results. In this regard, an improved setup for the *in vitro* exposure of cells to electric fields is presented, which allows the exposure of cells to more electric field polarization directions by simultaneously allowing higher electric field homogeneity. In conclusion, this thesis makes an important contribution to the field of bioelectromagnetics.

Contents

1 Introduction

Electromagnetic fields (EMFs) are used in the frame of versatile biomedical applications. Thereby, EMF frequency is a determining parameter for the interaction of EMFs with treated tissues. While higher frequencies are predominantly associated with heating of biological tissue [10], EMFs in the low and medium frequency spectrum (with a frequency up to $3\,\mathrm{MHz}$) are in the focus of many biomedical studies since their application is known to promote or inhibit biological processes. EMFs are for example used in regenerative medicine. The healing or replacement of diseased tissues and organs with minimal side effects is one major target in regenerative medicine. Treatment of affected parts with triggering of endogenous body mechanisms is one promising approach to reach this target. The key building blocks of every tissue and organ are biological cells. The control over cellular mechanisms would be a milestone in regenerative medicine.

Cellular reprogramming refers to the modification of epigenetic markers for the conversion of cell type or for the alteration of developmental potential (the ability of a stem cell to differentiate into different cell lineages [11]). Thus, cellular reprogramming is a promising application to be used e.g. for the treatment of Parkinson. Parkinson is a disease where dopaminergic neurons in the midbrain die. The reprogramming of somatic cells as fibroblasts into dopaminergic neurons provides one promising approach for the treatment of the neurodegenerative disorder [12, 13]. However, conventional reprogramming methods often lack efficiency [14] which means that the conversion rate of cells is low.

Enhancement of existing reprogramming methods are of major interest. It was shown that exposure of cells and gold nanoparticles (AuNPs) to EMFs in the low frequency spectrum can enhance the drawback of poor reprogramming efficiency [13]. One hypothesis is that AuNPs cause a local enhancement of magnetic field strength which affects biological responses towards a higher reprogramming efficiency [13, 15]. A similar rationale led to the use of graphene nanosheets in combination with EMFs [16]. Furthermore, during reprogramming, besides AuNPs also magnetic nanoparticles have been applied in combination with EMFs [17, 18]. However, AuNPs have the advantage of higher bio-compatibility than many other nanoparticle materials [19, 20].

While for cellular reprogramming the magnetic field component is in the focus, Tumor Treating Fields (TTFields) is a medical application example where the electric field component is of major interest. TTFields are electric fields with an electric field magnitude $E \approx 100\,\mathrm{V_{RMS}/m}$ and a frequency $100\,\mathrm{kHz} < f < 500\,\mathrm{kHz}$, used to slow down the proliferation of glioblastoma cells (highly malignant brain tumor cells). Different clinical studies showed an impact of TTFields on cancerous cells up to some months of progression free survival [21].

During cellular reprogramming and TTFields application, the mechanisms of interaction between EMFs and biological cells from a perspective of physical laws are still not fully understood [1, 13, 22]. Biological cells consist of different cell compartments with specific functions and complex reaction cascades. While biological responses to the treatment of cells with EMFs are well studied [13, 21, 23] it is still difficult to determine the initial interaction of the EMFs with a cell. Furthermore, the impacts of AuNPs in combination with EMFs are not clear yet [13]. These gaps in knowledge aggravate a systematic enhancement of reprogramming efficiency as well as tumor treatment efficiency. A good understanding of the interaction mechanisms with consideration of physical laws has the potential to determine and tune relevant parameters (like frequency or field intensity) for further enhancement of the respective application.
This thesis contributes to the investigation of interactions of sub MHz EMFs with cells and AuNPs from a physical perspective. Due to the relatively low frequencies and the considered electromagnetic material properties of cells, the electric and magnetic field components can be regarded as decoupled [2]. Thus two application examples (TTFields and cellular reprogramming) are chosen, while considering the magnetic field with typical parameters from cellular reprogramming and the electric field with typical parameters from TTFields. Thereby, the thesis is structured as follows:
After the introduction, the second chapter covers the theoretical basics. Electromagnetic exposure parameters used during cellular reprogramming and the related field of cell differentiation as well as the application of nanoparticles with focus on AuNPs are introduced. Subsequently an introduction to TTFields follows. After the application examples are explained, the state of the art of electromagnetic modelling of biological cells is introduced to provide a solid basis for the calculations of EMF distributions. In this regard, existing lumped element models of cells and the state of the art of numerical modelling of cells with full-

wave simulations are introduced. Furthermore, the physics of EMFs at material interfaces are explained, which leads to the introduction of Mie Scattering. Subsequently, known impacts from EMFs on biological cells with consideration of physical laws are explained, which provides the basis for the determination of possible interaction mechanisms. Finally in the theoretical basics, existing experimental approaches are introduced. The state of the art of *in vitro* reprogramming and TTFields experiments with cell cultures, which allow the validation of theories with associated calculations, are explained. Furthermore, experimental setups are introduced, which can enable the measurement of material parameters, to be used in analytical and numerical calculations.

In the third chapter, the magnetic field interaction with cells and AuNPs is in the focus. The Fourier Analysis of the often used pulsed electromagnetic field (PEMF) excitation allows the determination of relevant spectral components for subsequent investigations. Calculated results of magnetic field distributions within cells and AuNPs are presented and based thereon, mechanisms of action are assessed. The results are discussed. Finally, a first version of implementation of an exposure setup for *in vitro* experiments is presented.

Chapter four covers the electric field interaction with cells. A new concept of an electric lumped element model of a cell is introduced. This lumped element model is adaptable to different cells and allows an approximation of the electric field distribution within cells. The applicability of the new lumped element model is shown by electric field calculations within a model cell and comparison to Mie Scattering and numerical electromagnetic full-wave calculations. The exposure of AuNPs to electric fields is also considered and possible outcomes of mechanisms of action are evaluated. Subsequently, the results are discussed. Afterwards, an enhanced design of *in vitro* cell culture experimental setup is introduced, which in contrast to existing designs allows higher electric field homogeneity while also allowing more polarization directions of the electric field relative to the cell. Finally and to allow the consideration of cell culture medium in future investigations, the implementation of a capacitive measurement method is shown which allows the measurement of the specific conductivity of solutions containing ions even at frequencies down to around one kHz.

Chapter five is a conclusion and outline of this work, where the results are summarized and ideas for possible further studies are provided.

2 Theoretical Basics

2.1 Cell Differentiation and Cellular Reprogramming

Cells are the building blocks of human tissues and every human cell develops from stem cells. As the origin of all human cells, stem cells are of major interest in regenerative medicine as they can be applied for healing or replacement of diseased tissue [24].

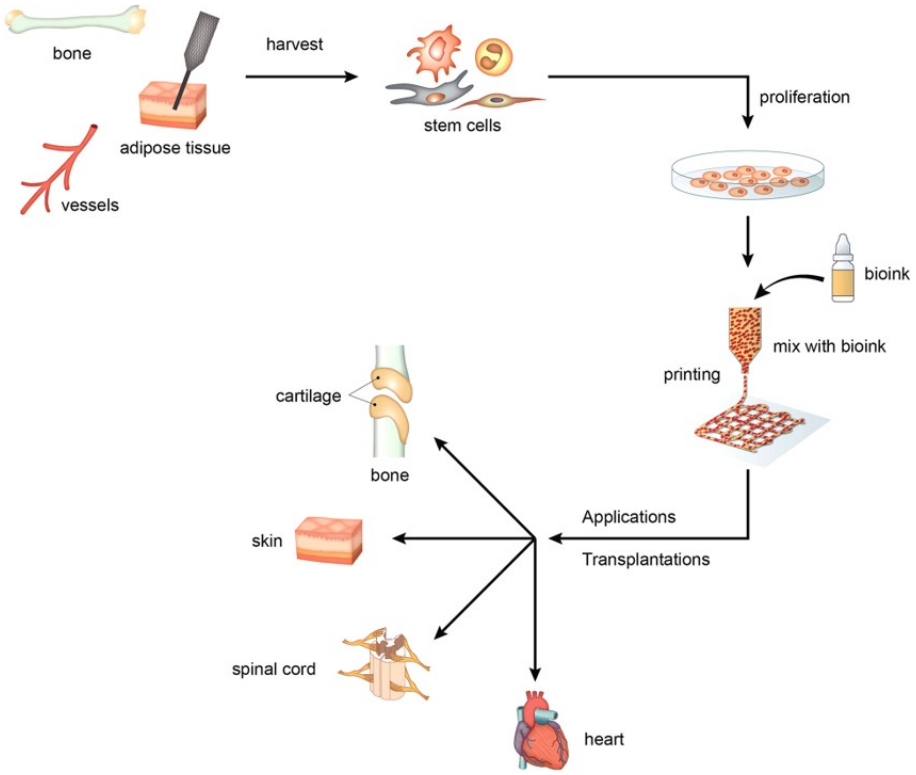

Figure 2.1: Principle of 3D bioprinting from stem cells [25].

Figure 2.1 shows an example of application of stem cells in tissue engineering: 3D tissue printing. Stem cells can be extracted from a donor or a patient and reproduced *ex vivo*. Depending on the structure of the tissue to be printed a single cell type or multiple cell types

can be used. The cells are placed in bioink which is usually hydrogel providing an appropriate environment for the cells e.g. by containing chemicals for cell growth. The printed synthetic tissue can be transplanted. While the development of different complex tissues is the focus of current research, structures like a meniscus can already be printed [26].
Besides the *ex vivo* processing of stem cells there are also approaches for *in vivo* manipulation of stem cells to achieve the repair of damaged tissue, e.g. with stem cell-based bone regeneration in mice [27].
The different approaches in regenerative medicine make use of the two fundamental abilities of stem cells: the ability to self-renew and the ability to differentiate into many cell lineages [28]. Self-renewal is the process of cell division. The cell lineage describes the development path of the initial stem cell to the cell it develops (differentiates) into [29]. The plasticity (also known as developmental potency) determines the range of cell lineages the cell can differentiate to [11]. Thus, the higher the potency of a cell is, the more developmental opportunities does the cell have.

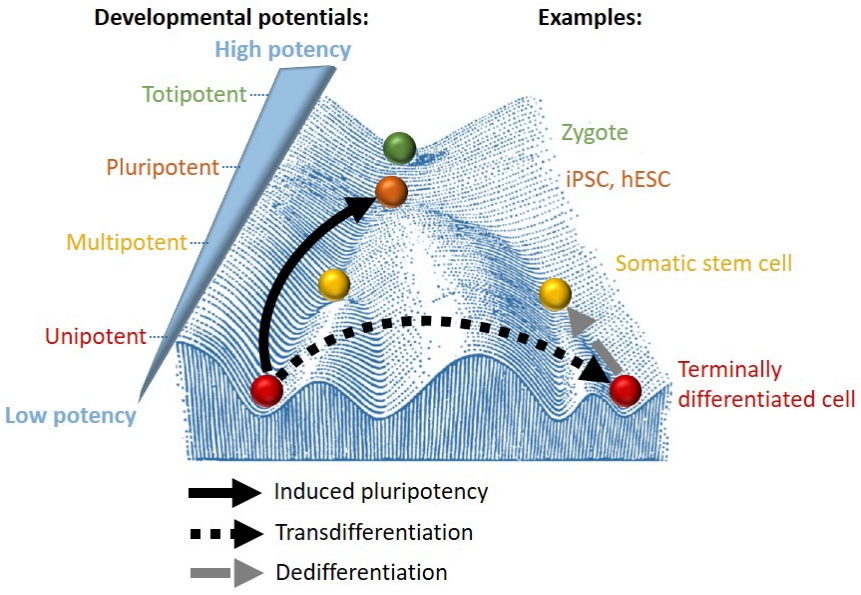

Figure 2.2: Developmental potentials of cells on the basis of Waddington's epigenetic landscape model [30] (modified reprint from [31]).

Different levels of potency are distinguished. Conrad Hal Waddington described the developmental potential of a cell with his epigenetic landscape model [30], which is the basis of

Figure 2.2. In Waddington's model, a marble rolling down a hill into a valley is used as an allegory for the loss of developmental potential of a cell. Each passed bifurcation point represents progressive loss of possibilities for the cell to develop into other cell lineages. In **Figure 2.2** the different colors indicate the respective differential potential as well as a related example for a cell. After human fertilization, the zygote is the stem cell with highest potency (totipotent). A zygote can i. a. differentiate into an human embryonic stem cell (hESC) which is a pluripotent cell and which can develop to a cell of the three germ layers. Cells with a multipotent plasticity have less self-renew capacity than pluripotent cells [32, 33] and can develop into a relatively narrow spectrum of terminally differentiated cells (e.g. blood stem cells, which can further differentiate into several blood cells).

The process of differentiation is unidirectional. During differentiation a cell develops from a state of higher potency towards a state of lower potency. However, cells can be manipulated into cells of other lineages or cells with higher developmental potency. Dedifferentiation is the reverse process of differentiation (**Figure 2.2**, gray arrow). During induced pluripotency, highly specialized (unipotent) cells are driven into a pluripotent state, resulting in induced pluripotent stem cells (iPSCs) (**Figure 2.2**, black arrow). During transdifferentiation cells are transformed to other cells outside their natural cell lineage (**Figure 2.2**, dashed black arrow). Another example for transdifferentiation than the one shown in **Figure 2.2** is the transformation of an unipotent cell into a somatic stem cell of other cell lineage [34]. Furthermore, a transdifferentiated cell can be an unipotent cell or a somatic stem cell obtained from a somatic stem cell of another lineage [34].

Differentiation, induced pluripotency, transdifferentiation and dedifferentiation can be used for cellular reprogramming. According to Lujan et al. [35] there are three major approaches to reprogramming. One reprogramming procedure involves the reprogramming of a differentiated cell into a stable iPSC (direct reprogramming) and subsequent differentiation of the iPSC to the target cell. Compared to the first approach, a second approach leads through an unstable iPSC state and is referred to as indirect reprogramming. A third approach is the transdifferentiation of a differentiated cell into another fully differentiated cell and thus also a form of direct reprogramming.

The reprogramming to iPSCs results in similar properties as in embryonic stem cells, e.g. high self-renew capacity and high potency, both attractive properties for deployment in regenerative medicine. While embryonic stem cell research is controversial and heavily restricted in many countries [33, 36, 37] research with iPSCs is not facing such obstacles. However, iPSCs

are associated with relatively high carcinogenic potential [38, 39]. Reprogramming in form of transdifferentiation avoids the pluripotent state and thus circumvents the carcinogenic potential associated with iPSCs. However, conventional reprogramming methods, whether through iPSCs or through transdifferentiation, often lack efficiency [14, 40, 41]. Thus, enhancement of existing reprogramming methods is of major interest. The application of EMFs and nanoparticles in the frame of reprogramming is one promising approach.

2.1.1 Electromagnetic Exposure Methods and Parameters

The application of EMFs in the frame of cell differentiation and cellular reprogramming is very diverse. In the frame of cell differentiation processes and reprogramming many different exposure setups have been applied. Information concerning experimental setup of the individual studies and also information concerning applied EMF parameters are provided in different depths. For this thesis, due to the vast number of studies available, only representative full-text articles have been considered where the EMF excitation method was identifiable. Although, an in-depth literature review was conducted, the studies listed here do not mirror the full range of published studies. One example for a relatively comprehensive literature review is provided by Maziarz et al. [42].

As part of the literature research, three superordinate categories have been established for different EMF exposure parameters and setups, namely:

- Extremely low frequency EMFs (ELF-EMFs),
- Pulsed EMFs (PEMFs) and
- Piezoelectric and Triboelectric Nanogenerators (PENGs and TENGs).

ELF-EMFs and PEMFs are integral to this thesis as these excitation forms are mainly applied during cellular reprogramming, induced pluripotency and induced differentiation. Table 2.1 offers a representative overview of relevant studies on induced pluripotency, combined EMFs

Category	Ref., Year	NP characteristics	Treated cells	Excitation
Induced Pluripotency	[43], 2014	–	mouse fibroblasts and human dermal fibroblasts	ELF-EMF
Reprogramming	[13], 2017	Thiol-capped AuNPs	Mouse fibroblasts to induced dopaminergic (iDA) neurons, Human peripheral blood cells to human iDA neurons and *in vivo* in Parkinson disease mouse models.	PEMF
	[15], 2021	AuNPs conjugated with Arg-Gly-Asp (RGD) peptides	*In vivo* injection into dentate gyrus of morris water mice hippocampi	ELF-EMF
	[16], 2021	graphene nanosheets	*In vivo* mice Glia cells into (iDA) neurons	ELF-EMF
Induced Differentiation	[44], 2013	Polyethylene glycol (PEG) -ylated Fe_3O_4 NPs	hBM-MSCs *in vivo* in rats	PEMF
	[18], 2014	PEG-phospholipid encapsulated Fe_3O_4 NPs	hBM-MSCs	ELF-EMF
	[17], 2014	PEG-phospholipid encapsulated Fe_3O_4 NPs	hBM-MSCs	ELF-EMF

Table 2.1: Representative studies in the fields of induced pluripotency, reprogramming and induced cell differentiation with application of ELF-EMFs or PEMFs and NPs.

and NPs promoted cellular reprogramming, and EMFs and NPs promoted induced cell differentiation. As the amount of studies related to cellular reprogramming is relatively low, cell differentiation studies have also been considered, and a tabular overview of representative EMF promoted cell differentiation studies is provided in table 6.1 of the annex. Since PENGs and TENGs are motion-activated, their use is mainly restricted to *in vivo* studies.

Although there are other less common EMF stimulation methods used for cell differentiation, including the application of static electric and magnetic fields [45, 46] and the Radio Electric Assymetric Conveyer used for cellular reprogramming [47–50], these were not used for analysis in this study due to lack of detail on the waveform of the emitted EMFs. It is also worth noting that electromagnetic stimulation in cells can be achieved with pharma-

cologicals, which can alter transmembrane potential [51].

In the following, the three categories (ELF-EMF, PEMF, and PENGs/TENGs) will be explained in more detail.

Extremely low frequency electromagnetic fields
When extremely low frequency EMFs (ELF-EMFs) are applied, exposure to sinusoidal magnetic fields is in the focus of the respective study. An overview of parameters applied in the frame of ELF-EMF is provided in table 2.2. Most studies applied frequencies around $f = 50\,\mathrm{Hz}$ and magnetic flux densities around $B = 1\,\mathrm{mT}$.

Frequency	Magnetic flux density	Reference
$1\,\mathrm{Hz} \leq f \leq 100\,\mathrm{Hz}$	$5\,\mu\mathrm{T} \leq B \leq 1\,\mathrm{mT}$	[52]
$f = 7\,\mathrm{Hz}$	$B = 100\,\mu\mathrm{T}$	[53]
$f = 15\,\mathrm{Hz}$	$B = 1\,\mathrm{mT}$ and $B = 5\,\mathrm{mT}$	[54, 55] and [56, 57]
$f = 30\,\mathrm{Hz}$ and $f = 45\,\mathrm{Hz}$	$B = 1\,\mathrm{mT}$	[58] and [17]
$f = 50\,\mathrm{Hz}$	$0.2\,\mathrm{mT} \leq B \leq 5\,\mathrm{mT}$	[16, 18, 39, 43, 59–64]
$f = 60\,\mathrm{Hz}$	$B = 0.7\,\mathrm{mT}$ and $B = 0.2\,\mathrm{mT}$	[65] and [15]

Table 2.2: Overview of representative ELF-EMF exposure parameters.

Pulsed electromagnetic fields
In the frame of PEMF excitation, the excited magnetic field can consist of symmetrical or unsymmetrical pulses with a specific on-time and a specific off-time repeating with a repetition frequency f_{rep} [66–69]. Furthermore, these pulses can be modulated with higher frequency bursts [13, 44, 70–76] with an on-time t_{burst} and a burst repetition frequency f_{burst}. **Figure 2.3** shows an example of a PEMF excitation containing high frequency bursts. There, the burst duration is $t_{\mathrm{burst}} = 0.25\,\mu\mathrm{s}$, the burst repetition frequency is $f_{\mathrm{burst}} = 4\,\mathrm{kHz} = 1/0.25\,\mathrm{ms}$ and the repetition frequency is $f_{\mathrm{rep}} = 50\,\mathrm{Hz} = 1/20\,\mathrm{ms}$. *N* corresponds to the number of bursts. The shape of the bursts as well as the shape of the modulated excitation is rectangular in this example.

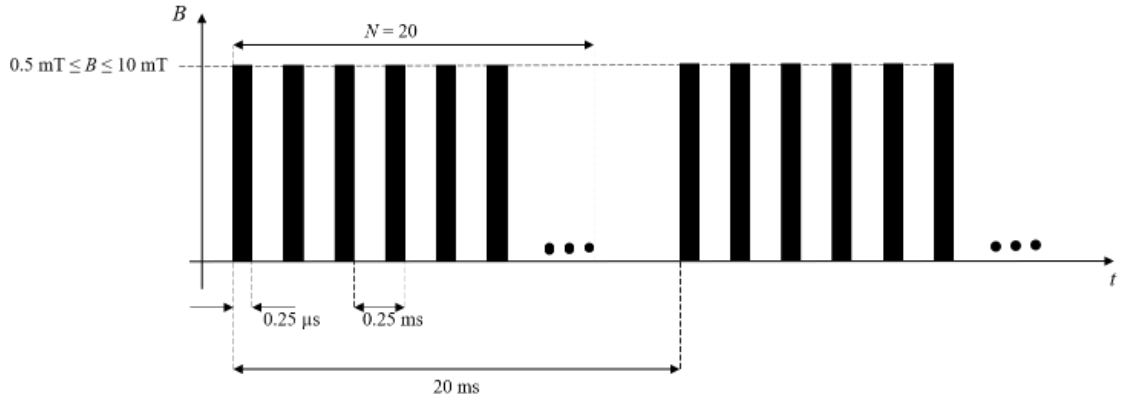

Figure 2.3: Example of PEMF excitation used in [13, 44, 70].

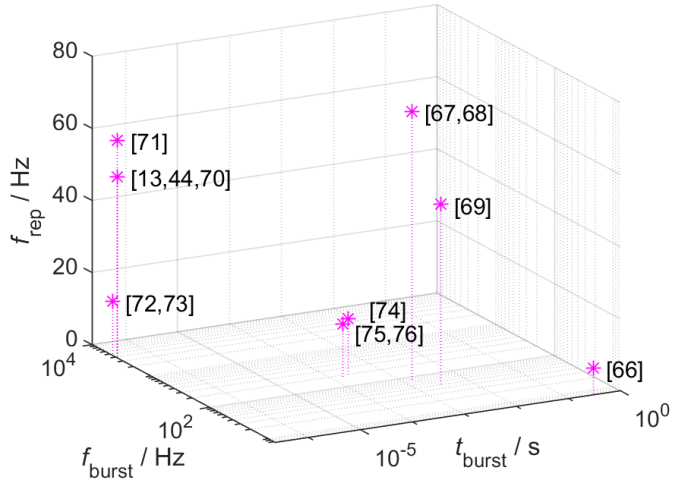

Figure 2.4: PEMF parameters chosen in the studies listed in the tables 6.1 and 2.1.

Figure 2.4 shows a three-dimensional plot of the parameters t_{burst}, f_{burst} and f_{rep} used in the studies with PEMF excitation from the tables 6.1 and 2.1. There, t_{burst} and f_{burst} are shown in logarithmic scale. The values in the square brackets indicate the corresponding references. The shapes of the applied pulses are not considered in this plot.

In **Figure 2.4** f_{rep} is within the range $7.5\,\mathrm{Hz} \leq f_{\mathrm{rep}} \leq 75\,\mathrm{Hz}$. This frequency range is very close to the so called *extremely low frequency* band, which includes frequencies from $3\,\mathrm{Hz}$ to $30\,\mathrm{Hz}$ [77]. In the studies [13, 44, 70–73] bursts with frequencies around $f_{\mathrm{burst}} = 4\,\mathrm{kHz}$ were applied. This frequency lies in the so called *very low frequency* band [77]. In the other

seven publications shown in **Figure 2.4**, the burst frequencies are equal or very close to the repetition frequency of the respective study (within the extremely low frequency or super low frequency band [77]). $f_{\mathrm{burst}} = f_{\mathrm{rep}}$ means that only a regular pulse is applied without any modulating bursts. In this case, the burst duration t_{burst} is the on-time of the pulse.
Figure 2.4 shows, that without consideration of the exact pulse shape and without consideration of the magnetic flux densities applied, the representative studies can be categorized by consideration of the characteristic parameters t_{burst}, f_{burst} and f_{rep}. Two categories can be obtained:

1. Studies with a burst frequency around $f_{\mathrm{burst}} = 4\,\mathrm{kHz}$ [13, 44, 70–73] and
2. studies with f_{burst} around or equal to f_{rep} and with a pulse duration in the range of $0.15\,\mathrm{ms} \leq t_{\mathrm{burst}} \leq 3\,\mathrm{ms}$ [66–69, 74–76].

The magnetic flux densities applied with PEMF excitation are in a range between $B = 0.13\,\mathrm{mT}$ and $B = 10\,\mathrm{mT}$ [66, 71].
The studies using PEMF in combination with nanoparticles applied an excitation according to **Figure 2.3**. This is the PEMF excitation analyzed and considered in the frame of the investigations for this work.
Beyond the presented PEMF excitation parameters, there are also niche categories of PEMFs in the frame of cell differentiation and cellular reprogramming, e.g. high-intensity pulsed electromagnetic stimulation (HIPEMS) [78], biphasic electric current (BEC) stimulation [79–81] and nanosecond pulsed electric fields (nsPEFs) [82]. HIPEMS are characterized by their relatively high magnetic flux densities between $B = 0.5\,\mathrm{T}$ and $B = 10\,\mathrm{T}$. In the frame of BECs two successive almost rectangular electric pulses of opposite polarities are applied [79–81]. When nsPEFs are applied in the frame of cell differentiation, the excited electric pulse durations are in the nanosecond scale. Furthermore, there are many different off-the-shelve devices for the generation of PEMFs applying different wave-forms. One example of such a device used in the frame of cell differentiation generates different square wave sequences over a specific period of time [83, 84]. However, the reason behind the choice of specific excitation parameters is usually not provided.

Piezoelectric and triboelectric nanogenerators
EMF excitation with PENGs and TENGs depend on a mechanical force exertion and are therefore rather applied in the context of *in vivo* studies. PENGs and TENGs are usually motion

activated by the individual to be treated. Thus, the excited EMF is as irregular as the motion which excites it [85]. Due to the irregular EMF excitation, nanogenerators are not suited for an initial investigations of mechanisms of action between EMFs and cells. Furthermore, the working principle of TENGs is in the scope of relatively recent research [86–88]. However, as described before, PENGs and TENGs are out of the scope of this work.

In conclusion, several studies provide valuable insights into EMF promotion of differentiation and reprogramming with very different cell lineages as can be seen in table 6.1 of the annex and in studies of table 2.1. Many different exposure setups were developed and far more exposure parameters such as magnetic and electric field intensities, frequencies and general wave-forms as well as durations of exposure and exposure repetition rates have been applied.

2.1.2 Application of Nanoparticles

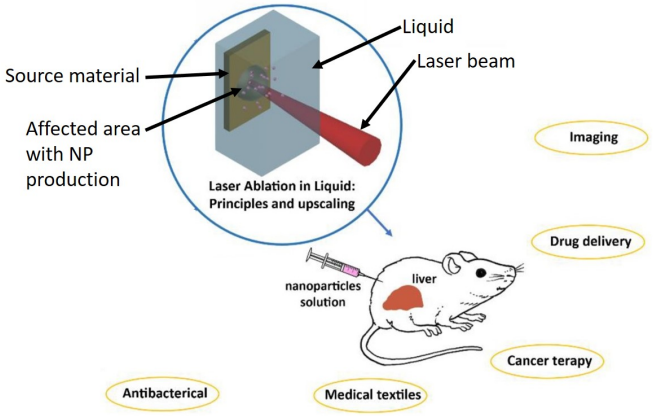

Figure 2.5: Examples of areas using nanoparticles generated by laser ablation in liquids. Modyfied illustration from [89].

Particles within a size range between $1\,\mathrm{nm}$ and $100\,\mathrm{nm}$ are often defined as nanoparticles [90, 91] (the exact size range is controversial [92]). Nanoparticles can be synthetically produced but also occur naturally, e.g. as a product of combustion or in form of ultrafine grains of sand [93]. There are different techniques allowing the synthetic production of

nanoparticles. A short summary of techniques is provided by Wolfgang R. Fahrner [94]. For example, nanoparticles can be produced with laser-ablation. During laser ablation a high energetic laser beam removes particles from a bulk source material. This method has the advantage that the produced nanoparticles have the same material composition as the source bulk material [94, 95]. **Figure 2.5** shows examples of areas related to biomedicine where laser ablated nanoparticles are used [89] such as imaging and cancer therapy. In each of the fields a whole range of different nanoparticles are applied, e.g. shown by Han et al. for biomedical imaging [96].

Figure 2.6 illustrates different properties of nanoparticles. Nanoparticles can be classified by a variety of different characteristics, like size, material and shape. A key feature of nanoparticles is their high surface-area to volume ratio. Thus, compared to bigger bulk materials, a higher ratio of atoms is located at the surface, which results in size-dependent alteration of chemical and physical properties of a nanoparticle [93]. Furthermore, nanoparticles can be polymetric, inorganic or lipid based [97], and they exist in different shapes [98]. Moreover, properties of nanoparticles like biocompability can be altered by coatings and noparticles can be functionalized to bind to specific target molecules.

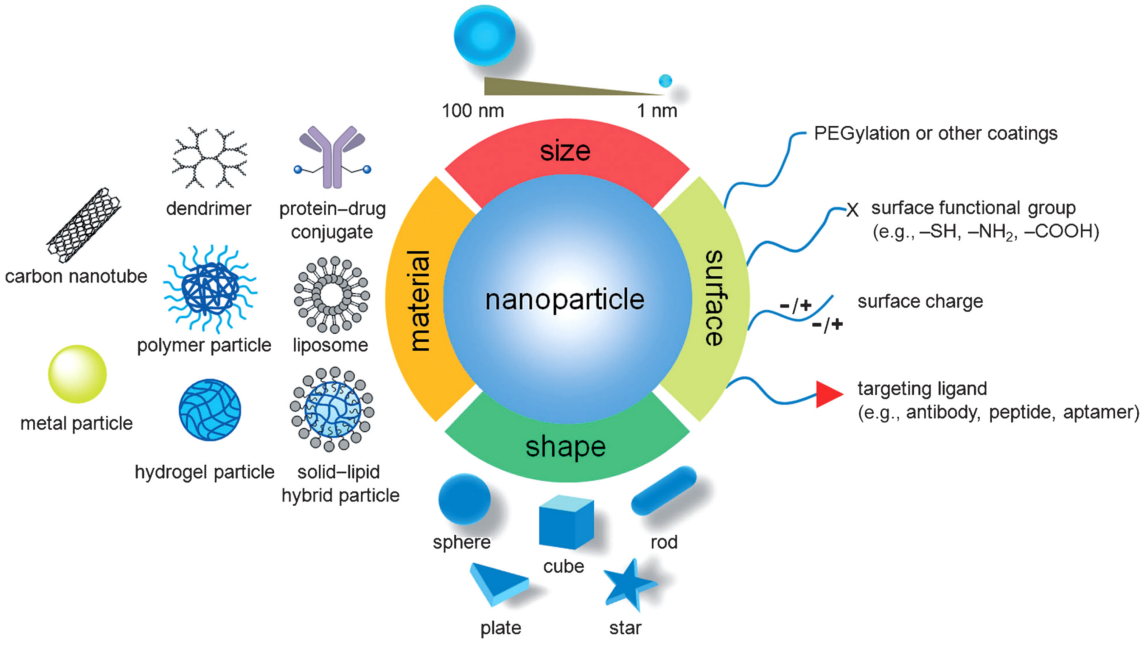

Figure 2.6: Examples of different nanoparticle properties from [99, 100].

When in contact with a cell membrane, nanoparticles can be brought into a cell by different uptake mechanisms [101, 102]. Thereby energy-dependent uptake pathways are distinguished from energy-independent uptake pathways such as diffusion [102]. The entering pathway of a nanoparticle depends on different factors as size of the nanoparticle, its shape, its surface functionalization as well as surface charge, but also on abilities of the cell which it is in contact with [101].

The process of endocytosis describes different energy-dependent uptake pathways of cells. The most common pathway for nanoparticles is receptor-mediated endocytosis, which is illustrated in **Figure 2.7**. The principle of receptor-mediated endocytosis is that a ligand, which is bound to a nanoparticle bounds to a receptor molecule of the cell membrane. The binding triggers the formation of the invagination process. At the end of the process, an early endosome (the product vesicle including the NP) is formed which is located in the cell [103]. The early endosome develops further into a late endosome with susscessive dissipation of the vesicle, leading to endosomal release in the cytoplasm [103]. The nanoparticles can remain within the cytoplasm or be forwarded into the nucleus, triggering biological reaction cascades.

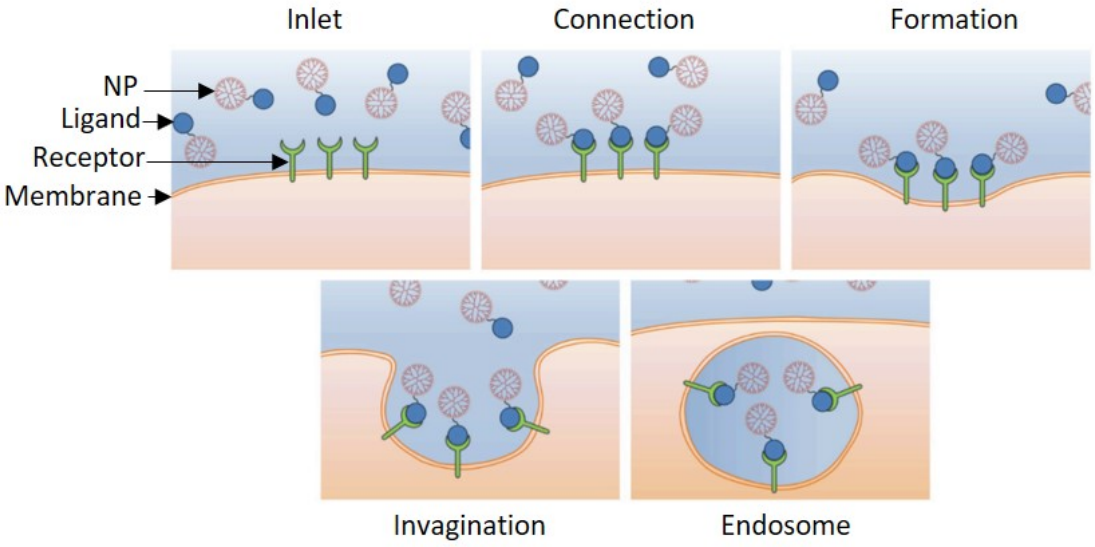

Figure 2.7: Endocytosis of a nanoparticle. Modyfied illustration from [102].

In the frame of cell differentiation many different NP materials as gold, silver and carbon based nanoparticles have been investigated [104]. Due to the different chemical and physi-

cal properties of the nanoparticles, their versatile interactions with cells are not fully understood [104]. However, it is known that nanoparticles can promote cell differentiation as they e.g. mechanically trigger signaling pathways or function as carries of nucleic acids relevant in cell differentiation [104]. A variety of review articles provide a thorough overview on the nanomaterials used, treated cells and chemical modifications of the particles [104–106].
Compared to other nanomaterials, gold nanoparticles (AuNPs) are known for their low toxicity and ease of sythesization [107]. With these attributes, AuNPs are strong candidates for application in induced cell differentiation [107]. Thus, AuNPs are i.a. applied for induced mesenchymal stem cell, embryonic stem cell and neuron cell differentiation [107]. In this regard, AuNPs in a range of different sizes, different shapes and with different surface coatings were applied [107]. Furthermore, the particles were led into the cells or formed scaffolds on which cells were planted, triggering a range of different biological processes which are subject of current investigations [107].
Cellular reprogramming is a process where cells are changed due to modifications on epigenetic marks. In contrast to alteration of deoxyribonucleic acid (DNA) sequences, modification in epigenetics allows the regulation of the expression of genes. This regulation can be achieved by penetration of a cell with specific reprogramming factors as for example transcription factors, which can lead to iPSCs.
The cell penetration of reprogramming factors can be achieved with viruses. However, during application of viruses the carcinogenic potential might be enhanced [38, 39]. Non-viral delivery methods for reprogramming factors, such as the electroporation of cell membranes and the transport by nanoparticles are in the focus of interest [106].
In electroporation a static electric field is applied to the cells. Under the electric field, the outer cell membrane, the lipid bilayer, forms pores allowing foreign substances to enter the cell. The foreign substances usually include messenger ribonucleic acid (mRNA). A disadvantage of this reprogramming method is that treated cells show immune responses which are activated by introduction of long mRNAs [106, 108]. Thus, an alternative delivery method includes nanoparticles. EMFs in combination with NPs have been applied as genetic transporters for reprogramming of cells. Due to their size, NPs have a relatively large surface area, allowing molecular cargo [106]. In magnetofection, under a promoting externally applied magnetic field, magnetic NPs can be led and accumulated in close vicinity to target cells [106, 109–118]. Usually, the magnetic fields are realized by application of permanent magnets [110, 112] with magnetic flux densities around up to $B = 250\,\mathrm{mT}$ [112, 117]. The

high concentration of the nanoparticles in close vicinity of the cell leads to unspecific endocytosis [119]. Thus, during magnetofection, the cell's membrane remains intact, which is an advantage of the method compared to electroporation. Furthermore, relatively high transfection efficiencies and also high reprogramming efficiencies can be achieved [106].
Magnetofection is usually conducted with superparamagnetic iron oxide nanoparticles (SPIONs) [109, 115, 116, 118]. To enhance biocompatibility of iron oxide NPs, a coating is necessary prior to application [120, 121]. Polyethylene glycol (PEG) is a widely used polymer for nanoparticle coating, i.a. because of non-toxicity and low cost.
Besides SPIONs, also gold nanoparticles (AuNPs) are applied for cellular reprogramming. The reasons thereof are i.a. their biocompatibility, the possibility of non-destructive membrane penetration, tuneable particle size and relatively easy surface functionalization [122]. Compared to other sizes, AuNPs with a diameter around 50 nm are known for their high efficiency to penetrate cell membranes [123]. For the penetration of the nucleus, diameters smaller than 10 nm are known to be better suited [123]. However, the particles need surface functionalization for receptor-mediated endocytosis. AuNPs in combination with PEMFs were used by Yoo et al. for the direct reprogramming of somatic fibroblasts into induced dopaminergetic neurons [13]. Chang et al. applied AuNPs in combination with ELF-EMFs for an increase of hipocampal neurogenesis [15]. In both studies, AuNPs are assumed to be able to locally concentrate and enhance magnetic field intensities, providing the opportunity of locally focused treatment of targeted tissue. This thesis mainly concentrates on the approaches used in this two studies and considers AuNPs in combination with EMFs and PEMFs for treatment of cells.

2.2 Tumor Treating Fields

Glioblastoma represents the most common primary brain tumor in adult patients, generally associated with median overall survival of about 15 months despite contemporary multimodal therapy, involving surgical resection, radiotherapy, and chemotherapy [124, 125]. Tumor recurrence is the case in almost all patients with ultimate mortality close to 100 % [124, 126, 127]. Tumor Treating Fields (TTFields) represent a relatively new treatment modality for malignant tumors, including glioblastoma. Several studies indicate the ability of TTFields to extend progression free survival by several months [21]. The tumor treating field application system used in clinical practice in Germany since 2015 [128] consists of transducer arrays placed non-invasively on the shaved scalp of a patient, which generate alternating electromagnetic fields impacting the brain tumor.

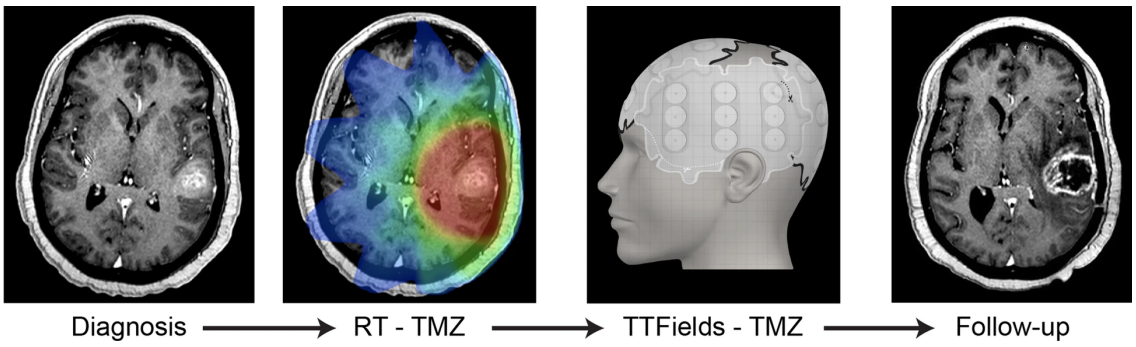

Figure 2.8: Principle approach of TTFields treatment in glioblastoma patients from [129].

TTFields in glioblastoma patients are usually combined with chemotherapy by application of temozolomide (TMZ)[129]. **Figure 2.8** shows the principle treatment approach. First imaging techniques are applied to obtain a diagnosis. The red area in **Figure 2.8** indicates exemplary the affected brain region. Subsequently, patients are treated with radiotherapy as well as chemotherapy with TMZ for a period of three to six weeks. Afterwards, patients can be treated wit TTFields combined with TMZ for a minimum duration of six months or until treatment failure [129].
From a technical point of view the term TTField refers to a sinusoidal electromagnetic field with a frequency $100\,\mathrm{kHz} < f < 500\,\mathrm{kHz}$, and an electric field magnitude $E \approx 100\,\mathrm{V_{RMS}/m}$

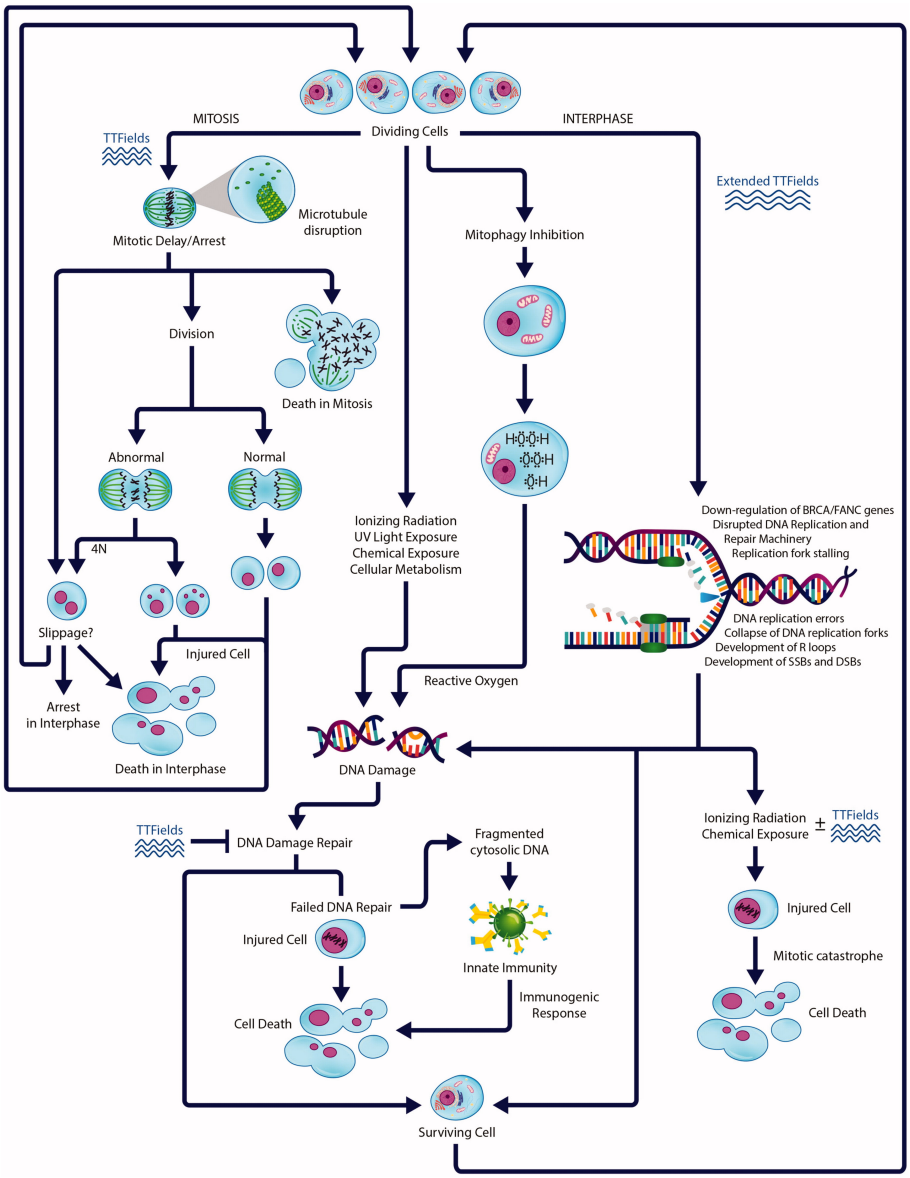

Figure 2.9: Impacts from TTFields on cell replication from [23]. Reprinted by permission of Informa UK Limited, trading as Taylor & Taylor & Francis Group©2023.

at the tumor. While clinical trials have shown the efficacy of treatment with TTFields in glioblastoma patients and exposure setups are approved to be used in clinical practice, the mechanisms of action triggered in tumorous cells by TTFields are still investigated [23]. **Figure 2.9** shows many different pathways of cell division for cancerous cells which are affected by TTFields and TTFields in combination with radio- or chemotherapy. While the details of

the different specific pathways are beyond the scope of this thesis, it can be seen that many different cell compartments and stages of cell division can be disturbed by TTFields. However, deep knowledge about the physical mechanisms of action by which the individual cellular responses are triggered is still missing. A thorough knowledge of mechanisms of action can lead to a systematic improvement of TTFields (specifically TTFields parameters as electric field magnitude and electric field frequency) and is therefore of major importance.

2.3 Electromagnetic Modelling of Biological Cells

To assess the interactions between EMFs and biological tissue, the elementary component of the tissue, the biological cell, is often considered. Depending on the focus and goal of the investigation, different cell models can be applied to study the interactions between EMFs and cells.

During EMF exposure of tissues, whole cell clusters rather than single cells are treated. In the case of *in vitro* studies, cells can be cultured in suspension or in plated forms [130]. Thereby, cells in suspension usually have spherical shapes and adherent cells have rather polygonal morphology [130] or elongated shapes [131]. Furthermore, cells are usually grown in cell culture medium with supplements as nutrient, growth factors as well as components controlling physicochemical properties as the pH of cell culture [130]. Thus, EMFs do not only interact with individual exposed cells and their cell compartments, but rather with cell clusters and the cell culture medium with its ingredients. The scenario of *in vivo* exposure is even more complex. *In vivo*, usually different layers of tissues with different EM properties (like muscle tissue and fat tissue) are treated. The composition of different materials is usually highly inhomogeneous. This brings a high grade of complexity to the assessment of possible interactions between EMFs and biological tissue.

To investigate physiological interaction of EMFs with tissues, *in vitro* experiments are usually conducted before considering the *in vivo* case. However, there are a large number of potential cellular entry points of the EMF mechanisms of action. Theoretical models can be used to limit their amount. In this regard, different tools and approaches are common to get an overview of general electromagnetic behavior of cells.

The most commonly used EM cell model is either a *single-shell* or a *double-shell* model [1, 2, 132–138] of perfectly spherical cells as shown in **Figure 2.10**. Single-shell models of cells contain two cell layers, the plasma membrane and the cytoplasm. Double-shell models contain the layers of the single shell model plus two layers of the nucleus, the nuclear membrane (called nuclear envelope) and the nucleoplasm.

Considering a cell with cell radius $r_{\mathrm{cell}} = 5\,\mu\mathrm{m}$ and the double layer cell model from **Figure 2.10**, electromagnetic and dimensional parameters listed in table 2.3 are typical values for the individual cell layers.

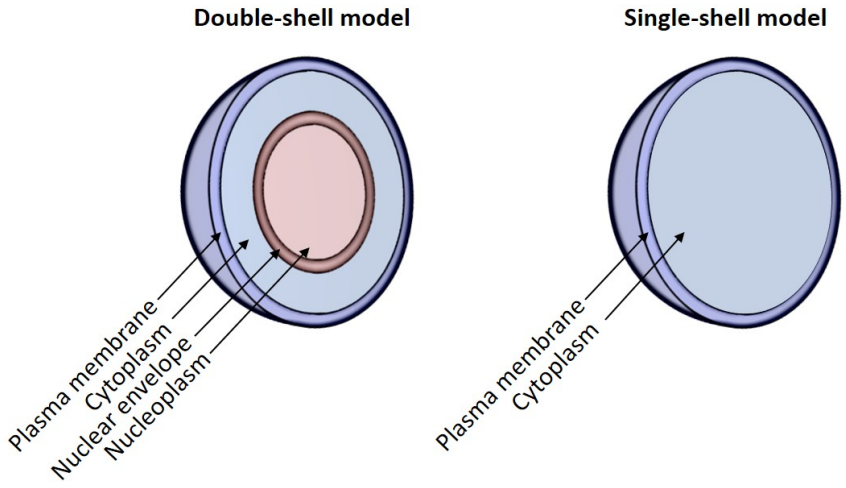

Figure 2.10: Double-shell and single-shell cell model.

Layer	Dimensional parameter	Relative permittivity	Specific Conductivity
Cytoplasm	$r_{\mathrm{cp}} = 5\,\mu\mathrm{m}$	$\varepsilon_{\mathrm{r,cp}} = 80$	$\sigma_{\mathrm{cp}} = 1.3$ S/m
Plasma membrane	$t_{\mathrm{pm}} = 5\,\mathrm{nm}$	$\varepsilon_{\mathrm{r,pm}} = 9.44$	$\sigma_{\mathrm{pm}} = 0$ S/m
Nucleoplasm	$r_{\mathrm{np}} = 3.4\,\mu\mathrm{m}$	$\varepsilon_{\mathrm{r,np}} = 80$	$\sigma_{\mathrm{np}} = 3.9$ S/m
Nuclear Envelope	$t_{\mathrm{ne}} = 17\,\mathrm{nm}$	$\varepsilon_{\mathrm{r,ne}} = 7$	$\sigma_{\mathrm{ne}} = 83$ µS/m

Table 2.3: Representative parameters for the layers of a double shell cell model.

The parameter t corresponds to the layer thickness, ε_r is the relative permittivity and σ refers to the specific conductivity. The values for the parameters were chosen from [2] with adjustments to the used cell radius.

For some cell types, the EM material parameters for all layers of the cell model from **Figure 2.10** are well studied [1, 133, 134, 136]. In [134] typical dielectric material properties for eukaryotic cells from spherical lymphocytes were obtained. In other studies, representative dielectric parameters for glioblastoma cells were chosen [1, 2]. In general, the dielectric parameters for the cell layers differ slightly for different cell types, but the fundamental electromagnetic behavior of the individual layers relative to each other does not change that much. This is because the electromagnetic behavior of plasma is dominated by its aqueous structure, while the electromagnetic behavior of membranes are mainly dominated by their lipid structures. Accordingly, plasma has higher specific electrical conductivity than membranes. It has to be noted though that the plasma membrane is electrically and biologically

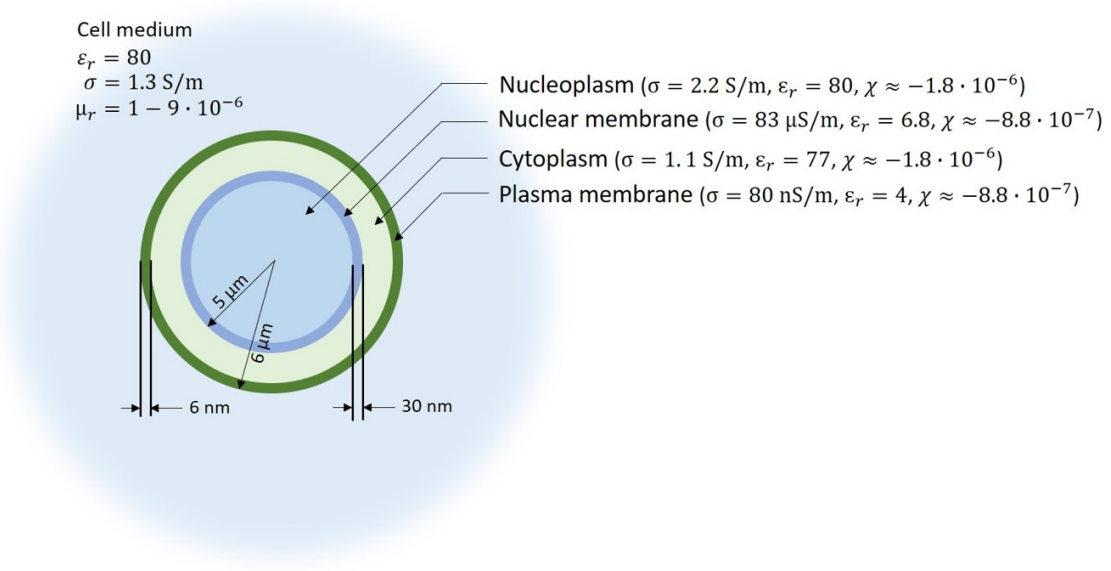

Figure 2.11: Double-shell cell model of a typical fibroblast.

different than the nuclear membrane. One reason is that the plasma membrane consists of one lipid bilayer, whereas the total nuclear envelope consists of two lipid bilayers. Similiarly, there are structural differences between the cytoplasm and the nucleoplasm. These structural differences are mirrored in differences of EM properties.
Fibroblasts are cells which were used in the frame of cellular reprogramming with EMFs [13] and provide a good example. **Figure 2.11** shows the dimensional and EM material parameters which are typical for a fibroblast. The parameters of the fibroblast model from **Figure 2.11** were obtained from [134, 139–142]. Additionally, in **Figure 2.11**, the cell model is located in a typical cell culture medium with the provided EM parameters [1].

In fact, cells are not perfectly spherical. Furthermore, they consists of many more cell compartments than those considered in the models of **Figure 2.10** and **Figure 2.11**. The models therefore represent a vast simplification and cannot predict the exact EMF distribution caused by local shape differences or inhomogeneous EM tissue properties.
A cell under division can be modeled with an hourglass shape [1]. Transferred on a fibroblast cell, the cell model can be build up as shown in **Figure 2.12**.

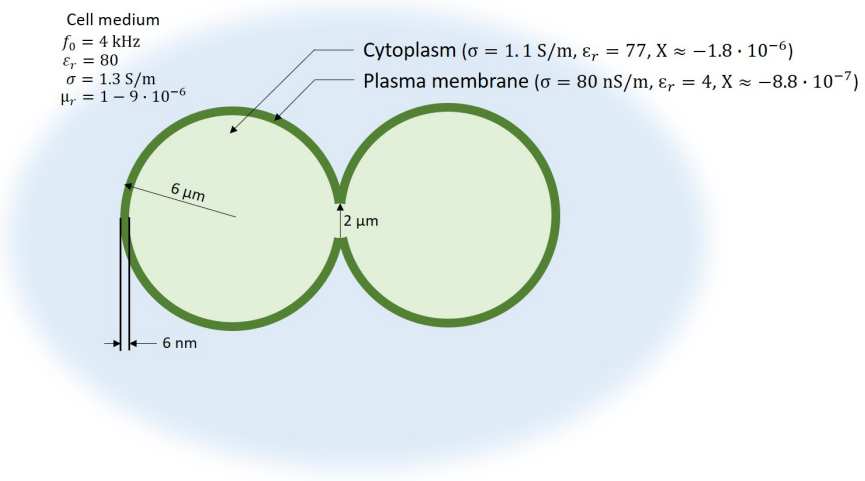

Figure 2.12: Model of a mitotic fibroblast cell.

Although the cell models shown cannot predict the exact EMF distribution caused by local shape differences or inhomogeneous EM properties, their application allows a sufficient estimation of the relative EMF distribution between the different cell layers, caused by their different EM properties.
When the EMF distribution within the cell models from **Figure 2.10** is of interest, different approaches can be utilized to obtain it. Three approaches will be introduced in the following. First, lumped element models will be introduced. These models allow the approximation of the electric field magnitude in the different cell layers. Subsequently, a numerical approach will be introduced which is used by electromagnetic modelling software and finally the calculation with Mie Scattering will be introduced.

2.3.1 Lumped Element Models of Cells

The cell models from **Figure 2.10** can be expressed as electrical lumped element models, when considering the cell exposed to an external electric field with one direction of polarization. In a lumped element model of the cell, the electrical properties of the individual cell layers are cumulated by resistors and capacitors. A lumped element model has the advantage, that it provides a summarized overview of the general electrical behavior at first

glance. Furthermore, current distributions within the different cell layers can be approximated. There are very different approaches for the determination of the lumped element parameters (resistivities and capacitances).

Total cell impedances can be measured and lumped element parameters can be identified by curve fitting to the measurements. However, the reason that the complexity of the mathematical fitting rises with rising amount of parameters might be one reason that often only single-shell models are used [1, 133, 143–149]. Besides the lumped element parameters, the model itself with associated arrangement of lumped elements can be the result of curve fittings [144–146]. Furthermore, mathematical curve fitting can also be performed to numerical calculations. In [1] the lumped element parameters are obtained by application of

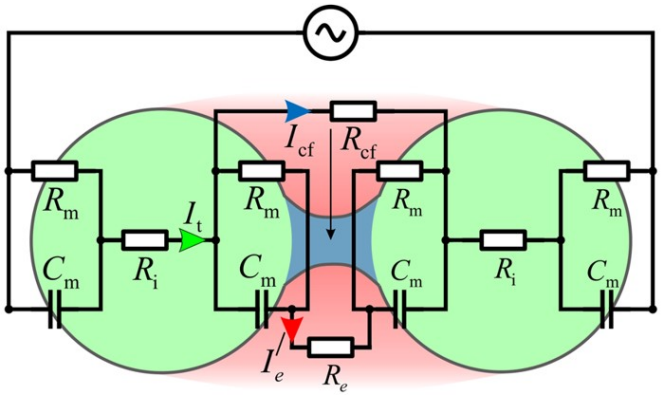

Figure 2.13: Lumped Element model of a mitotic cell from [1]

numerical EM calculations of current distributions within the single-shell cell model. The according lumped element model is shown in **Figure 2.13**. The innovation of this lumped element representation is that the mitotic cell is represented by a similar lumped element model of two non-mitotic cells which are connected by resistors representing the cleavage furrow and the extracellular medium. In **Figure 2.13**, *R* represents the resistivity, *C* represents the capacitance and *I* is the current. The index m denotes parameters of the membrane, the index i denotes parameters of the interior of the cell, the index cf stands for the cleavage furrow and the index e stands for the extracellular medium. I_t is the total current.

Other methods for the determination of lumped element parameters with curve fitting include the consideration of dispersion effects due to the EM properties of the cellular compartments. Thereby different fundamental equations and models can be applied as the Debye equation and the Clausius-Massotti equation or the Cole-Cole equation [146–149].

Analytical formulas for the determination of lumped element parameters are rare. In this regard, cells can be assumed to be cubical [145]. With known relative permittivities and specific conductivities of the individual cell layers, lumped element parameters for cubical cells can be easier determined than for spherical cells. However, the applicability of the parameters is questionable. The assumption of a spherical shape of the cell has been demonstrated to be sufficient for many studies [1, 137, 144, 150–153].

2.3.2 Numerical Electromagnetic Modelling of Biological Cells

The finite difference time domain (FDTD) method is a very common approach for the numerical solution of electromagnetic problems. As the method's name suggests, it provides solutions in the time domain and is therefore particularly suited for electromagnetic arrangements where the time propagation of electromagnetic field is of relevance (as in the case of pulsed excitation). In the frame of the FDTD method, not only the simulation (three dimensional) space needs to be discretized, but also the simulation time. In order to achieve numerical stability, the following condition must be fulfilled [154].

$$\Delta t \leq \frac{1}{v\sqrt{\frac{1}{\Delta x^2}+\frac{1}{\Delta y^2}+\frac{1}{\Delta z^2}}} \tag{2.1}$$

Thereby, v is the phase velocity of the EM wave within a regarded medium, Δx, Δy and Δz are the discretization steps in the respective Cartesian space direction and Δt is the discretization step in the time domain. Assuming an uniform discretization step size in space, (2.1) means, that a reduction of spacial discretization step size by a factor of a half, the computational simulation time will be increased by a factor of sixteen. This makes the FDTD method rather unsuited for the solution of electromagnetic problems, where the object under exposure is relatively small compared to the considered wavelength. The simulation of such a case often demands not only plenty of time but also an excessive amount of computational storage space.

In some cases, as in the case of simulation of cells under exposure to EMFs, the application of solvers working with quasistatic approximations is much less consuming.

Sim4Life (ZMT Zurich MedTech AG, Switzerland, https://www.zmt.swiss/) is a numerical EM simulation software with different solvers which are suited for different simulation scenarios. The quasistatic solvers can be used, when the following conditions apply [155]

$$\omega^2 \varepsilon \mu d^2 \ll 1 \tag{2.2}$$

and

$$\omega \sigma \mu d^2 \ll 1. \tag{2.3}$$

ω is the angular frequency, ε is the total electric permittivity, μ is the electric permeability, σ is the specific electric conductivity and d is the maximum length scale.
For a typical eukaryotic cell a maximum diameter of $d_{\mathrm{Cell}} = 20\,\mu\mathrm{m}$, a maximum relative permittivity of around $\varepsilon_{\mathrm{r,np}} = 300$ and a maximum specific conductivity of around $\sigma_{\mathrm{np}} = 3\,\mathrm{S/m}$ (corresponding to the maximum permittivity and specific conductivity of the nucleoplasm) can be assumed when considering values from [134]. With these values and reformulation of (2.2) and (2.3) the maximum frequency can be obtained at which the quasi static approach can be applied. For this frequency f both of the following equations have to apply

$$4\pi^2 \varepsilon_{\mathrm{np}} \mu d_{\mathrm{Cell}}^2 = 5.27 \cdot 10^{-23} \ll \frac{1}{f^2} \tag{2.4}$$

and

$$2\pi \sigma_{\mathrm{np}} \mu d_{\mathrm{Cell}}^2 = 9.47 \cdot 10^{-15} \ll \frac{1}{f}. \tag{2.5}$$

By comparing both conditions, it can be seen that (2.4) is the limiting condition resulting in $f \ll 1.4 \cdot 10^{11}$. The calculations with the quasistatic approach and the implemented quasistatic solvers can be applied for frequencies up to hundreds of megahertz.

The quasistatic approach allows a decoupling of the electric and the magnetic field and facilitates mathematical calculations of EM problems [155]. The software *Sim4Life* provides six different solvers for the solutions of EM problems which allow the application of the quasistatic approach. The choice of the suited solver for the EM problem at hand depends on the choice of excitation and the EM material properties. For example, some solvers are suited for EM problems which are dominated by displacement currents where the approximation $\omega\varepsilon \gg \sigma$ applies. All solvers have in common that the excitation with an electric field or a magnetic field can only be performed indirectly by application of electric potentials or electric currents respectively.

The software *Comsol Multiphysics* (COMSOL AB, Sweden, https://www.comsol.com) also contains solvers which apply static and quasi static approximations.

2.3.3 EMFs at Material Interfaces and Mie Scattering

When a body like a cell is brought into an external EMF, the EMF propagation will change. Phenomena like reflection/ scattering and attenuation occur. The EMF distribution can be analytically calculated. Even though, the complexity of calculation is strongly dependent on the regarded scenario, the overall approach remains usually the same. In order to demonstrate such an approach exemplarily, in the following a standard and relatively simple example of reflection of an EMF is shown: the reflection of a transversal EM (TEM) wave on a planar surface. Afterwards, the more complex scenario of a sphere within a TEM wave is considered.

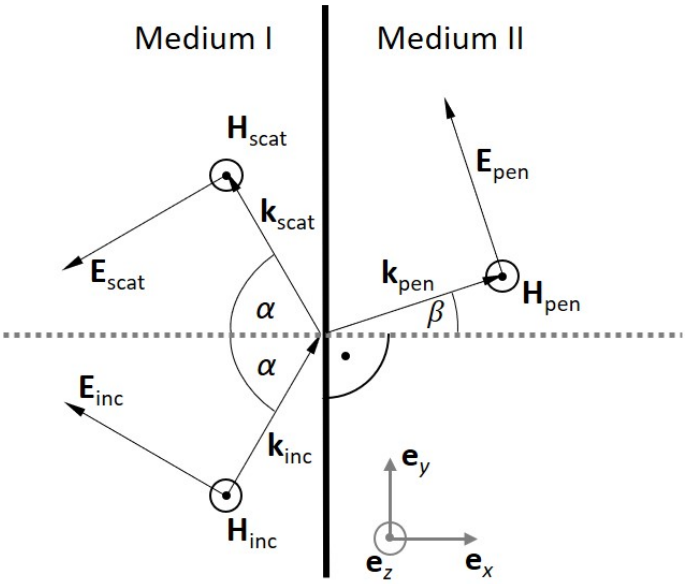

Figure 2.14: Reflection and transmission of a TEM wave on a planar surface.

One of the simplest forms of reflection of an EM Wave is a TEM wave reflected at the interface of two infinite half spaces as shown in **Figure 2.14**. There, the interface of medium one and medium two is assumed to be extended infinitely in the direction of y with its unity vector $\mathbf{e}_\mathrm{y}$ and in the direction of z with according unity vector $\mathbf{e}_\mathrm{z}$. $\mathbf{e}_\mathrm{x}$ is the unity vector in x-direction. The direction of wave propagation in **Figure 2.14** is indicated by the wave vector $\mathbf{k}$ with its magnitude k called the propagation constant. The index 'inc' denotes the incident wave, the index 'scat' indicates the reflected wave components and the index 'pen' denotes

the transmitted wave components. Exemplarily, the incident wave is chosen to be excited in medium one, propagating in the direction of x and y. The incident electric field is chosen to be a superposition of an electric field component normal to the interface and an electric field component parallel to the interface. With the chosen directions of the incident wave propagation and the incident electric field, the direction of the incident magnetic field has to be parallel to $\mathbf{e}_z$. The resulting reflected and transmitted wave components are shown in **Figure 2.14**. With the incident electric field, the angle of incidence α and all EM material parameters of both media as known parameters, all wave compartments can be determined. This will be shown in the following.

The wave equation for the electric field can be derived from Maxwell equations. In an homogeneous and isotropic medium, with specific electric conductivity σ, permeability μ and total permittivity ε the Maxwell equations with magnetic field vector $\mathbf{H}$ and electric field vector $\mathbf{E}$ can be formulated as follows

$$\nabla \times \mathbf{H} = \sigma \mathbf{E} + \varepsilon \frac{\partial \mathbf{E}}{\partial t} \tag{2.6}$$

$$\nabla \times \mathbf{E} = -\mu \frac{\partial \mathbf{H}}{\partial t} \tag{2.7}$$

$$\nabla \cdot \mathbf{E} = 0 \tag{2.8}$$

$$\nabla \cdot \mathbf{H} = 0. \tag{2.9}$$

The rotation of (2.7) can be expressed as $\nabla \times (\nabla \times \mathbf{E}) = \nabla (\nabla \mathbf{E}) - \nabla^2 \mathbf{E}$. By using this relation and by inserting equations (2.6) and (2.8) into it, the following equation can be obtained:

$$\nabla \times (\nabla \times \mathbf{E}) = -\nabla^2 \mathbf{E} = -\mu \frac{\partial}{\partial t} (\nabla \times \mathbf{H}) = -\mu \sigma \frac{\partial \mathbf{E}}{\partial t} - \mu \varepsilon \frac{\partial^2 \mathbf{E}}{\partial t^2}. \tag{2.10}$$

Equation (2.10) can be reformulated into the following vector wave equation

$$\nabla^2 \mathbf{E} - \mu \sigma \frac{\partial \mathbf{E}}{\partial t} - \mu \varepsilon \frac{\partial^2}{\partial t^2} \mathbf{E} = 0 \tag{2.11}$$

Equation (2.11) is linear. Thus, electric fields of arbitrary time dependence can be formed from superposition of time harmonic solutions [156]. By assuming a time-harmonic electric

field $\mathbf{E} = \mathbf{E}(\mathrm{e}^{\mathrm{j}\omega t})$, with the angular frequency ω, (2.11) can be written as

$$\nabla^2\mathbf{E} + k^2\mathbf{E} = 0, \tag{2.12}$$

with $k^2 = \mu\varepsilon\omega^2 - \mathrm{j}\sigma\mu\omega$, as the square of the wave number. Considering a harmonically oscillating wave, the electric fields from **Figure 2.14** can be expressed as

$$\begin{aligned}
\mathbf{E}_{\mathrm{inc}} &= E_0\mathrm{e}^{\mathrm{j}\omega t}\mathrm{e}^{-\mathrm{j}k_{\mathrm{inc}}(\cos(\alpha)x+\sin(\alpha)y)}\left(\sin(\alpha)\mathbf{e}_{\mathrm{x}} + \cos(\alpha)\mathbf{e}_{\mathrm{y}}\right)\\
\mathbf{E}_{\mathrm{scat}} &= E_{\mathrm{scat}}\mathrm{e}^{\mathrm{j}\omega t}\mathrm{e}^{-\mathrm{j}k_{\mathrm{inc}}(-\cos(\alpha)x+\sin(\alpha)y)}\left(-\sin(\alpha)\mathbf{e}_{\mathrm{x}} - \cos(\alpha)\mathbf{e}_{\mathrm{y}}\right)\\
\mathbf{E}_{\mathrm{pen}} &= E_{\mathrm{pen}}\mathrm{e}^{\mathrm{j}\omega t}\mathrm{e}^{-\mathrm{j}k_{\mathrm{pen}}(\cos(\beta)x+\sin(\beta)y)\mathbf{r}}\left(-\sin(\beta)\mathbf{e}_{\mathrm{x}} + \cos(\beta)\mathbf{e}_{\mathrm{y}}\right).
\end{aligned} \tag{2.13}$$

The amplitude of electric field excitation E_0 is known whereas E_{scat} and E_{pen} have to be determined. k is chosen to be the positive root of k^2.

Similarly, it can be shown that the corresponding magnetic fields have the form

$$\begin{aligned}
\mathbf{H}_{\mathrm{inc}} &= H_0\mathrm{e}^{\mathrm{j}\omega t}\mathrm{e}^{-\mathrm{j}k_{\mathrm{inc}}(\cos(\alpha)x+\sin(\alpha)y)}\mathbf{e}_{\mathrm{z}},\\
\mathbf{H}_{\mathrm{scat}} &= H_{\mathrm{scat}}\mathrm{e}^{\mathrm{j}\omega t}\mathrm{e}^{-\mathrm{j}k_{\mathrm{inc}}(-\cos(\alpha)x+\sin(\alpha)y)}\mathbf{e}_{\mathrm{z}},\\
\mathbf{H}_{\mathrm{pen}} &= H_{\mathrm{pen}}\mathrm{e}^{\mathrm{j}\omega t}\mathrm{e}^{-\mathrm{j}k_{\mathrm{pen}}(\cos(\beta)x+\sin(\beta)y)}\mathbf{e}_{\mathrm{z}}.
\end{aligned} \tag{2.14}$$

Furthermore, Snell's law describes the relation between the incident wave angle α and the propagation angle β as follows [157]

$$\beta = \arcsin\left(\frac{k_{\mathrm{inc}}}{k_{\mathrm{pen}}}\sin(\alpha)\right). \tag{2.15}$$

Assuming the specific electric conductivity in medium one to be zero facilitates the following calculations. The general approach of the calculations would remain the same for a non-zero conductivity. By application of (2.6) and consideration that the conductivity in medium one equals zero, the following equations can be obtained

$$
\begin{aligned}
(\nabla \times \mathbf{H}_{\text{inc}})\,\mathbf{e}_{\text{x}} &= \frac{\partial H_{\text{inc}} \mathrm{e}^{\mathrm{j}\omega t} \mathrm{e}^{-\mathrm{j}k_{\text{inc}}(\cos(\alpha)x+\sin(\alpha)y)}}{\partial y} \\
&= -\mathrm{j}\omega\varepsilon_0 E_0 \mathrm{e}^{\mathrm{j}\omega t} \mathrm{e}^{-\mathrm{j}k_{\text{inc}}(\cos(\alpha)x+\sin(\alpha)y)} \sin(\alpha), \\
(\nabla \times \mathbf{H}_{\text{scat}})\,\mathbf{e}_{\text{x}} &= \frac{\partial H_{\text{scat}} \mathrm{e}^{\mathrm{j}\omega t} \mathrm{e}^{-\mathrm{j}k_{\text{inc}}(-\cos(\alpha)x+\sin(\alpha)y)}}{\partial y} \\
&= -j\omega\varepsilon_0 E_{\text{scat}} \mathrm{e}^{j\omega t} \mathrm{e}^{-\mathrm{j}k_{\text{inc}}(-\cos(\alpha)x+\sin(\alpha)y)} \sin(\alpha), \\
\left(\nabla \times \mathbf{H}_{\text{pen}}\right)\mathbf{e}_{\text{x}} &= \frac{\partial H_{\text{pen}} \mathrm{e}^{\mathrm{j}\omega t} \mathrm{e}^{-\mathrm{j}k_{\text{pen}}(\cos(\beta)x+\sin(\beta)y)}}{\partial y} \\
&= -(\sigma_2 + \mathrm{j}\omega\varepsilon_2) E_{\text{pen}} \mathrm{e}^{\mathrm{j}\omega t} \mathrm{e}^{-\mathrm{j}k_{\text{pen}}(\cos(\beta)x+\sin(\beta)y)} \sin(\beta).
\end{aligned}
\tag{2.16}
$$

ε_2 is the total permittivity of medium two, σ_2 is the specific conductivity of medium two and the permittivity of medium one is ε_0, which is the vacuum permittivity.
From (2.16) and (2.14) the magnetic fields can be obtained as

$$
\begin{aligned}
\mathbf{H}_{\text{inc}} &= \frac{\omega\varepsilon_0 E_0}{k_{\text{inc}}} \mathrm{e}^{\mathrm{j}\omega t} \mathrm{e}^{-\mathrm{j}k_{\text{inc}}(\cos(\alpha)x+\sin(\alpha)y)} \mathbf{e}_{\text{z}}, \\
\mathbf{H}_{\text{scat}} &= \frac{\omega\varepsilon_0 E_{\text{scat}}}{k_{\text{inc}}} \mathrm{e}^{\mathrm{j}\omega t} \mathrm{e}^{-\mathrm{j}k_{\text{inc}}(-\cos(\alpha)x+\sin(\alpha)y)} \mathbf{e}_{\text{z}}, \\
\mathbf{H}_{\text{pen}} &= \frac{k_{\text{pen}} E_{\text{pen}}}{\mu\omega} \mathrm{e}^{\mathrm{j}\omega t} \mathrm{e}^{-\mathrm{j}k_{\text{pen}}(\cos(\beta)x+\sin(\beta)y)} \mathbf{e}_{\text{z}}.
\end{aligned}
\tag{2.17}
$$

One boundary condition at the interface is that the tangential component of the electric field is steady. Thus

$$
\mathbf{E}_{\text{inc}}\mathbf{e}_{\text{y}} + \mathbf{E}_{\text{scat}}\mathbf{e}_{\text{y}} = \mathbf{E}_{\text{pen}}\mathbf{e}_{\text{y}}. \tag{2.18}
$$

Additionally, the tangential component of the magnetic field is steady, since there is no surface current at the interface. Thus

$$
\mathbf{H}_{\text{inc}}\mathbf{e}_{\text{z}} + \mathbf{H}_{\text{scat}}\mathbf{e}_{\text{z}} = \mathbf{H}_{\text{pen}}\mathbf{e}_{\text{z}}. \tag{2.19}
$$

Considering the surface normal vector parallel to $\mathbf{e}_{\text{x}}$ and the surface itself located at $x = 0$, (2.18) results in

$$
(E_0 - E_{\text{scat}})\,\mathrm{e}^{-\mathrm{j}k_{\text{inc}}\sin(\alpha)y}\cos(\alpha) = E_{\text{pen}}\mathrm{e}^{-\mathrm{j}k_{\text{pen}}\sin(\beta)y}\cos(\beta). \tag{2.20}
$$

By application of (2.15), (2.20) can be expressed as

$$(E_0 - E_{\text{scat}}) \frac{\cos(\alpha)}{\cos(\beta)} = E_{\text{pen}}. \tag{2.21}$$

Furthermore, by application of (2.15) and (2.17), (2.19) can be formulated into

$$\frac{\omega \varepsilon_0 E_0}{k_{\text{inc}}} + \frac{\omega \varepsilon_0 E_{\text{scat}}}{k_{\text{inc}}} = \frac{k_{\text{pen}} E_{\text{pen}}}{\mu \omega}. \tag{2.22}$$

The wave impedances n_{inc} and n_{pen} are

$$n_{\text{inc}} = \frac{E_{\text{inc}}}{H_{\text{inc}}} = \frac{k_{\text{inc}}}{\omega \varepsilon_0} = \frac{\mu \omega}{k_{\text{inc}}}, \tag{2.23}$$

$$n_{\text{pen}} = \frac{E_{\text{pen}}}{H_{\text{pen}}} = \frac{\mu \omega}{k_{\text{pen}}}. \tag{2.24}$$

Application of (2.21) to (2.24) leads to the following equations

$$E_0 \frac{n_{\text{inc}} \cos(\alpha) - n_{\text{pen}} \cos(\beta)}{n_{\text{inc}} \cos(\alpha) + n_{\text{pen}} \cos(\beta)} = E_{\text{scat}}, \tag{2.25}$$

$$E_0 \frac{2 n_{\text{pen}} \cos(\alpha)}{n_{\text{inc}} \cos(\alpha) + n_{\text{pen}} \cos(\beta)} = E_{\text{pen}}. \tag{2.26}$$

With equation (2.25) and (2.26), the electric fields from (2.13) as well as the magnetic fields from (2.17) are determined.

As shown by this relatively simple example of reflection, the overall approach for the determination of electric and magnetic fields is emanating from Maxwell equations. The Maxwell equations lead to the general vector wave equation, which predefines the general form of electric and magnetic field propagation. With the knowledge of the incident electric field magnitude (which can be seen as an excitation), EM material properties and application of boundary conditions, the unknown parameters of the electric and magnetic fields can be determined.

In the following, a more complex scenario will be treated. The overall approach of determination of electric and magnetic field components however remains the same.

In 1908 Gustav Mie formulated a solution for an electromagnetic wave scattered by a spherical particle [158]. Thereby, the spherical particle is placed in an electrically lossless medium. In order to gain a solution for the scattering of an electromagnetic field on a spherical particle, first Maxwell's equations and solutions to the general vector wave equation have to be considered. Since a sphere is in the focus, the general solution should be expressed in spherical coordinates. A general solution to the vector wave equation will be introduced in spherical coordinates. It will be shown that any vector function fulfilling the vector wave equation, as the electric and magnetic field, can be expressed by this solution. The descriptions and mathematical derivations which are presented, are an outline of the overall approach to the solutions. Some deeply mathematical derivations are beyond the scope of this work, as the derivation of the solution of the Legendre differential equation.

The target is to find a general solution of the vector wave equation from (2.12) in spherical coordinates. In the following, it will be shown that any electric field vector function fulfilling (2.12) can be expressed as an infinite series of other functions which are solutions to a scalar wave function. In order to achieve this, a new vector function is introduced

$$\mathbf{M} = \nabla \times (\mathbf{C}\psi(r,\vartheta,\varphi)). \tag{2.27}$$

$\mathbf{C}$ is a constant vector and ψ is a scalar function which depends on the spherical coordinates r (the radial distance from the coordinate origin), ϑ (the elevation angle) and φ (the azimuth angle). Similarly to (2.11) and by application of (2.27), the vector wave equation with argument $\mathbf{M}$ can be formulated as [159]

$$\nabla^2\mathbf{M} + k^2\mathbf{M} = \nabla \times \left[\mathbf{C}(\nabla^2\psi(r,\vartheta,\varphi) + k^2\psi(r,\vartheta,\varphi))\right]. \tag{2.28}$$

Equation (2.28) shows that $\mathbf{M}$ satisfies the vector wave equation, only if ψ satisfies the scalar wave equation

$$\nabla^2\psi(r,\vartheta,\varphi) + k^2\psi(r,\vartheta,\varphi) = 0. \tag{2.29}$$

The function ψ can be separated into $\psi = R(r)A(\vartheta,\varphi)$. With the so called separation functions, the first term in (2.29) can be written as

$$\Delta\psi = \frac{1}{r^2}\frac{\partial}{\partial r}\left(r^2\frac{\partial R(r)A(\vartheta,\varphi)}{\partial r}\right) + \frac{1}{\sin(\vartheta)}\frac{\partial}{\partial\vartheta}\left(\sin(\vartheta)\frac{\partial R(r)A(\vartheta,\varphi)}{\partial\vartheta}\right) + \frac{1}{\sin^2(\vartheta)}\frac{\partial^2 R(r)A(\vartheta,\varphi)}{\partial\varphi^2}. \tag{2.30}$$

By insertion of equation (2.30) into (2.29) and introduction of the constant C_1, the following differential equations can be obtained

$$\frac{\partial}{\partial r}\left(r^2\frac{\partial R(r)}{\partial r}\right) + \left(k^2r^2 - C_1\right)R(r) = 0, \tag{2.31}$$

$$\frac{1}{\sin(\vartheta)}\frac{\partial}{\partial\vartheta}\left(\sin(\vartheta)\frac{\partial A(\vartheta,\varphi)}{\partial\vartheta}\right) + \frac{1}{\sin^2(\vartheta)}\frac{\partial^2 A(\vartheta,\varphi)}{\partial\varphi^2} + C_1A(\vartheta,\varphi) = 0. \tag{2.32}$$

Equation (2.32) is a differential equation of a spherical harmonics function $A(\vartheta,\varphi)$ and C_1 represents its Eigenvalue [160]. This spherical harmonics function can be further separated into $A(\vartheta,\varphi) = \Theta(\vartheta)\Phi(\varphi)$. By inserting this separation into (2.32) and introducing another separation constant C_2, the following two differential equations can be obtained

$$\sin(\vartheta)\frac{\partial}{\partial\vartheta}\left(\sin(\vartheta)\frac{\partial\Theta(\vartheta)}{\partial\vartheta}\right) + (C_1\sin^2(\vartheta) - C_2)\Theta(\vartheta) = 0 \tag{2.33}$$

$$\frac{\partial^2\Phi(\varphi)}{\partial\varphi^2} + C_2\Phi(\varphi) = 0. \tag{2.34}$$

Equation (2.34) has two linearly independent solutions with the boundary condition $\Phi(\varphi = n2\pi) = \Phi(\varphi = (n+1)2\pi)$ [159, 161]

$$\Phi_{\mathrm{e}}(\varphi) = \cos(a\varphi) \tag{2.35}$$

$$\Phi_{\mathrm{o}}(\varphi) = \sin(a\varphi). \tag{2.36}$$

The index 'e' stands for even, since the cosine is an even function. The index 'o' stands for odd since the sine function is an odd function.
In (2.35) and (2.36), a is a natural number including zero. Since $C_2 = a^2$ (outcome of (2.34)),

and by introducing $\xi = \cos(\vartheta)$, the function $\Theta(\vartheta)$ can be written as $\Theta(\vartheta) = V(\xi)$ and (2.33) can be reformulated and converted into

$$\frac{\partial^2 V(\xi)}{\partial \vartheta^2} + \frac{\xi}{\sqrt{1-\xi^2}} \frac{\partial V(\xi)}{\partial \vartheta} + \left(C_1 - \frac{a^2}{\sqrt{1-\xi^2}} \right) V(\xi) = 0. \tag{2.37}$$

Furthermore, (2.37) can be formulated as [160]

$$\left(1-\xi^2\right) \frac{\partial^2 V(\xi)}{\partial \xi^2} - 2\xi \frac{\partial V(\xi)}{\partial \xi} + \left(C_1 - \frac{a^2}{1-\xi^2} \right) V(\xi) = 0. \tag{2.38}$$

Equation (2.38) is a Legendre differential equation. It can be shown that C_1 represents Eigenvalues in the form of $C_1 = p(p+1)$ with $p \geq a$. p is the degree of spherical harmonics function. The derivation of this solution can be found in [160]. The associated Legendre functions of the first kind P_p^a provide solutions for differential equation (2.38), with

$$P_p^a(\xi) = \frac{\left(1-\xi^2\right)^{a/2}}{2^p p!} \frac{\mathrm{d}^{p+a}}{\mathrm{d}\xi^{p+a}} \left(\xi^2 - 1\right)^p. \tag{2.39}$$

Since C_1 is obtained, by substitution of function $R(r) = W(r) r^{-1/2}$, the differential equation from (2.31) can be converted to

$$\frac{\partial^2 W(r)}{\partial r^2} + \frac{1}{r} \frac{\partial W(r)}{\partial r} \left(k^2 - \frac{\left(p+\frac{1}{2}\right)^2}{r^2} \right) W(r) = 0. \tag{2.40}$$

The spherical Bessel functions in (2.41) and (2.42) provide solutions for the Bessel differential equation in (2.40) [159]

$$j_p(r) = \sqrt{\frac{\pi}{2r}}\, J_{p+\frac{1}{2}}(r), \tag{2.41}$$

$$y_p(r) = \sqrt{\frac{\pi}{2r}}\, Y_{p+\frac{1}{2}}(r). \tag{2.42}$$

In (2.41) and (2.42), $J_{p+1/2}$ and $Y_{p+1/2}$ are the ordinary Bessel functions. Also, any linearly independent combination of (2.41) and (2.42) are solutions to (2.40). Two such combinations are the spherical Hankel functions [159]

$$h_p^{(1)}(r) = j_p(r) + \mathrm{j}y_p(r), \tag{2.43}$$

$$h_p^{(2)}(r) = j_p(r) - \mathrm{j}y_p(r). \tag{2.44}$$

Now, solutions for differential equation (2.29) can be generated with the solutions (2.35), (2.36), (2.39) and (2.41) to (2.44). Two solutions for (2.29) are [159]

$$\psi_{\mathrm{e}ap} = \cos(a\varphi) P_p^a(\cos(\vartheta)) z_p(r), \tag{2.45}$$

$$\psi_{\mathrm{o}ap} = \sin(a\varphi) P_p^a(\cos(\vartheta)) z_p(r). \tag{2.46}$$

Here again, the index 'e' stands for even, since the cosine is an even function. The index 'o' stands for odd since the sine function is an odd function, and z_p is any of the functions from (2.41) to (2.44). So far the scalar function ψ was only introduced to find a solution for $\mathbf{M}$, which similarly to $\mathbf{E}$, fulfills the vector wave equation. The solution of $\mathbf{M}$ can be obtained from (2.26) by insertion of (2.45) and (2.46):

$$\mathbf{M}_{\mathrm{e}ap} = \nabla \times (\mathbf{C}\psi_{\mathrm{e}ap}), \tag{2.47}$$

$$\mathbf{M}_{\mathrm{o}ap} = \nabla \times (\mathbf{C}\psi_{\mathrm{o}ap}). \tag{2.48}$$

If $\mathbf{C}$ is chosen to the vector $\mathbf{C} = \mathbf{r} = r\mathbf{e}_r + \vartheta\mathbf{e}_\vartheta + \varphi\mathbf{e}_\varphi$, then (2.47) and (2.48) are solutions in spherical coordinates [159]. The vector $\mathbf{e}$ is a unit vector in the direction of its index.
Fundamental solutions to the general vector wave equation however, are also provided by a general vector function $\mathbf{N}$, which can be defined by [159]

$$\mathbf{N}_{\mathrm{e}ap} = \frac{\nabla \times \mathbf{M}_{\mathrm{e}ap}}{k}, \tag{2.49}$$

$$\mathbf{N}_{\mathrm{o}ap} = \frac{\nabla \times \mathbf{M}_{\mathrm{o}ap}}{k}. \tag{2.50}$$

Superposition of the solutions (2.47) to (2.50) also fulfills the vector wave equation. Furthermore, the vector functions $\mathbf{M}$ and $\mathbf{N}$ are divergence free. Any vector function $\mathbf{V}$ can be expressed as [159]

$$\mathbf{V} = \sum_{a=0}^{\infty} \sum_{p=a}^{\infty} L_{eap}\mathbf{M}_{eap} + L_{oap}\mathbf{M}_{oap} + K_{eap}\mathbf{N}_{eap} + K_{oap}\mathbf{N}_{oap}. \tag{2.51}$$

L_{eap}, L_{oap}, K_{eap} and K_{oap} are scalar coefficients. A huge advantage of this expression is, that it contains separated functions for each of the spherical coordinates (r, ϑ and φ). With this solution, the electric field $\mathbf{E}$ can be expressed in spherical coordinates and in spherical basis (in contrast to e.g. Cartesian basis).

In a TEM wave, the electric field, the magnetic field and the direction of propagation are transversal on each other. In the frame of Mie Scattering on a spherical object, an incident TEM wave with index 'inc' is propagating according to **Figure 2.15** towards a sphere. The

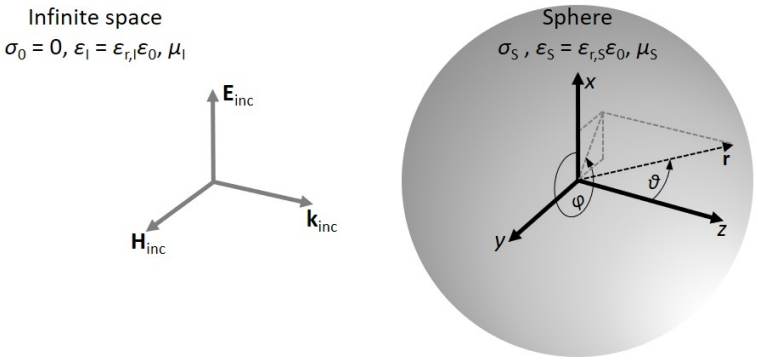

Figure 2.15: Transversial EMF on a spherical object.

origin of the coordinate system is located in the center of the sphere with conductivity σ_S, permeability μ_S and permittivity ε_S. The incident wave originates from an infinite space with zero conductivity σ_0, permeability μ_I and permittivity ε_I. The vector $\mathbf{k}_{inc}$ is oriented in z-direction. Its magnitude is the wavenumber and its direction indicates the direction of wave propagation. The incident electric field $\mathbf{E}_{inc}$ is polarized in x-direction and the incident magnetic field $\mathbf{H}_{inc}$ is polarized in y-direction.
In Cartesian coordinates, $\mathbf{E}_{inc}$ is

$$\mathbf{E}_{inc} = E_0 e^{jk_{inc}z}\mathbf{e}_x. \tag{2.52}$$

Accordingly, $\mathbf{H}_{inc}$ can be expressed as

$$\mathbf{H}_{\text{inc}} = \frac{k_{\text{inc}} E_0}{\mu_{\text{I}} \omega} \mathrm{e}^{\mathrm{j} k_{\text{inc}} z} \mathbf{e}_y. \tag{2.53}$$

To determine the scattered electric field and the transmitted electric field, first the incident electric field $\mathbf{E}_{\text{inc}}$ is expressed in vector spherical harmonic functions according to (2.51) [159]. Due to mathematical orthogonality relations, it can be shown that in (2.51) $L_{eap} = K_{\text{o}ap} = 0$. Also, it can be shown that the rest of the coefficients vanish except for $a = 1$ [159]. $\mathbf{E}_{\text{inc}}$ can be expressed in the form

$$\mathbf{E}_{\text{inc}} = \sum_{p=1}^{\infty} L_{\text{o}1p} \mathbf{M}_{\text{o}1p} + K_{\text{e}1p} \mathbf{N}_{\text{e}1p}. \tag{2.54}$$

Furthermore, since $\mathbf{E}_{\text{inc}}$ has to be finite at the origin of coordinate system, $j_p(r)$ from (2.41) is the Bessel function needed for the solution of $\mathbf{M}$ and $\mathbf{N}$. The coefficients are [159]

$$L_{o1p} = \mathrm{j}^p E_0 \frac{2p+1}{p(p+1)}, \tag{2.55}$$

$$K_{e1p} = -\mathrm{j} E_0 \mathrm{j}^p \frac{2p+1}{p(p+1)}. \tag{2.56}$$

According to (2.7), the incident magnetic field can be gained with the curl of equation (2.54) and is [159]

$$\mathbf{H}_{\text{inc}} = -\frac{k_{\text{inc}} E_0}{\omega \mu_{\text{I}}} \sum_{p=1}^{\infty} \mathrm{j}^p \frac{2p+1}{p\,(p+1)} \left(\mathbf{M}_{\text{e}1p} + j \mathbf{N}_{\text{o}1p} \right). \tag{2.57}$$

At an interface of two materials, the parallel part of the incident electric and incident magnetic field vector is steady. Assuming an incident electric field $\mathbf{E}_{\text{inc}} = E_{\text{r,inc}} \mathbf{e}_{\text{r}} + E_{\vartheta,\text{inc}} \mathbf{e}_{\vartheta} + E_{\varphi,\text{inc}} \mathbf{e}_{\varphi}$ on a spherical object with a scattered electric field $\mathbf{E}_{\text{scat}} = E_{\text{r,scat}} \mathbf{e}_{\text{r}} + E_{\vartheta,\text{scat}} \mathbf{e}_{\vartheta} + E_{\varphi,\text{scat}} \mathbf{e}_{\varphi}$ and a sphere penetrating electric field $\mathbf{E}_{\text{pen}} = E_{\text{r,pen}} \mathbf{e}_{\text{r}} + E_{\vartheta,\text{pen}} \mathbf{e}_{\vartheta} + E_{\varphi,\text{pen}} \mathbf{e}_{\varphi}$ the following equation applies at the interface of the sphere to the surrounding medium

$$\mathbf{E}_{\text{inc}} + \mathbf{E}_{\text{scat}} + \mathbf{E}_{\text{pen}} = \left(E_{r,\text{inc}} + E_{r,\text{scat}} + E_{r,\text{pen}} \right) \mathbf{e}_{\text{r}}. \tag{2.58}$$

Since the parallel part of the electric field relative to the surface is steady, the sum in direction of $\mathbf{e}_\vartheta$ and in direction of $\mathbf{e}_\varphi$ is zero. This applies also for the magnetic field and can be expressed as

$$\left(\mathbf{E}_{\mathrm{inc}}+\mathbf{E}_{\mathrm{scat}}+\mathbf{E}_{\mathrm{pen}}\right)\times\mathbf{e}_{\mathrm{r}}=\left(\mathbf{H}_{\mathrm{inc}}+\mathbf{H}_{\mathrm{scat}}+\mathbf{H}_{\mathrm{pen}}\right)\times\mathbf{e}_{\mathrm{r}}=0. \tag{2.59}$$

The boundary conditions applied for (2.58) and (2.59) are the same as the boundary conditions applied for (2.18) and (2.19) in the case of the planar interface.
With the boundary conditions and mathematical orthogonality relations, the scattered and penetrating fields can be obtained [159]

$$\mathbf{E}_{\mathrm{pen}}=E_0\sum_{p=1}^{\infty}\mathrm{j}^p\frac{2p+1}{p\,(p+1)}\left(c_p\mathbf{M}_{\mathrm{o}1p}-\mathrm{j}d_p\mathbf{N}_{\mathrm{e}1p}\right), \tag{2.60}$$

$$\mathbf{H}_{\mathrm{pen}}=-\frac{k_{\mathrm{pen}}E_0}{\omega\mu_{\mathrm{S}}}\sum_{p=1}^{\infty}\mathrm{j}^p\frac{2p+1}{p\,(p+1)}\left(d_p\mathbf{M}_{\mathrm{e}1p}+\mathrm{j}c_p\mathbf{N}_{\mathrm{o}1p}\right), \tag{2.61}$$

$$\mathbf{E}_{\mathrm{scat}}=E_0\sum_{p=1}^{\infty}\mathrm{j}^p\frac{2p+1}{p\,(p+1)}\left(-q_p\mathbf{M}_{\mathrm{o}1p}+\mathrm{j}o_p\mathbf{N}_{\mathrm{e}1p}\right), \tag{2.62}$$

$$\mathbf{H}_{\mathrm{scat}}=\frac{k_{\mathrm{inc}}E_0}{\omega\mu_{\mathrm{I}}}\sum_{p=1}^{\infty}\mathrm{j}^p\frac{2p+1}{p\,(p+1)}\left(o_p\mathbf{M}_{\mathrm{e}1p}+\mathrm{j}q_p\mathbf{N}_{\mathrm{o}1p}\right). \tag{2.63}$$

To explicitly determine the scattered and penetrating electromagnetic fields, it is necessary to determine the expansion coefficients c_p, d_p, o_p and q_p. This can be done with (2.54), (2.57) and (2.60) to (2.63) by consideration of boundary conditions and by consideration of mathematical orthogonality relations. The solutions for the so called expansion constants can be found in [157, 159].
The sphere from **Figure 2.15** can be layered with different materials. This is the case, when the sphere is replaced by the EM cell model from **Figure 2.10**. The principle approach for the determination of the electric and magnetic fields remains the same as in the case of a simple sphere. In the case of a layered sphere from different materials, more coefficients have to be determined due to the different layers. Approaches and solutions for a layered sphere and the determination of the coefficients can be found in [157].

2.3.4 Mie Scattering Calculations in MATLAB

Different research groups developed different tools in order to allow ready to use Mie Scattering calculators for different application scenarios. One example of a web based calculator is [162]. An established implementation for the calculation of Mie Scattering on a layered sphere, is a MATLAB program by Dr. Jan Schäfer called *MatScat* [163], which is available for free. The script is developed on the basis of the Mie Scattering theory presented in [159, 164]. Furthermore, Jan Schäfer wrote his PhD thesis on the implementation and application of analytical and numerical methods for the solution of Maxwell equations in the frame of light propagation in biological tissue [157]. Theoretical explanations to his *MatScat* implementation can be found in his dissertation. Since *MatScat* was used (with small modifications) for Mie Scattering calculations within this work, the principle structure of the program and the calculations will be introduced in this section.

Figure 2.16 schematically illustrates the MatScat code. The superordinate MATLAB script which allows starting the program and the following MATLAB functions were modified for the purpose of this work, primarily in order to enable desired graphical illustrations of the electric and magnetic fields.
In the superordinate MATLAB script the EM material properties and dimensions of the layers are specified. There, the EM problem definition takes place. Functions are called up for the specification of material properties and the definition of grid points. The subsequent MATLAB function according to **Figure 2.16** calls up the main code of Jan Schäfer's MatScat [163] program and plots the desired results of EMF distributions. From there the necessary EM and dimensional parameters are handed over to further calculation functions. The function calcmie_nf can be regarded as the head of the program. In this function, the near-field calculations for the scattering problem are initialized and the calculated solutions are collected. Therefore, first expcoeff_mie_strat and subsequently nfmie is called up. In expcoeff_mie_strat the coefficients for electric and magnetic field calculations are determined for the outer medium in which the sphere is located. These coefficients are handed over to calcmie_nf and further to nfmie. The function nfmie calles up the function expcoeff_mie_strat_int, which calculates the expansion coefficients within the different sphere layers. With the information of all expansion coefficients, the electric and magnetic

field values are calculated in nfmie. Since the field values are calculated there, nfmie can be regarded as the core of the program.

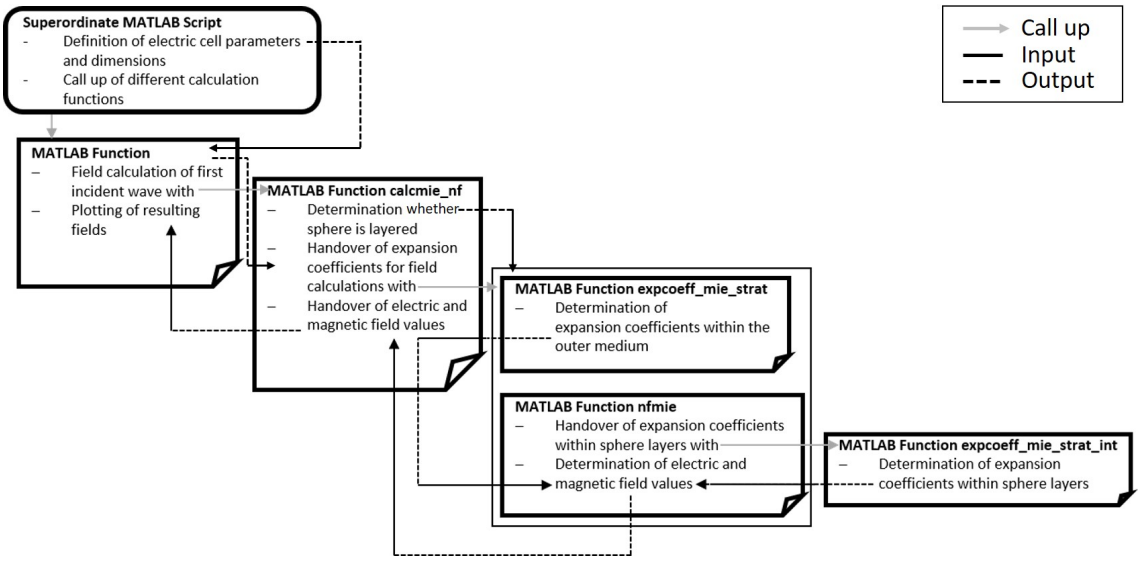

Figure 2.16: Schematics of MatScat code with minor modifications.

2.4 Impacts from Electromagnetic Fields on Biological Cells and Gold Nanoparticles

When it comes to impacts from EMFs on biological cells, most often biological effects are described which have been observed in the frame of *in vitro* cell experiments. Such effects include for example deformations of cells or unusual accumulation of ions. These biological effects can be the results of biological chain reactions. However, the initial entry point of the EMFs into the cells is related to the conversion of the energy from the EMFs into other energy forms like energy of movement and thermal energy into the cell. Such energy conversions can be described from a physical perspective qualitatively by principles of scientific theories. Scientific laws defined by physical formulas, allow the quantification of the energies or related quantities. Scientific theories allow a reasonable formulation of hypothesis on what *might* be the entry points of EMFs into biological cells. It has to be considered that rather than one single EMF effect on cells, it is more likely that different EMF parameters and exposure setups as well as different environmental/ biological conditions trigger different mechanisms of action [152, 165, 166].
However, the formulation of hypothesis is the fundament of scientific research. One way to validate a hypothesis is to quantify it with application of appropriate formulas. The quantification demands models which sufficiently mirror the reality while reducing complexity. One example of such a model for a cell is provided in the cell models from **Figure 2.10**.
When considering physical effects, it is reasonable to assume that EMF energy introduced into a cell can only influence the cell when it is higher than the thermal energy of the exposed cell. For example an EMF can cause a mechanical force on a cell compartment which is not effective, when the force is smaller than the force causing thermal motion. However, it has been shown that magnetic field intensities with energy levels under thermal noise have an effect on some cells [167]. The underlying mechanisms of action are yet to be discussed. One reason might be sensory characteristics of cells. In this regard, cells might have the ability to sense specific stimuli with biological or chemical sensors. One intuitive example of such sensors are photosensitive sensors [167]. In the frame of osteogenesis, one mechanism of action proposed is mechanotransduction [168]: It is proposed that certain EMFs cause mechanical kinetics within cells (similar to the inverse piezoelectric effect), which cause bioelectric signals promoting osteogenesis. Thereby, the motion of ion-carrying extracellu-

lar fluid in the bone matrix causes electrical signals [168].
Additionally, the introduced EMF energy might overcome the thermal energy but still be too small to cause a biological response of the cell. When a hypothesis is validated with quantifying formulas, this has to be taken under consideration.

In this section, different hypothesis concerning entry points of EMFs into biological cells will be introduced on the basis of theories from a physical perspective. The focus is on theories which might apply for the interaction of EMFs with cells during cell differentiation and cellular reprogramming. This is the reason why mainly low frequency and static EMFs are considered but PEMFs also play a role. Furthermore, where possible, formulas are introduced which allow the quantification of the theories.

The intensity of both electric and magnetic fields plays a major role in the interaction of EMFs with a medium. Therefore, the section focused first on electric field effects, with a subsequent focus on magnetic field effects. In addition, static and low-frequency effects were discussed before higher frequency effects were considered.

Energy is the integral of power over time. Similarly, the power within a volume can be defined as the integral of a power density over the closed surface of the volume. The Poynting vector $\mathbf{S}$, defined as $\mathbf{S} = \mathbf{E} \times \mathbf{H}$ [169], is a key quantity in the study of electromagnetism. Its magnitude indicates the EM power density while its direction points towards the direction of energy flux. The EMF energy introduced into a cell is dependent on the electric field and the magnetic field penetrating the cell and on the duration of exposure.
The electric and the magnetic field introduced into a cell (with specific EM material properties) depend on the applied frequency [153]. However, the material properties are also dispersive. This can be illustrated with the relative permittivity of water, which is a major component of cells. An example of the frequency dependency of the relative permittivity of water can be seen in **Figure 2.17**. The complex permittivity is the superposition of the real part (relative permittivity) ε' and the imaginary part ε'' which represents the electric losses in the medium. From **Figure 2.17** it can be seen that the real and the imaginary part of the complex permittivity are frequency dependent quantities. At relatively low frequencies, the dipole molecules within the medium can be oriented by the EMF. The real part of the

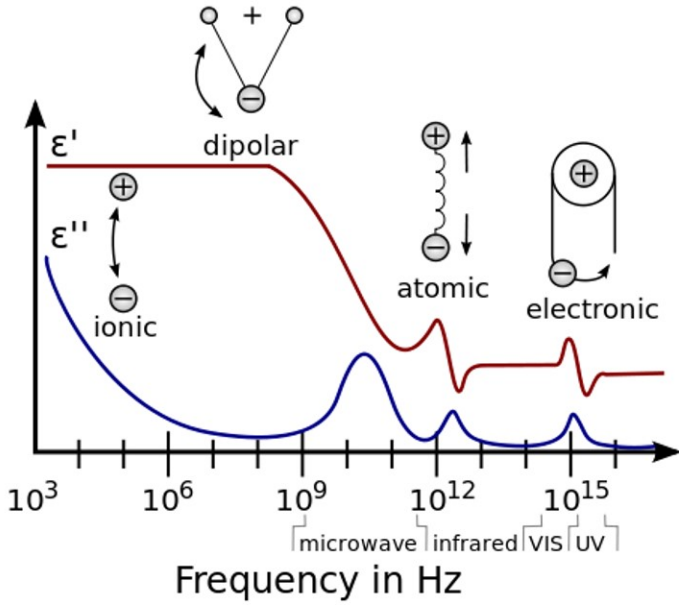

Figure 2.17: Example of frequency dependency of the complex permittivity of dispersive media from [170]

complex permittivity is high. Furthermore, ions within the medium can be separated, which results in a high imaginary part. At higher frequencies ions and electric dipoles within the medium cannot be separated and oriented due to inertia. Imaginary and real part of the complex permittivity drop until at sufficiently high frequencies local maxima occur due to other physical phenomena as vibration of atoms or excitation of electrons. The recipient of the EMF energy changes with changing frequency.
Since electric and magnetic field intensities and the applied frequency play major roles when it comes to interaction of EMFs with media, first electric field effects are described and subsequently magnetic field effects are described. Furthermore, in the respective section first static/ low frequency effects are described.

2.4.1 Electric Field Impacts

A static electric field can cause alterations of the cell shape and also alterations to the membrane tension, causing related ion movements into exposed cells [10]. Change of Ca^{2+}

concentration within cells is observed in many studies concerning differentiation and reprogramming and is the main effect considered in the frame of excitation with static electric fields [10, 46].
Alternating electromagnetic stimulation is often chosen due to naturally occurring EMFs within the human body and the idea, that imitating these frequencies might lead to stimulation of natural functioning [10]. At very low frequencies, the interior of cells is shielded from electric fields due to the capacitive properties of cell membranes [1, 2, 145, 171, 172]. However, a local separation of charged ions can occur even at low frequencies. Ion separation can take place within the extracellular medium as well as at the interface of the exposed cell membrane to the cell culture medium [10]. Low frequency and static electric fields can influence exposed electrically charged cell compartments by electrostatic force exertion. Compartments with an electric dipole can experience a torque moment [173]. Bond angles between affected compartments might change and cause alterations in cell fate.
To reach an effective action of an electrostatic force in an exposed cell, a threshold electric field intensity is necessary. In human tissue, the threshold electric field magnitude is well studies. For particles with a size of approximately 10 µm, the threshold electric field magnitude is around $E_{\mathrm{th}} = 10\,\mathrm{V/cm}$ [174]. For molecules with an approximate diameter of 100 Å the threshold electric field magnitude shifts towards $E_{\mathrm{th}} = 10\,\mathrm{kV/cm}$ [174]. In this regard calculations of interaction of an electric field with cytoplasmic ions are performed in [152]. The calculations confirm that electrostatic force exertion due to lower electric field magnitudes is very unlikely.

In telophase/ cytokinesis, cells have an hourglas shape, probably leading to enhanced electric field intensities within their cleavage furrow [1]. A sufficiently high electric field intensity can cause heating within a cell. A parameter which is associated with an increase in temperature is the specific absorption rate SAR [1, 175]. The SAR is proportional to the square of electric field magnitude E

$$SAR = \frac{c_{\mathrm{T}} \Delta T}{\Delta t} = \frac{\sigma E^2}{\rho}. \tag{2.64}$$

c_{T} is the specific heat capacity, ΔT is the increase in temperature, Δt is the time of exposure, σ is the specific electric conductivity and ρ is the volumetric mass density [1, 175]. Equation

(2.64) assumes non-thermodynamic conditions (no transfer of heat from the exposed object).

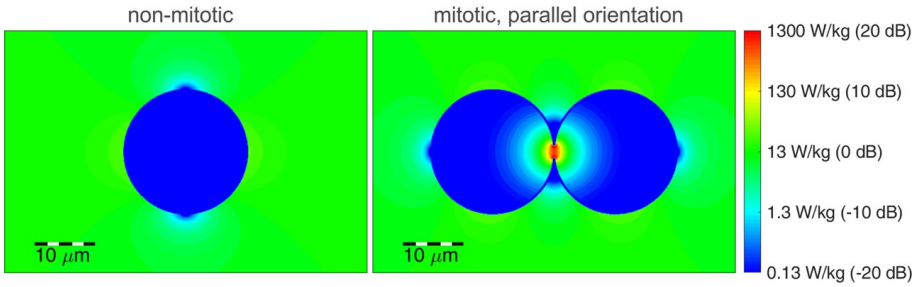

Figure 2.18: SAR within a non-mitotic and a mitotic cell from [1]

Figure 2.18 shows the SAR within a non-mitotic and a mitotic cell exposed to an electric field with $E = 100\,\mathrm{V_{RMS}/m}$ and a frequency $f = 100\,\mathrm{kHz}$. The direction of the external electric field is parallel to the mitotic axis of the cell. The SAR is normalized to the mean SAR of a culture medium surrounding the cell. It can be seen that the SAR within the cleavage furrow (red region in the mitotic cell) is higher than in the rest of the cell. Thus, the increase in temperature in the cleavage furrow must be higher relative to the medium and relative to the rest of the cell. However, it is difficult to quantify the increase in temperature within a cell. To quantify the increase in temperature experimentally, advanced measurement equipment would be necessary. An analytical approach to the quantification of a temperatur increase would demand detailed knowledge about heat transfer mechanisms within such a small region as the cleavage furrow and with such a high gradient in SAR.

Dielectrophoretic (DEP) force can act on molecules in a non-uniform electric field. The effect of DEP force on microtubules, which are cell compartments i.a. important for cell division, is well studied [152, 176]. An interaction of EMF with microtubules might lead to abnormal spindle formation and even mitotic arrest. The magnitude of DEP force F_{DEP} per length of microtubule l_{mt} in the cytoplasm can be calculated with [176]

$$\frac{F_{\mathrm{DEP}}}{l_{\mathrm{mt}}} = \frac{1}{4}\pi r_{\mathrm{mt}}^2 \varepsilon_{\mathrm{cp}} \left(\frac{\omega^2 \varepsilon_{\mathrm{cp}}(\varepsilon_{\mathrm{mt}} - \varepsilon_{\mathrm{cp}}) + \sigma_{\mathrm{cp}}(\sigma_{\mathrm{mt}} - \sigma_{\mathrm{cp}})}{\omega^2 \varepsilon_{\mathrm{cp}}^2 + \sigma_{\mathrm{cp}}} \right) \nabla |\mathbf{E}|^2. \tag{2.65}$$

The index 'cp' denotes parameters of the cytoplasm and the index 'mt' denotes parameters of the microtubule. The microtubule is tubular, with radius r_{rm}. ε indicates the total permittivity and σ is the specific conductivity. F_{DEP} is always acting towards the direction of highest electric field intensity. The magnitude of F_{DEP} can be frequency dependent, since the gradient of electric field also might be dependent on the applied frequency [152].
Despite the effect in the interior of a cell, electric field distribution within several cells can become inhomogeneous. This might cause DEP force effects on whole cells, which is shown in [177].

The resting potential of cell membranes is in the range of 0.1 V per approximately 10 nm membrane thickness resulting in an intrinsic electric field magnitude of $E = 10^7\,\mathrm{V/m}$ [10, 152]. To get a cellular response, a perturbation of the membrane potential in the range of 100 µV is necessary [178].
In general, pulsed electric fields are known to act on the outer cell membrane when the pulse frequency is relatively small, and to act on the inner cell membrane and on intracellular organelles, when the frequency is relatively high [166]. The exact definition of the frequency ranges are usually not provided.

2.4.2 Magnetic Field Impacts

The relative permeability of human body and thus also of cells is generally very close to that of vacuum [179], making the body- and also cells almost transparent to applied magnetic fields.
Typical magnitudes of magnetic forces known to affect cells (like forces on mechanosenitive ion channels) are in the range of pN or nN [180, 181]. Microtubules possess an unisotropic magnetic susceptibility and are known to align along strong magnetic flux densities in the range of 5 T to 9 T [180, 182–184]. Cell compartments with unisotropic magnetic susceptibility align to magnetic fields also in absence of a field gradient [184]. Other cell compartments with slightly inhomogeneous magnetic susceptibility are lipids. Lipids however are not known to orient even under high magnetic field intensities since their anisotropy is too small [185]. Under the formation of liposomes, the small anisotropies of the lipids sums up,

allowing orientation of the whole structure under a magnetic field. Thus, a magnetic field can cause a deformation of the cell membrane and deformation of nuclear envelope [184–187]. The deformation of a spherical liposome under a magnetic field is shown in **Figure 2.19**. $\chi_{\parallel}$

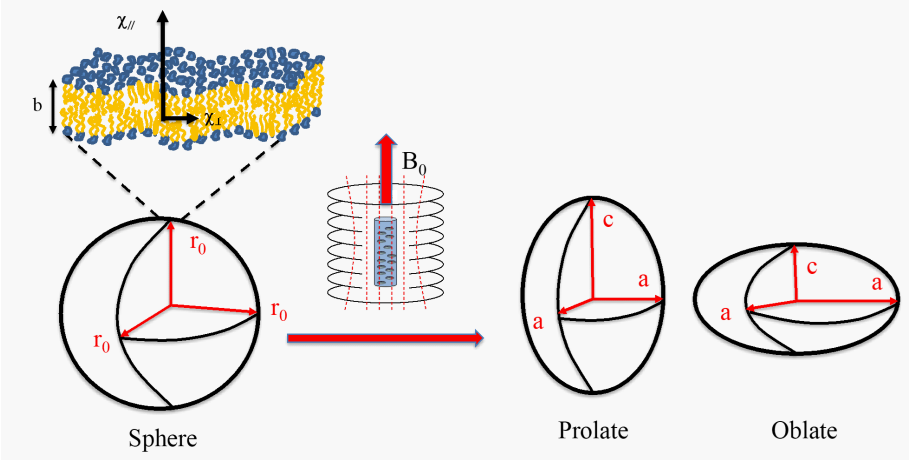

Figure 2.19: Deformation of a liposome exposed to a magnetic field according to Supplementary [185].

is the susceptibility of the membrane parallel to the direction of magnetic flux B_0, $\chi_{\perp}$ is the susceptibility of the membrane perpendicular to the direction of B_0. b is the membrane thickness, r_0 is the initial radius of spherical liposome and a and c are the length of the semi-axes of the ellipsoids as shown in **Figure 2.19**. The deformation can be approximately quantified by the following formula [185, 187]:

$$c - a \approx -\xi \frac{r_0^3 \Delta\chi b B_0^2}{\mu_0 k_C}, \tag{2.66}$$

with $\Delta\chi = \chi_{\parallel} - \chi_{\perp}$. ξ is a constant factor, which is equal to $\xi = 1/18$ for symmetric bilayers. k_C is the average elasticity modulus of the liposome. The ratio $\Delta\chi/k_C$ is in the range $-10^{13}\mathrm{J}^{-1} \leq \Delta\chi/k_C \leq -10^{9}\mathrm{J}^{-1}$ with mean value $\Delta\chi/k_C = -10^{11}\mathrm{J}^{-1}$ [185, 188–191]. $r_0 = 5\,\mu\mathrm{m}$ and $b = 5\,\mathrm{nm}$. Since $\Delta\chi$ is negative for a biological membrane, $c - a$ results in a value greater zero and the liposome will be prolate according to **Figure 2.19**.

The volume of the liposome can be assumed to remain the same before and during exposure to a magnetic field. This consideration results in $r_0^3 \approx a^2 c$ and by inserting (2.66) the

following equation can be obtained [185]:

$$a^3 - \xi \frac{r_0^3 \Delta\chi b}{\mu_0 k_C} B_0^2 a^2 - r_0^3 = 0. \tag{2.67}$$

Static magnetic fields may affect ion channels within cell membranes due to deformation of channels [10]. An explanation of the deformation of ion channels might be the deformation of the membrane. Furthermore, it has been shown that mechanical deformation of the nuclear envelope has significant effects on the cell proliferation [192].

When a charged particle moves within a static magnetic field, the Lorentz force acts on the particle. In [193] magnetic flux density thresholds are calculated which cause effective Lorentz forces on ions with a strength to overcome the diffusion distance. The ions are considered in physiological saline. The threshold magnetic flux density B_{th} for univalent ions (as Na^+) is determined as $B_{\mathrm{th}} = 5.7\,\mathrm{MT}$. The thresholds for bivalent ions as Ca^{2+} and trivalent ions as Fe^{3+} are in the same order of magnitude. Threshold magnitudes of the magnetic flux density in the range of megatesla are also determined in [194]. Additionally, in [195] calculations for the impact of Lorentz force on ions in aqueous solutions have been conducted. There it is shown that magnetic flux densities up to 1 T have no impact on the dynamics of considered ions within the solutions.

Due to water and lipid material properties, most human tissue and also cells have diamagnetic properties. Electrolyte ions have weakly diamagnetic properties [180, 196]. Ferromagnetic particles within human tissue appear usually in non-significant concentration and are assumed to be the results of contamination from the exterior of the body [196]. The concentration of paramagnetic molecules as O_2 or Fe^{++} are too low to cause a change of magnetic susceptibility of the tissue [196]. Paramagnetic and diamagnetic materials which are located in a constant magnetic field cause non-homogeneous fields.
Diamagnetic materials in non-uniform magnetic fields are attracted towards lower field intensities. Paramagnetic materials in gradiant magnetic fields are attracted towards higher field intensities [180]. When the magnetic field within a body (like a cell or cell component) is constant and the body is located in a gradient magnetic field, similiarly to the dielec-

trophoretic force, a magnetophoretic force can be defined [197]:

$$\mathbf{F}_{\text{mag}} = -\frac{V\chi}{\mu_0}(\mathbf{B}\cdot\nabla)\mathbf{B}. \tag{2.68}$$

In (2.68) the susceptibility of the body is χ and the body's volume is V [180, 184]. In diamagnetic levitation a magnetophoretic force on a diamagnetic material is used to lift the material againts gravitational force [184, 198, 199]. It was shown that $(\mathbf{B}\cdot\nabla)\mathbf{B}$ in the range of 100 T^2/m affect paramagnetic molecules as $FeCl_3$, if they appear in certain critical concentration, causing a volume effect [193].

In magnetic resonance imaging (MRI), a physical phenomenon called Larmor precession is used. In an external magnetic field, the proton of a H^+ atom experiences a precession around the magnetic field. The Larmor precession occures due to the spin and magnetic dipole moment properties of the proton in combination with the magnetic field acting on the magnetic dipole moment. This is similar to the precession of a gyroscope due to spin and gravitational force acting on the mass. However, a magnetic field with magnetic flux density $\mathbf{B}$ exerts a magnetic torque force $\mathbf{M}_{\text{mag}}$ on a body with possession of a magnetic dipole moment $\mathbf{m}$:

$$\mathbf{M}_{\text{mag}} = \mathbf{m}\times\mathbf{B} \tag{2.69}$$

The proton possess a Bohr magneton magnetic moment, which aligns only to relatively high magnetic flux densities far above 1 T [184].

Besides direct effects on cells, static magnetic fields are also known to have an impact on aqueous solutions [10]. Observations due to static magnetic fields can also be the outcome of influences on the exposed cell culture medium.

Although the mechanisms are not clear yet, it is striking that in the frame of exposure to low frequency magnetic fields, often influences on ion channels can be observed. Time varying magnetic fields induce electric fields within cells. Thus, this induction rather than the magnetic field itself might be one reason of biological effects. Induced electric fields however, are

rather small at low frequencies as applied in the frame of many cell differentiation processes using ELF-EMF. This effect is certainly more relevant when PEMF are used. In [200] the transmembrane voltage due to PEMF exposure has been calculated analytically. In the applied model, a current in coils results in a magnetic field within a cell suspended in a cell culture medium, which further induces an electric field within the cell. It is shown that a pulsed magnetic flux density with an amplitude around $B = 5.5\,\mathrm{T}$ and $t = 20\,\mu\mathrm{s}$ duration causes a transmembrane voltage with peak amplitude of $V_\mathrm{m} = 0.5\,\mathrm{V}$ [200]. Transmembrane voltages, in the range of 0.5 V to 1 V, are known to cause a poration of cell membranes [166, 201]. High intensity magnetic fields in general are known to cause permeabilization of cell membranes [202, 203].
Such high intensity magnetic fields play a minor role in the frame of cell differentiation and reprogramming.

Some studies apply static magnetic fields in combination with NPs. Magnetic NPs under an externally applied magnetic field, are found to potentially lead to high-gradient magnetic fields (HGMFs) in their close vicinity [194]. These fields are known to have versatile effects on cells and specially on cell differentiation. This might have several reasons: the magnetic force acting on a magnetic dipole is proportional to the magnetic field gradient, thus within strong field gradients, magnetic forces can act on cell compartments owning a magnetic dipole. Such a gradient in magnetic field can have assisting or opposing effects on ions migration through cell membranes, changing the resting potential within cell membranes according to the Nernst equation [194],

$$V_m = \frac{\mathrm{R}T}{\mathrm{zF}} \ln\left(\frac{n_\mathrm{o}}{n_\mathrm{i}}\right) \pm \frac{p}{\mathrm{ze_{charge}}} \left|\frac{\mathrm{d}\mathbf{B}}{\mathrm{d}l}\right| L. \tag{2.70}$$

Here, V_m is the potential difference between the two cell membrane sides, R is the gas constant, F is the Faraday constant, n_o defines the ion concentration outside the cell whereas n_i defines the ion concentration inside the cell, p is the magnetic dipole moment of regarded ion, $\mathbf{B}$ is the magnetic flux density vector, its spacial derivative is in the direction of the dipole moment, z is the ion valence (+1 or -1), $\mathrm{e_{charge}}$ is the elementary charge and L stands

for the half cell length.

According to [194], the gradient of a magnetic field in radial direction due to a magnetic NP can be calculated with

$$\frac{\mathrm{d}B_{//}}{\mathrm{d}r} = \frac{2\mu_0 M_\mathrm{S} r_\mathrm{NP}^3}{r^4}. \tag{2.71}$$

$B_{//}$ is the magnetic flux density in direction of the magnetic moment, its derivative is in respect to the radial distance r from the particle, M_S is the saturation magnetization and r_NP is the radius of the magnetic NP. μ_0 is the vacuum permeability.
For a Fe_3O_4 NP with $M_S = 510\,\mathrm{kA\,m^{-1}}$ and a particle radius of $r_\mathrm{NP} = 5\,\mathrm{nm}$, the gradient of magnetic flux density in radial direction closely to the NP's surface is around $2.6 \cdot 10^8\,\mathrm{T/m}$. Located at the membrane's surface, this gradient is sufficient to change the membrane potential locally [194]. It was shown that a magnetic flux density gradient of 100 T/m has already an effect on mesenchymal stem cell differentiation [194, 204].

In the low frequency regime several studies with AuNPs were conducted. The majority of studies do not address the physical interaction mechanism between nanoparticles and magnetic fields [205–209]. Other studies hypothesize that the presence of nanoparticles causes relevant magnetic field alterations, such as changes in local field distribution or field enhancement, which lead to enhancement of biological responses [13, 15, 210, 211].
Plain bulk gold material is diamagnetic with a volume magnetic susceptibility of $\chi_\mathrm{p} = -3.4 \cdot 10^{-5}$ [212]. Depending on their size, shape and surface modifications the magnetic susceptibilities of AuNPs are known to differ significantly from that of bulk gold. At the nanoscale, magnetic phenomena are influenced by both volume and surface effects, which modify the electronic structure of materials. While in bulk metals charge carriers can move steadily through energy states, there is a transfer towards discrete energy states (due to the quantum confinement effects) in nanoparticles [213]. New magnetic properties arise due to the geometric confinement of electrons and the large fraction of surface atoms present in nanoparticles [213]. Thereby, surface charges can be transferred to the inner part of the material due to energy minimization and imbalanced spins of charges near the surface of nanoparticles can appear. Imbalanced spins near the surface of an atom give rise to additional magnetic moments [214].
While the magnetic properties of plain AuNPs can already be different compared to bulk

gold material, in surface modified particles the binding of molecules can cause significant additional alterations of magnetic properties. This changes are caused by rearrangement of charge carriers due to the surface modifications [213, 215]. Since the surface of a particle is the primarily affected region, the significance of the bond particles in terms of change of magnetic properties decreases for bigger particle sizes with lower surface to volume ratios. Surface modified AuNPs can obtain stronger diamagnetic material properties than bulk gold material and even para- and ferromagnetic properties [216–218]. In thiol-capped AuNPs an appearance of magnetic moment is associated with charge transfer from the capping molecules [213, 215]. Thiolated AuNPs can have hysteresis magnetization curves with remnant magnetization and coercitive field [219]. The details of physical interplay of the surface atoms of AuNPs with the (very different) binding partners are yet to be explained. Furthermore, relations to the sizes of the AuNPs need to be generally specified. In this regard and to the best of our knowledge, there is no theory with scientific consensus which allows a prediction of the magnetic properties of AuNPs due to surface modification. Broad and detailed overviews over the different experimental findings and formulations of possible theories explaining the experimental results are provided elsewhere [217, 218]. The lack of detailed knowledge makes it difficult to quantify the limits of possible magnetic susceptibility values for surface modified AuNPs. The magnetization curves of dodecanethiol-capped AuNPs[220] reveal a mass magnetic susceptibility in the range of $\chi_{\mathrm{p,mass}} = 5 \cdot 10^{-6}\,\mathrm{m^3/kg}$ at a temperature of $T = 300\,\mathrm{K}$, while the magnetic susceptibility increases even further at lower temperatures. For comparison: The mass magnetic susceptibility of bulk gold is not only negative in sign but also at least three orders of magnitude smaller (approximately $\chi_{\mathrm{p,mass}} = -1.76 \cdot 10^{-9}\,\mathrm{m^3/kg}$ [213, 221]). An example of a diamagnetic response is provided for thiolated polyethylene glycol AuNPs where the volume magnetic susceptibility is determined as $\chi_{\mathrm{p}} = -4.9 \cdot 10^{-4}$, which is one order of magnitude higher than the susceptibility of bulk gold material. In another study employing AuNPs coated with methoxy-polyethylene glycol a transient magnetization of nanoparticles is hypothesized which causes a magnetic field enhancement in the same order of the exciting magnetic field [13].
The magnetic energy E of a nanoparticle can be calculated with [197]

$$E = -\frac{\mu_0 \chi_{\mathrm{p}} V}{2} H^2, \tag{2.72}$$

(μ_0 is the vacuum permeability), χ_p is the magnetic susceptibility of the particle, V its volume and H the magnetic field magnitude. To estimate whether a magnetic field can have a significant impact on a gold nanoparticle, the magnetic energy is usually compared to thermal energy. Furthermore, the magnetic force per particle volume $\mathbf{f}$ is [194, 197]

$$\mathbf{f} = \mu_0 \chi_\mathrm{p} (\mathbf{H} \cdot \nabla) \mathbf{H}. \tag{2.73}$$

Thus, to achieve a magnetic force density in the range of gravitational force density which is approximately $f_\mathrm{g} = 10^4 \mathrm{N/m}^3$ [194], very high magnetic fields in combination with magnetic field gradients are necessary.

2.5 Experimental Exposure Setups and Determination of EM Material Properties

In vitro cell experiments are an integral part of the development of new treatment methods and strategies in biomedicine. Usually *in vitro* experiments are applied prior to elaborate *in vivo* studies and allow the empirical evaluation of ideas and theories concerning new therapeutic applications. When it comes to the investigation of mechanisms of action triggered by EMFs on cells from a physical perspective, *in vitro* cell experiments can allow the validation of theoretical calculations. Especially for this purpose, the design of the exposure setup needs to fulfill certain criteria as for example possibly high EMF homogeneity at the exposed cells to affect all cells equally. Different experimental setups have been used in the frame of cell differentiation and cellular reprogramming with EMFs, as well as TTFields experiments. In this chapter, the principles of the exposure setups will be introduced.

Besides the direct exposure of cells to EMFs, experimental setups can also be used to obtain electromagnetic material parameters for theoretical, analytical and numerical investigations of mechanisms of action. Since in the frame of cell culture experiments, cells are surrounded by nurturing culture medium, the electromagnetic parameters of the medium are of interest. A capacitive approach will be introduced, which allows the determination of these parameters.

2.5.1 EMF Exposure Setups for in vitro Cell Culture Experiments

Exposure to magnetic fields

Magnetic field excitation in the frame of *in vitro* cell culture experiments is usually conducted with one of the following exposure setups:

- a single permanent magnet,
- several permanent magnets,
- a single solenoid coil or

- Helmholtz coils.

Permanent magnets are commercially available in different sizes and with different magnetic field strengths. They are ready to use and do not need any external energy supply. Their magnetic field is constant over time. Over large time periods permanent magnets lose their magnetic strength. Permanent magnets have a relatively inhomogeneous magnetic field, which can be slightly modified by application of several magnets.
A magnetic field can be excited by a current within a solenoid coil. The magnetic field strength depends on the dimensional properties of the coil, the number of turns and the current strength within the coil. The most homogeneous magnetic field within a designated volume (as a cell culture dish) can be achieved with Helmholtz coils.

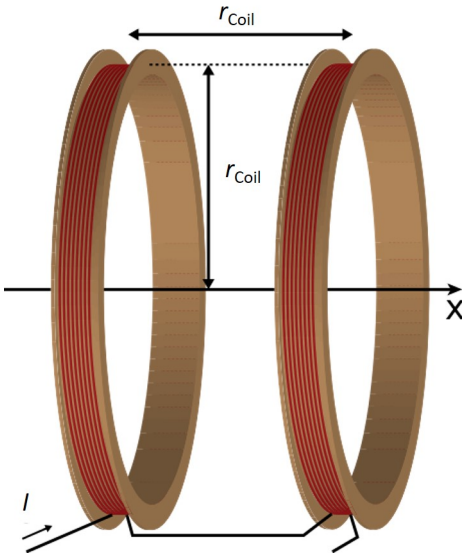

Figure 2.20: Arrangement of Helmholtz Coils from [222].

Helmholtz coils are two identical coils according to **Figure 2.20**. r_{Coil} is the coil radius and the distance between the two coils. The magnetic flux density along the x-axis can be calculated with

$$\mathbf{B}(x) = \frac{\mu_0 I}{2}\left(\frac{r_{\mathrm{Coil}}^2}{\left(r_{\mathrm{Coil}}^2 + \left(x - \frac{r_{\mathrm{Coil}}}{2}\right)^2\right)^{3/2}} + \frac{r_{\mathrm{Coil}}^2}{\left(r_{\mathrm{Coil}}^2 + \left(x + \frac{r_{\mathrm{Coil}}}{2}\right)^2\right)^{3/2}}\right)\mathbf{e}_x. \tag{2.74}$$

In (2.74) $x = 0$ is in the middle between the two coils.

The diameter of the wire has to be appropriately chosen for the current flowing through the solenoid coil. Due to self-inductance and self-capacitance, solenoid coils exhibit resonant behavior at certain frequencies. Thus, they have to be designed for the target frequencies and target magnetic flux densities. However, when designed carefully, desired magnetic flux densities as well as time courses of magnetic fields can be achieved.

Exposure to electric fields

An EMF exposure setup for *in vitro* cell culture experiments with the focus on electric field

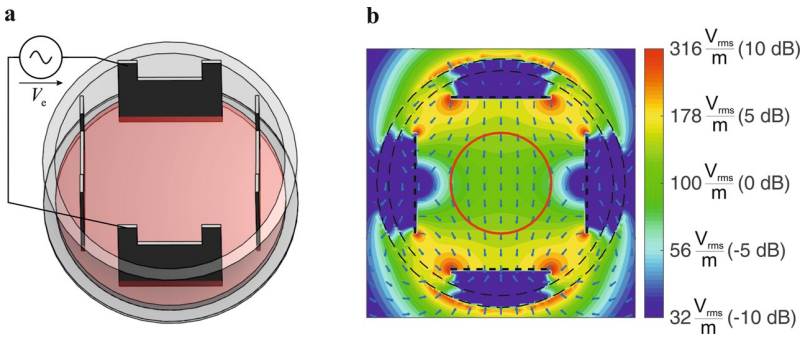

Figure 2.21: a) EMF exposure setup and b) numerical simulation of the resulting electric field distribution from [1].

component is introduced in [1] and shown in **Figure 2.21 a)**. In this setup, four stainless steel electrodes are mounted into the cell culture dish. One facing pair of two electrodes is excited with the sinusoidal voltage V_e. In this example V_e is chosen appropriately for TTFields to achieve an electric field magnitude RMS value of 100 V/m in the centre of the petri dish. After a defined time period, the excitation can be switched to the other pair of electrodes in order to achieve a perpendicular polarization direction of the electric field. **Figure 2.21 b)** shows the electric field distribution within the petri dish for a frequency $f = 100\,\mathrm{kHz}$. The centre of the petri dish with boundaries marked by the red circle has a diameter of 15 mm and can be used for the cultivation of cells. Within this area, the target electric field can be approximately realized. This setup design has the advantage that implemented materials can be acquired relatively easy, the principle design can be adapted to different cell culture

dishes and different electric field intensities and polarization directions can be used.

Overall experimental design for cell culture experiments

EMF exposure setups according to **Figure 2.20** and **Figure 2.21 a)** need at least external

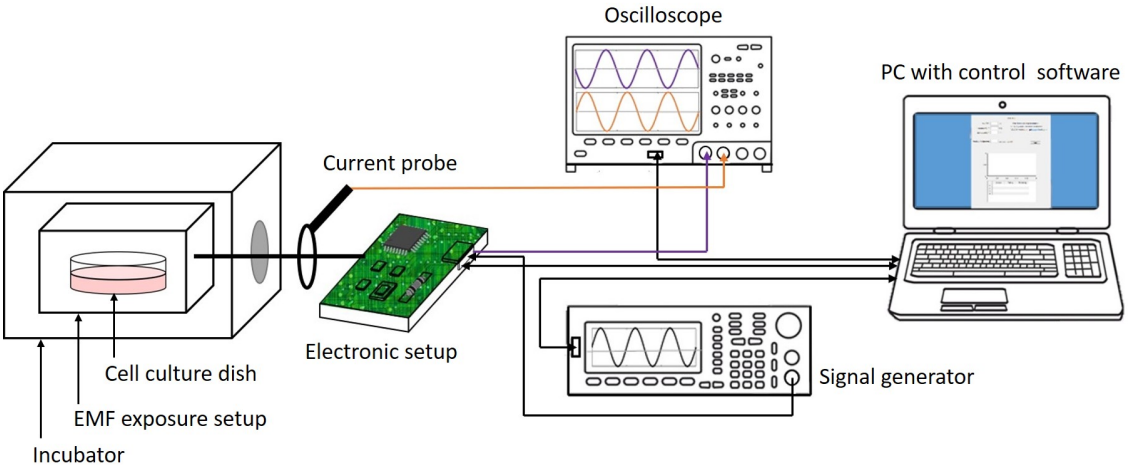

Figure 2.22: Principle overall design of an experimental setup for *in vitro* EMF experiments on cells.

energy supply to function. In many cases many more elements are integral parts of the overall experimental setup. **Figure 2.22** shows the principle experimental setup as often applied in laboratories. During *in vitro* cell culture experiments, environmental conditions as CO_2 content, temperature and humidity of ambient air have to be strictly controlled. This is the reason why the EMF exposure setup and the cell culture dish have to be placed within an incubator. A signal generator can be used to achieve a desired time course of the excitation. An oscilloscope allows the monitoring of applied voltages and currents. An electronic setup is necessary, when the excitation of the signal generator needs to be modified. Typical elements of an electronic setup can be amplifiers and attenuators as well as filters and microcontrollers. A PC with control software can facilitate the control and data storage of experiments. Despite the components shown in **Figure 2.22** also other components can be part of the experimental setup. These include EMF probes and equipment for temperature monitoring within the cell medium.

2.5.2 Capacitive Determination of Material Properties

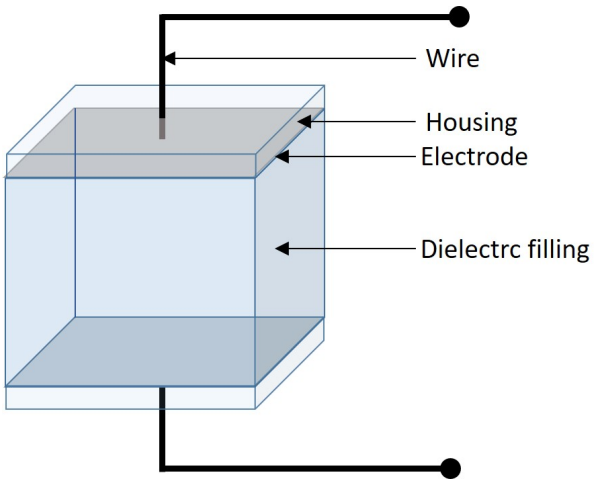

Figure 2.23: Example of a capacitor containing a dielectric filling.

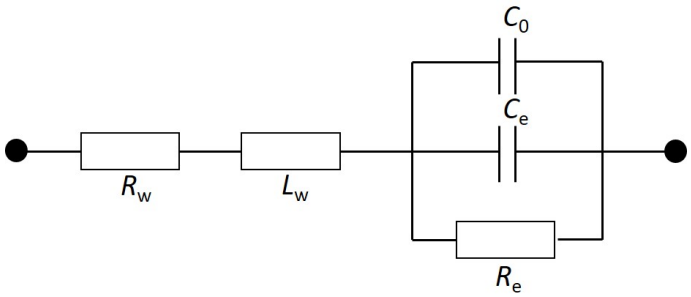

Figure 2.24: Lumped element model of a capacitor containing a dielectric filling according to [223].

An example of a capacitor containing a dielectric filling is shown in **Figure 2.23**. The electromagnetic behavior of the capacitor can be described by the lumped element model from **Figure 2.24** [223]. R_w represents the resistivity of the supply wire and L_w its inductance. C_e represents the ideal capacitance of the electrode configuration containing the dielectric material by neglecting stray electric fields and R_e represents the resistivity of the electrode configuration. C_0 is the stray capacitance. The total impedance Z_cap of the lumped element model can be calculated with

$$Z_\mathrm{cap} = R_\mathrm{w} + \mathrm{j}\omega L_\mathrm{w} + \left(\mathrm{j}\omega C_\mathrm{tot} + \frac{1}{R_\mathrm{e}}\right)^{-1}. \tag{2.75}$$

Thereby ω is the circular frequency and $C_{\mathrm{tot}} = C_{\mathrm{e}} + C_0$. By measuring the impedance Z_{cap} over a frequency range and fitting (2.75) to the measured curves, values for R_{w}, L_{w}, C_{tot} and R_{e} can be obtained [223]. The specific conductivity of the dielectric filling can be calculated with the distance d between the electrodes and the area A of the electrode:

$$\sigma = \frac{d}{AR_{\mathrm{e}}}. \tag{2.76}$$

The relative permittivity of the dielectric filling can be calculated with [223]

$$\varepsilon_{\mathrm{r}} = \frac{C_{\mathrm{e}}}{K}. \tag{2.77}$$

K is the constant of the capacitor and can be obtained by calibration measurements. The impedances of two materials with well known relative permittivities must be measured and K can be calculated with [223]

$$K = \frac{C_{\mathrm{tot},1} - C_{\mathrm{tot},2}}{\varepsilon_{\mathrm{r},1} - \varepsilon_{\mathrm{r},2}} \tag{2.78}$$

The index 1 and 2 refer to the respective material with known permittivity. For the determination of the relative permittivity of the dielectric filling according to (2.77), also C_{e} has to be obtained. Since $C_{\mathrm{e}} = C_{\mathrm{tot}} - C_0$, first C_0 must be calculated from one of the calibration measurements

$$C_0 = C_{\mathrm{tot},1} - K\varepsilon_{\mathrm{r},1}. \tag{2.79}$$

However, when two electrodes are brought into an electrolyte solution, which is a liquid containing dissolved ions, and a voltage is applied to the electrodes, an ion current can be excited [224]. Depending on the chemical constitution of the electrolyte solution, the material of the electrodes and the frequency of electric excitation, different electrochemical and physical phenomena can occur at the interface of the solution and the electrodes. Electrochemical reactions as corrosion of the electrodes do not occur when the electrode material is chosen appropriately. At low frequencies and with typical electrolyte solutions as cell culture medium, a phenomenon which often occurs is polarization of the electrodes. In the frame of electrode polarization, some dissolved ions of the solution assemble at the electrode with opposite charge as schematically shown in **Figure 2.25**. The ions at the electrodes

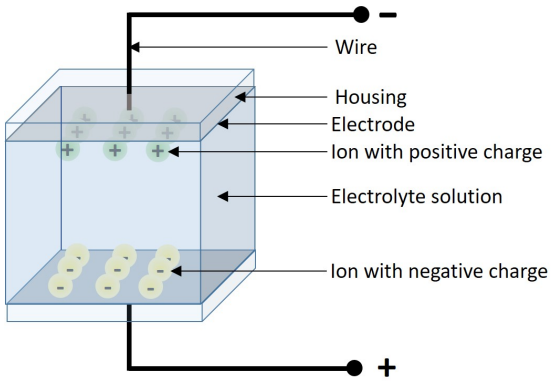

Figure 2.25: Electrode polarization effect within a capacitor containing electrolyte solution.

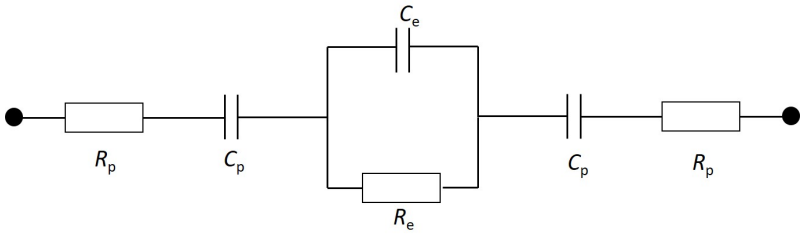

Figure 2.26: Lumped element model of a capacitor containing electrolyte solution with consideration of electrode polarization according to [225].

build up an additional capacitance by simultaneously increasing the resistivity of the configuration. A lumped element model taking electrode polarization into account is shown in **Figure 2.26** [225]. The index p refers to lumped element parameters caused by the polarization effect. The lumped element model from **Figure 2.26** assumes an ideal capacitor without any wire impedance and without stray capacitance. There are different models describing the exact physical dynamics behind the polarization of the electrodes which are described comprehensively in [226]. The polarization effect at the electrodes is frequency dependent. At very high frequencies, the ions cannot follow the reversion of electric field polarization.

Hermann Schwan proposed to model the effect of electrode polarization as shown in **Figure 2.25** with the lumped element model from **Figure 2.27** [227]. The fundament of his theory is the lumped element model from **Figure 2.26**, but he expressed the electric behavior with the frequency-dependent capacitance $C(\omega)$ and the frequency-dependent resistivity

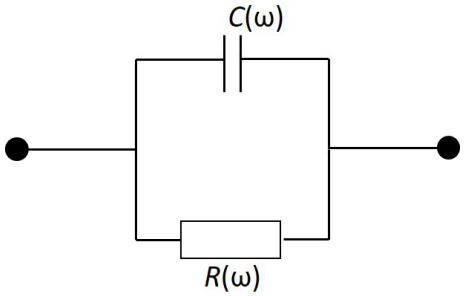

Figure 2.27: Lumped element model of a capacitor containing electrolyte solution according to [227].

$R(\omega)$. The resistivity can be calculated by application of the measured impedance Z_{measure} of the electrode configuration as [227]

$$R(\omega) = \frac{|Z_{\mathrm{measure}}|^2}{\mathrm{Re}(Z_{\mathrm{measure}})}. \tag{2.80}$$

Furthermore, $C(\omega)$ can be obtained with [227]

$$C(\omega) = -\frac{\mathrm{Im}(Z_{\mathrm{measure}})}{\omega |Z_{\mathrm{measure}}|^2}. \tag{2.81}$$

At sufficiently high frequencies over a certain cut-off frequency f_{c} the electrode polarization effect becomes negligible or vanishes even. For $f > f_{\mathrm{c}}$ the frequency dependent resistivity and capacitance can be approximated with $R(\omega) = R_{\mathrm{e}}$ and $C(\omega) = C_{\mathrm{e}}$. Accordingly, the specific conductivity and the relative permittivity can be calculated with (2.76) and (2.77), where the constant K can be approximated with [223]

$$K = \frac{\varepsilon_0 A}{d}. \tag{2.82}$$

In this model, the impedance of the wire and the stray impedance are assumed to be negligible compared to the impedance due to the electrolyte solution.

There are different techniques allowing to take electrode polarization into account and to eliminate its impact on the determination of electromagnetic material parameters. These techniques include mathematical, graphical and experimental approaches [227–230]. How-

ever, these techniques are limited to certain conditions. For example, the *electrode distance variation technique* cannot be applied for cases where the impedance due to electrode polarization is much bigger than the impedance of the electrolyte [227, 228].
Electrode polarization is strongly dependent on the electrode material. Platinum is an electrode material which is often used in biomedical applications. It is bio-compatible and more resistant to corrosion than many other materials including copper [226]. Furthermore, the polarization impedance at platinum electrodes is known to be lower than the polarization impedance of many other electrode materials [228]. *Platinum black* electrodes can be produced by platinizing platinum electrodes. A detailed description of the manufacturing process can be found in [231]. Platinum black electrodes have a highly porous surface [228]. This porous surface results in a higher effective surface area for the polarization effect [232]. A higher effective surface area results in a higher capacitance C_{p} and in a lower resistivity R_{p}. The total polarization impedance becomes smaller while the impedance of the electrolyte does not change. The higher the electrolyte impedance compared to the polarization impedance, the lower is the cut-off frequency f_{c} [232].

3 Magnetic Field Interactions with Cells and AuNPs

3.1 Fourier Analysis of PEMF Excitation

The work presented in this section was partly conducted in the frame of a conference proceeding [233]. I developed the idea and the content. Dr. Annette Hoffmeister and Professor Boris Chichkov supervised the work.

In section 2.1.1 PEMF excitation was introduced as a classical excitation method used during cellular reprogramming with magnetic fields. In the following, this excitation method will be analyzed to find significant spectral components, which might dominate the interaction with cells and trigger biological responses.
A classical PEMF usually refers to an (almost) rectangular and pulsed magnetic field as shown in **Figure 2.3**. In the frame of cell reprogramming and cell differentiation, a classical PEMF excitation function f_{PEMF} can mathematically be described by multiplication of two rectangular pulse functions f_1 and f_2.

The according functions as well as the resulting function f_{PEMF} are shown in **Figure 3.1**. Mathematically, the three functions can be expressed as [233]:

$$f_{\mathrm{PEMF}} = f_1(t) f_2(t), \tag{3.1}$$

$$f_1(t) = \begin{cases} 1 & aT_1 \leq t \leq (aT_1 + t_{\mathrm{LF}}) \\ 0 & (aT_1 + t_{\mathrm{LF}}) < t \leq (a+1)\,T_1 \end{cases}, \tag{3.2}$$

$$f_2(t) = \begin{cases} 1 & aT_2 \leq t \leq (aT_2 + t_{\mathrm{burst}}) \\ 0 & (aT_2 + t_{\mathrm{burst}}) < t \leq (a+1)\,T_2 \end{cases}. \tag{3.3}$$

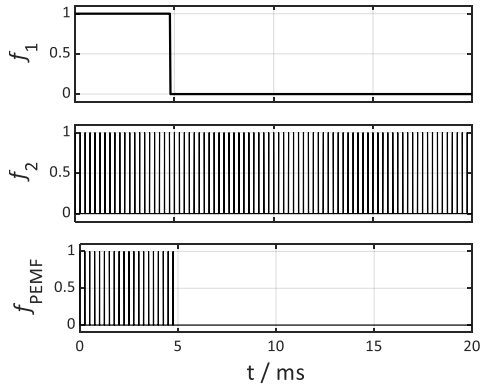

Figure 3.1: Time-dependence of the functions f_1, f_2 and f_{PEMF}.

f_{PEMF} is normalized to an amplitude of one. Index 1 refers to the respective parameters of f_1 and index 2 refers to the respective parameters of f_2. a is a natural number including zero, T is the duration of one period and t_{burst} and t_{LF} represent the respective pulse widths with $t_{\mathrm{LF}} = 4.8\,\mathrm{ms}$, $t_{\mathrm{burst}} = 0.25\,\mathrm{s}$, $T_1 = 20\,\mathrm{ms}$ and $T_2 = 0.25\,\mathrm{ms}$. The real, continuously differentiable periodical functions f_1 and f_2 can be described by converging Fourier series [234] with angular frequency ω [233]:

$$f_1(t) = f_{0,1} + \sum_{k=1}^{\infty} \left[f_{\mathrm{s}k,1} \sin(k\omega_1 t) + f_{\mathrm{c}k,1} \cos(k\omega_1 t) \right] \tag{3.4}$$

$$f_2(t) = f_{0,2} + \sum_{n=1}^{\infty} \left[f_{\mathrm{s}n,2} \sin(n\omega_2 t) + f_{\mathrm{c}n,2} \cos(n\omega_2 t) \right]. \tag{3.5}$$

$f_{0,1}$ and $f_{0,2}$ are constants and $f_{sk,1}$, $f_{ck,1}$, $f_{sn,2}$ and $f_{cn,2}$ are coefficients [233]:

$$\begin{aligned}
f_{0,1} &= \frac{1}{T_1}\int_0^{T_1} f_1(t)\mathrm{d}t = \frac{t_{\mathrm{LF}}}{T_1},\\
f_{0,2} &= \frac{1}{T_2}\int_0^{T_2} f_2(t)\mathrm{d}t = \frac{t_{\mathrm{burst}}}{T_2},\\
f_{sk,1} &= \frac{2}{T_1}\int_0^{T_1} f_1(t)\sin(k\omega_1 t)\mathrm{d}t = \frac{-2}{T_1 k\omega_1}\left(\cos(k\omega_1 t_{\mathrm{LF}})-1\right),\\
f_{sn,2} &= \frac{2}{T_2}\int_0^{T_2} f_2(t)\sin(n\omega_2 t)\mathrm{d}t = \frac{-2}{T_2 n\omega_2}\left(\cos\left(n\omega_2 t_{\mathrm{burst}}\right)-1\right),\\
f_{ck,1} &= \frac{2}{T_1}\int_0^{T_1} f_1(t)\cos\left(k\omega_1 t\right)\mathrm{d}t = \frac{2}{T_1 k\omega_1}\sin\left(k\omega_1 t_{\mathrm{LF}}\right),\\
f_{cn,2} &= \frac{2}{T_1}\int_0^{T_2} f_2(t)\cos(n\omega_2 t)\mathrm{d}t = \frac{2}{T_2 k\omega_2}\sin\left(n\omega_2 t_{\mathrm{burst}}\right).
\end{aligned} \tag{3.6}$$

By reformulating f_1 in Euler's form, the following equation can be gained [233]

$$\begin{aligned}
f_1(t) &= f_{0,1}\\
&+\sum_{k=1}^{\infty}\left[\frac{\sqrt{f_{sk,1}^2+f_{ck,1}^2}}{2}\left(\mathrm{e}^{-\mathrm{j}\left(k\omega_1 t-\arctan\left(\frac{f_{sk,1}}{f_{ck,1}}\right)\right)}+\mathrm{e}^{\mathrm{j}\left(k\omega_1 t-\arctan\left(\frac{f_{sk,1}}{f_{ck,1}}\right)\right)}\right)\right].
\end{aligned} \tag{3.7}$$

This reformulation shows that f_1 has the constant direct current offset $f_{0,1}$ and additionally, discrete spectral components at positive frequencies $f=(k\omega_1)/(2\pi)$ with the spectral amplitudes F_1 of [233]

$$F_1(k) = \frac{\sqrt{f_{sk,1}^2+f_{ck,1}^2}}{2} = \frac{\sqrt{2-2\cos\left(k\omega_1 t_{\mathrm{LF}}\right)}}{2k\pi}. \tag{3.8}$$

Figure 3.2 shows the spectral components of f_1 for positive frequencies up to $f=500\,\mathrm{Hz}$. As indicted by (3.8), the local amplitude maxima follow the function $1/(k\pi)$ at the frequencies $f=k\omega_1/(2\pi)=k\cdot 50\,\mathrm{Hz}$. The spectral amplitudes decrease at least with $1/(k\pi)$.

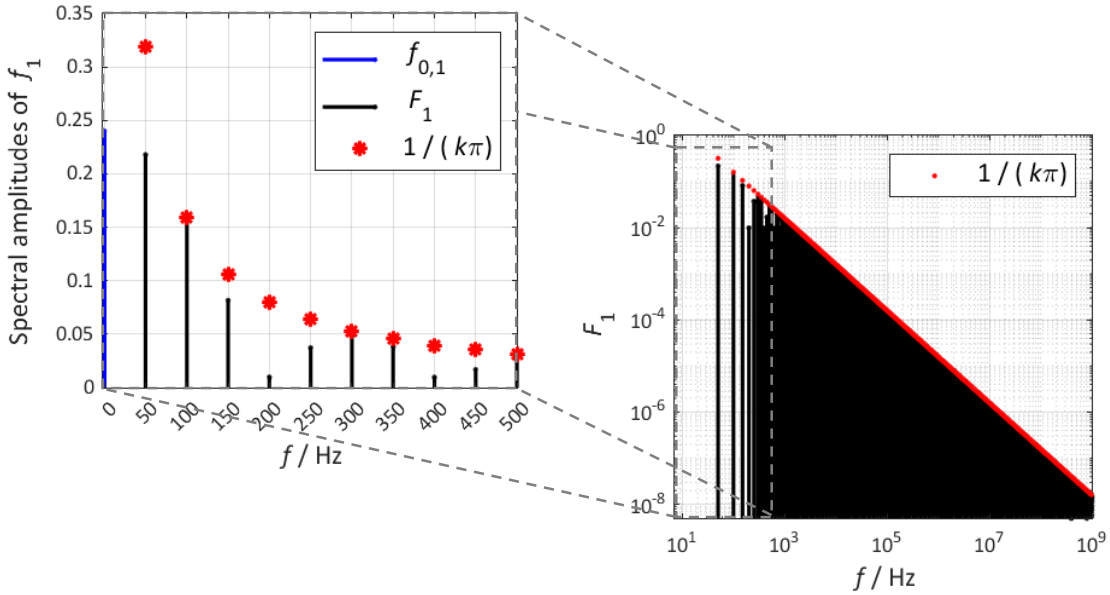

Figure 3.2: Spectral components of f_1.

Similarly, f_2 has spectral components at positive frequencies $f = n\omega_2/(2\pi)$ with the spectral amplitudes F_2 of [233]

$$F_2(n) = \frac{\sqrt{f_{sn,1}^2 + f_{cn,1}^2}}{2} = \frac{\sqrt{2 - 2\cos(n\omega_2 t_{\text{burst}})}}{2n\pi}. \tag{3.9}$$

The spectral components of f_2 are shown in **Figure 3.3**. As predicted by (3.9), the local amplitude maxima follow the function $1/(n\pi)$ at the frequencies $k\omega_2/(2\pi) = n \cdot 4\,\text{kHz}$.

With (3.4) and (3.5), f_{PEMF} can be expressed as [233]

$$\begin{aligned} f_{\text{PEMF}} = & f_{0,1} f_{0,2} + f_{0,1} \sum_{n=1}^{\infty} \left[f_{\text{sn},2} \sin(n\omega_2 t) + f_{\text{cn},2} \cos(n\omega_2 t) \right] \\ & + f_{0,2} \sum_{k=1}^{\infty} \left[f_{\text{sk},1} \sin(k\omega_1 t) + f_{\text{ck},1} \cos(k\omega_1 t) \right] \\ & + \sum_{k=1}^{\infty} \left[f_{\text{sk},1} \sin(k\omega_1 t) + f_{\text{ck},1} \cos(k\omega_1 t) \right] \sum_{n=1}^{\infty} \left[f_{\text{sn},2} \sin(n\omega_2 t) + f_{\text{cn},2} \cos(n\omega_2 t) \right]. \end{aligned} \tag{3.10}$$

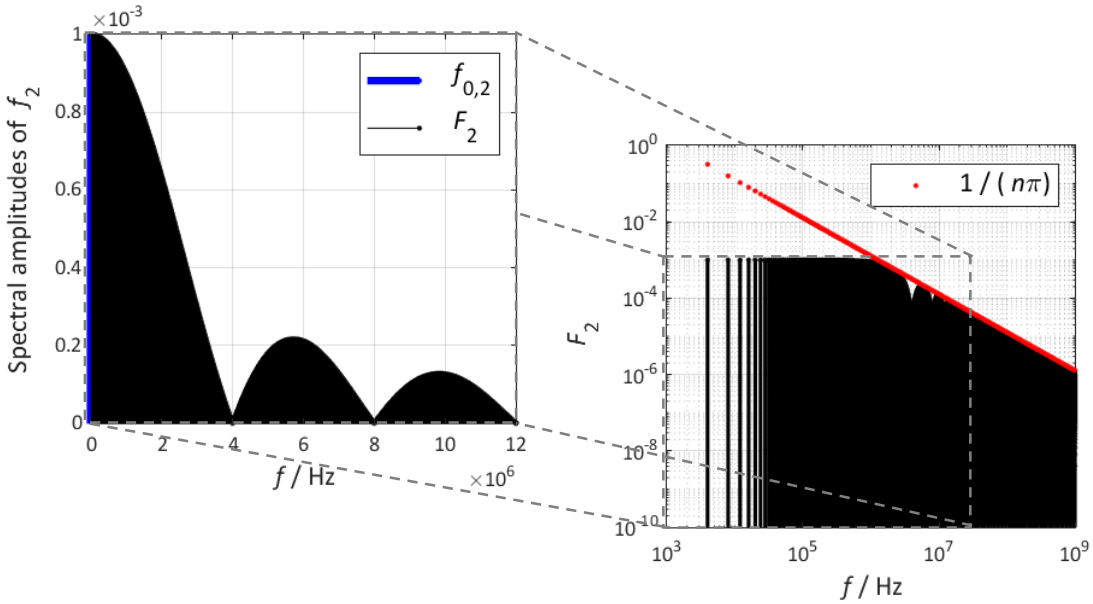

Figure 3.3: Spectral components of f_2.

The Fourier series approximation of f_1 and f_2, as well as f_{PEMF} can be seen in **Figure 3.4** for $k = 1000$ and $n = 5000$. It can be seen that a sufficient approximation of the functions is achieved when comparing the results to those of **Figure 2.3**.

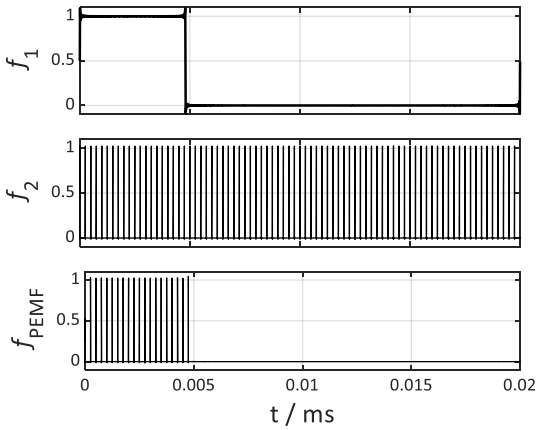

Figure 3.4: Approximation of the functions f_1, f_2 and f_{PEMF} with a maximum of $k = 1000$ and $n = 5000$ according to [233].

However, the spectral components of f_{PEMF} have to be determined yet. The first summand in (3.10) is the constant spectral amplitude. In the second summand, the spectral amplitudes are the ones of f_2 multiplied by the factor $f_{0,1}$. Finally, the third summand contains the spectral amplitudes of f_1 multiplied with $f_{0,2}$.

With (3.7), the fourth summand of (3.10) can be written as [233]:

$$
\begin{aligned}
&\sum_{k=1}^{\infty}\left[F_1(k)\left(\mathrm{e}^{-\mathrm{j}\left(k\omega_1 t-\arctan\left(\frac{f_{sk,1}}{f_{ck,1}}\right)\right)}+\mathrm{e}^{\mathrm{j}\left(k\omega_1 t-\arctan\left(\frac{f_{sk,1}}{f_{ck,1}}\right)\right)}\right)\right]\\
&\sum_{n=1}^{\infty}\left[F_2(n)\left(\mathrm{e}^{-\mathrm{j}\left(n\omega_2 t-\arctan\left(\frac{f_{sn,2}}{f_{cn,2}}\right)\right)}+\mathrm{e}^{\mathrm{j}\left(n\omega_2 t-\arctan\left(\frac{f_{sn,2}}{f_{cn,2}}\right)\right)}\right)\right]\\
&=\sum_{k=1}^{\infty}\sum_{n=1}^{\infty}F_1(k)F_2(n)\,\mathrm{e}^{-\mathrm{j}\left((k\omega_1+n\omega_2)t-\arctan\left(\frac{f_{sk,1}}{f_{ck,1}}\right)-\arctan\left(\frac{f_{sn,2}}{f_{cn,2}}\right)\right)}\\
&+\sum_{k=1}^{\infty}\sum_{n=1}^{\infty}F_1(k)F_2(n)\mathrm{e}^{-\mathrm{j}\left((k\omega_1-n\omega_2)t-\arctan\left(\frac{f_{sk,1}}{f_{ck,1}}\right)+\arctan\left(\frac{f_{sn,2}}{f_{cn,2}}\right)\right)}\\
&+\sum_{k=1}^{\infty}\sum_{n=1}^{\infty}F_1(k)F_2(n)\mathrm{e}^{\mathrm{j}\left((k\omega_1-n\omega_2)t-\arctan\left(\frac{f_{sk,1}}{f_{ck,1}}\right)+\arctan\left(\frac{f_{sn,2}}{f_{cn,2}}\right)\right)}\\
&+\sum_{k=1}^{\infty}\sum_{n=1}^{\infty}F_1(k)F_2(n)\mathrm{e}^{\mathrm{j}\left((k\omega_1+n\omega_2)t-\arctan\left(\frac{f_{sk,1}}{f_{ck,1}}\right)-\arctan\left(\frac{f_{sn,2}}{f_{cn,2}}\right)\right)}\\
&=\sum_{k=1}^{\infty}\sum_{n=1}^{\infty}2F_1(k)F_2(n)\cos\left((k\omega_1+n\omega_2)t-\arctan\left(\frac{f_{sk,1}}{f_{ck,1}}\right)-\arctan\left(\frac{f_{sn,2}}{f_{cn,2}}\right)\right)\\
&+\sum_{k=1}^{\infty}\sum_{n=1}^{\infty}2F_1(k)F_2(n)\cos\left((k\omega_1-n\omega_2)t-\arctan\left(\frac{f_{sk,1}}{f_{ck,1}}\right)+\arctan\left(\frac{f_{sn,2}}{f_{cn,2}}\right)\right)
\end{aligned}
\tag{3.11}
$$

With the reformulation of the forth summand of (3.10), it is illustrated that f_{PEMF} contains spectral components at combined frequencies of frequencies from f_1 and f_2. **Figure 3.5** shows the spectral components of f_{PEMF}. Local spectral amplitude maxima appear at frequencies $f=(n\cdot 4\,\mathrm{kHz})\pm 50\,\mathrm{Hz}$. The spectrum is very similar to the frequency spectrum of f_2.

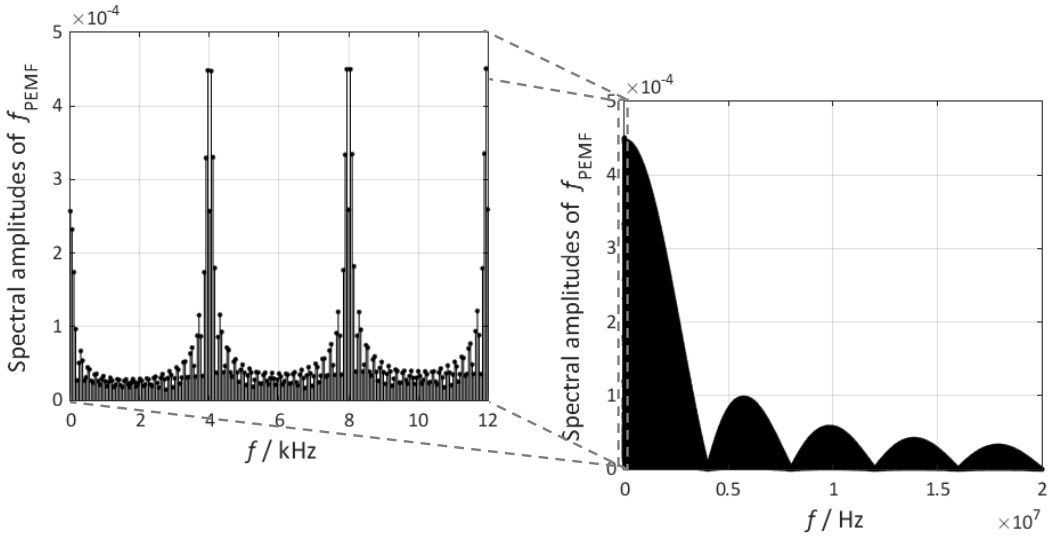

Figure 3.5: Spectral components of f_{PEMF} on the basis of [233].

In scientific studies using PEMF excitation with f_{PEMF} on cells, the term *frequency* is often related to the repetition frequency of the pulse, $f = 50\,\mathrm{Hz}$. However, the dominant spectral components are in the range of multiples of $f = 4\,\mathrm{kHz}$, which suggest to shift the attention towards these frequencies when it comes to the investigation of mechanisms of action. Furthermore, an overall agreement on the use of the frequency term would allow for independent verification and facilitate comparison between different studies as well as investigations of mechanisms of action.

Based on this frequency analysis and if not stated differently, the following investigations of possible interaction mechanisms of EMF with cells focuses on the frequencies $f = 50\,\mathrm{Hz}$, as the classical frequency of ELF-EMF and $f = 4\,\mathrm{kHz}$ as the fundamental frequency in the considered PEMF excitation.

3.2 Magnetic Field Distribution in Cells and AuNPs

The work presented in this section was partly conducted in the frame of a peer-reviewed journal publication [8]. In the frame of this work [8], I collaborated closely with the Computational Photonics group of the Hannover Centre for Optical Technologies (HOT), Leibniz University Hannover. I developed the idea and the content of the paper. Dr. Atefeh Habibpourmoghadam (HOT) provided additional literature references to achieve a comprehensive study and verified the methods and results. Dr. Andrey Evlyukhin provided his expertise concerning the mathematical modelling of micro and nano photonics and verified the applied mathematical models and formulas. Dr. Annette Hoffmeister initiated the project. Professor Antonio Calà Lesina (HOT) and Professor Boris N. Chichkov supervised the work.

For the evaluation of the mechanisms of action triggered by magnetic fields on exposed cells and cells with AuNPs, their magnetic response has to be evaluated. In this section, the applied calculation methods are introduced and the magnetic field distribution within cells and cells with AuNPs is shown. Subsequently, the results allow a discussion of possible mechanisms of action triggered in the cell. The presented calculations not only allow a first estimate on possible mechanisms of action but also provide a basis for further studies to come. Thus, this section contributes to the investigation of mechanisms of action triggered by magnetic fields in the frame of cellular reprogramming.

3.2.1 Calculation Formulas and Methods

All results were cross-validated with analytical formulas and numerical electromagnetic simulations. In the following first the analytical considerations and calculation formulas will be introduced and subsequently, the numerical electromagnetic simulation models and methods will be presented.

Analytical considerations and calculation formulas

Due to high water content, the effective magnetic susceptibility of cells, including major

compartments like the cytosol, is in the range of 10^{-6} [194, 235]. Lipid structures in cells have even lower magnetic susceptibilities than compartments with high water content [194]. However, due to their higher magnetic susceptibility, the magnetic response of AuNPs to low-frequency magnetic fields is generally much stronger than the response of eukaryotic cells. Therefore, in our investigations, we neglect the specific cellular environment and consider AuNPs located in air. The permeability of the cells is approximated with the vacuum permeability μ_0.

Ampère's circuital law in differential form and in frequency domain describes the rotation of the magnetic field $\mathbf{H}$ as the sum of different current density contributions,

$$\nabla \times \mathbf{H} = (\sigma - \mathrm{j}\omega\varepsilon)\mathbf{E} + \nabla \times \mathbf{M}. \tag{3.12}$$

In equation (3.12) $\mathbf{E}$ is the electric field vector, σ is the electrical conductivity and ε is the material permittivity, while $\mathbf{M}$ is the magnetization of it. The first summand in (3.12) describes conductive and displacement currents and the second summand describes a current density due to magnetization. The magnetic dipole moment $\mathbf{m}$ of the considered volume can be expressed with a volume integral over the current densities from (3.12),

$$\begin{aligned} \mathbf{m} &= \iiint_V \mathbf{r} \times ((\sigma - \mathrm{j}\omega\varepsilon)\mathbf{E} + \nabla \times \mathbf{M})\mathrm{d}V \\ &= (\alpha_\mathrm{e} + \alpha_\mathrm{m})\mathbf{H}_\mathrm{inc}. \end{aligned} \tag{3.13}$$

V is the volume of the particle, $\mathbf{r}$ is the position vector, α_m is the magnetic polarizability which is connected to the magnetization $\mathbf{M}$ and α_e is the magnetic polarizability which is connected to the conductive and displacement currents. In general the magnetic dipole moment contribution due to magnetization $\mathbf{M}$ has a static contribution and a frequency-dependent contribution [236]. However, in the considered frequency range up to $f = 4\,\mathrm{kHz}$ (see section 3.1) the corresponding shortest wavelength in free space is $\lambda = 75\,\mathrm{km}$. When considering a cell in the micrometer scale or even an AuNP in the nanometer scale, for the magnetization the static approximation can be applied. In case of a spherical object with

radius R_p, this results in [237]

$$\alpha_\mathrm{m} = \frac{4\pi R_\mathrm{p}^3 \chi_\mathrm{p}}{3+\chi_\mathrm{p}}. \tag{3.14}$$

χ_p is the volume magnetic susceptibility with the relative magnetic permeability being $\mu_\mathrm{r} = 1+\chi_\mathrm{p}$.

For an elliptical particle, the magnitude of magnetization caused by the polarizability α_m is [238]

$$M_i = \frac{\chi_\mathrm{p}}{1+N_i\chi_\mathrm{p}} \mathbf{H}_\mathrm{inc}\mathbf{e}_i, \qquad i \in \{x,y,z\} \tag{3.15}$$

and N_i is a shape dependent (demagnetization) factor. The shape of the particle affects the magnetic field distribution. The Cartesian axes are elements of the index i and indicate the orientation of the magnetization. Since a sphere has point-symmetry relative to its center, its demagnetization factor is constant in all directions and equals $N_i = 1/3$ [239].

The demagnetization factors of a prolate elliptical particles (with the semi-axes l_x, l_y and l_z, where $l_x = l_y$ and $l_z > l_x$, and $l_z/l_y = p$) can be calculated with [240]

$$N_z = \frac{1}{p^2-1}\left(\frac{p}{2(p^2-1)^{0.5}} \ln\left(\frac{p+(p^2-1)^{0.5}}{p-(p^2-1)^{0.5}}\right) - 1\right), \tag{3.16}$$

$$N_x = N_y = \frac{p}{2(p^2-1)}\left(p - \frac{1}{2(p^2-1)^{0.5}} \ln\left(\frac{p+(p^2-1)^{0.5}}{p-(p^2-1)^{0.5}}\right)\right). \tag{3.17}$$

Similarly to the case of a prolate elliptical particle, the magnetization of an oblate ellipsoid can be calculated with (3.15). Considering an oblate particle with the semi-axes l_x, l_y and l_z, where $l_z = l_x$ and $l_z > l_y$, the demagnetization factors can be calculated with [240]

$$N_z = N_x = \frac{1}{2(p^2-1)}(p^2(p^2-1)^{-0.5} \arcsin\left((p^2-1)^{0.5}/p\right) - 1), \tag{3.18}$$

$$N_y = \frac{p^2}{p^2-1}\left(1 - \frac{1}{(p^2-1)^{0.5}} \arcsin\left((p^2-1)^{0.5}/p\right)\right). \tag{3.19}$$

Assuming the propagation constant in free space as k_0, in the quasi-static approximation

(negligible retardation), with $R_\mathrm{p}k_0 \ll 1$, α_e can be expressed with [241, 242]

$$\alpha_\mathrm{e} = -\frac{3V}{2}\left(1 - \frac{3}{R_\mathrm{p}^2 k^2} + \frac{3}{R_\mathrm{p}k}\cot(R_\mathrm{p}k)\right), \tag{3.20}$$

where k is the propagation constant in the considered spherical medium. For $R_\mathrm{p}k \ll 1$ and with Taylor series expansion,

$$\alpha_\mathrm{e} = \frac{VR_\mathrm{p}^2 k^2}{10}. \tag{3.21}$$

With the determination of the magnetic polarizabilities α_m and α_e the magnetic field inside the sphere can be calculated with

$$\mathbf{H} = \frac{1}{4\pi}\left(-\frac{\mathbf{m}}{r^3} + \frac{3(\mathbf{m}\,\mathbf{r})\mathbf{r}}{r^5}\right) + \mathbf{H}_\mathrm{inc}. \tag{3.22}$$

Furthermore, if $\alpha_\mathrm{e} \ll \alpha_\mathrm{m}$, the magnetic field inside the sphere can be calculated with the static approximation

$$\mathbf{H} = -\frac{\chi_\mathrm{p}}{3+\chi_\mathrm{p}}\mathbf{H}_\mathrm{inc} + \mathbf{H}_\mathrm{inc}. \tag{3.23}$$

The analytical formulas shown so far allow the calculation of the magnetization of a spherical object. In the following, the interaction of several spherical objects will be considered for the case that $\alpha_\mathrm{e} \ll \alpha_\mathrm{m}$. The magnetic dipole moment of one individual particle is excited by the incident magnetic field. When other particles are added, they change the initial magnetic field which is experienced by the first particle and influence its magnetic dipole moment. In a configuration of N particles, where $N \in \mathbb{N}, N \geq 2$, the magnetic moment of each particle can be calculated with

$$\mathbf{m}_\mathrm{n} = \alpha_\mathrm{m}(\mathbf{H}_\mathrm{inc} + \sum_{k=1,k\neq n}^{N} \mathbf{H}_\mathrm{k}(\mathbf{r}_\mathrm{n} - \mathbf{r}_\mathrm{k})). \tag{3.24}$$

The index n indicates the n-th particle and the index k indicates the other particles which interact with it. The magnetic field contribution of the k-th particle can be calculated with [243]

$$\mathbf{H}_\mathrm{k} = \frac{1}{4\pi}(-\frac{\mathbf{m}_\mathrm{k}}{r^3} + \frac{3(\mathbf{m}_\mathrm{k}\cdot\mathbf{r})\mathbf{r}}{r^5}). \tag{3.25}$$

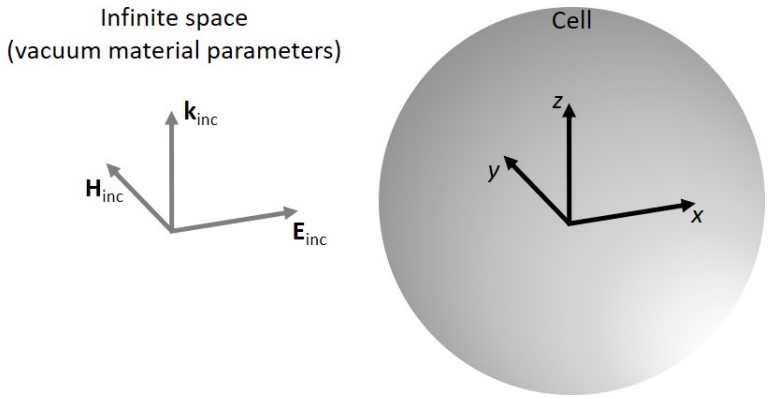

Figure 3.6: Orientation of incident EMF in Mie Scattering calculations.

Since in biological applications the surface of a nanoparticle is usually modified to improve its biocompatibility, targetability, stability, and functionality [244], the magnetic susceptibility of the particle can differ significantly from the susceptibility of bulk gold material due to charge carrier redistribution within the particle (see section 2.4.2). Diamagnets obtain a magnetic susceptibility smaller than zero, while superconductors are considered *ideal diamagnets* with a magnetic susceptibility of -1 [245, 246]. Paramagnetic materials obtain magnetic susceptibilities higher than zero and the magnetic susceptibility of ferromagnetic materials can be in the range of hundreds of thousands as in the case of iron [247]. In the following investigations a wide range of magnetic susceptibilities from $-0.9 \leq \chi_{\mathrm{p}} \leq 10^5$ is chosen, as the possible limits of magnetic susceptibilities for surface modified AuNPs are not yet determined. This range is probably wider than realistic magnetic susceptibility values for modified AuNPs; however, it allows to investigate the limits of possible magnetic field interaction.

To investigate EMF propagation within an exposed cell, calculations of the distributions were conducted with Mie Scattering in MATLAB as described in section 2.3.4. Since the frequencies of interest in the frame of cellular reprogramming are predominantly $f = 50\,\mathrm{Hz}$ and $f = 4\,\mathrm{kHz}$ (see section 3.1), the calculations were performed for each of these frequencies. In the calculations, the Cartesian coordinate system is located at the center of the spherical cell and the incident EMF is oriented as shown in **Figure 3.6**. Considering a cell with cell radius $r_{\mathrm{cell}} = 5\,\mu\mathrm{m}$, electromagnetic and dimensional parameters listed in table 2.3 were

chosen for the cell layers of an unspecific cell.

Numerical electromagnetic simulation models and methods

For the different results to be presented, two different numerical electromagnetic simulation tools (*Comsol Mutiphysics* and *Sim4Life*, see section 2.3.2) were applied.

In Comsol Multiphysics the Magnetic Fields (mf) interface under the AC/DC Electromagnetic Fields was used. The geometry consisted mainly of the gold nanoparticles with the corresponding shapes and material properties for the respective investigation, located inside an (spherical) environment with vacuum material properties. An additional layer around the environment built up the infinite element domain (from the virtual domains) to absorb outgoing EMFs. The incident magnetic field was excited by setting a background magnetic vector potential which resulted in the target incident magnetic field. However, when evaluating the results, the total magnetic field was normalized to the incident magnetic field. The target frequencies of the respective investigations were set in the study section and material sweeps were conducted where necessary. Magnetic dipole moments were determined numerically in the derived values section, by volume integration of the magnetization.

The magnetic response of a fibroblast cell model was investigated with electromagnetic calculations in Comsol Multiphysics with the cell models shown in **Figure 2.11** and in **Figure 2.12**.

For the modelling of the nanoparticle in Sim4Life, the *Structured Magneto Quasi-Static* solver was used. Since the simulation software does not allow the direct excitation of a magnetic field, a Helmholtz coil arrangement, similar to the one shown in **Figure 2.20** was applied to achieve a locally almost constant magnetic field distribution. For the Helmholtz

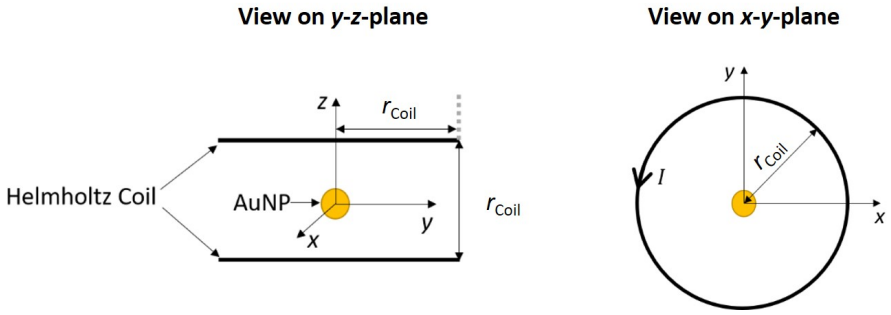

Figure 3.7: Illustration of the numerical simulation model of an AuNP exposed to a magnetic field.

coil arrangement, the coil radius was set to $r_{\mathrm{coil}} = 40\,\mathrm{nm}$. The schematic arrangement of numerical simulation is presented in **Figure 3.7**. The center of the AuNP is located at the origin of the coordinate system. The current *I* within both coils is equal in direction and magnitude. To realise a magnetic flux density magnitude $|\mathbf{B}_{\mathrm{inc}}| = 1\,\mathrm{mT}$ along the z-Axis caused by the Helmholtz coil arrangement, the current was $I = 44.485\,\mu\mathrm{A}$. The AuNP is considered to possess a bulk specific electrical conductivity of gold which is $\sigma_{\mathrm{Au}} = 41\,\mathrm{MS/m}$.

3.2.2 Calculation Results of Magnetic Field Distributions in Cells and in AuNPs

In this section briefly the magnetic field distribution within the cell model will be presented. Subsequently, the results of the magnetic response of the AuNPs will be shown in several paragraphs. The response of AuNPs with various characteristics (such as size, number, magnetic susceptibility and shape) is investigated. The excitation is a sinusoidal external magnetic field with frequencies up to hundreds of Megahertz. Starting from spherical particles with bulk gold material properties, the transition of the stationary magnetic response to the dynamic magnetic response in dependence from the applied frequency and the particle size is shown and the applicability of analytical formulas for the calculation of the magnetic response is presented. This serves as a fundament for the subsequent investigations. Furthermore, the magnetic field response of a particle with bulk gold material properties is shown while considering the intensity as well as the gradient of the magnetic field. The impact of the particle size on both quantities is presented. Additionally, the interaction of two neighbouring spherical particles as a function of their magnetic susceptibility is investigated. The last investigation serves as a starting point for an investigation of the interaction of several particles. Moving on, first the magnetic field response of individual prolate and oblate elliptical particles in relation to that of spherical nanoparticles is examined. Furthermore, the interaction behavior of the differently shaped particles with each other is investigated. To explore possible limits of magnetic field response, the configurations of AuNPs that result in maximum magnetic field enhancement are determined. Subsequently, arrays of spherical AuNPs are exemplary considered and their magnetic responses are investigated. Thereby, emphasis is put on an example of diamagnetic particles used during cell culture experiments [13]. Since cellular reprogramming has been performed on cells planted on such an array while exposed to a magnetic field [13], possible limits of magnetic field responses in dependence on distribution of the particles relative to the incident magnetic field are investigated.

Magnetic response of a cell

Figure 3.8 shows the results of the normalized secondary magnetic field, where $H_{\mathrm{norm}} = (H - H_{\mathrm{inc}})/H_{\mathrm{inc}}$ (H being the total magnetic field magnitude) within a spherical fibroblast and a mitotic fibroblast. In both cases, the alteration of the magnetic field is six orders of magnitude smaller than the incident field. The enhancement of the magnetic field is higher in case of the mitotic cell and has its maximum along $y = 0$ around the mitotic furrow. The magnetic field distribution of the mitotic cell is approximately the superposition of the magnetic field of two individual spherical cells, placed directly close to each other along $x = 0$.

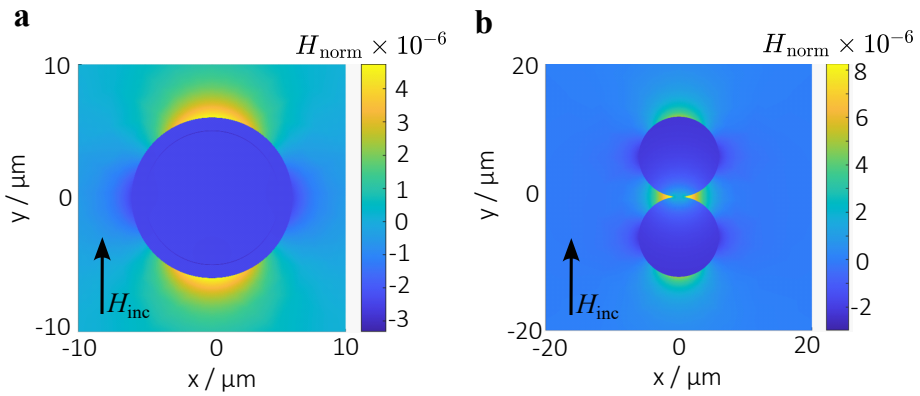

Figure 3.8: Numerical electromagnetic calculation of total normalized magnetic field within a fibroblast cell at $f = 4\,\mathrm{kHz}$. a) Spherical cell model and b) mitotic cell model .

At the considered frequency of $f = 4\,\mathrm{kHz}$, the determining factors for the magnetic field distribution are the magnetic susceptibilities. The most relevant susceptibilities in the cell are the parameters of the (relatively thin) outer cell membrane and the cytoplasm, which together can be regarded to build up a global *effective susceptibility*. The ratio between the *effective susceptibility* of the cell and the susceptibility of the surrounding cell medium determines the magnetic response. The plasma membrane has a susceptibility of $\chi = -8.8 \cdot 10^{-7}$, the cytoplasm has a susceptibility value of $\chi = -1.8 \cdot 10^{-6}$, while the cell medium is considered with $\chi = -9 \cdot 10^{-6}$ (see section 2.3).

The susceptibility of bulk gold material is $\chi = -3.4 \cdot 10^{-5}$, while the magnitude of surface-modified AuNPs can be even orders higher. This is the reason why the magnetic response of an AuNP must be at least approximately one order of magnitude higher than the response of a single cell. Furthermore, AuNPs are much smaller than cells, and as mentioned before,

the magnetic response of a cell is relatively weak. Therefore, the investigation of AuNPs in medium air provides a sufficient approximation of AuNPs located closely to the cell.

Magnetic response of a spherical AuNP with bulk material properties

Figure 3.9 illustrates the ratio of the magnitudes of the two magnetic polarizability contributions, $|\alpha_\mathrm{e}|/|\alpha_\mathrm{m}|$, as a function of frequency f and particle radius R_p. To model the behavior of a spherical AuNP, the material parameters for bulk gold was used, specifically the electrical conductivity $\sigma_\mathrm{p} = 41\,\mathrm{MS/m}$, the relative permittivity $\varepsilon_\mathrm{r,p} = 1$, and the magnetic susceptibility $\chi_\mathrm{p} = -3.4 \cdot 10^{-5}$. **Figure 3.9** shows that for $R_\mathrm{p} \leq 100\,\mathrm{nm}$ and $f \leq 100\,\mathrm{MHz}$, $|\alpha_\mathrm{m}| \geq |\alpha_\mathrm{e}|$. Since the frequencies of interest are $f < 1\mathrm{MHz}$, $|\alpha_\mathrm{m}| \gg |\alpha_\mathrm{e}|$ applies and the magnetic dipole moment induced in the nanoparticle can be obtained with the static approximation $\mathbf{m} = \alpha_\mathrm{m}\mathbf{H}_\mathrm{inc}$. Furthermore, the magnetic field inside the sphere can be calculated with (3.23). **Figure 3.10**a shows an AuNP with radius $R_\mathrm{p} = 10\,\mathrm{nm}$ that

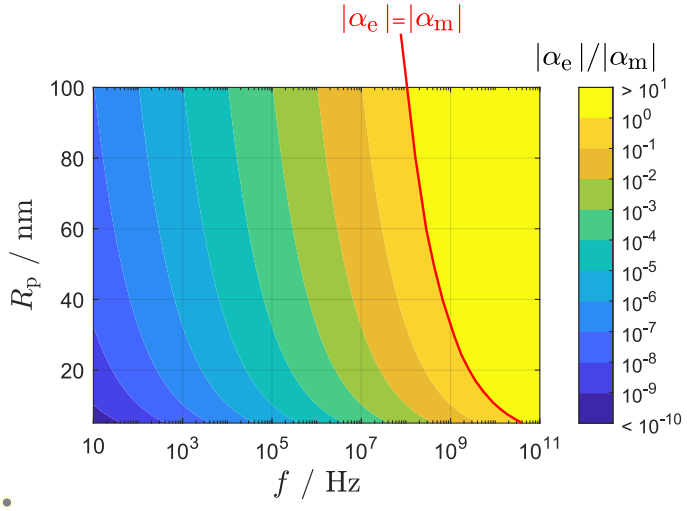

Figure 3.9: Ratio of the two magnetic polarizability contributions due to the AuNP from [8].

is exposed to $\mathbf{H}_\mathrm{inc}$. The figure illustrates the normalized secondary magnetic field, where $H_\mathrm{norm} = (H - H_\mathrm{inc})/H_\mathrm{inc}$ (H being the total magnetic field magnitude). The diamagnetic AuNP shows maximum enhancement of the overall magnetic field when the incident magnetic field is oriented tangential to the surface of the sphere, and the magnetic field is weakest where the incident magnetic field is oriented perpendicularly relative to the surface of the sphere. The inverse would be the case for a particle with positive magnetic susceptibility.

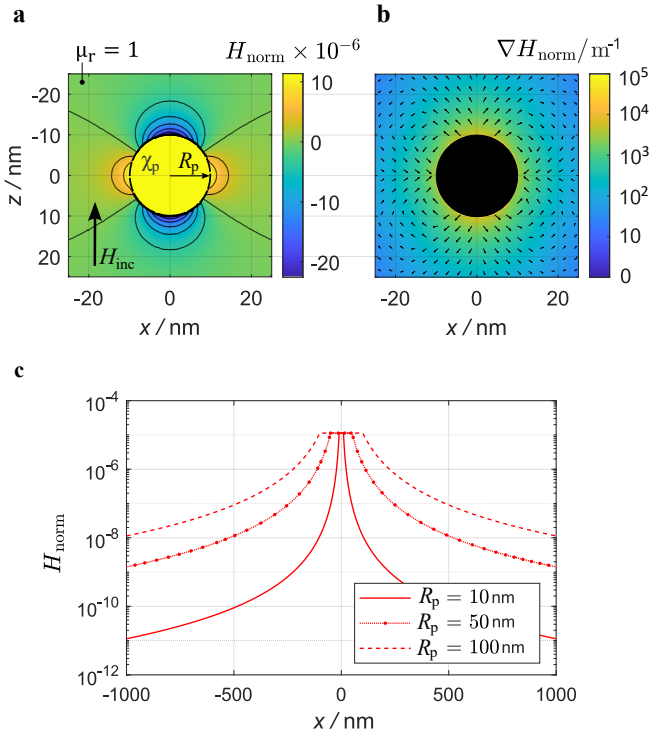

Figure 3.10: (a) Normalized magnetic field and (b) its gradient due to an AuNP. (c) Magnitude of normalized magnetic field along the x-axis for different AuNP sizes from [8].

However, the maximum magnetic field enhancement is in the order of 10^{-5} relative to the incident field. **Figure 3.10**b shows the gradient of **Figure 3.10**a outside the particle, where the gradient magnetic field reaches the maximum order of 10^4. These relatively high magnetic field gradient values are confined to the immediate vicinity of the sphere.

When considering (3.14) the polarizability of the particle depends on its radius R_p and its susceptibility χ_p. **Figure 3.10**c shows the magnetic field distribution of the same arrangement as in **Figure 3.10**a along the x-axis for different particle sizes. It can be seen that the maximum magnetic field remains the same for all three particle sizes while the maximum gradient of the magnetic field varies significantly with the size of the particle. The maximum magnetic field gradient decreases with increasing particle size.

The frequencies of interest for cellular reprogramming are $f = 50\,\mathrm{Hz}$ and $f = 4\,\mathrm{kHz}$. **Figure 3.9** shows that the magnetic polarizability contribution from α_e is negligible at these frequencies. However, for the sake of comprehensiveness, the dynamic magnetic response at these both frequencies will be shown in the following. Thereby, the radius of AuNP is

exemplary set to $r_{\mathrm{NP}} = 5\,\mathrm{nm}$. The radius of AuNP is chosen to the lower limit of usual particle sizes for *in vitro* experiments. Such relatively small particles exhibit a high rate of cell penetration [248].
For this investigation, electromagnetic simulations according to the model from **Figure 3.7** are performed. Before the results of magnetic field distribution within the AuNP is evaluated, first the incident magnetic flux density within the simulation area is evaluated in absence of the NP. The aim is to make sure that the incident magnetic flux density in close vicinity to the NP is sufficiently constant.

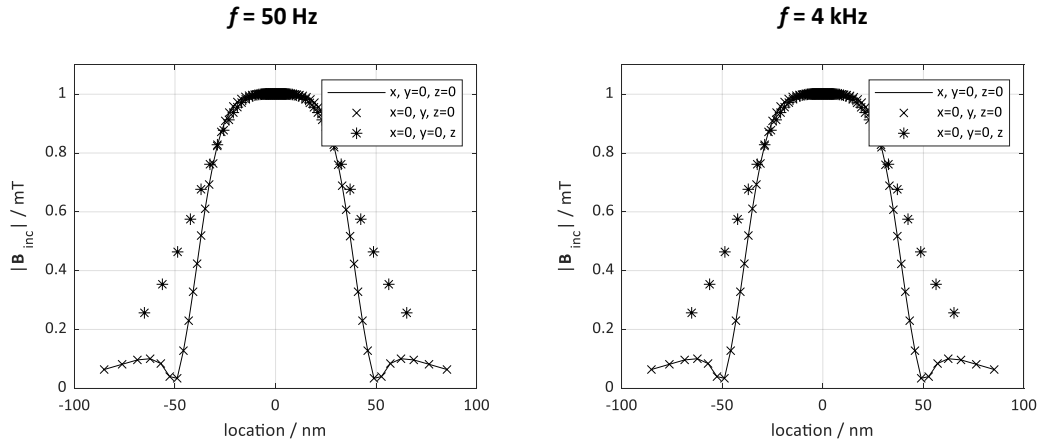

Figure 3.11: Evaluation of $|\mathbf{B}_{\mathrm{inc}}|$ along the three Cartesian axes from **Figure 3.7** but in absence of AuNP.

The results are presented in **Figure 3.11**. $|\mathbf{B}_{\mathrm{inc}}|$ is plotted along the x-, y- and z-axis. Since the AuNP is to be placed at the origin and has a radius of $r_{\mathrm{NP}} = 5\,\mathrm{nm}$, it can be seen that in close vicinity of the AuNP, the magnitude of incident magnetic flux density is sufficiently constant.

Equation (3.12) shows that a magnetic field in an AuNP, induces an electric field $\mathbf{E}$ with a connected electric current density $\mathbf{J}_{\mathrm{ind}}$. Gold has a relatively high specific electrical conductivity ($\sigma_{\mathrm{Au}} = 41\,\mathrm{MS/m}$), which results in a domination of the conductive current contribution compared to the displacement current contribution.
Since the magnetic field acting on the AuNP is oriented in positive z-direction (see **Figure 3.7**), $\mathbf{J}_{\mathrm{ind}}$ rotates around the z-Axis and its magnitude dependents on the x- and y-

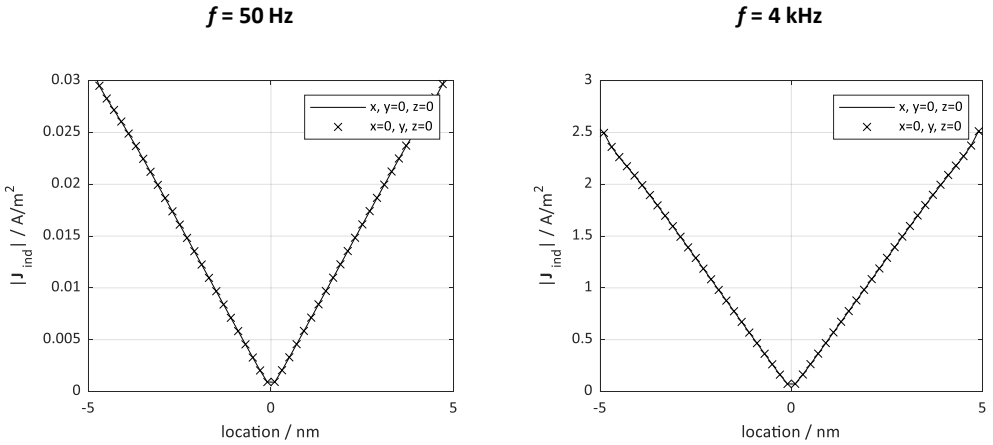

Figure 3.12: Results of $|\mathbf{J}_{\text{ind}}|$ obtained with numerical EM simulations within an AuNP according to **Figure 3.7**.

coordinates. The results of the magnitude of $\mathbf{J}_{\text{ind}}$ for both target frequencies are presented in **Figure 3.12**. The induced current density $\mathbf{J}_{\text{ind}}$ is plotted along the x- and y-axis. $\mathbf{J}_{\text{ind}}$ increases linearly with the location and scales also linearly with the frequency.
To validate the resulting current densities from the numerical simulations, the current densities were also calculated with analytical formulas.
The following equation is Faraday's law of induction

$$\oint_C \mathbf{E}\, d\mathbf{s} = \frac{\mathrm{d}}{\mathrm{d}t} \iint_A \mathbf{B}\, \mathrm{d}\mathbf{A}. \tag{3.26}$$

According to this law, an alternating magnetic field with magnetic flux density $\mathbf{B}$ through a surface $\mathbf{A}$ is directly connected to an electric field $\mathbf{E}$ within a closed curve along $\mathbf{s}$. **Figure 3.13** illustrates the magnetic flux density causing an induced electric field $\mathbf{E}_{\text{ind}}$ within the AuNP. The magnitude of $\mathbf{E}_{\text{ind}}$ dependents only on the radial distance r from the z-axis. Applying 3.26 and $\mathbf{J}_{\text{ind}} = \sigma_{\text{Au}}\mathbf{E}_{\text{ind}}$, the magnitude of induced electric current density is

$$|\mathbf{J}_{\text{ind}}| = \pi r \sigma_{\text{Au}} f |\mathbf{B}_{\text{inc}}|. \tag{3.27}$$

The results of the analytically calculated electric current densities are presented in **Figure 3.14** for both target frequencies. $|\mathbf{J}_{\text{ind}}|$ is plotted in dependence from the axial radius r

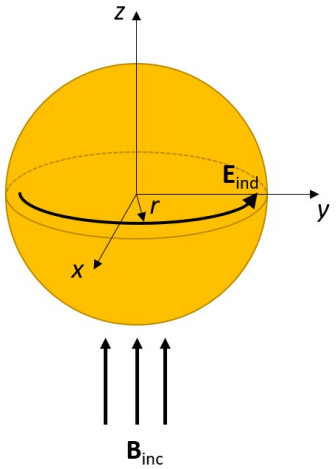

Figure 3.13: Induced electric field $\mathbf{E}_{\text{ind}}$ at $z = 0$, caused by an incident magnetic flux density $\mathbf{B}_{\text{inc}}$.

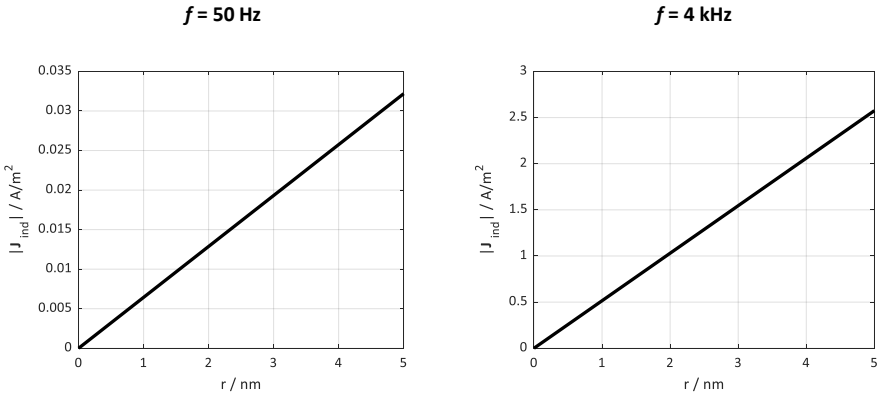

Figure 3.14: Results of $|\mathbf{J}_{\text{ind}}|$ obtained analytically.

from the z-axis. Comparing **Figure 3.12** and **Figure 3.14**, and considering the rotational symmetry of the configuration along the z-axis, it can be concluded that the numerical and analytical results for the induced current densities within the AuNP are consistent.

Ampère's circuital law states, that an induced current density $\mathbf{J}_{\text{ind}}$ causes an induced magnetic field $\mathbf{B}_{\text{ind}}$ rotating around the closed current loop. This can be seen schematically for the case of the AuNP in **Figure 3.15**. The magnetic flux density $\mathbf{B}_{\text{ind}}$ can be calculated with

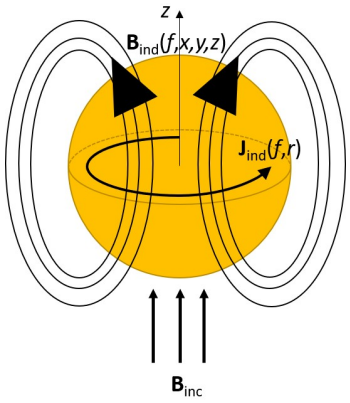

Figure 3.15: Induced magnetic flux density $\mathbf{B}_{\text{ind}}$ as a result of the induced current density $\mathbf{J}_{\text{ind}}$.

the Biot Savart equation

$$\mathbf{B}_{\text{ind}} = \frac{\mu_0}{4\pi} \iiint_V \mathbf{J}\left(\mathbf{R}'\right) \times \frac{\mathbf{R}-\mathbf{R}'}{|\mathbf{R}-\mathbf{R}'|^3} \mathrm{d}V'. \tag{3.28}$$

The parameters with a prime indicate the area with current flow and $\mathbf{R}$ is the three-dimensional position vector in spherical coordinates. In Cartesian base and with spherical parameters, the induced magnetic flux density can be determined as follows

$$\begin{aligned}
\mathbf{B}_{\text{ind}} &= C_1 \int_0^{2\pi} \int_0^{\pi} \int_0^{R_{\text{NP}}} C_2 \, \mathrm{d}R' \mathrm{d}\vartheta' \mathrm{d}\varphi', \\
C_1 &= \frac{\mu_0 \sigma_{\text{Au}} |\mathbf{B}_{\text{inc}}|}{4}, \\
C_2 &= R' \sin(\vartheta') \begin{pmatrix} -\sin(\varphi') \\ \cos(\varphi') \\ 0 \end{pmatrix} \times \frac{\begin{pmatrix} x - R' \sin(\vartheta') \cos(\varphi') \\ y - R' \sin(\vartheta') \sin(\varphi') \\ z - R' \cos(\vartheta') \end{pmatrix}}{\left| \begin{pmatrix} x - R' \sin(\vartheta') \cos(\varphi') \\ y - R' \sin(\vartheta') \sin(\varphi') \\ z - R^{(}\vartheta') \end{pmatrix} \right|^3} R'^2 \sin\left(\vartheta'\right).
\end{aligned} \tag{3.29}$$

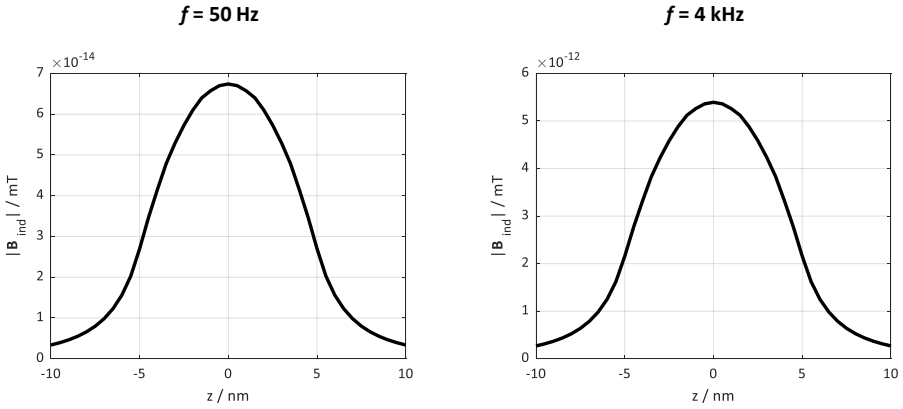

Figure 3.16: Results of analytically calculated $|\mathbf{B}_{\mathrm{ind}}|$.

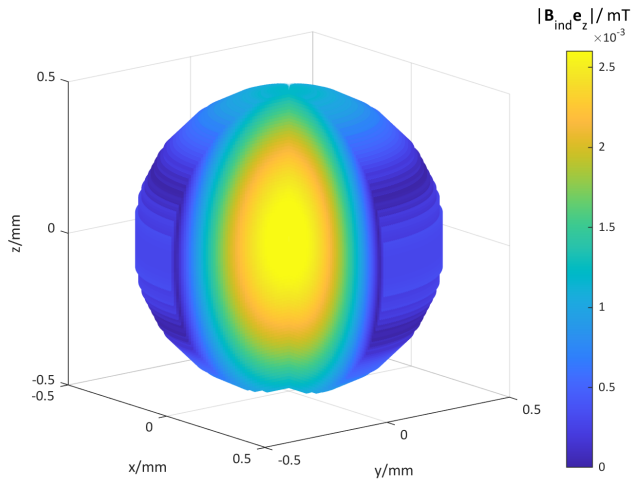

Figure 3.17: Three dimensional Mie Scattering results of $|\mathbf{B}_{\mathrm{ind}}|$ with coordinate system according to **Figure 3.7** at $f = 50\,\mathrm{Hz}$.

The according results along the z-axis are presented in **Figure 3.16** for both target frequencies. The results are obtained by solving (3.29) (with $x = 0$ and $y = 0$) in MATLAB. Since the magnitude of magnetic flux density depends linearly on the frequency, the ratios of magnitude of magnetic flux densities are in the range of the ratios of the applied frequencies. From **Figure 3.16** however, it can be seen, that the maximum magnitude of induced magnetic flux density due to conductive current distribution ($|\mathbf{B}_{\mathrm{ind,max}}| = 5.3\,\mathrm{fT}$) is at least twelve orders of magnitude smaller than the magnitude of incident magnetic flux density

$|\mathbf{B}_{\mathrm{inc}}| = 1\,\mathrm{mT}$. The obtained ratios of the incident magnetic flux density and the induced magnetic flux densities due to electric conductivity for the both frequencies agree with the ratios of $|\alpha_{\mathrm{e}}|/|\alpha_{\mathrm{m}}|$ from **Figure 3.9**.
Figure 3.17 shows the three dimensional result of the induced magnetic field due to specific electric conductivity within a fictional gold particle. This results shows that the particle would need to be huge (radius around 0.5 mm), to achieve an induced magnetic flux density which still is three orders of magnitude smaller than the incident magnetic flux density.

From (3.23) it is obvious that for the spherical particle the magnitude of the secondary magnetic field inside a particle becomes bigger with increasing magnitude $|\chi_{\mathrm{p}}|$, until saturation is reached for $|\chi_{\mathrm{p}}| \gg 3$. To analyze the interaction behavior of particles, in the following the interaction of two spherical particles as a function of their magnetic susceptibility is analysed.

Magnetic response of two spherical AuNPs
When two identical particles are brought next to each other due to symmetry they have the same magnetic dipole moment which can be expressed as

$$\mathbf{m}_{\mathrm{n=1}} = \mathbf{m}_{\mathrm{n=2}} = \begin{pmatrix} m_{\mathrm{x,0}} + m_{\mathrm{x,coupling}} \\ m_{\mathrm{y,0}} + m_{\mathrm{y,coupling}} \\ m_{\mathrm{z,0}} + m_{\mathrm{z,coupling}} \end{pmatrix}. \tag{3.30}$$

The indices x, y and z indicate the orientations in Cartesian coordinates. The index zero refers to the dipole moment of each particle in the absence of interaction with the other particle. The index 'coupling' indicates the additional magnetic dipole moment resulting from the interaction between the particles.

Figure 3.18a-d show two touching AuNPs arranged along the $y-$axis. In **Figures 3.18**a and b the magnetic field vector is parallel to the $y-$axis and thus parallel to the arrangement of particles. The ratio $m_{\mathrm{y,coupling}}/m_{\mathrm{y,0}}$ of the two magnetic dipole contributions can be found in **Figure 3.18**a for diamagnetic particles and in **Figure 3.18**b for para- and ferromagnetic particles. The results for the magnetic field oriented normal to the arrangement of the AuNPs (magnetic field vector along the $z-$axis) can be found in **Figures 3.18**c and d. The details of

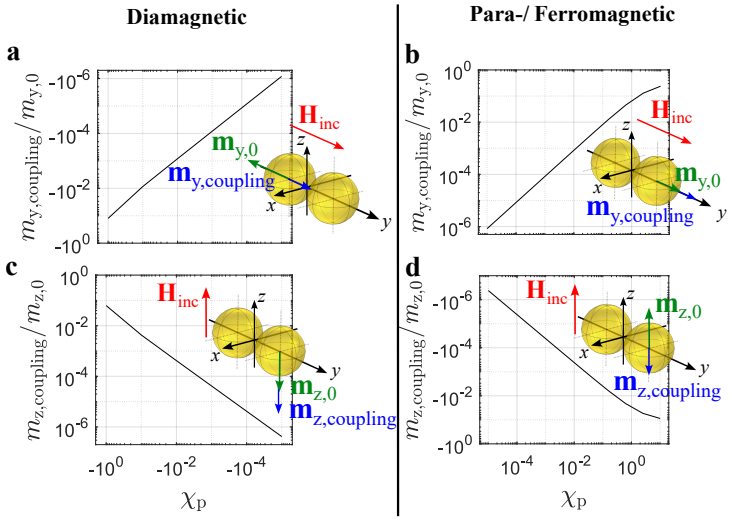

Figure 3.18: Coupling of two identical spherical AuNPs from [8]. (a) Diamagnetic particles with incident magnetic field in y-direction. (b) Para-/ferromagnetic particles with incident magnetic field in y-direction. (c) Diamagnetic particles with incident magnetic field in z-direction. (d) Para-/ferromagnetic particles with incident magnetic field in z-direction.

the calculations are shown in the methods section.

Considering **Figure 3.18**a and b, the particles are arranged along the y-axis and the incident magnetic field is parallel to the arrangement of particles. According to (3.24) the magnetic moment of one particle is

$$m_{1,\mathrm{y}} = \alpha_{\mathrm{m}} H_{\mathrm{inc,y}} + \alpha_{\mathrm{m}} H_{2,\mathrm{y}}. \tag{3.31}$$

Furthermore, according to (3.25),

$$H_{2,\mathrm{y}} = \frac{1}{2\pi} \frac{m_{2,\mathrm{y}}}{(2R_{\mathrm{p}})^3}. \tag{3.32}$$

Since the particles are identical, $m_{1,\mathrm{y}} = m_{2,\mathrm{y}}$ and

$$m_{1,\mathrm{y}} = \alpha_{\mathrm{m}} H_{\mathrm{inc,y}} + \alpha_{\mathrm{m}} \frac{1}{2\pi} \frac{m_{1,\mathrm{y}}}{(2R_{\mathrm{p}})^3}. \tag{3.33}$$

Considering (3.14) for the polarizability, this results in

$$m_{1,\mathrm{y}} = \alpha_{\mathrm{m}} H_{\mathrm{inc,y}} \left(1 + \frac{\chi_{\mathrm{p}}}{12 + 3\chi_{\mathrm{p}}}\right). \tag{3.34}$$

Thus, the magnitude of the magnetic dipole moment of each particle according to **Figure 3.18**a and b can be calculated with

$$m_{\mathrm{y},0} = \alpha_{\mathrm{m}} \mathbf{H}_{\mathrm{inc}} \mathbf{e}_{\mathrm{y}}, \tag{3.35a}$$

$$m_{\mathrm{y,coupling}} = m_{\mathrm{y},0} \frac{\chi_{\mathrm{p}}}{12 + 3\chi_{\mathrm{p}}}. \tag{3.35b}$$

Similarly, considering Figure 3.18c and d, the particles are arranged along the y-axis and the incident magnetic field is normal to the arrangement of particles. According to (3.24) the magnetic moment of one particle is

$$m_{1,\mathrm{z}} = \alpha_{\mathrm{m}} H_{\mathrm{inc,z}} + \alpha_{\mathrm{m}} H_{2,\mathrm{z}}. \tag{3.36}$$

Furthermore, according to (3.25),

$$H_{2,\mathrm{z}} = -\frac{1}{4\pi} \frac{m_{2,\mathrm{z}}}{(2R_{\mathrm{p}})^3}. \tag{3.37}$$

Since the particles are identical, $m_{1,\mathrm{z}} = m_{2,\mathrm{z}}$ and

$$m_{1,\mathrm{z}} = \alpha_{\mathrm{m}} H_{\mathrm{inc,z}} - \alpha_{\mathrm{m}} \frac{1}{4\pi} \frac{m_{1,\mathrm{z}}}{(2R_{\mathrm{p}})^3}. \tag{3.38}$$

Considering (3.14) for the polarizability, this results in

$$m_{1,\mathrm{z}} = \alpha_{\mathrm{m}} H_{\mathrm{inc,z}} (1 - \frac{\chi_{\mathrm{p}}}{24 + 9\chi_{\mathrm{p}}}). \tag{3.39}$$

Thus, the magnetic dipole moments of the particles shown in Figure 3.18a and b can be calculated with

$$m_{\mathrm{z},0} = \alpha_{\mathrm{m}} \mathbf{H}_{\mathrm{inc}} \mathbf{e}_{\mathrm{z}}, \tag{3.40a}$$

$$m_{\mathrm{z,coupling}} = -m_{\mathrm{z},0} \frac{\chi_{\mathrm{p}}}{24 + 9\chi_{\mathrm{p}}}. \tag{3.40b}$$

Figure 3.18 illustrates that $m_{\mathrm{z,coupling}}/m_{\mathrm{z},0}$ can be positive or negative, depending on the susceptibility χ_{p} and the orientation of the magnetic field vector relative to the particle

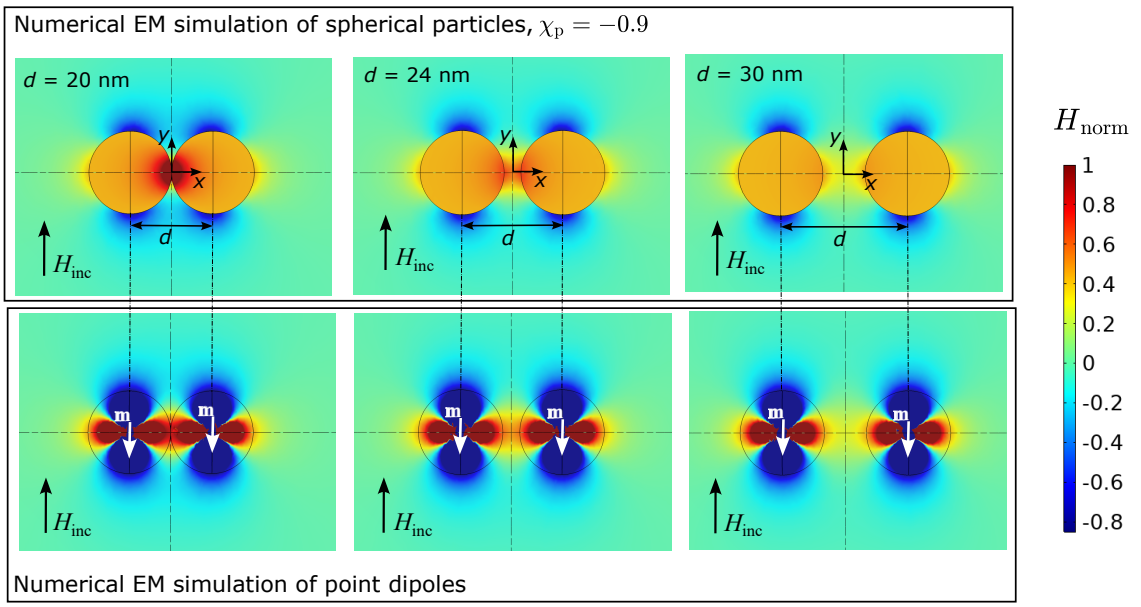

Figure 3.19: Numerical EM simulation of spherical particles at different distances d and point dipoles with equivalent dipole moment $\mathbf{m}$ as the spherical particles from [8]. View on the longitudinal axis cross-section of the sphere through the center ($z = 0$).

arrangement. This means that the interaction of the particles can cause an increase or a decrease of the individual magnetic dipole moments. Additionally, the Figures show that for all configurations, the coupling increases with increasing magnitude $|\chi_p|$, while in the case of para- and ferromagnetic particles saturation is reached around $\chi_p = 10$.

In the investigation of the interaction of the particles, the spherical nanoparticles are approximated with point dipoles. **Figure 3.19** shows the magnetic field distribution around a spherical particle and around point dipoles with equivalent magnetic dipole moment. Regardless of the distance between the particles, the point dipole approximation results in the same magnetic field distribution (in the region outside the particle) as the spherical particles.

While in the last paragraphs a spherical particle and the interaction of two identical spherical particles was considered, next the interaction of elliptical particles will be treated and compared to the spherical case. Ellipsoidal AuNPs are among the particle shapes commonly used in the frame of biomedicine [249]. Furthermore, it was found that ellipsoidal particles

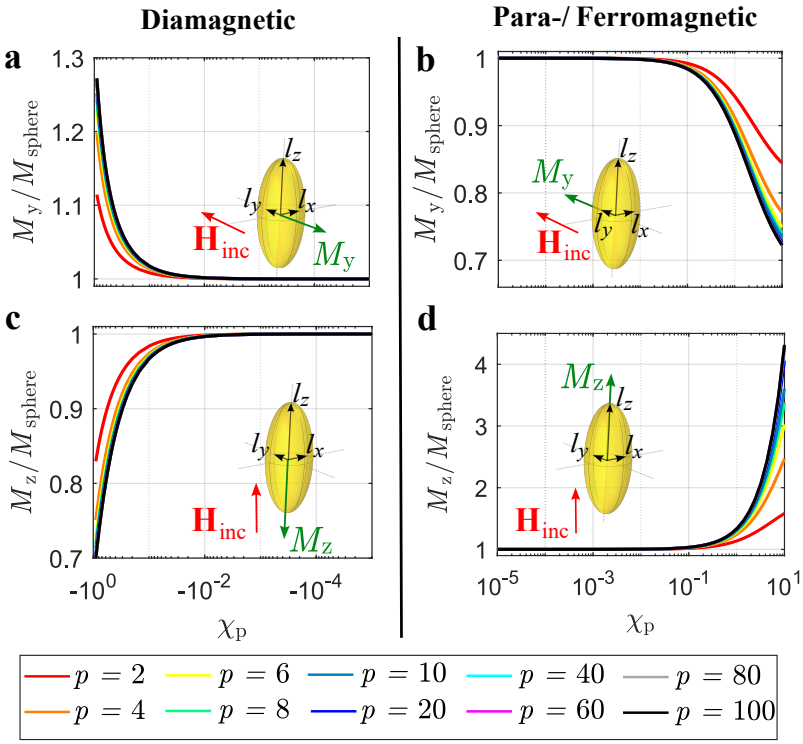

Figure 3.20: Relative magnetization in a prolate AuNP from [8]. (a) Diamagnetic particle with incident magnetic field in *y*-direction. (b) Para-/ferromagnetic particle with incident magnetic field in *y*-direction. (c) Diamagnetic particle with incident magnetic field in *z*-direction. (d) Para-/ferromagnetic particle with incident magnetic field in *z*-direction.

thiolated with polyethylene glycol can exhibit strong diamagnetic properties [216].

In the following, the magnetic responses of individual prolate and oblate elliptical particles are investigated as a function of the different axis ratios as well as a function of different magnetic susceptibilities. The aim is to explore the limits of magnetic response and to determine the maximum magnetization of the differently shaped particles.

Individual elliptical particles

Figures 3.20a-d depict a prolate elliptical particle with semi-axes of lengths l_x, l_y and l_z, where $l_z > l_y$ and $l_y = l_x$. The indices denote the orientation of the length parallel to the respective axis, while $l_z/l_y = p$.

Figure 3.20 shows the prolate elliptical particle with the incident magnetic field vector oriented either along the major axis of the particle (**Figure 3.20**c and d) or one of the minor axes (**Figure 3.20**a and b). The graphs in **Figure 3.20** show the relationship between the

respective magnetization of the particle relative to the magnetization of a sphere, dependent on the particle's susceptibility, and different ratios of the major axis length to the minor axis length ($l_z/l_y = p$). Depending on the magnetic susceptibility and orientation of the magnetic field vector relative to the particle, the magnetization of the prolate particle can be greater or lower than the magnetization of a sphere with the same susceptibility. The biggest enhancement in magnetization is found for $\chi_\mathrm{p} > 1$ with the magnetic field vector oriented parallel to the particle's major axis (**Figure 3.20**d).

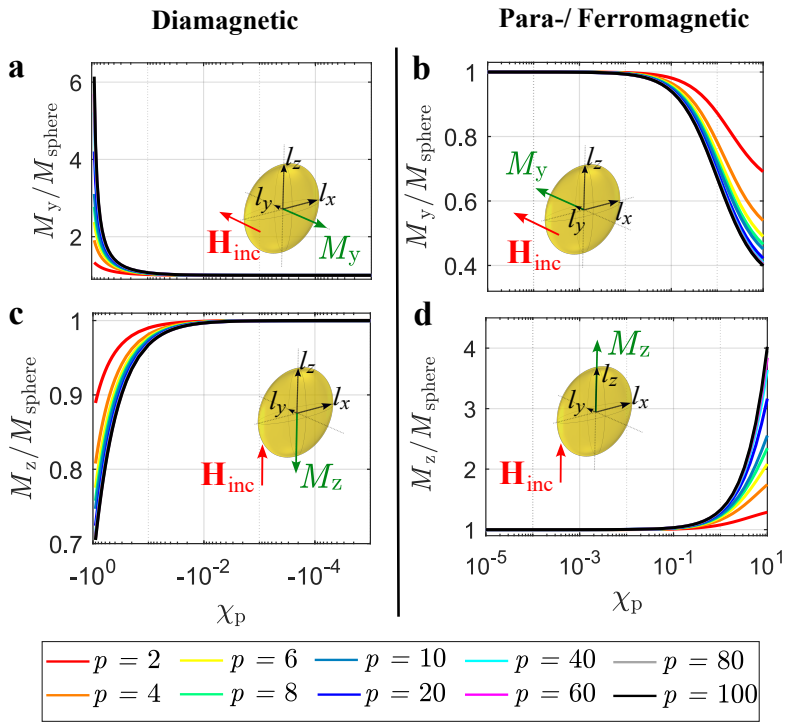

Figure 3.21: Relative magnetization in an oblate AuNP from [8]. (a) Diamagnetic particle with incident magnetic field in *y*-direction. (b) Para-/ferromagnetic particle with incident magnetic field in *y*-direction. (c) Diamagnetic particle with incident magnetic field in *z*-direction. (d) Para-/ferromagnetic particle with incident magnetic field in *z*-direction.

The graphs in **Figure 3.21** show the magnetization of oblate particles relative to the magnetization of a sphere with the same magnetic susceptibility. The highest magnetization occurs when the incident magnetic field vector is perpendicular to the minor axis of the oblate particle and $\chi_\mathrm{p} > 1$ (**Figure 3.21**d).

When comparing **Figure 3.21**d to **Figure 3.20**d, it is evident that the prolate particle induces a much higher magnetization at $\chi_\mathrm{p} > 1$ than the oblate particle. Interestingly, when comparing the diamagnetic particles in **Figure 3.21**a and **Figure 3.20**a, the oblate particle yields a higher magnetization.
The comparison of **Figure 3.20** and **Figure 3.21** allows assumptions of the magnetic field interaction of the individual particles, especially the quantification of the impact of the three different shapes (spherical, prolate and oblate ellipsoidal). However, the interaction of two elliptical particles is yet to be investigated and compared to the interaction of spherical particles. The aim is to identify the configuration of two identical particles that results in maximum magnetization.

Coupling of two particles: Comparison between the shapes
In the following, the magnetization of two interacting particles is investigated. Thereby, different axis ratios for the elliptical particles as well as different relative orientations of the particles to each other and to the incident magnetic field are considered.

First diamagnetic particles are investigated. **Figure 3.18**c shows the configuration that generates the highest magnetic dipole moment for diamagnetic spherical particles. Positive coupling of diamagnetic particles can be achieved when the incident magnetic field is normal

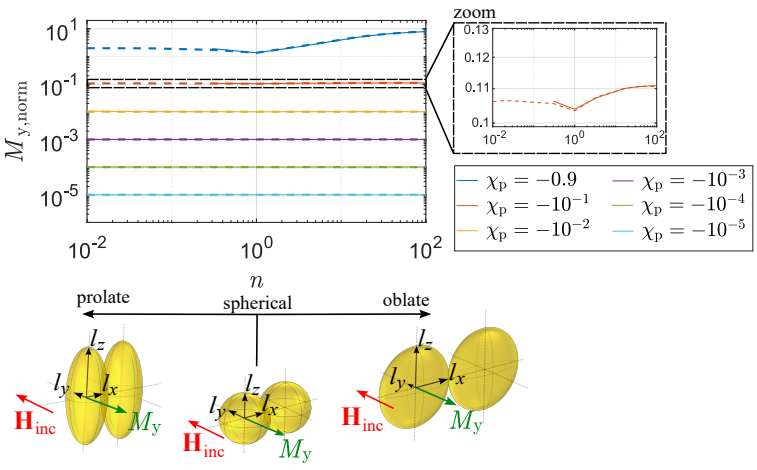

Figure 3.22: Coupling of diamagnetic particles with different shapes and axis ratios from [8].

to the particle configuration (e.g. the incident magnetic field in z-direction and the arrangement of particles in y-direction as in **Figure 3.18**c. Additionally, for elliptical diamagnetic particles, magnetization is highest when the magnetic field is oriented along one of the semi axes (as seen in **Figure 3.20**a and **Figure 3.21**a). The maximum coupling of particles is achieved when they are brought as closely together as possible. Based on these information, **Figure 3.22** shows the configurations of diamagnetic particles with different shapes that result in maximum magnetization. The graph illustrates $M_{\mathrm{y,norm}}$, which is the magnitude of magnetization in y-direction, normalized to the incident magnetic field. Different colors represent the different susceptibilities. $M_{\mathrm{y,norm}}$ is plotted as a function of the configurational parameter n, which represents the ratio of the lengths of the axes

$$n = \begin{cases} 1/p & \text{for prolate particles} \\ p & \text{for oblate particles} \end{cases} \tag{3.41}$$

The principle approach for the calculation of the coupling of two spheres can be applied also for elliptical particles. Considering **Figure 3.22**, the magnetization after coupling of the particles can be expressed as

$$m_{\mathrm{y}} = M'_{\mathrm{y}} V H_{\mathrm{inc,y}} - M'_{\mathrm{y}} V \frac{1}{4\pi} \frac{m_{\mathrm{y}}}{(2l_{\mathrm{x}})^3}. \tag{3.42}$$

Here,

$$M'_{\mathrm{y}} = \frac{\chi_{\mathrm{p}}}{1 + N_{\mathrm{y}} \chi_{\mathrm{p}}} \tag{3.43}$$

is the Magnetization magnitude from (3.15) normalized to the incident magnetic field. The magnetic dipole moment is

$$m_{\mathrm{y}} = M'_{\mathrm{y}} V H_{\mathrm{inc,y}} \left(1 - \frac{M'_{\mathrm{y}} V}{4\pi (2l_{\mathrm{x}})^3 + M'_{\mathrm{y}} V}\right). \tag{3.44}$$

The normalized magnetization can be expressed as

$$M_{\mathrm{y,norm}} = \frac{m_{\mathrm{y}}}{V H_{\mathrm{inc,y}}} = M'_{\mathrm{y}} \left(1 - \frac{M'_{\mathrm{y}} V}{4\pi (2l_{\mathrm{x}})^3 + M'_{\mathrm{y}} V}\right). \tag{3.45}$$

The numerically obtained results in **Figure 3.22** from Comsol Multiphysics are depicted using dashed lines, while the results obtained analytically are represented with solid lines. Generally, the numerically and analytically obtained results are in good agreement, with the magnetization increasing with higher magnetic susceptibility magnitudes, which is unsurprising. It can be noticed, that for $\chi_\mathrm{p} \leq -10^{-1}$ the analytical results are obtained for $n > 0.3$. The reason thereof is that a limit for the applicability of (3.25) is reached for a very long prolate particle's short-range area, and (3.25) has been used for the calculation of $M_{\mathrm{y,norm}}$. However, for all other susceptibility values and shapes, there is significant agreement between the analytical and numerical results.
At $\chi_\mathrm{p} = -0.9$, it is noticeable that the oblate particle with the maximum ratio of major axis to minor axis (n) generates the highest magnetization. This trend can also be observed in magnified inset on the other curves. Additionally, in magnified inset, it is observed that both prolate and oblate particles yield higher magnetization than spherical particles.
Figure 3.23 illustrates a result similar to that shown in **Figure 3.22**, but for the coupling of para-/ferromagnetic particles. With a similar approach as before, the magnetization of an elliptical particle from Figure 3.23 can be obtained with

$$m_\mathrm{z} = M'_\mathrm{z} V H_{\mathrm{inc,z}} + M'_\mathrm{z} V \frac{1}{2\pi} \frac{m_\mathrm{z}}{(2l_\mathrm{z})^3}, \tag{3.46}$$

with

$$M'_\mathrm{z} = \frac{\chi_\mathrm{p}}{1 + N_\mathrm{z}\chi_\mathrm{p}}. \tag{3.47}$$

Accordingly,

$$M_{\mathrm{z,norm}} = \frac{m_\mathrm{z}}{V H_{\mathrm{inc,z}}} = M'_\mathrm{z}\left(1 + \frac{M'_\mathrm{z} V}{2\pi(2l_\mathrm{z})^3 - M'_\mathrm{y} V}\right). \tag{3.48}$$

Figure 3.23 demonstrates excellent agreement between the numerically and analytically obtained results. The prolate particles exhibit the highest magnetization which is in contrast to the diamagnetic particles, where the oblate particles yield to highest magnetization.

Example: spherical arrays of particles
One major study used surface modified AuNPs for biological reprogramming [13]. There, fibroblast cells were planted on an array of spherical particles and exposed to a magnetic field [13]. The arrangement of particles raises the question: how do the particles interact with each other? Specifically, the determination of the number of particles that interact

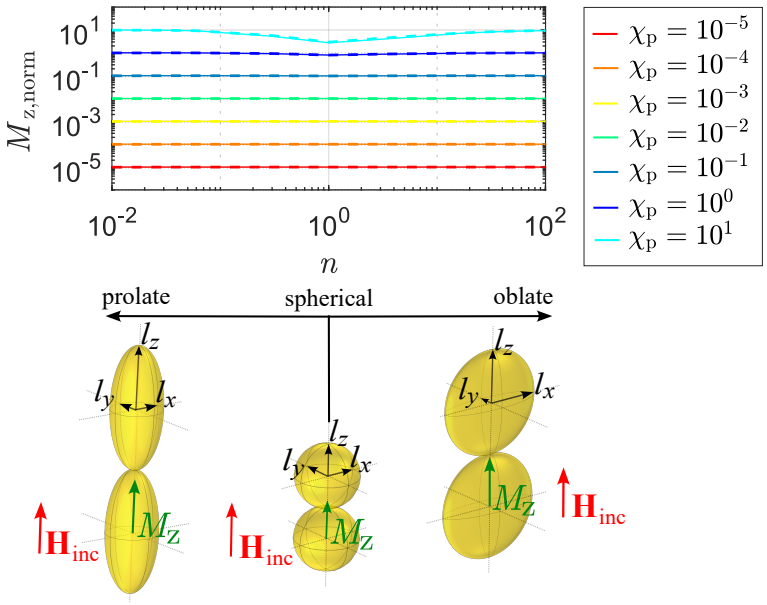

Figure 3.23: Coupling of para-/ ferromagnetic particles with different shapes and axis ratios from [8].

with one another in such an array is of interest. To determine the number of particles that interact with each other in an array, first focus is put on a line of particles, as illustrated in **Figure 3.24**.

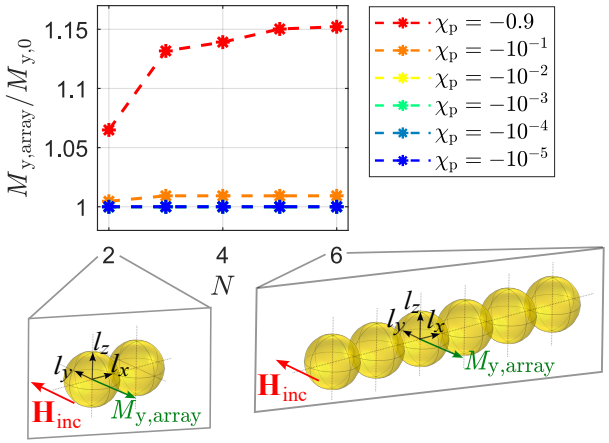

Figure 3.24: Coupling in a line of spherical diamagnetic particles from [8].

To enhance the magnetization of the diamagnetic particles in the array due to their interactions, as in the result of **Figure 3.18**c, a magnetic field perpendicular to the direct connection vectors between the particle centers is applied. The number of particles in a line is gradually increased from $N = 2$ to $N = 6$, as shown in **Figure 3.24**. The Figure plots the ratio of the maximum magnetization ($M_{\mathrm{y,array}}$) within the line of particles to the magnetization of a single particle without any interactions ($M_{\mathrm{y},0}$). The asterisks indicate the corresponding $M_{\mathrm{y,array}}/M_{\mathrm{y},0}$ values for each particle number, while the dashed lines show how this ratio changes with N. The colors in the Figure represent different magnetic susceptibility values. The susceptibility curves for $\chi_{\mathrm{p}} \geq -10^{-2}$ overlap, indicating a lack of significant increase in magnetization due to particle interaction at these levels. However, for susceptibility values lower than $\chi_{\mathrm{p}} \leq -10^{-1}$, there is a relevant increase in $M_{\mathrm{y,array}}/M_{\mathrm{y},0}$, showcasing meaningful particle interaction. The maximum interaction between particles saturates at $N = 3$ for $\chi_{\mathrm{p}} = -10^{-1}$, whilst for $\chi_{\mathrm{p}} = -0.9$, saturation is reached at $N = 5$ particles. Based on the susceptibility values considered, it can be inferred that a maximum of five particles aligned in a single row can result in relevant enhancement in magnetization. Expanding the number of particles in the row only leads to an increase in the area covered by the maximum magnetization, but does not enhance the maximum magnetization itself.

Similar to **Figure 3.24**, **Figure ??** shows results for particle interaction in the form of $M_{\mathrm{y,array}}/M_{\mathrm{y},0}$ for para-/ ferromagnetic particles. The arrangement of particles relative to the incident magnetic field is chosen on the basis of the results from **Figure 3.18**a to obtain an enhancement of magnetization. The results show that the onset of increased $M_{\mathrm{y,array}}/M_{\mathrm{y},0}$ begins at $\chi_{\mathrm{p}} \geq 10^{-1}$, and the number of interacting particles increases with higher magnetic susceptibility values. While saturation is reached at $N = 9$ for $\chi_{\mathrm{p}} \leq 10^{1}$, it is reached at $N = 15$ for $\chi_{\mathrm{p}} \geq 10^{2}$. Remarkably an increase of $\chi_{\mathrm{p}} = 10^{3}$ to $\chi_{\mathrm{p}} = 10^{5}$ leads to almost overlapping curves. This means that $M_{\mathrm{y,array}}/M_{\mathrm{y},0}$ cannot be further increased due to interaction of particles in one row, even at higher susceptibility values. At extremely high magnetic susceptibility values, $M_{\mathrm{y,array}}$ can be maximum four times higher than $M_{\mathrm{y},0}$.

Figure 3.25: Coupling in a line of spherical para-/ ferromagnetic particles from [8].

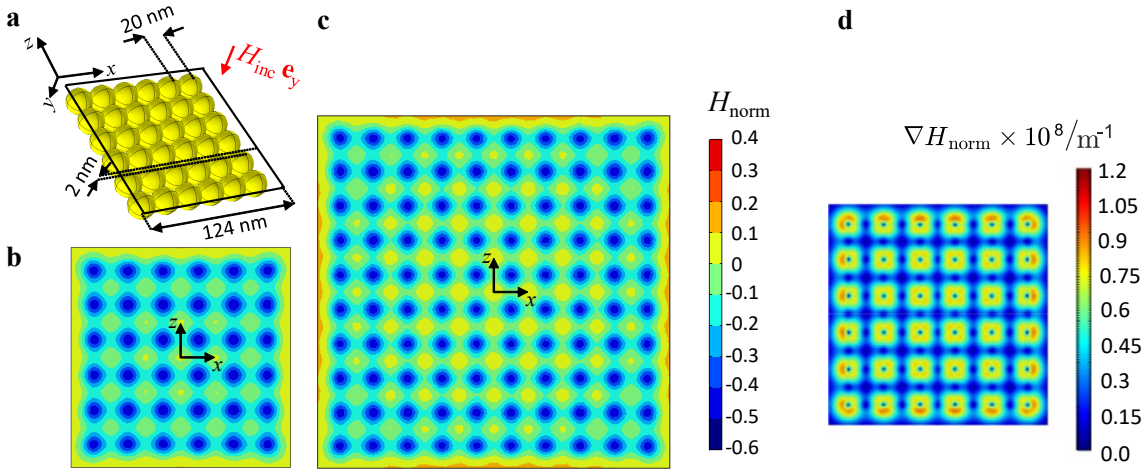

Figure 3.26: Array of spherical diamagnetic particles from [8]. (a) Schematic illustration of the 6×6 particles array. (b) Magnetic field distribution above the array. (c) Magnetic field distribution above a 10×10 particles array. (d) Gradient magnetic field above the 6×6 particles array.

Returning to an array of diamagnetic particles as used in a study for biological reprogramming of cells [13], the limits of magnetic field alteration due to the particles interaction is investigated in the following. **Figure 3.26**a shows an array of AuNPs, six particles wide and six particles tall, exposed to a magnetic field perpendicular to the array plane. The particles have a diameter of $R_\mathrm{p} = 10\,\mathrm{nm}$ and are placed directly beneath each other without any additional spacing. The magnetic field H_norm is determined within the black rectangular area displayed in **Figure 3.26**a, which is then illustrated in **Figure 3.26**b. The same arrangement is analyzed for an array of 10 by 10 nanoparticles, as depicted in **Figure 3.26**c. **Figures 3.26**b and c use the same scale. Comparing the two plots, it is evident that there is no significant enhancement in the magnetic field due to more particles. Although the alignment of the particles enables an enhancement in magnetization, it leads to an increase in magnetic field between the particles and a reduction in magnetic field on the particles' surface. This results in a range of $-0.5 \leq H_\mathrm{norm} \leq 0$, showing that the magnetic field above the array is lower than the incoming field. The magnetic field gradient of the arrangement from **Figure 3.26**a and b is shown in **Figure 3.26**d. The magnetic field gradient peaks at approximately 10^7.

The magnetic field distribution from **Figure 3.10**a shows that the magnetic field enhancement on an AuNP is maximum at the positions where the incident magnetic field is tangential to the surface of the particle. To obtain a magnetic field enhancement above an array of diamagnetic particles, this characteristic is exploited. In contrast to the arrangement from **Figure 3.26**a, **Figure 3.27**a shows a configuration where a partial enhancement of the magnetic field on top of the particles is excited. The incoming magnetic field is running parallel to the z-direction. The particles are closely positioned in the x-direction while there is a 60 nm distance between neighboring particles in the z-direction. The spacing results in a decrease of negative coupling (as in the result of **Figure 3.18**a) between the diamagnetic particles. By implementing this configuration, the magnetic field is increased by a factor of 0.3 directly above the particles.

The findings from **Figure 3.22** indicate that the magnetization and magnetic field interaction of particles could be enhanced by utilizing prolate/oblate particles with low/ high configurational parameter n. However, when dealing with spherical diamagnetic particles, achieving magnetic field enhancement in the range of the incident magnetic field necessitates magnetic susceptibility values in the range of $\chi_\mathrm{p} = -0.9$ and a very specific particle arrangement, as chosen in **Figure 3.27**.

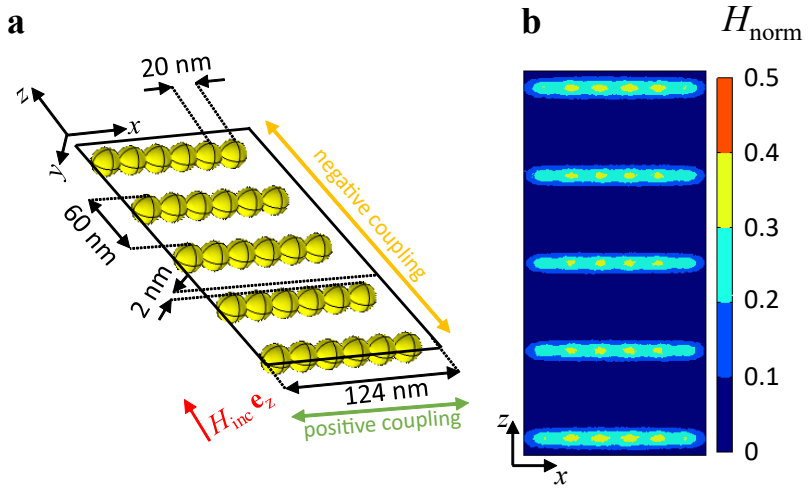

Figure 3.27: Modified array of spherical diamagnetic particles from [8]. (a) Schematic illustration. (b) Magnetic field distribution above the array.

3.3 Implementation of a Magnetic Field Exposure Setup for In Vitro Cell Experiments

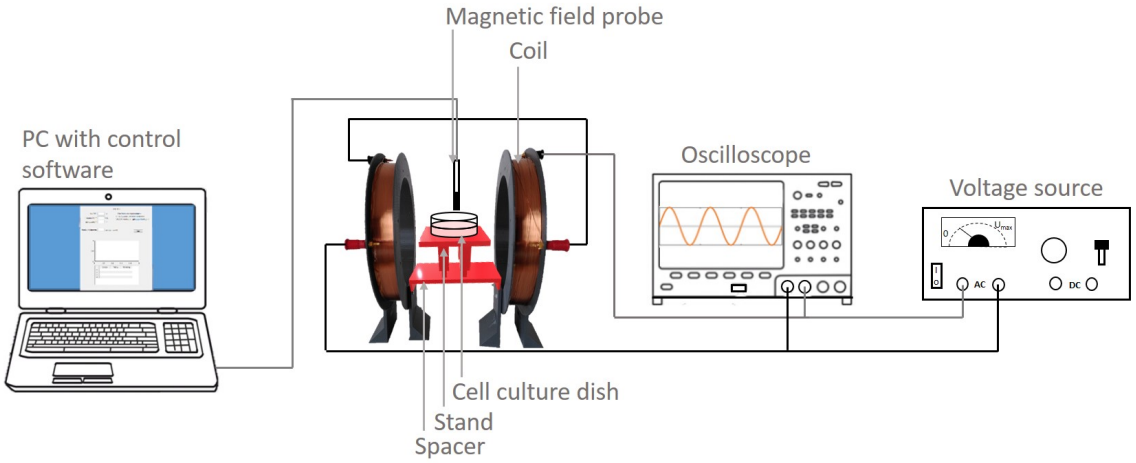

Figure 3.28: Overview of implemented magnetic field exposure setup.

In the frame of this thesis, a first application setup was designed with the aim to allow cell culture experiments for cellular reprogramming. An experimental setup can be used to validate theories on the basis of analytical and numerical calculations. A schematic illustration of the magnetic field exposure setup for *in vitro* cell experiments is shown in **Figure 3.28**. The core of the setup are two coils forming a Helmholtz coil according to **Figure 2.20**. The coils were produced by the Institute for Drive Systems and Power Electronics, Leibniz University Hannover. I organized and accompanied the production and integrated them into the setup. This setup had to be realized in a very short period of time. Thus, it was kept possibly simple such that it could be used with equipment which was already available at the Institute of Quantum Optics and at the Institute for Drive Systems and Power Electronics.

I designed and 3D-printed a spacer and a matching cell culture dish from polylactic acid (PLA) to keep the coils at a constant distance and the cell culture dish at a constant height, right in the area of maximum field uniformity. The voltage source is a *Straton Serie 5311* isolation transformer which allows a DC or AC power supply at a frequency $f = 50\,\mathrm{Hz}$. The source allows the manual setting of an output voltage U_{out} in the range between $0 \leq U_{\mathrm{out}} \leq 30\,\mathrm{V_{RMS}}$ via a rotary control knob. An oscilloscope (Rigol DS2072A) allows the monitoring of the output signal. The magnetic field probe is a *Metrolab Technology THM1176-LF* probe, which

allows the measurement of three dimensional magnetic flux densities up to a magnetic flux density magnitude of $B = 8\,\mathrm{mT}$ with an accuracy around $B_{\mathrm{ac}} = \pm 20\,\mu\mathrm{T}$. The magnetic field probe is connected to the PC via USB port and can be controlled with the off the shelve software *Metrolab EZMag3D*. The setup is designed for the placement of the coils in a CO_2 incubator for cell cultivation.

Each of the coils has a diameter of 220 mm and 96 turns of wire copper with a diameter of $0.5\,\mathrm{mm}$. The coils can be used within a frequency range of $0 \leq f \leq 30\,\mathrm{kHz}$. At higher frequencies, possible interference due to resonant behavior of the coils might occur. Furthermore, due to heating of the copper wires at high input voltages, the coils are suited to produce a maximum magnetic flux density of $B_{\mathrm{max}} = 1.5\,\mathrm{mT}$. This magnetic flux density corresponds to $U_{\mathrm{out}} = 24\,\mathrm{V_{RMS}}$.

Figure 3.29 shows the temperature T of the coils as a function of magnetic flux density magnitude B and time t. The temperature was measured with a *VOLTCRAFT IR 500-12S* infrared thermometer directly at the copper coils (there was no significant difference between the temperature development of the two coils). The dots indicate the measurements and the curve indicates the temperature development. At $t = 0$, the coils were at room temperature ($T = 26.5\,^{\circ}\mathrm{C}$). The magnitude of magnetic flux density was set to $B = 1\,\mathrm{mT}$. After three

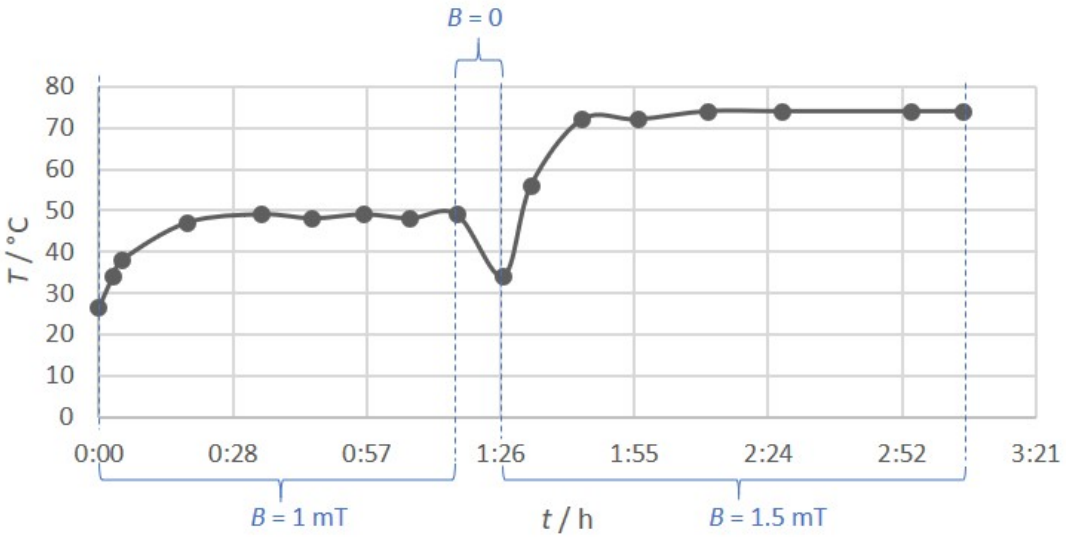

Figure 3.29: Magnetic flux dependent heating of the coils over time.

minutes, at $t = 0:03\,\mathrm{h}$, the temperature at the coils was already increased ($T = 34\,^{\circ}\mathrm{C}$). After $t = 0:35\,\mathrm{h}$ the temperature had saturated at $48\,^{\circ}\mathrm{C} \leq T \leq 49\,^{\circ}\mathrm{C}$. At $t = 1:17\,\mathrm{h}$ the voltage generator was turned off ($B = 0$) for ten minutes. The temperature decreased to $T = 34\,^{\circ}\mathrm{C}$. Subsequently, the magnetic flux density was set to $B = 1.5\,\mathrm{mT}$, at $t = 1:27\,\mathrm{h}$ and the temperature started increasing. Seventeen minutes later, at $t = 1:44\,\mathrm{h}$ the temperature $T = 72\,^{\circ}\mathrm{C}$ was reached and it saturated at $t = 2:11\,\mathrm{h}$ with $T = 74\,^{\circ}\mathrm{C}$.
The temperature between the coils (at the location where the cell culture dish has to be placed) was measured as well and did not change significantly over the time-course of the measurements. These temperature measurements were performed in absence of an incubator. Since *in vitro* experiments have to be performed within an incubator, it is crucial to repeat the temperature measurements in the actual cell environment. Depending on the size of the chamber, the overall temperature at the cells might be affected, which might influence the experimental outcome and be the source of a systematic error.
Furthermore, the measurements show that the increase in temperature is significant directly at the coils. A relatively high temperature in the range of $T \geq 70\,^{\circ}\mathrm{C}$ at the coils can reduce the lifetime of the copper coils through damages on the insulating coating. To allow the application of higher magnetic flux densities while avoiding high temperature increase of the coils, a second pair of coils was produced by the Institute for Drive Systems and Power Electronics, Leibniz University Hannover. The new coils had 1000 turns each, which allowed higher magnetic flux densities at the same current flow as with the old coils (with 96 turns). However, the integration of the new coils into an experimental setup was beyond the scope of this thesis.

3.4 Magnetic Field Interaction: Discussion and Conclusion

In this chapter 3, first the relevant frequencies in the frame of cellular reprogramming were determined in section 3.1. While it is well known that $f = 50\,\mathrm{Hz}$ is a typical frequency when ELF-EMFs are applied, the classical PEMF excitation was investigated with Fourier analysis. Thereby, $f = 4\,\mathrm{kHz}$ was determined as the most relevant spectral component. With the knowledge of the relevant frequencies, the magnetic field distribution within a cell model and different AuNP models were investigated in section 3.2. The analytical and numerical

models which were therefore applied were presented in subsection 3.2.1 before the results were shown in subsection 3.2.2.
It was shown that an external magnetic field with the considered frequencies penetrates the cell without significant alteration. The cell is almost *invisible* for the magnetic field. Considering possible mechanisms of action triggered in the cell, the described mechanisms of section 2.4.2 cannot realistically be triggered. Equation (2.66) describes the deformation of the membrane structures within a cell due to their inhomogeneous magnetic susceptibilities. Considering a typical magnetic flux density magnitude of one millitesla, for the fibroblast cell shown in **Figure 2.11**, the deformation of the plasma membrane/ nuclear envelope would be in the range of femtometer. Magnetic forces on ions in cells and cell culture medium are rather unlikely in the frame of cellular reprogramming, since the magnetic flux densities applied are below the threshold of one tesla, as described in section 2.4.2. Even a magnetophoretic effect on molecules containing iron can be excluded, since much higher magnetic flux densities and/ or gradient fields would be necessary (see equation (2.68)).

For the AuNPs, it was shown that in the frequency regime of interest, their magnetic response can be approximated with application of the static magnetic polarizability. Furthermore, the dynamic response becomes relevant for $f \geq 100\,\mathrm{MHz}$. The magnetic field distribution within and around an AuNP with bulk gold material properties, as well as its magnetic field gradient were shown. These results showed that the magnetic field around an AuNP is partially enhanced and partially decreased, depending on the considered position relative to the particle. However, the alteration in the magnetic field is approximately five orders of magnitude smaller than the incident magnetic field while the maximum magnetic field gradient (normalized to the incident magnetic field) is in the order of $10^5\,\mathrm{m}^{-1}$. Considering the magnetic energy E of a particle as defined by (2.72), the magnetic field contribution of an AuNP with bulk gold material parameters is too small to cause significant energy alterations. Furthermore, the magnetic force per particle volume $\mathbf{f}$ (2.73) is even lower than the gravitational force density. However, the obtained results also show that the gradient of the magnetic field can be tuned with the particle size.
Furthermore, the interaction of two identical spherical particles was investigated as a function of different magnetic susceptibilities and different polarization directions relative to the arrangement of particles. It was shown that the magnetic dipole moments of two im-

mediately neighboring particles can be enhanced or lowered due to their interaction. In this regard, the determining factors are the orientation of the magnetic field relative to the arrangement of nanoparticles, and the susceptibility of the particles.
Subsequently, the magnetic response of elliptical particles was investigated. The magnetization of prolate and oblate ellipsoids relative to the magnetization of a spherical particle was shown as a function of different axis ratios of the elliptical particles. The results show that the maximum magnetization can be reached for prolate para-/ferromagnetic ellipsoids and oblate diamagnetic ellipsoids. Furthermore, depending on the orientation of the magnetic field relative to the elliptical particle, the magnetization can also be lower relative to the magnetization of a spherical particle.
Subsequently, the magnetic coupling of two identical particles was examined for the different shapes. In this regard, it was shown that in the cases of positive interaction (interaction causing an increase in magnetization), the elliptical particles show stronger interaction than spherical particles. Thereby, for diamagnetic particles, the oblate ellipsoids show the strongest interaction while for para-/ferromagnetic particles the prolate ellipsoids interact most strongly with the magnetic field.
Emanating from an example taken from literature, the interaction of spherical particles in an array was investigated. It could be shown that the determining coupling factor is the magnitude of the magnetic susceptibility: the higher the magnitude $|\chi_\mathrm{p}|$, the more particles can interact with each other. However, for the considered susceptibility range $-0.9 \leq \chi_\mathrm{p} \leq 10^5$ in case of diamagnetic particles maximum five particles can couple effectively in one row and in case of ferromagnetic particles, maximum fifteen particles can couple effectively in one row. Finally and exemplary, the magnetic field and the magnetic field gradient above arrays of diamagnetic nanoparticles was investigated. The main findings of these investigations are that for the case of positive coupling of particles, depending on the orientation of the incident magnetic field relative to the array surface, the incident magnetic field can be enhanced or lowered. The results show that an extreme diamagnetic susceptibility of $\chi_\mathrm{p} = -0.9$ can achieve a magnetic field enhancement in the range of the incident magnetic field. Since there is the hypothesis that a relevant increase in magnetic field was reached with strong diamagnetic AuNPs experimentally [13], with the shown results it can be inferred that the magnetic susceptibility for such an increase in the magnetic field must be in the range of $\chi_\mathrm{p} = -0.9$.
In section 3.3 a basic setup for the *in vitro* exposure of cells with magnetic fields was pre-

sented, as realised in the frame of the work for this thesis at the Institute of Quantum Optics. This setup provides an example of possible first experimental arrangement which can be used at the Institute of Quantum Optics.

4 Electric Field Interactions with Cells and Cells in Combination with AuNPs

In this chapter, first a new lumped element model of a cell will be introduced. This model can be used to approximate the electric field within the different cell layers of individual spherical cells only by application of formulas containing dimensional an EM material properties. While the lumped element model derived by mainly focusing on the frequencies used during TTFields ($f \approx 100\,\mathrm{kHz}$), subsequently the electric field distribution within cells and nanoparticles is shown also at frequencies typically used during cellular reprogramming ($f = 50\,\mathrm{Hz}$ and $f = 4\,\mathrm{kHz}$). Thereby, approximations with the lumped element model are used where possible and compared to Mie Series and numerical EM calculations. Before the results are shown in section 4.2.2, the calculation methods are explained briefly in section 4.2.1.
Afterwards an enhancement of existing electric field exposure setups for *in vitro* cell culture experiments is proposed. Compared to existing setups, the proposed model allows the exposure of cells with more homogeneous electric fields while also allowing the exposure to more polarization directions.
Afterwards and to allow the consideration of electrical conductivity of nutrient cell media in future calculations, the implementation of a capacitive measurement method is shown.
Finally, a discussion and conclusion of the chapter is presented.

4.1 New Concept of an Electrical Lumped Element Model of a Cell

The work presented in this section was conducted at the Institute of Microwave and Measurement Systems, Leibniz University Hannover, in the frame of a peer reviewed journal publication [2]. I developed the idea and the content of the paper. Professor Dirk Manteuffel supervised the work.

An electrical lumped element model of a cell is a condensed representation of the electrical behavior of the cell. It allows the approximation of the electric field distribution within a considered cell model.
In the following, a lumped element model and corresponding analytical formulas are presented, which allow an approximation of lumped element parameters of singe shell and double shell spherical cell models. Compared to other lumped element models (see section 2.3), huge advantages of the presented formulas are that they apply for frequencies up to several megahertz and that they only contain dimensional parameters and EM material parameters (conductivity and permittivity) of spherical cells. During investigations of mechanisms of action in the frame of exposure of individual cells to electric fields, this lumped element model can be applied to approximate electric current and electric field proportions within different cell layers without the application of more advanced mathematical methods as Mie Scattering or numerical calculations. This model can i.a. be applied in the frame of Tumor Treating Fields investigation of mechanisms of action.

Figure 4.1 shows on the right side the cross section of a cell located in an unidirectional external electric field $\mathbf{E}_{\mathrm{inc}}$. The cell layers are the same as in the double shell model in **Figure 2.10**.

The total electric field distribution $\mathbf{E}_{\mathrm{tot}}$ within the cell is shown on the left side plot. Here, the magnitude $|\mathbf{E}_{\mathrm{tot}}|$ is plotted normalized to the magnitude $|\mathbf{E}_{\mathrm{inc}}|$ in dB scale. The direction of $\mathbf{E}_{\mathrm{tot}}$ is indicated by the arrows. The electric field distribution is calculated analytically with application of Mie Scattering (as shown in **Figure 3.6**) for a representative glioblastoma cell model with according electric and dimensional parameters as listed in table 4.1 (lower

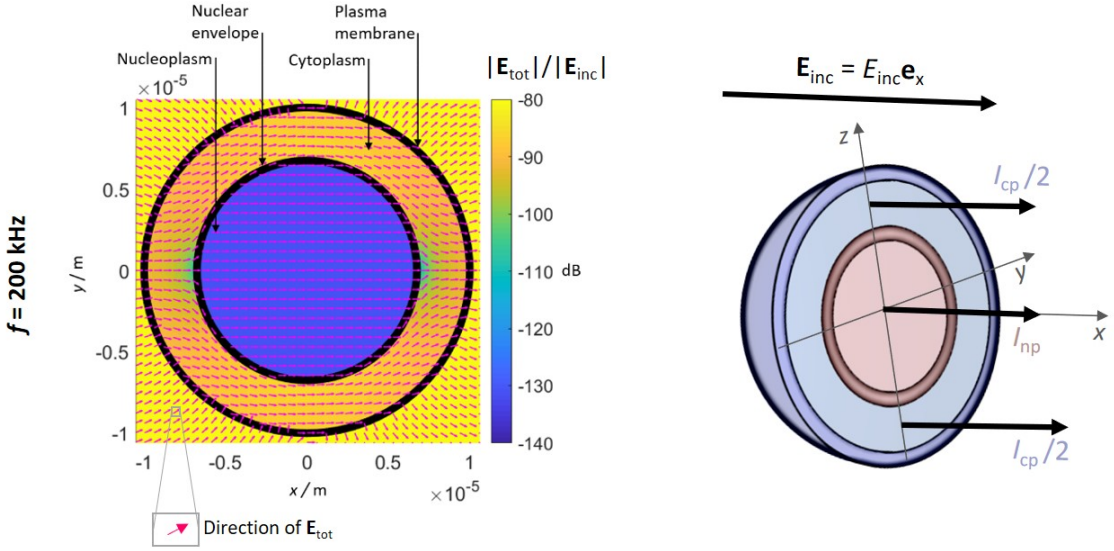

Figure 4.1: Electric Field distribution within a spherical cell model (left) and schematic illustration of resulting concentrated currents (right). Modified illustration from [2] © 2011 IEEE.

limits). r denotes the (outer) radius of the layer, ε_r is its relative permittivity and σ is its specific conductivity.

Layer	r	ε_r	σ
Cytoplasm	$r_\mathrm{cp} = 9.995\,\mu\mathrm{m}$	$\varepsilon_\mathrm{r,cp} = 80$	$\sigma_\mathrm{cp} = 1.3\,\mathrm{S/m}$
Plasma membrane	$r_\mathrm{pm} = 10\,\mu\mathrm{m}$	$\varepsilon_\mathrm{r,pm} = 9.44$	$\sigma_\mathrm{pm} = 0\,\mathrm{S/m}$
Nucleoplasm	$6.694\,\mu\mathrm{m} \leq r_\mathrm{np} \leq 8.879\,\mu\mathrm{m}$	$\varepsilon_\mathrm{r,np} = 80$	$\sigma_\mathrm{np} = 3.9\,\mathrm{S/m}$
Nuclear envelope	$6.73\,\mu\mathrm{m} \leq r_\mathrm{np} \leq 8.929\,\mu\mathrm{m}$	$7 \leq \varepsilon_\mathrm{r,ne} \leq 100$	$\sigma_\mathrm{ne} = 83\,\mu\mathrm{S/m}$

Table 4.1: Parameters for the layers of a double shell glioblastoma cell model.

$\mathbf{E}_\mathrm{tot}$ within the cell causes a proportional electric current density within the cell. Considering the distribution of $\mathbf{E}_\mathrm{tot}$ within the different cell layers, the current densities can be integrated to the current I_cp within major parts of the cytoplasm and the current I_np within major parts of the nucleoplasm (as shown in the right side of **Figure 4.1**).

Since only electric field contribution is considered in the cell model, the deduced lumped element model consists of capacitors and resistors. From the electric field distribution in

Figure 4.1 a comprehensive lumped element model can be deduced which is shown in **Figure 4.2**. The indexes of the lumped element parameters indicate their affiliation to specific layers.

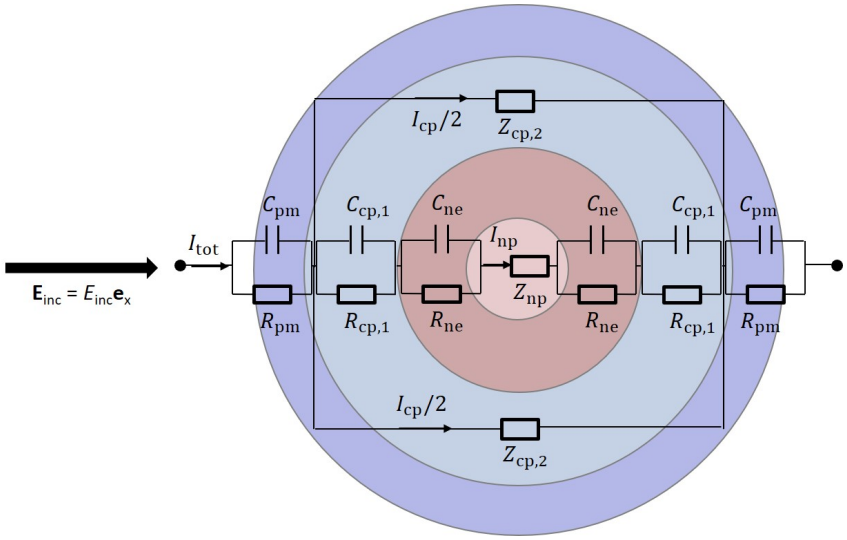

Figure 4.2: Lumped Element model of a spherical cell obtained from the electric field distribution in **Figure 4.1**. Illustration from [2] © 2011 IEEE.

The considerations behind the lumped element model from **Figure 4.2** will be explained in the following. As can be seen from the electric field distribution, $\mathbf{E}_{tot}$ is almost constant within the nucleoplasm. The resulting electric current density distribution is proportional to the electric field and thus also constant within the nucleoplasm. The constant current density can be integrated over the volume of the nucleoplasm and concatenated into the current I_{np}. Furthermore, the nucleoplasm has dielectric and dissipative material characteristics. Due to this property and with consideration of the electric field distribution, $Z_{np} = (R_{np}^{-1} + j\omega C_{np})^{-1}$, which means that the impedance of the nucleoplasm can be presented by a capacitance parallel to a resistivity.

Another fact that can be deduced from the electric field distribution is that I_{np} enters the nucleoplasm through one half of the nuclear envelope and symmetrically exits the nucleoplasm through the other half of the nuclear envelope. This is the reason behind the arrangement of the capacitances and resistivities of the nuclear envelope as illustrated in **Figure 4.2**.

When considering the cytoplasm, only part of the total current within it enters the nuclear envelope. This part is equal to I_{np} and flows through the impedance $Z_{cp,1} = (R_{cp,1}^{-1} + j\omega C_{cp,1})^{-1}$.

The remaining current through the cytoplasm (I_{cp}) splits into half and each half flows through $Z_{\mathrm{cp},2} = (R_{\mathrm{cp},2}^{-1} + \mathrm{j}\omega C_{\mathrm{cp},2})^{-1}$.
The total current I_{tot} entering the cell, penetrates it through the plasma membrane and exits it symmetrically.

From the electric field distribution of **Figure 4.1** it can be seen that the magnitude of electric field within the cytoplasm is much higher than the magnitude of electric field within the nucleoplasm. The reason thereof lies in the well known shielding properties of the membrane structures at frequencies up to several megahertz [1, 133, 134, 145]. Therefore, it is reasonable to assume, that the impedance $Z_{\mathrm{cp},1}$ is much smaller than the impedance of the nuclear envelope and furthermore, that it does not play a significant role in the representation of the electrical behavior of the cell. With this simplification in mind, the lumped element model from **Figure 4.2** can be approximated with the lumped element model shown in **Figure 4.3**.

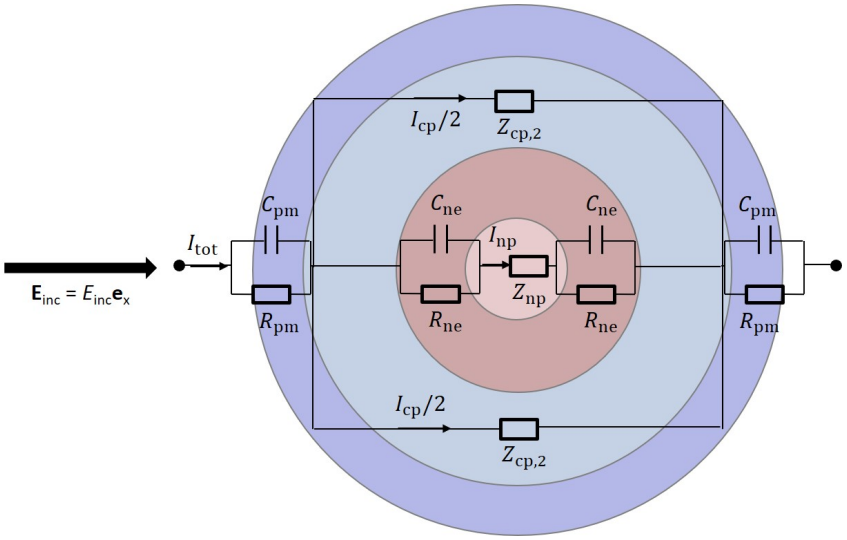

Figure 4.3: Reduced lumped element model of a spherical cell. Illustration from [2] © 2011 IEEE.

The total capacitance $C_{\mathrm{PatchClamp}}$ and the total resistivity $R_{\mathrm{PatchClamp}}$ of the plasma membrane can be measured with the patch clamp technique. When thinking of a capacitor, the capacitance is proportional to the area of the electrodes. In the case of a resistor, the resistivity is inversly proportional to the area normally oriented to the current flow. Thus, C_{pm}

and R_{pm} can be obtained from $C_{\mathrm{PatchClamp}}$ and $R_{\mathrm{PatchClamp}}$ with

$$C_{\mathrm{pm}} = 0.5\, C_{\mathrm{PatchClamp}}, \tag{4.1}$$

$$R_{\mathrm{pm}} = 2\, R_{\mathrm{PatchClamp}}. \tag{4.2}$$

Due to its electromagnetic material properties, the nuclear envelope can be treated as a spherical capacitor. As such, the capacitance and the resistivity can be calculated with

$$C_{\mathrm{ne}} = \frac{2\pi\, \varepsilon_{\mathrm{ne}} r_{\mathrm{ne}} r_{\mathrm{ne}}}{r_{\mathrm{ne}} - r_{\mathrm{ne}}}, \tag{4.3}$$

$$R_{\mathrm{ne}} = \frac{r_{\mathrm{ne}} - r_{\mathrm{np}}}{2\sigma_{\mathrm{ne}}\pi\, r_{\mathrm{ne}} r_{\mathrm{np}}}. \tag{4.4}$$

In general, the dissipation power P_{d} within a volume V can be calculated by application of the specific conductivity σ, the complex electric field vector $\mathbf{E}$ and its conjugate complex $\mathbf{E}^*$ [169]

$$P_{\mathrm{d}} = \iiint_V \sigma \mathbf{E}\mathbf{E}^* \mathrm{d}V. \tag{4.5}$$

The reactive power P_{r} can be obtained with the total permittivity ε [169]

$$P_{\mathrm{r}} = \mathrm{j}\omega \iiint_V \varepsilon \mathbf{E}\mathbf{E}^* \mathrm{d}V. \tag{4.6}$$

Within a lumped element model, the formulas are

$$P_{\mathrm{d}} = I^2 R, \tag{4.7}$$

$$P_{\mathrm{r}} = \mathrm{j}\omega C U^2. \tag{4.8}$$

I is the current through a resistor with resistivity R and U is the voltage over a capacitor with capacitance C.

The impedance of the nucleoplasm Z_{np} can be approximated with R_{np}, if $|P_{\mathrm{d,np}}| \gg |P_{\mathrm{r,np}}|$. When assuming a constant electric field within the nucleoplasm,

$$\begin{aligned} |P_{\mathrm{d,np}}| &\gg |P_{\mathrm{r,np}}|, \\ \sigma_{\mathrm{np}} \frac{4\pi r_{\mathrm{np}}^3}{3} \mathbf{E}\mathbf{E}^* &\gg \omega \varepsilon_{\mathrm{np}} \frac{4\pi r_{\mathrm{np}}^3}{3} \mathbf{E}\mathbf{E}^*, \\ \sigma_{\mathrm{np}} &\gg \omega \varepsilon_{\mathrm{np}}, \\ \sigma_{\mathrm{np}} &\gg 2\pi f \varepsilon_{\mathrm{np}}, \end{aligned} \tag{4.9}$$

This condition can be expressed in terms of frequency f as

$$f \ll \frac{\sigma_{\mathrm{np}}}{2\pi \varepsilon_{\mathrm{np}}}. \tag{4.10}$$

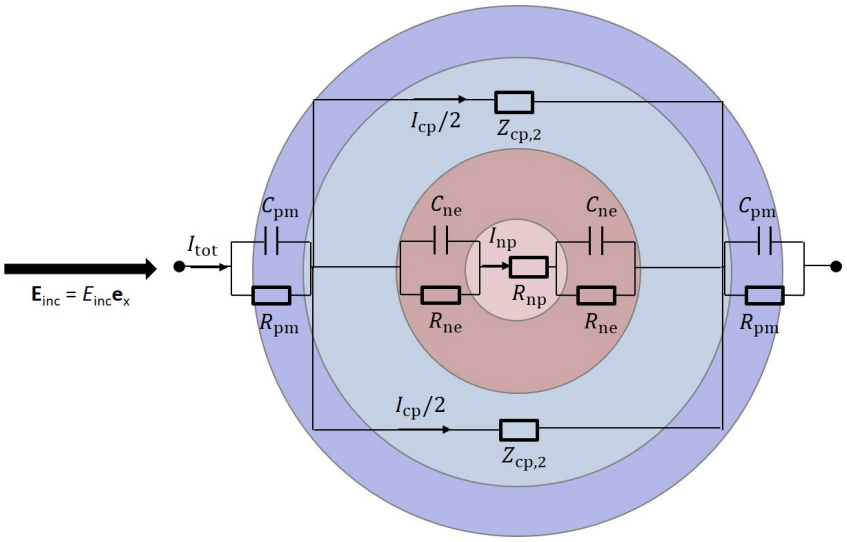

Figure 4.4: Further reduced lumped Element model of a spherical cell. Illustration from [2] © 2011 IEEE.

When this condition applies, the lumped element model from **Figure 4.3** can be converted to the lumped element model from **Figure 4.4**.

The resistivity of the nucleoplasm can be defined by application of the power equations (4.5) and (4.7). Assuming a constant electric field, the resistivity can be obtained with

$$\begin{aligned} P_{\mathrm{d,np}} &= \sigma_{\mathrm{np}} \frac{4\pi r_{\mathrm{np}}^3}{3} \mathbf{E}\mathbf{E}^* = I_{\mathrm{np}}^2 R_{\mathrm{np}}, \\ P_{\mathrm{d,np}} &= \sigma_{\mathrm{np}} \frac{4\pi r_{\mathrm{np}}^3}{3} \mathbf{E}\mathbf{E}^* = \mathbf{E}\mathbf{E}^* \sigma_{\mathrm{np}}^2 r_{\mathrm{np}}^4 \pi^2 R_{\mathrm{np}}. \end{aligned} \tag{4.11}$$

The resistivity of the nucleoplasm is

$$R_{\mathrm{np}} = \frac{4}{3\sigma_{\mathrm{np}} \pi \, r_{\mathrm{np}}}. \tag{4.12}$$

Similarly to (4.9), if

$$f \ll \frac{\sigma_{\mathrm{cp}}}{2\pi\varepsilon_{\mathrm{cp}}} \tag{4.13}$$

applies, the impedance of the cytoplasm $Z_{\mathrm{cp},2}$ can be approximated with $R_{\mathrm{cp},2}$. Then, the lumped element model from **Figure 4.4** can be transformed into the lumped element model from **Figure 4.5**.

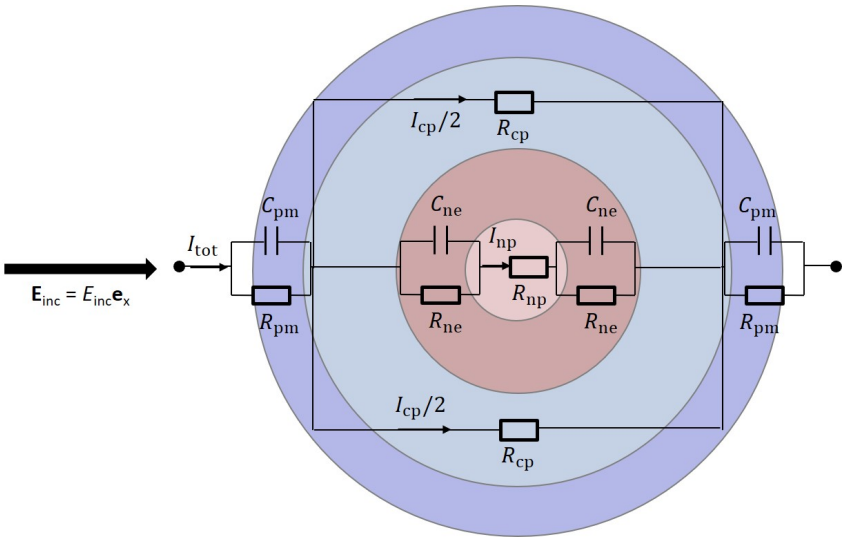

Figure 4.5: Final lumped Element model of a spherical cell including all reductions. Illustration from [2] © 2011 IEEE.

Similarly to the derivation of (4.12), $R_{\mathrm{cp},2}$ can be obtained, when the electric field within the cytoplasm is considered as constant. However, from the electric field distribution in **Figure 4.1**, it can be seen that this is not the case. By assuming a constant electric field and by derivation of $R_{\mathrm{cp},2}$ with similar formulas applied for the derivation of R_{np}, the calculated $R_{\mathrm{cp},2}$ will be higher than the actual resistivity. However, this approach can be used to obtain a maximum value $R_{\mathrm{cp,max}}$ for $R_{\mathrm{cp},2}$:

$$R_{\mathrm{cp,max}} = \frac{8\left(r_{\mathrm{cp}}^3 - r_{\mathrm{ne}}^3\right)}{3\sigma_{\mathrm{np}}\pi\left(r_{\mathrm{cp}}^2 - r_{\mathrm{ne}}^2\right)}. \tag{4.14}$$

Since the relative permittivities of the plasma membrane and the nucleoplasm are equal (see table 4.1) and the specific conductivity within the cytoplasm is smaller than the one of the nucleoplasm, (4.15) is the relevant frequency condition within the derivations applied. This condition results in

$$f \ll 290\,\mathrm{MHz}. \tag{4.15}$$

The frequencies of interest within this investigation are much smaller than $f = 290\,\mathrm{MHz}$. TTFields operate at frequencies in the kilohertz regime, which means that the lumped element model from **Figure 4.5** with the derived formulas for the lumped element parameters is applicable in the frame of TTFields.

To validate the obtained lumped element model with according formulas, the lumped element parameters of **Figure 4.5** were calculated with the presented formulas and compared to parameters obtained from Mie Series calculations (as described in the section 2.3.3 and 2.3.4). Therefore, material and dimensional properties according to table 4.1 were considered.

When considering the lumped element model, the currents I_{np} and I_{cp} can be determined normalized to the current $I_{\mathrm{tot}} = I_{\mathrm{np}} + I_{\mathrm{cp}}$. The respective normalized currents are called $I_{\mathrm{np,LE}}$ and $I_{\mathrm{cp,LE}}$. When considering Mie Series calculations, the currents within the nucleoplasm and within the cytoplasm were calculated by discrete integration of the current densities within the respective layers. These according normalized currents are named $I_{\mathrm{np,Mie}}$, $I_{\mathrm{cp,Mie}}$.

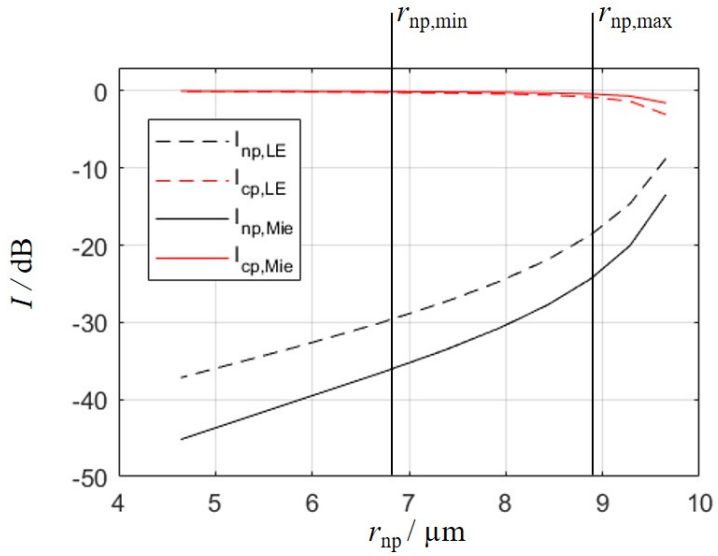

Figure 4.6: Dependency of normalized currents from different nucleoplasm sizes. Illustration from [2] © 2011 IEEE.

Figure 4.6 shows the currents obtained with the different methods as a function of the radius of nucleoplasm r_{np}. $r_{np,min}$ and $r_{np,max}$ mark the limits of usual sizes for glioblastoma nuclei. The currents are plotted in dB scale.

From the results in **Figure 4.6** it can be seen that $I_{cp,LE}$ is slightly underestimated and $I_{np,LE}$ is clearly overestimated for all nucleoplasm radii. It can be seen that the offset between $I_{cp,LE}$ and $I_{cp,Mie}$ rises with rising nucleoplasm sizes and that the offset between $I_{np,LE}$ and $I_{np,Mie}$ becomes smaller.

One reason for the offsets might be found in the impedance $Z_{cp,1}$ from **Figure 4.2**. $Z_{cp,1}$ has been neglected in the applied lumped element model from **Figure 4.5**. Its consideration would increase the total impedance the current I_{np} has to pass, which would cause a higher current $I_{cp,LE}$ and a lower current $I_{np,LE}$. For relatively small r_{np}, I_{cp} is much higher than I_{np}. For relatively big r_{np}, both currents approach each other. That means that for small r_{np}, the neglect of $Z_{cp,1}$ has almost no impact on $I_{cp,LE}$ whereas the impact on $I_{np,LE}$ is much bigger. For relatively big r_{np}, the impact on both currents becomes almost equal.

Another reason for the offset is that for the calculation of the currents with the lumped element model, $R_{cp,max}$ is applied, which is a maximum estimation for the resistivity of the

cytoplasm. This approximation has similar consequences for the currents $I_{\mathrm{np,LE}}$ and $I_{\mathrm{cp,LE}}$ as the neglect of $Z_{\mathrm{cp},1}$.

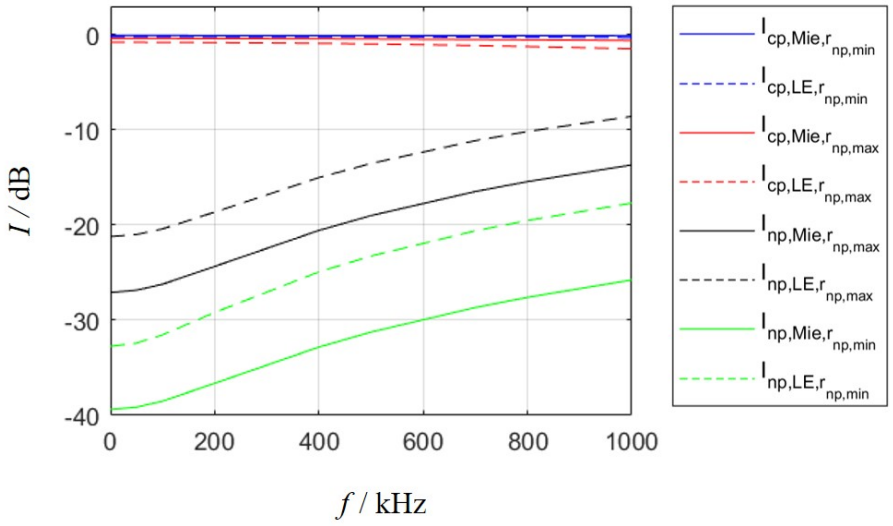

Figure 4.7: Frequency dependency of the normalized currents. Illustration from [2] © 2011 IEEE.

Figure 4.7 shows the same currents for the two different nucleoplasm radii in dependence on the frequency f. It can be seen that the offset between the curves obtained with the lumped element model and the curves obtained with Mie Series calculations is almost constant for the whole shown frequency range. The maximum offset is approximately 8 dB for I_{np} at the minimum nucleoplasm radius. Since the offset is already present at $f = 0$ for all curves, the reason probably lies in the calculation of the resistivities. In case of the cytoplasm, in the lumped element model an over-estimation of R_{cp} was performed with the application of equation (4.14). This leads to an under-estimation of $I_{\mathrm{cp,LE}}$, while the error is higher in case of the bigger nucleus size. Furthermore, compared to $I_{\mathrm{np,Mie}}$, $I_{\mathrm{np,LE}}$ is over-estimated. Since this is the case already at $f = 0$, the reason probably lies in the calculation of one of the resistivities. Since the resistivity of the nuclear envelope is much bigger than the resistivity of the nucleoplasm, at $f = 0$ the resistivity R_{ne} dominates the impedance of the nucleus. Thus, an under-estimation of this resistivity must be a reason for the overestimated current within the nucleus. Considering equation (4.4), R_{ne} is approximated with the resistivity of a spherical capacitor. This is not the real scenario case for the membrane structures. When considering the vectors from **Figure 4.1** carefully with focus on the boundaries of the nu-

clear membrane around $x = 0$, it can be seen that there is almost no electric field. This can be considered in the calculation of R_{ne} by assuming a smaller effective radius r_{ne}. From (4.4) it can be seen that a smaller r_{ne} would lead to a bigger value for R_{ne}, leading to a correction of $I_{\mathrm{np,LE}}$ towards lower values.

Although the lumped element model with the approximation formulas cannot be used for the exact solution of the current distribution within the cell, the model provides a sufficient approximation of the overall electromagnetic behavior.

4.2 Electric Field Distribution in Cells and AuNPs

In the following, first the calculation methods for the determination of electric field distributions are introduced. Subsequently the calculation results are presented.

4.2.1 Calculation Methods

The overall methodical approach for the determination of the electric field within a cell and an AuNP is similar to the calculations of magnetic field distributions described in section 3.2. As before, the double shell cell model from **Figure 2.10** is applied with dimensional and EM material parameters according to table 2.3. The electric field distribution is calculated with Mie Series calculations according to **Figure 3.6**.

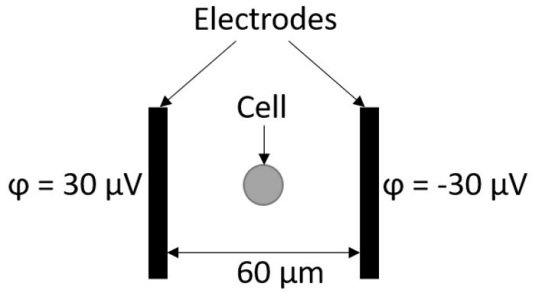

Figure 4.8: Illustration of the numerical simulation model for a cell exposed to an electric field.

To validate the results obtained with Mie Series calculations, numerical calculations are performed in *Sim4Life*. To obtain the numerical results for the electric field distribution, the *Unstructured Electro Quasi-Static* solver is applied. Since the direct excitation of an electric field with desired parameters is not possible with this solver, the cell model is placed between two electrodes, as schematically shown in **Figure 4.8**. φ is the electrical potential of a single electrode. The dimensional properties and the potentials are chosen to achieve an unidirectional and homogeneous electric field excitation with electric field amplitude $E_{\mathrm{inc}} = 1\,\mathrm{V/m}$ at the cell.

For the determination of the electric field distribution within the AuNP, the cell from **Figure 3.6** is replaced by an AuNP. The AuNP with radius $r_{\mathrm{NP}} = 5\,\mathrm{nm}$ is considered to possess a bulk specific electrical conductivity of gold which is $\sigma_{\mathrm{Au}} = 41\,\mathrm{MS/m}$.

4.2.2 Calculation Results of Electric Field Distributions in Cells and in AuNPs

Figure 4.9 shows the results of the electric field distribution within the cell, separated into the directional components and at both target frequencies. The magnitude of the total electric field $|\mathbf{E}_{\mathrm{tot}}|$ is normalized to the incident electric field magnitude $|\mathbf{E}_{\mathrm{inc}}|$ and plotted in dB scale.

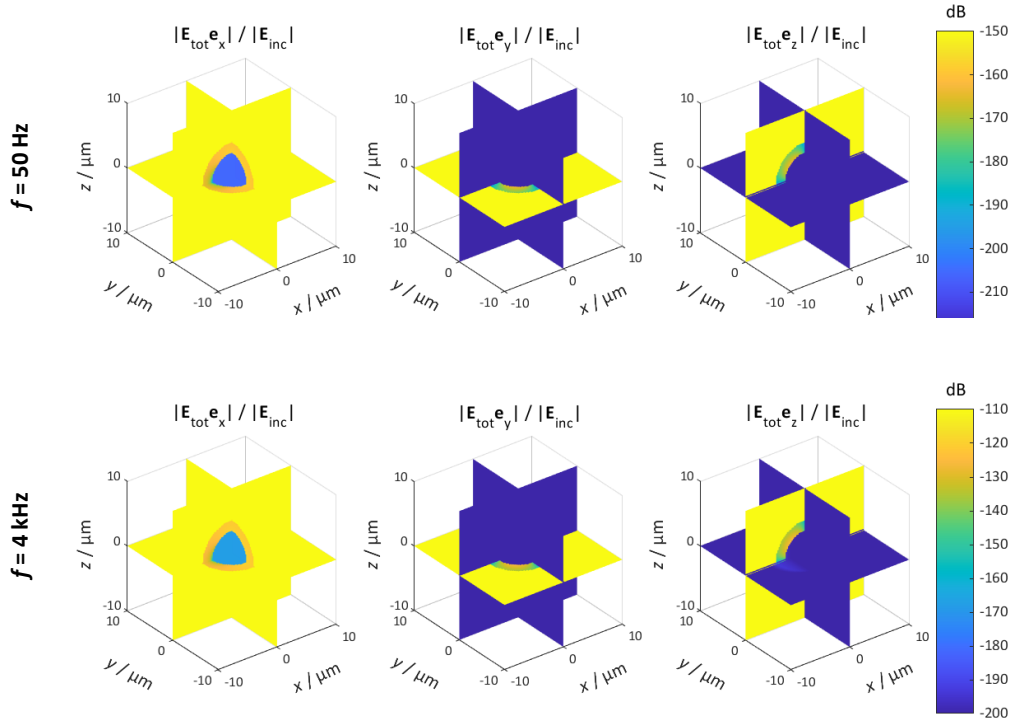

Figure 4.9: Mie Series calculation of total electric field distribution in the three directions of Cartesian space.

Comparing both frequencies, it can be seen that the principle electric field distributions are similar to each other, but the electric field magnitude at $f = 4\,\mathrm{kHz}$ is approximately 40 dB (corresponding to a factor of 100) higher than at $f = 50\,\mathrm{Hz}$. The electric field in x-direction is the dominant directional component, since $\mathbf{E}_{\mathrm{inc}}$ is oriented in x-direction. Without further descriptions in the plots, the cytoplasm can be distinguished from the nucleus: The cell electric field proportion entering the cytoplasm is lower than the external electric field and the proportion entering the nucleus is even lower. This principle electric field distribution was to be expected when considering the lumped element model of the cell from **Figure 4.5**. At relatively low frequencies, as applied here, the total impedance of the cell is dominated by the capacitive properties of the plasma membrane and the nuclear envelope. The total capacitance has a shielding impact against the external electric field and the capacitance of the nuclear envelope has a shielding impact against the electric field within the cytoplasm. **Figure 4.10** shows the ratio $|\mathbf{E}_{\mathrm{tot}}|/|\mathbf{E}_{\mathrm{inc}}|$ in the xy-plane. The only difference between the left plots and the right plots is the scale. The plots on the left show the field distribution inside the cell and the plots on the right have the focus outside the cell. It can be seen that

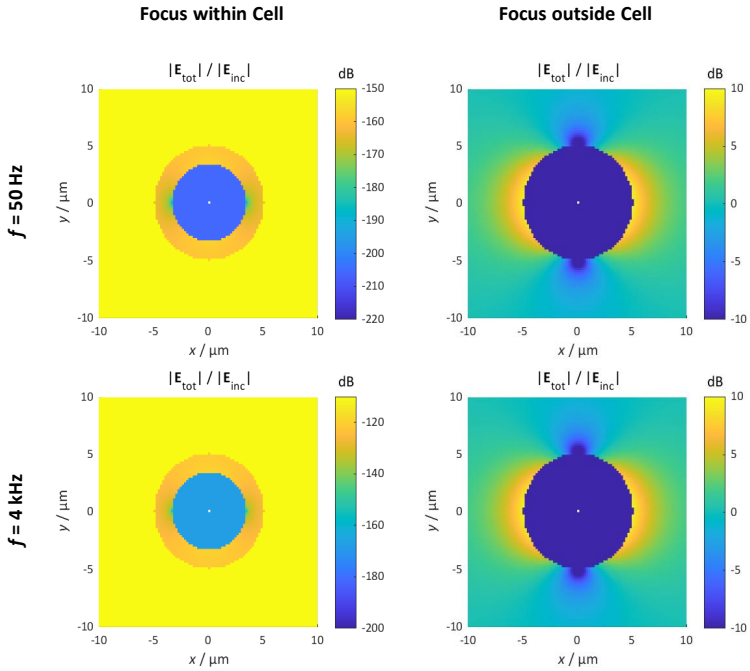

Figure 4.10: Mie Series calculation of total electric field distribution in two scales.

there is a significant electric field gradient within the cytoplasm ($y = 0$, focus within cell) as well as in the immediate vicinity of the cell ($y = 0$ and $x = 0$, focus outside cell) for both frequencies. Furthermore, the applied frequency does not significantly alter the electric field distribution outside the cell but the fraction of the cell-penetrating electric field is about 40 dB higher at $f = 4\,\mathrm{kHz}$ than at $f = 50\,\mathrm{Hz}$. For both frequencies, the ratio between the electric field within the cytoplasm $\mathbf{E}_{\mathrm{cp}}$ and the electric field within the nucleoplasm $\mathbf{E}_{\mathrm{np}}$ is approximately 40 dB (factor 100). These ratios of the electric fields within the different cell layers can also be approximated with the lumped element model from **Figure 4.5**, which is also shown in **Figure 4.11** a).

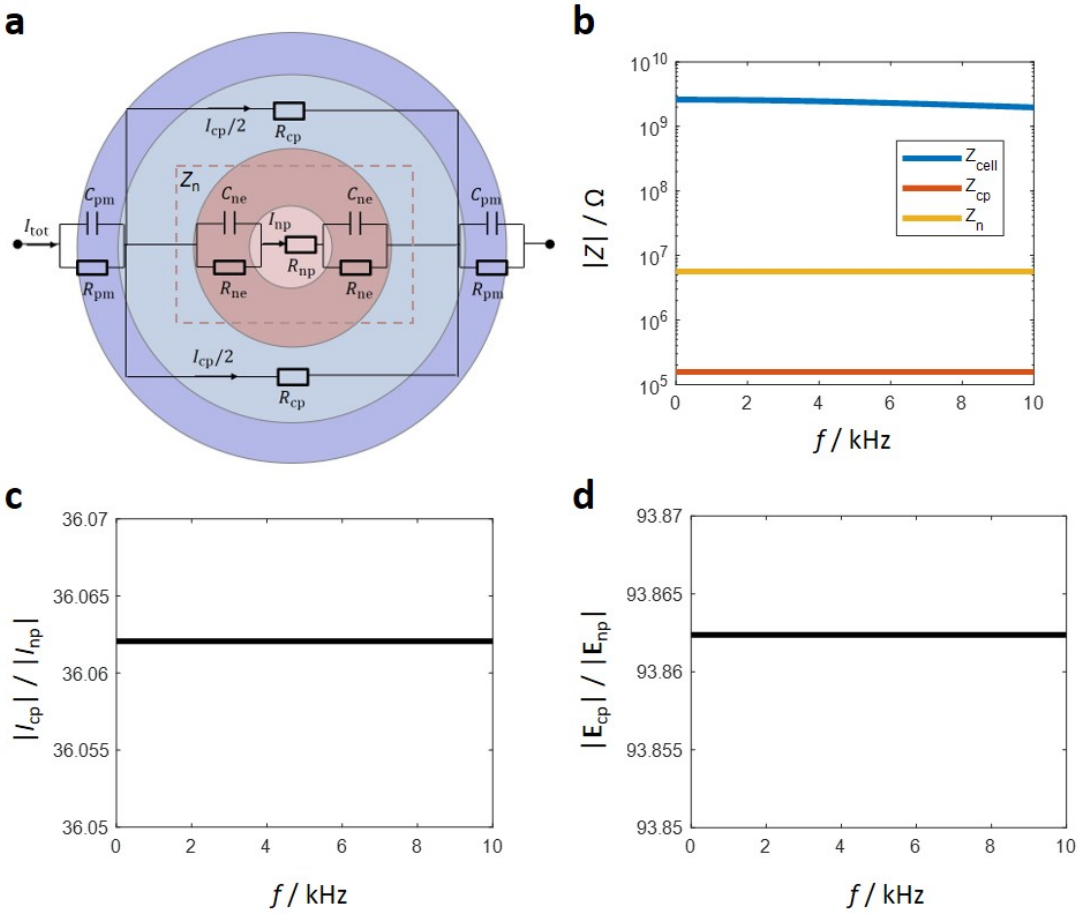

Figure 4.11: Calculations with the lumped element model from **Figure 4.5** with respective parameters.

The total impedance of the lumped element model from **Figure 4.11** a) is Z_{cell}, the total impedance of the nucleus (including the nuclear envelope and the nucleoplasm) is Z_{n} and the total impedance of the cytoplasm is Z_{cp}. **Figure 4.11** b) shows the magnitudes of the three impedances for a frequency range up to $0 \leq f \leq 10\,\mathrm{kHz}$. The impedances are calculated with the lumped element parameters according to the formulas from section 4.1 and dimensional and EM parameters according to table 2.3. With the results for the impedances, the ratio of the currents is plotted in **Figure 4.11** c), where $|I_{\mathrm{cp}}|/|I_{\mathrm{np}}| = |Z_{\mathrm{np}}|/|Z_{\mathrm{cp}}|$. It can be seen that for the frequency range of interest, the ratio of the two current magnitudes is almost constant. Furthermore, the current ratio can also be formulated as

$$\frac{|I_{\mathrm{cp}}|}{|I_{\mathrm{np}}|} = \frac{|\mathbf{E}_{\mathrm{cp}}|\sigma_{\mathrm{cp}}A_{\mathrm{cp}}}{|\mathbf{E}_{\mathrm{np}}|\sigma_{\mathrm{np}}A_{\mathrm{np}}}. \tag{4.16}$$

A is the cross-sectional area of the respective layer indicated by the index. With reformulation of (4.16), the ratio of the electric field magnitudes $|\mathbf{E}_{\mathrm{cp}}|/|\mathbf{E}_{\mathrm{np}}|$ is obtained and plotted in **Figure 4.11** d). It can be seen that the ratio of $|\mathbf{E}_{\mathrm{cp}}|/|\mathbf{E}_{\mathrm{np}}|$ approximated with the lumped element model is very close to the factor of approximately 100 obtained with Mie Series calculations.

The results from **Figure 4.9** to **Figure 4.11** show that just a small proportion of the incident electric field enters the cell. However, these results are obtained by application of mean values of EM properties for a cell according to table 2.3. It is well known that highly conductive materials shield an externally applied electric field. Thus, in order to achieve the greatest possible penetration of the electrical field into the cell, the electrical material properties as specified in table 4.2 were used instead of the according parameters from table 2.3. Subsequently, the parameters are further changed according to table 4.3.

Layer	Changed relative permittivity	Changed specific Conductivity
Cytoplasm	–	$\sigma_{\mathrm{cp}} = 0.033\,\mathrm{S/m}$
Plasma membrane	$\varepsilon_{\mathrm{r,pm}} = 16.8$	–

Table 4.2: First changed EM parameters of the layers of a double shell cell model.

Layer	Changed relative permittivity	Changed specific conductivity
Cytoplasm	–	$\sigma_{\mathrm{cp}} = 0.033\,\mathrm{S/m}$
Plasma membrane	$\varepsilon_{\mathrm{r,pm}} = 16.8$	–
Nucleoplasm	–	$\sigma_{\mathrm{np}} = 0.25\,\mathrm{S/m}$
Nuclear Envelope	$\varepsilon_{\mathrm{r,ne}} = 100$	–

Table 4.3: Second changed EM parameters of the layers of a double shell cell model.

Instead of using mean values, the parameters in the two tables are the limit values extracted from [134]. To achieve higher electric field penetration, the permittivities of the membranes were set to the highest limits and the conductivities of the cytoplasm and nucleoplasm were set to lower limits. The respective parameters were chosen because the membranes have predominantly capacitive properties and the cytoplasm and the nucleoplasm have predominantly conductive properties.

In **Figure 4.12** the results are presented for a frequency of $f = 4\,\mathrm{kHz}$, since the electric field penetration is higher than at lower frequencies. First the normalized field distributions from Mie Series calculations are presented. The applied material parameters are indicated under the respective plot, while the parameters which are grayed out are equal as before. From **Figure 4.12**, it can be seen that the overall fraction of the electric field penetrating the cell is dominated by the electrical material parameters of the cytoplasm. Electrical parameters of the nucleus determine the fraction that penetrates the nucleus. However, a significant modification of electrical parameters of the cell increases the magnitude of the penetrating electric field proportion up to 40 dB. The normalized magnitude of cell-entering electric field has a maximum value of about -90 dB (area of cytoplasm in **Figure 4.12**), which corresponds to a factor in the range of 10^{-5}.
In **Figure 4.12** the ratios of $|\mathbf{E}_{\mathrm{cp}}|/|\mathbf{E}_{\mathrm{np}}|$ calculated with the lumped element model can also be seen for the modified electrical material parameters. For the first set of parameter modifications the ratio remains as before. For the second set of modifications, the ratio is significantly different. These two results mirror the results of the respective Mie Series calculations of the same figure.

Besides the cell, also the AuNP exposed to an electric field is studied. Since materials with very high electrical conductivity shield their interior from an externally applied electric field, it must be assumed that an externally applied electric field does not significantly penetrate

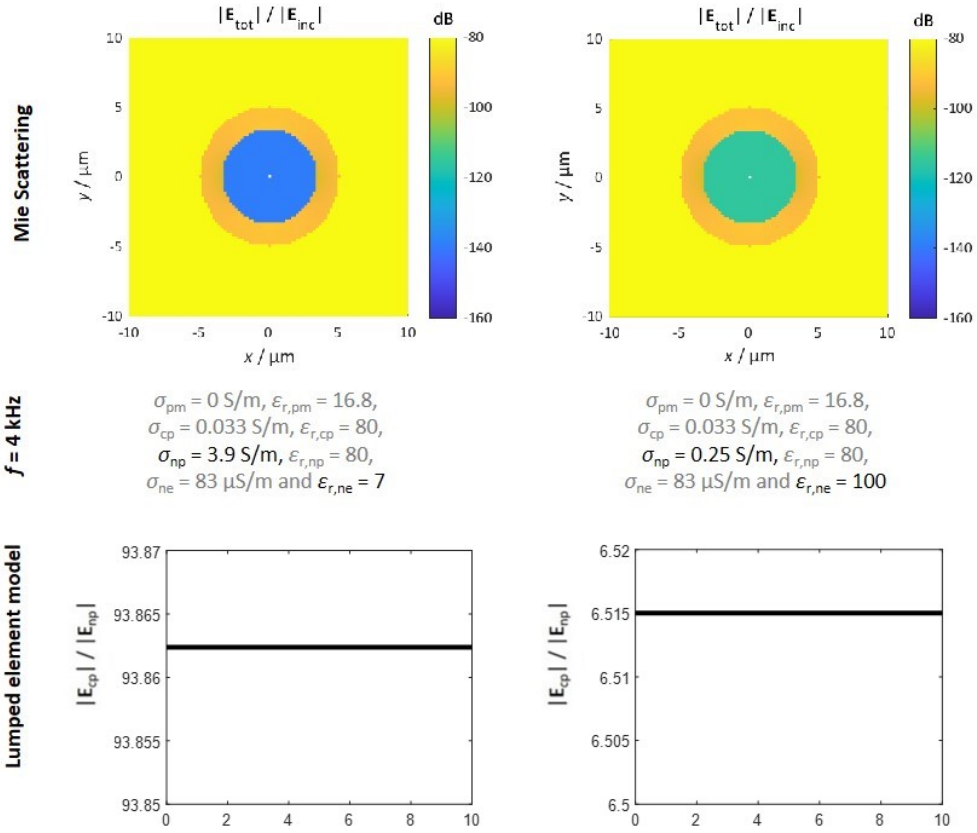

Figure 4.12: Mie Scattering calculation of total electric field distribution and ratio of electric fields by application of the lumped element model with changed EM parameters.

an AuNP ($\sigma_{\mathrm{Au}} = 41\,\mathrm{MS/m}$). The respective results obtained with Mie Series approach are presented in **Figure 4.13**.

The results of **Figure 4.13** show that there is no significant difference between the electric field distributions in close vicinity of the AuNP at both frequencies. As expected, the electric field fraction that penetrates the AuNP is very small (maximum of -260 dB, corresponding to a factor of 10^{-13}).

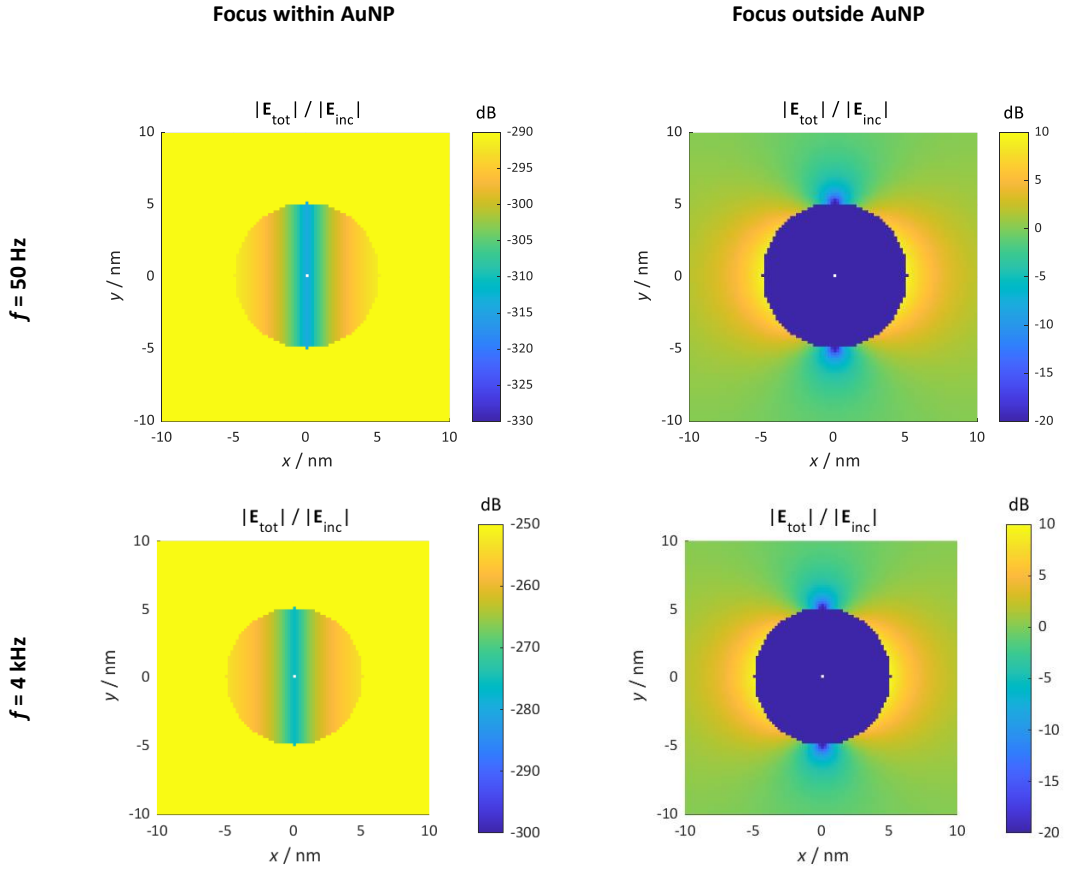

Figure 4.13: Mie series calculations of total normalized electric Field within an AuNP.

4.2.3 Assessment of Mechanisms of Action between Electric Fields, Cells and AuNPs

The results shown in section 4.2.2 are obtained for the relevant frequencies in cellular reprogramming. However, during cellular reprogramming cells are exposed to magnetic fields. The excitation of an alternating magnetic field always results in an excitation of an electric field component. However, the electric field is so small that it is usually neglected. Since information concerning the electric field strength excited during cellular reprogramming with magnetic fields is missing, in the following a TEM wave is considered, as the relation between magnetic field strength and electric field strength is well known. However, it should be noted that this consideration leads to a significant over-estimation of the electric field

contribution in regard to cellular reprogramming.
In a TEM wave the magnitudes of the electric field component and the magnetic field component are linked by the wave impedance, as shown in (2.23). Considering a magnetic flux density magnitude of $|\mathbf{B}_{\mathrm{inc}}| = 1\,\mathrm{mT}$, the electric field component of the TEM wave excited in vacuum has a magnitude of approximately $|\mathbf{E}_{\mathrm{inc}}| = 300\,\mathrm{kV/m}$.
According to the results of **Figure 4.12**, the maximum magnitude of electric field within the cytoplasm is 90 dB smaller than the excited electric field value. Thus, the maximum magnitude of electric field penetrating the cell is in the range of $|\mathbf{E}_{\mathrm{pen,max}}| = 30\,\mathrm{V/m}$. Considering the applied cell model, observed biological effects during cellular reprogramming under exposure cannot be explained by electrostatic forces (see section 2.4.1).

To evaluate whether DEP forces on microtubules might occur in the frame of reprogramming, (2.65) is solved with parameters from table 4.4. The according parameters of the microtubule are from [176]. The parameters of the cytoplasm are the same as for calculations behind the results of **Figure 4.10**.

Parameter	Value
r_{mt}	12.5 nm
$\varepsilon_{\mathrm{mt}}$	0.89 nF/m
σ_{mt}	250 mS/m
$\varepsilon_{\mathrm{cp}}$	0.70832 nF/m
σ_{cp}	1.3 S/m

Table 4.4: Parameters for the calculation of DEP force on microtubules in cytoplasm.

Considering the field gradients within the cytoplasm along $y = 0$ from **Figure 4.10**, the following statement can be made: the electric field magnitude has a maximum gradient of approximately 20 dB per micrometer. At $f = 4\,\mathrm{kHz}$ and over a distance of approximately 1 µm, the cytoplasm contains electric field magnitudes of approximately $|\mathbf{E}_{\mathrm{tot}}| = 10^{-6}|\mathbf{E}_{\mathrm{inc}}|$ and $|\mathbf{E}_{\mathrm{tot}}| = 10^{-7}|\mathbf{E}_{\mathrm{inc}}|$. The respective gradient term for the calculation of the DEP force can be obtained with:

$$\nabla|\mathbf{E}|^2 = \frac{(10^{-12} - 10^{-14})|\mathbf{E}_{\mathrm{inc}}|^2}{\mu\mathrm{m}} \tag{4.17}$$

Assuming $|\mathbf{E}_{\mathrm{inc}}| = 300\,\mathrm{kV/m}$ (for a TEM wave), the DEP force per lenght of microtubule is in the range of 10^{-21} N/m. This force is too small to be effective [152, 176]. Any effect on other cell compartments due to DEP force exertion cannot be excluded since DEP effects on other compartments are not as well studied as for microtubules.
Thermal effects within the cell due to the obtained electric field intensities can also be excluded when comparing electric field magnitudes obtained here with those obtained by [1]. With the applied cell model, there is no indication of electric field induced mechanism of action within an exposed cell.
However, it has to be taken into account, that the applied cell model considers a perfectly spherical, single cell with homogeneous electromagnetic material properties. Real biological cells are not perfectly spherical and furthermore, real cells change their shape during the cell cycle. Furthermore, considering several cells under exposure, electric field distribution within cells can become inhomogeneous. This might cause DEP force effects on whole cells, which is shown to have biological impact [177].

Except the cells, also AuNPs were considered. AuNPs also cause electric field inhomogeneities (see results of **Figure 4.13**). However, a single nanoparticle causes inhomogeneities within a very small volume, which might be too small to affect cell compartments much bigger than the particle. Very small cell compartments in the nanometer scale might be affected.

4.3 Enhancement of Electric Field Exposure Setup for In Vitro Cell Experiments

The work presented in this section was conducted at the Institute of Microwave and Wireless Systems, Leibniz University Hannover and published in the frame of a conference contribution [250]. I developed the idea and the content of the paper. Lukas Berkelmann conducted numerical EM simulations in related former studies [1]. Professor Anaclet Ngezahayo consulted as an expert in the field of biology. Professor Dirk Manteuffel supervised the work.

An exposure setup for cell culture experiments with focus on electric field component is shown in **Figure 2.21**. This setup consists of four electrodes which are located within a cell culture dish and allow the excitation of an electric field in two different polarization directions (as explained in section 2.5).

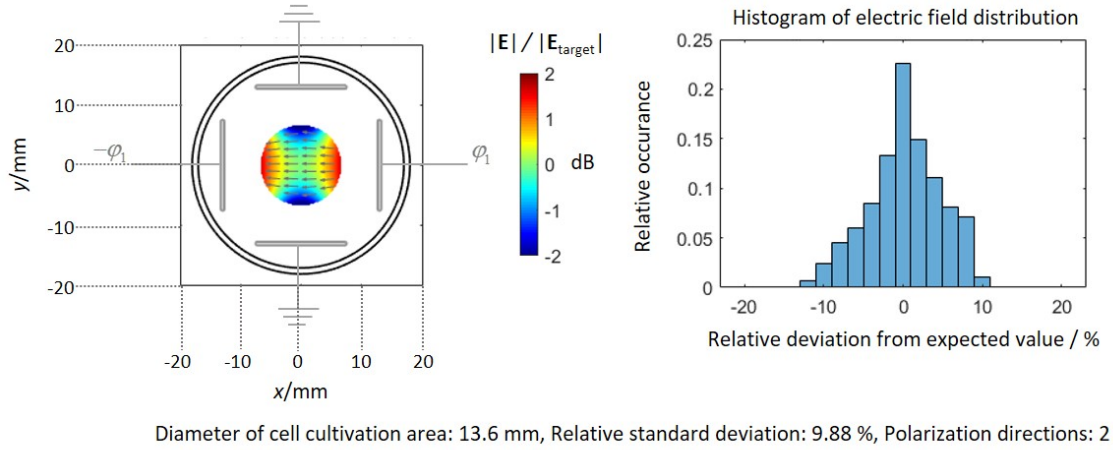

Figure 4.14: Electric field distribution within the cell cultivation area of the setup from **Figure 2.21** on the left and histogram of the electric field values on the right.

Figure 4.14 shows on the left side the electric field distribution of the setup including cell culture medium, the cell culture dish and the four electrodes immersed in the medium. φ_1 and $-\varphi_1$ are the chosen potentials at the active electrodes. The potentials have been chosen to produce a target electric field of $|\mathbf{E}_{\text{target}}| = 100\,\text{V}_{\text{RMS}}\text{m}^{-1}$ at the centre of the cell culture

dish. The gray arrows indicate the electric field direction. The magnitude of the electric field distribution $|\mathbf{E}|$ within the cell cultivation are of 13.6 mm diameter is plotted normalized to the target field. Values are provided in dB scale.
On the right side of **Figure 4.14** a histogram can be found. The histogram shows the relative occurrence of the field values $|\mathbf{E}|$ in dependence of their relative deviation from the expected value $|\mathbf{E}_{\text{target}}| = 100\,\text{V}_{\text{RMS}}\text{m}^{-1}$. The diameter of cell cultivation area has been chosen to the maximum diameter where the relative standard deviation of $|\mathbf{E}|$ from $|\mathbf{E}_{\text{target}}|$ is under 10 %.

Since the direction of electric field polarization relative to the mitotic axis is significant for the electric field distribution within a cell, and cells can be oriented arbitrarily in the cultivation area, it is important to allow as many polarization directions of the electric field as possible. Furthermore, to enhance the quality of experiments even more, a larger area of field homogeneity would be favorable.

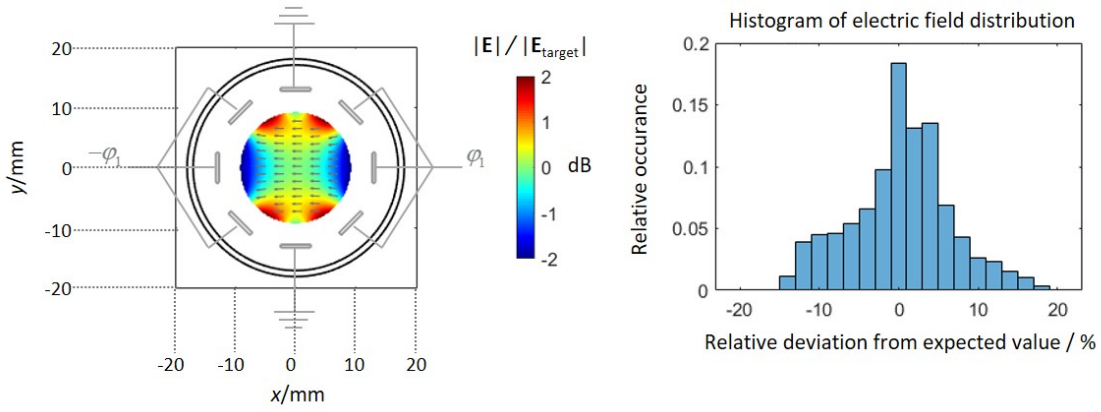

Figure 4.15: Electric field distribution within the cell cultivation area of the first modification on the left and histogram of the electric field values on the right.

An intuitive way to achieve more directions of polarization is to apply more electrodes. **Figure 4.15** shows such an example where eight electrodes are chosen. Furthermore, by activating six electrodes at the same time, three of which carry the same potential, a cell cultivation area with a diameter of 18.6 mm can be achieved, while the standard deviation is

9.9 %. The according histogram can be seen in **Figure 4.15** on the right side. When comparing the histogram from **Figure 4.15** with the histogram of the original setup, it can be seen that the relative deviation from the expected value reaches higher values. In fact, the opposite would be the aim. An enhancement of the relative deviation can be reached with smaller electrodes, which are further away from the centre of the cell cultivation area, as shown in **Figure 4.16**.

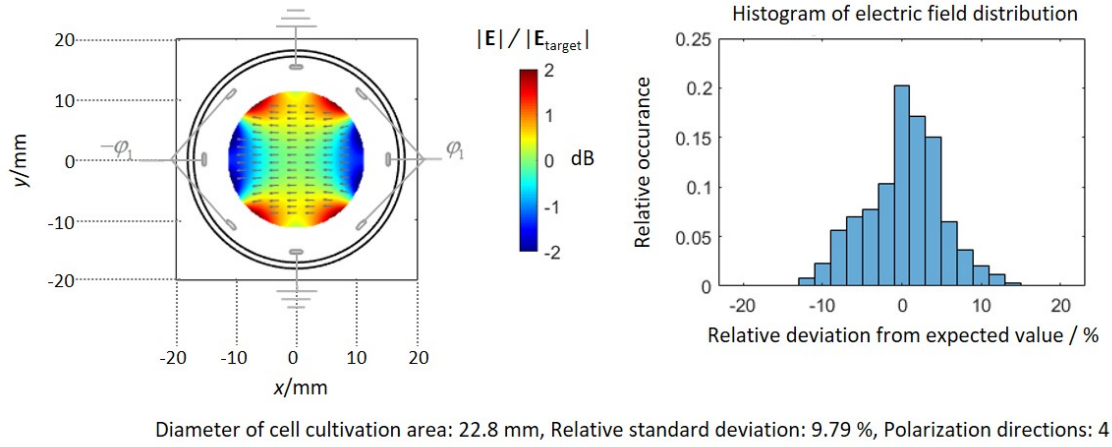

Figure 4.16: Electric field distribution within the cell cultivation area of the second modification on the left and histogram of the electric field values on the right.

Furthermore, with this configuration an even bigger cell cultivation area with a diameter of 22.8 mm can be reached. However, it is desirable to have a configuration of electrodes which shrinks the relative deviation from the expected value to a maximum extent.

When having a closer look on the electric field distributions in **Figure 4.16** and **Figure 4.15**, the main electric field within the cell cultivation area is caused by each facing pair of active electrodes (three facing pairs along $y = -10\,\mathrm{mm}$, $y = 0\,\mathrm{mm}$ and $y = 10\,\mathrm{mm}$ respectively). To realize an electric field distribution with possibly high homogeneity, the electric fields between the electrodes along $y = 10\,\mathrm{mm}$ and $y = -10\,\mathrm{mm}$ should be equal to the electric field along $y = 0\,\mathrm{mm}$.

Figure 4.17 shows the distances d_1 and d_2 between two pairs of electrodes. Alpha is the constant angle between two neighbouring electrodes. Approximating each pair of facing

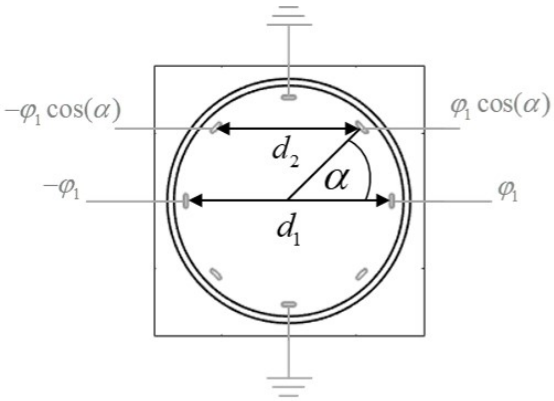

Figure 4.17: Illustration of the parameters for the third modification.

electrodes with an ideal plate capacitor, the electric field between the individual pairs can be approximated with

$$E = \frac{2\varphi}{d}. \tag{4.18}$$

E is the electric field magnitude between the electrodes and d is the distance between the electrode pair. To achieve the same electric field between the pair of electrodes with the distance d_2 as with the pair of electrodes with the distance d_1, the potential at the electrodes must be $\varphi = \varphi_1 \cos(\alpha)$, as shown in **Figure 4.17**.

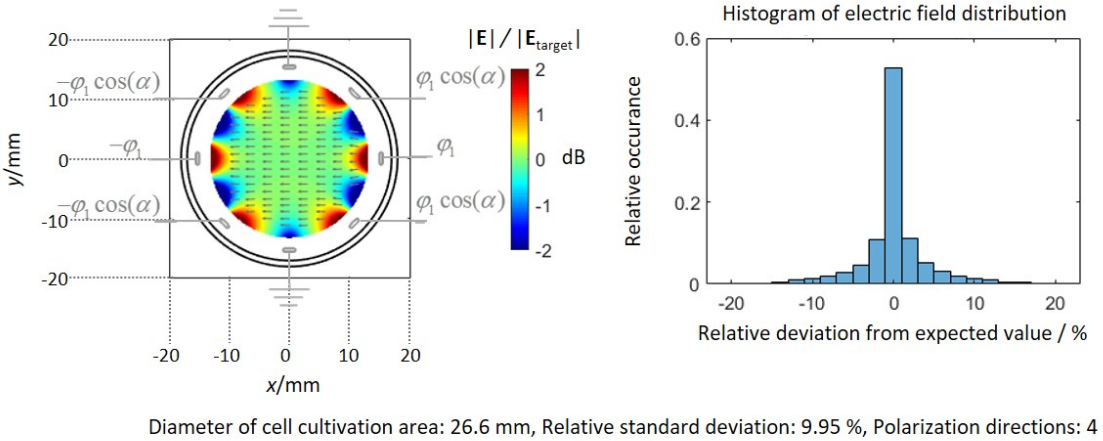

Figure 4.18: Electric field distribution within the cell cultivation area of the third modification on the left and histogram of the electric field values on the right.

The result of such an excitation of the electrodes can be seen in **Figure 4.18**. From the field distribution it can be seen that there the field homogeneity is much higher than in the cases shown before. This trend is also clearly recognizable when comparing the histograms. The relative occurrence of a relative deviation of zero is almost three times higher than in the cases shown before. However, from the electric field distribution it can also be seen that the electric field at the border of the cell cultivation area is as inhomogeneous as before.

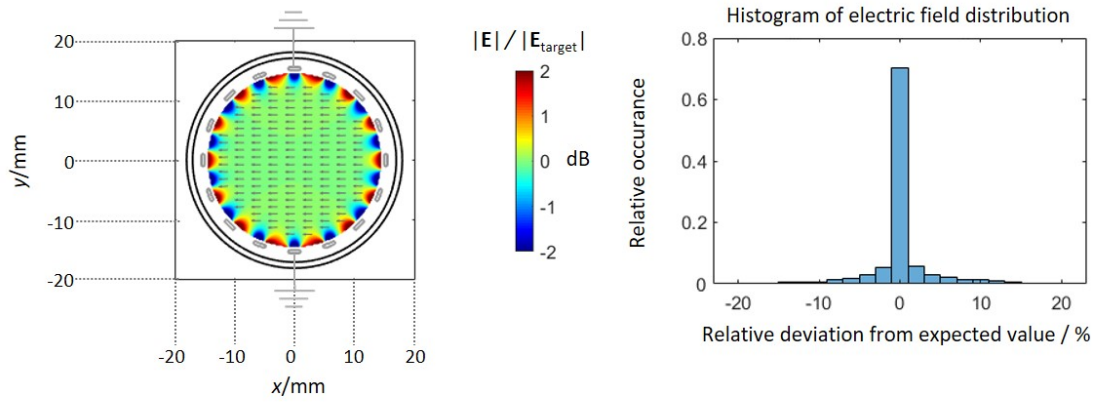

Figure 4.19: Electric field distribution within the cell cultivation area of the fourth modification on the left and histogram of the electric field values on the right.

Figure 4.19 shows the results of the same principle of excitation as in **Figure 4.17** and **Figure 4.18**. but with sixteen electrodes. It can be seen that a highly homogeneous electric field can be realised with this electrode configuration. Almost the whole petri dish can be used for cell cultivation. Furthermore, eight directions of electric field polarization can be applied with this configuration.

Conclusively, the targeted improvements have been fully achieved by changing the original electrode configuration from **Figure 4.14** to the final configuration from **Figure 4.19**.

4.4 Implementation of a Capacitive Measurement Method

The work presented in this section was conducted at the Institute of Microwave and Wireless Systems (IMW), Leibniz University Hannover, in the frame of a bachelor thesis of Hendrik Jäschke [6] which I supervised. I developed the idea. Furthermore, I decided about the course of action and managed the supply of needed materials. For this work different capacitor configurations with different electrode materials were needed. Copper electrodes were fabricated at the IMW. Furthermore, I established a connection to the Institute of Technical Chemistry, Leibniz University Hannover, where the platinum and platinum black electrodes were fabricated. With the provided electrodes, I built the capacitor configurations on the basis of a design from [223]. Hendrik Jäschke performed measurements under my guidance and conducted literature research for his thesis. Professor Dirk Manteuffel was the examiner of the bachelor thesis.

During cell culture experiments cells are located in nurturing cell culture medium. Thus, electromagnetic material parameters of the surrounding medium are relevant for theoretical, analytical and numerical investigations of EMF interaction mechanisms. In the following, the implementation and application of a capacitive measurement method is shown which allows the determination of the specific conductivity of solutions containing dissolved ions. This measurement method can be applied at frequencies down to one kilohertz and is therefore suited for the determination of specific conductivity of cell culture media used during cellular reprogramming and TTFields *in vitro* cell experiments. In the following first the principle approach and the methods are introduced and subsequently the measurement results are shown and discussed.

4.4.1 Principle Approach and Methods

For the capacitive determination of electrical material parameters, a capacitor configuration according to **Figure 4.20** was build. This design is based on the model presented in [223]. The copper electrodes in this design were etched on FR4 circuit board substrates and have a diameter of 30 mm. The bottom electrode is surrounded by a spacer (flange) from copolyester

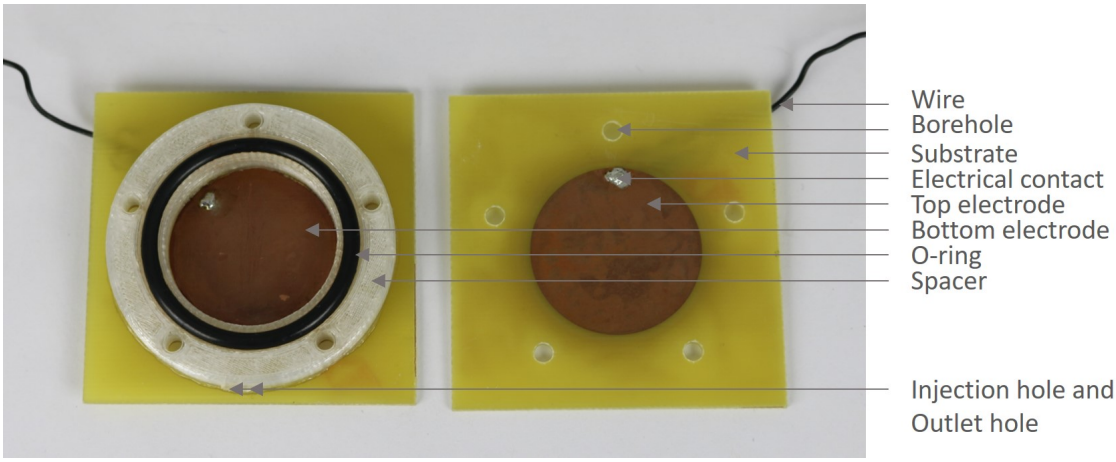

Figure 4.20: Applied capacitor with copper electrodes. A Modified configuration based on the model of [223].

with a thickness of 6 mm which was carefully glued on the substrate with epoxy based glue. The boreholes on the substrates allow the attachment of the upper electrode part to the bottom electrode part by Polytetrafluoroethylene (PTFE) screws. An o-ring within the spacer allows for a leakproof mounting. The electrical contact to the measurement equipment is realised through a wire. An injection hole on one side of the spacer allows to fill the capacitor with the medium under test (MUT) by application of a syringe with fine needle. A fine outlet hole is placed beside the injection hole.

Before each measurement, slowly, the capacitor was filled with the MUT through the injection hole, until a part of the MUT came out of the outlet hole. This procedure was chosen to avoid air within the capacitor. The impedance of the filled capacitor configuration was measured with an HP 4284A impedance analyzer. The wires of the capacitor were connected through HP 16048A connectors to the impedance analyzer. The analyzer was started 30 minutes before measurements were conducted in order to provide a sufficient warm-up time for the device. Furthermore, the analyzer was calibrated after the warm-up period. Impedance measurements were performed for a frequency range of $1\mathrm{kHz} \leq f \leq 1\mathrm{MHz}$. The lower frequency limit was chosen since the electrical material properties for MUTs of interest do not (significantly) change for even lower frequencies (see **Figure 2.17**). The upper frequency limit was chosen much higher than the typical frequencies of interest in the frame of cellular reprogramming and TTFields, which ensured the coverage of the frequency range of interest.

The determination of electrical material parameters was first conducted by consideration of the theory provided in section 2.5.2, specifically, by consideration of the lumped element model from **Figure 2.24** and application of the formulas provided in (2.75) to (2.79).
First, the impedances of the capacitor filled with air (empty cell) and purified water were measured over the above mentioned frequency range to obtain the constant K and the stray capacitance C_0. The measured impedances were fitted to the function in (2.75). The parameter fitting function from [251] was used in MATLAB. With the determination of the fitting parameters, the constant K was obtained with (2.78). The determined value was compared to the value obtained with the approximation formula (2.82) which resulted in $K = 1.043 \cdot 10^{-12}$ F. The relative permittivity of water was approximated with $\varepsilon_{\mathrm{r},1} = 80$ and the relative permittivity of air was approximated with $\varepsilon_{\mathrm{r},2} = 1$. These values are close to respective values provided in literature and small variations of the values towards exact literature values as in [223] did not change the overall results significantly. Once the constant K was known, the stray capacitance C_0 could be determined with (2.79). After the impedance measurement with water, the capacitor was opened, dried with lint free tissues and closed in order to be filled with the MUT of interest.

The first MUT chosen was isopropyl alcohol, also called isopropanol. This choice allowed the validation of the capacitor setup and the applied method, since its electrical material parameters are well known [252]. The room temperature was measured throughout the whole experimental procedure. A temperature around $22\ ^{\circ}\mathrm{C} \pm 0.5\ ^{\circ}\mathrm{C}$ was maintained. The specific conductivity of isopropanol at room temperature is around $\sigma = 3.5\ \mu\mathrm{S/m}$ [253] and can be approximated with zero. Its relative permittivity is approximately $\varepsilon_{\mathrm{r}} = 20$ [252].

After validation of the principle functioning of the setup, the next step was to determine electrical material properties of electrolyte solutions. As described in section 2.5.2, electrolyte solutions cause electrode polarization. Up to a cut-off frequency, the electrode polarization has major impact on the measured impedance. The cut-off frequency depends strongly on the electrode material. To determine the electrical material properties at low frequencies around $f = 1\mathrm{kHz}$, the aim was to chose an electrode material which would shift the cut-off frequency under $f = 1\mathrm{kHz}$. Therefore, platinum and platinum black electrodes were tested. The principle design was kept as before with the copper electrodes and can be seen in **Figure 4.21**.

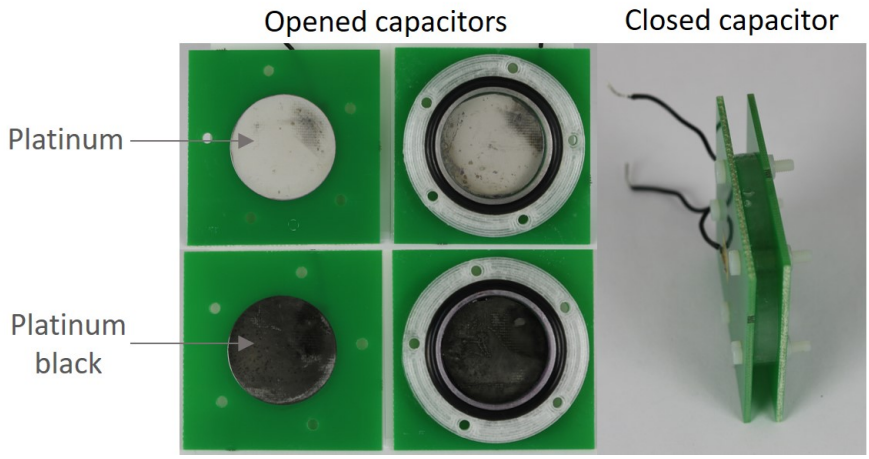

Figure 4.21: Applied capacitors with platinum and platinum black electrodes.

The platinum and platinum black electrodes were manufactured at the Institute of Physical Chemistry and Electrochemistry, Leibniz University Hannover. The black areas on the platinum electrodes are caused by the manufacturing process and do not interfere with the electrical properties of the platinum.

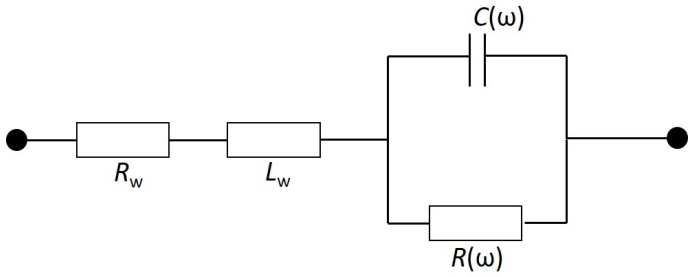

Figure 4.22: Modified lumped element model with consideration of wire impedance.

For the determination of the electrical material parameters of electrolyte solutions, the lumped element model from **Figure 2.26** was considered. This lumped element model was extended with the wire impedance $Z_w = R_w + j\omega L_w$ connected in series as in **Figure 2.24**, which resulted in the lumped element model from **Figure 4.22**. The measured impedance was fitted to the total impedance function of the lumped element model from **Figure 4.22** and the impact of the wire impedance was eliminated. The parameters $R(\omega)$ and $C(\omega)$ were

determined from the adjusted impedance which is equal to Z_{measure} in (2.80) and (2.81). For higher frequencies than the cut-off frequency f_{c}, the following approximations were made: $R(\omega \geq 2\pi f_{\mathrm{c}}) = R_{\mathrm{e}}$ and $C(\omega \geq 2\pi f_{\mathrm{c}}) = C_{\mathrm{e}}$. Then the specific conductivity and the relative permittivity were determined with (2.76) and (2.77).

To validate the procedure, an electrolyte solution with known electrical material parameters had to be chosen. Therefore, soldium chloride (NaCl) in form of salt was mixed with purified water. The electric conductivity of the solution can be approximated with the molar concentration c of NaCl, the Faraday constant F and the total ion mobility v_{tot} [254, 255],

$$\sigma = c v_{\mathrm{tot}} \mathrm{F}. \tag{4.19}$$

The total ion mobility of NaCl is $v_{\mathrm{tot}} = 13.1 \cdot 10^{-8} \mathrm{m^2 V^{-1} s^{-1}}$ [255]. To realize the target concentration c in a specific volume V of purified water, the needed mass of NaCl m_{NaCl} was determined with

$$m_{\mathrm{NaCl}} = c V M_{\mathrm{s}}. \tag{4.20}$$

M_{s} is the molar mass of NaCl, which is the sum of the molar mass of sodium and the molar mass of chloride $M_{\mathrm{s}} = 58.44\,\mathrm{g\,mol^{-1}}$.

Specific conductivity σ in S/m	Molar concentration c in mmol/l
0.02	1.581
0.1	7.91
0.3	23.715
0.5	39.53
0.8	63.24
1	79.1
2	158.1

Table 4.5: Calculated specific conductivity σ for different concentrations c of NaCl solutions using (4.19).

Table 4.5 shows the calculated specific conductivities and the according molar concentrations of the NaCl solutions by using (4.19).

4.4.2 Results and Discussion of Validation Measurements with Isopropyl Alcohol

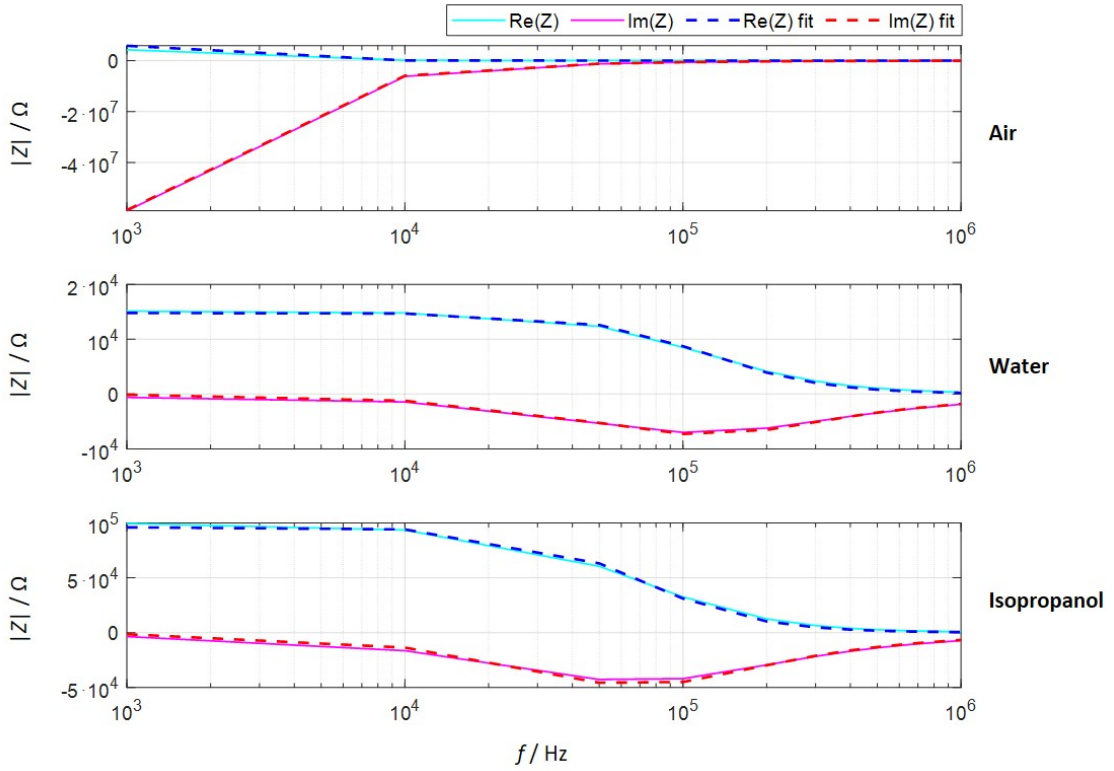

Figure 4.23: Results of the measured and fitted impedance curves for air, water and isopropanol.

Figure 4.23 shows the measured and fitted impedance magnitudes for air, purified water and isopropanol within the capacitor as a function of the frequency f. The blue curves show the magnitude of the real part and the magenta curves show the magnitudes of the imaginary part. Measured values are presented with solid lines and the respective fitted curves are dashed. It can be seen that the results of the measured curves and the results of the

fitted curves match very well over the whole frequency range. This indicates, that the underlying model is chosen appropriately to the capacitor configuration in combination with the chosen fillings.

Parameter	Magnitude and unit	Applied equation/ comment
K	$1.102 \cdot 10^{-12}$ F	(2.78)
C_0	$1.588 \cdot 10^{-12}$ F	(2.79)
C_{tot}	$2.39 \cdot 10^{-11}$ F	Result of fitting
R_{e}	96.145 kΩ	Result of fitting
R_{w}	1.8 mΩ	Result of fitting
L_{w}	$1.36 \cdot 10^{-11}$ H	Result of fitting
ε_{r}	20.25	(2.77)
σ	83.6 μSm^{-1}	Result of fitting

Table 4.6: Overview of obtained parameters in the frame of impedance measurements with isopropanol.

The calculated fitting parameters and the obtained electrical material parameters for the isopropanol can be found in table 4.6. It can be seen that the obtained relative permittivity almost matches the predicted literature value of $\varepsilon_{\mathrm{r}} = 20$. The obtained specific conductivity can be approximated with zero. This is a sufficient approximation for the specific conductivity of isopropanol.

The determination of electrical material parameters of isopropanol was successfully performed with the described procedure. However, isopropyl alcohol has a conductivity close to zero. With the presented results, the method is not validated for electrolyte solutions with relatively high specific conductivities. As explained in section 2.5.2 the underlying method applied for the shown results is not suited for determination of parameters of electrolyte solutions, since it does not consider electrode polarization.

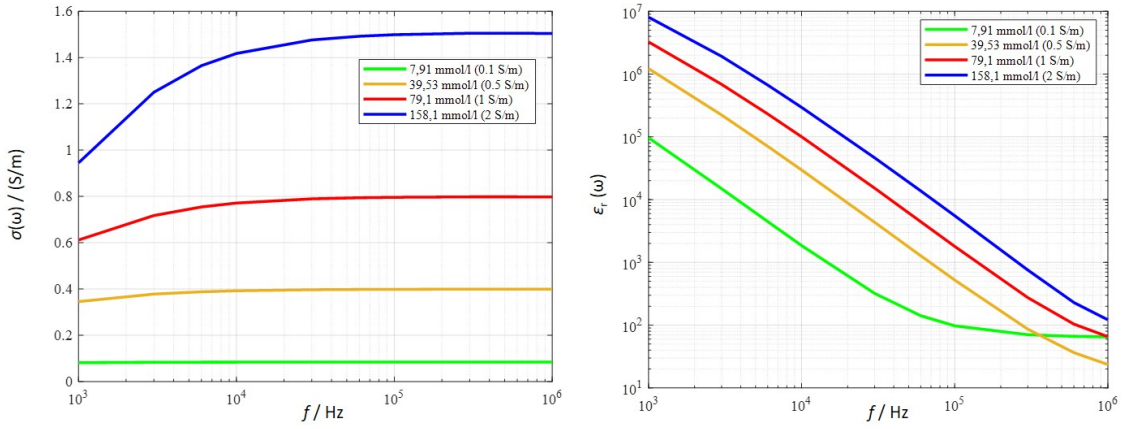

Figure 4.24: Results of the specific conductivity σ and relative permittivity ε_r of NaCl solutions at different concentrations obtained with platinum electrodes.

4.4.3 Results and Discussion of Validation Measurements with Sodium Chloride Solutions

Figure 4.24 on the left frame shows the obtained specific conductivities and the relative permittivities of different NaCl solutions with platinum electrodes. The conductivity values in the legend are calculated values according to table 4.5. Due to curve saturation, it can be seen that for all applied concentrations, the cut-off frequency is below $f = 100\,\mathrm{kHz}$, while the green curve with lowest concentration is already saturated at $f = 1\,\mathrm{kHz}$. Furthermore, the cut-off frequency rises with rising ion concentration. When comparing the obtained specific conductivities after the curves are saturated with the calculated values in the legend, the best match can be found for lowest concentration. The difference becomes higher with higher concentration and its maximum is 0.5 S/m for the highest concentration.
In the same figure on the right frame, the obtained relative permittivities are shown. Saturation of the curve is only reached for the lowest concentration (green curve). The obtained value of relative permittivity is around $\varepsilon_r = 80$, which is the expected value. In general, the cut-off frequencies are higher in the curves of the relative permittivity than in the curves of the specific conductivity. This indicates that the electrode polarization has an higher impact on the measured capacitance than on the measured resistance.

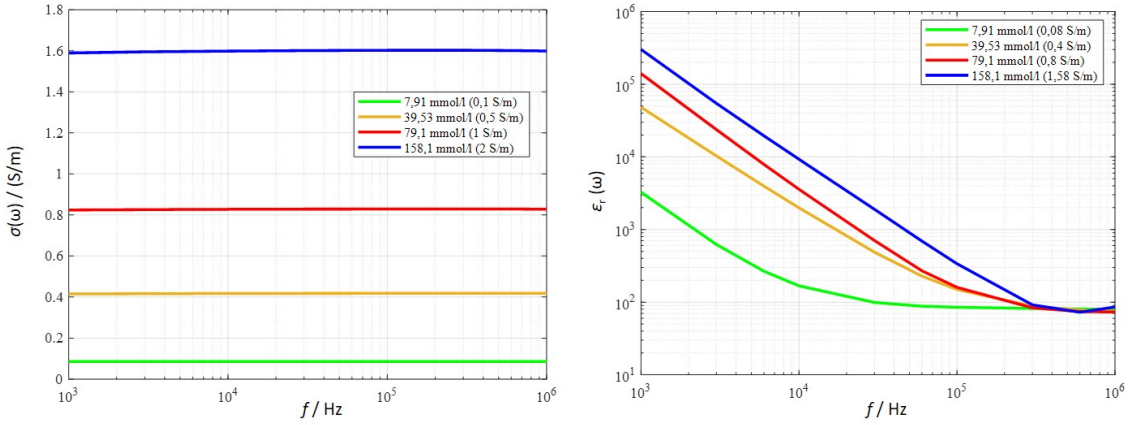

Figure 4.25: Results of the specific conductivity σ and relative permittivity ε_r of NaCl solutions at different concentrations obtained with platinum black electrodes.

Figure 4.25 shows the same parameters as **Figure 4.24** but the results are obtained with platinum black electrodes. The curves of the specific conductivities are all saturated already at $f = 1\,\mathrm{kHz}$. The curves of the relative permittivities reach saturation at frequencies under $f = 1\,\mathrm{MHz}$. The specific conductivity values obtained with platinum black electrodes are (except for the highest concentration) almost the same as the values which can be obtained with platinum electrodes after the curves are saturated. The difference in the obtained specific conductivities for the highest concentration is under 0.1 S/m. The relative permittivity values obtained with platinum black electrodes are around $\varepsilon_\mathrm{r} = 80$ and thus in the order of expected value.

The presented results indicate that the applied approach with platinum electrodes is rather suited for small concentrations of ions. However, for high ion concentrations up to $c = 158.1\,\mathrm{mmol/l}$ the specific conductivity can be approximated at higher frequencies up to $f = 100\,\mathrm{kHz}$. The specific conductivity values obtained with the described method are probably more precise than the values obtained with (4.19). The reason is that (4.19) is an approximating formula where no interactions of the ions in the solution are considered. Furthermore, the results of specific conductivities obtained with platinum electrodes are almost the same as those obtained with platinum black electrodes.
Most significantly, the platinum black electrodes reach the lowest cut-off frequencies. Remarkably, they are suited for the determination of specific conductivities for all applied con-

centrations even at frequencies down to $f = 1\,\mathrm{kHz}$. The determination of relative permittivities is also possible for all ion concentrations but at cut-off frequencies close to $f = 1\,\mathrm{MHz}$.

The approach with the platinum black electrodes was successfully applied for the determination of the specific conductivities of *Dulbecco's Modified Eagle Medium* (DMEM) and also DMEM with 10 % proportion of *Fatal Calf Serum* (FCS) [6], which are often applied cell culture media in the frame of *in vitro* cell experiments. The obtained values have been used for validations of parameters extrapolated from measurements with other methods at higher frequencies in the frame of a scientific reports publication [1]. For cell culture media as DMEM, the relative permittivity can be approximated with $\varepsilon_\mathrm{r} = 80$ since it must be close to the relative permittivity of water [1].

4.5 Electric Field Interaction: Discussion and Conclusion

At the beginning of this chapter in section 4.1 a new concept of a lumped element model of a cell was presented. Together with the presented calculation formulas, this model allows the approximation of lumped element parameters of single- and double shell cell models by application of dimensional and dielectric material parameters only. The developed model can be used to obtain the proportion of electric field and electric current within the different material layers of the cell.

In section 4.2 the electric field distribution in cells and AuNPs was investigated. First a cell with standard dielectric material properties was considered. The electric field distribution within different cell layers was presented. Furthermore, the new concept of lumped element model was used to calculate the electric field and the electric current ratios between the nucleoplasm and the cytoplasm. The results were compared to results obtained from Mie Series calculations and showed very good agreement. Subsequently the material parameters of the considered cell were changed to limit values extracted from literature. It was shown that the specific conductivity of the cytoplasm had the most dominant effect on the overall electric field proportion entering the cell and that the specific conductivity of the nucleoplasm significantly determines the proportion entering the nucleus. Parameters of the nucleus have no significant impact on the maximum electric field magnitude within the considered cell. Furthermore, the determined maximum electric field magnitude entering a cell is approximately $90\,\mathrm{dB}$ smaller than the external electric field, which corresponds to a linear factor in the range of 10^{-5}. However, the electric field magnitude immediately surrounding the cell is enhanced by a maximum of $10\,\mathrm{dB}$. Considering the relatively small electric field magnitude which is excited during the magnetic field excitation in cellular reprogramming, and the small proportion of electric field entering a cell, it appears unlikely that electric field interactions with cells are triggered during cellular reprogramming. Furthermore, it was shown that similarly to cells, AuNPs act as electric dipoles. Interestingly, the electric field outside an AuNP is in the same order of magnitude as the electric field outside a cell (maximum of $10\,\mathrm{dB}$).

In section 4.3, the state of the art electrode setup for *in vitro* cell culture experiments with electric fields (TTFields) was considered. It was shown that the field homogeneity, the cell cultivation area and the possible settings for electric field directions can be significantly

enhanced. To realize that, first the size of electrodes was decreased such that the amount of electrodes could be increased from four to eight electrodes. Such a relatively small change already leads to enhancement of electric field homogeneity and the possibility to excite more directions of electric field polarization. By adjusting the electric potentials at the electrodes, the field homogeneity further improves. The best result can be achieved for an adjustment of the electrode potentials, while using as many electrodes as possible. This was shown for a configuration of sixteen electrodes, which allow the excitation of electric field in eight polarization directions.

In section 4.4 the implementation of a capacitive measurement method for the determination of specific electric conductivity and electric permittivity of ion-solutions was presented. The setup was evaluated for three different electrode materials: copper, platinum and platinum black. It was shown that platinum black electrodes are best suited the determination of dielectric material parameters. With the applied method, the electric conductivity could be determined already at frequencies down to $f = 1\,\mathrm{kHz}$.

5 Conclusion and Outline

This work contributes to the understanding of electromagnetic field interaction with biological cells and gold nanoparticles in the frame of cellular reprogramming and TTFields application.
Prior to the investigations a thorough literature review is conducted. Aspects which are important for the understanding of cellular reprogramming and TTFields, and for the understanding of the electromagnetic modelling of cells are explained. In particular, a deep literature review allows the narrowing of extremely low frequency electromagnetic fields (ELF-EMFs) and pulsed electromagnetic fields (PEMFs) to the excitation methods of interest during cellular reprogramming. On the other hand, the literature review results in a well defined cell model in form of a double-shell spherical cell with specified electromagnetic material parameters.

When ELF-EMFs and PEMFs are applied, the magnetic field component is within the focus. ELF-EMFs have sinusoidal magnetic field components with a magnetic flux density around $1\,\mathrm{mT}$ at a frequency around $50\,\mathrm{Hz}$. PEMFs can have many different time propagations. Different PEMF excitations are categorized due to their repetition frequencies and durations of bursts. On the basis of this analysis, a representative PEMF excitation containing a repetition frequency of $50\,\mathrm{Hz}$ is chosen which is further examined with Fourier analysis.
The Fourier analysis reveals that the relevant spectral components of the PEMF excitation appear at $4\,\mathrm{kHz}$ and integer multiples. This result leads to the proposal to concentrate on these frequencies rather than on the repetition frequency of the excitation. Furthermore, for the following investigations, $50\,\mathrm{Hz}$ and $4\,\mathrm{kHz}$ are the considered frequencies for cellular reprogramming, due to their relevance in ELF-EMF excitation and in PEMF excitation respectively. In the frame of the investigations of mechanisms of action only sinusoidal electromagnetic fields are considered.
With the knowledge of the relevant frequencies, the magnetic field distribution within a cell model and different AuNP models are investigated. It is shown that the cell is almost invisible for the magnetic field. Considering AuNPs, first single, spherical particles with bulk

gold material properties are investigated. It is shown that their magnetic response can be approximated with application of the static magnetic polarizability. Furthermore, the dynamic response becomes relevant for $f \geq 100\,\mathrm{MHz}$. However, on the basis of the obtained results it is reasonable to conclude that the magnetic field contribution of an AuNP with bulk gold material parameters is probably too small to cause significant energy alterations leading to biological responses. However, different magnetic susceptibilities can be the outcome of surface modifications on the particles, which is also considered in the investigations by applying a wide range of possible magnetic susceptibility values $-0.9 \leq \chi_\mathrm{p} \leq 10^5$ for the particles. In this regard the interaction of two identical spherical particles is investigated as well as the magnetization of prolate and oblate ellipsoids. The results show that the maximum magnetization can be reached for prolate para-/ferromagnetic ellipsoids and oblate diamagnetic ellipsoids. Emanating from an example taken from literature, the interaction of spherical particles in an array is investigated. It is shown that the determining coupling factor is the magnitude of the magnetic susceptibility. Finally and exemplary, the magnetic field and the magnetic field gradient above arrays of diamagnetic nanoparticles is investigated. The results show that an extreme diamagnetic susceptibility of $\chi_\mathrm{p} = -0.9$ would achieve a magnetic field enhancement in the range of the incident magnetic field. When considering (surface-modified) AuNPs, the investigations provide an orientation for the significance of possible magnetic field alterations. The findings contribute to a better understanding of the limits, characteristics, and impact of AuNPs on magnetic field response, with potential applications in biomedical research and treatment, even beyond cellular reprogramming.
For the validation of the investigations of mechanisms of action with *in vitro* cell experiments, a laboratory setup with Helmholtz coils is implemented. This setup allows the excitation of an homogeneous magnetic field at a frequency of $50\,\mathrm{Hz}$ within the location of cells. It provides an example of possible first experimental arrangement which can be used at the Institute of Quantum Optics.

Regarding electric field interaction with biological cells, a new electrical lumped element model for the chosen spherical cell model is derived from theoretical considerations. This model allows the calculation of its lumped element parameters (resistivities and capacitances) with analytical formulas including dielectric material properties and dimensional properties only. The model itself provides a visualization of the electric behavior of the cell

at first glance. The derived formulas for the determination of lumped element parameters allow approximations of the electric field and current density distributions within the different layers relative to each other.
Furthermore, the electric field distribution in cells and AuNPs is investigated. A range of different possible electric material parameters of cell layers is considered in the investigations. The determined maximum electric field magnitude entering a cell is approximately $90\,\mathrm{dB}$ smaller than the external electric field, which corresponds to a linear factor in the range of 10^{-5}. However, the electric field magnitude immediately surrounding the cell is enhanced by a maximum of $10\,\mathrm{dB}$. Furthermore, it is shown that similarly to cells, AuNPs act as electric dipoles. Interestingly, the electric field outside an AuNP is in the same order of magnitude as the electric field outside a cell (maximum of $10\,\mathrm{dB}$). It is shown that the new concept of lumped element model of a cell can be applied to obtain the results for a cell.
Subsequently, the state of the art electrode setup for *in vitro* cell culture experiments with electric fields (TTFields) is considered. It is shown that by adjusting the electric potentials at the electrodes, while using sixteen electrodes, the cell cultivation area can be significantly increased, the electric field within the cultivation area becomes more homogeneous and the possible of electric field polarization directions can be quadrupled.
Finally, different experimental approaches are introduced. The implementation of a capacitive measurement method with platinum black electrodes allows the determination of the specific electric conductivity of ion solutions at very low frequencies in the range of $1\,\mathrm{kHz}$. The implemented method is tested for adequacy by measurements of conductivities of sodium chloride solutions with known conductivities. Thereby, the suitability of the implementation is shown. This implementation was used for the determination of the specific conductivities of Dulbecco's Modified Eagle Medium (DMEM) and DMEM containing Fatal Calf Serum, which are used as growing media in the frame of *in vitro* cell experiments. The determination of the specific conductivity allows the consideration of the respective materials in electromagnetic field calculations for further studies.

This work provides a starting point for investigations of mechanisms of action. It reduces the complexity of the real biological cell with the applied cell model and concentrates on sinusoidal electromagnetic field components of representative electromagnetic excitation methods in the frame of cellular reprogramming and TTFields application. In further studies,

different shapes of cells can be considered and the effect of their geometry on the electromagnetic field distribution can be investigated. Non-symmetric cell shapes might lead to enhancement of field inhomogeneities or electromagnetic fields might be enhanced in certain areas, as has already been shown for cells undergoing cytokinesis. When considering non-symmetrical shapes, the polarization direction of the electromagnetic field becomes important.

Impacts of gold nanoparticles on the electromagnetic field distribution within cells can be further tested. However, it has to be remembered that the theory is only valid within the boundaries of the applied model. The proof needs to be sought in reality by the observation of biological responses. In this regard, laboratory setup designs need to keep up with the demands of scientific studies and must be adjusted.

6 Annex

6.1 Supporting table

Category	Ref., Year	Differentiated cells	Excitation
Neurogenesis	[65], 1998	Chromaffin cells	ELF-EMF
	[52], 2004	Human neuroblastoma and rat pituitary GH3 cells	ELF-EMF
	[59], 2008	Neural stem cells (NSCs)	ELF-EMF
	[60], 2010	*In vivo* neurogenesis in mice	ELF-EMF
	[61], 2012	Human bone marrow-mesenchymal stem cells (hBM-MSCs)	ELF-EMF
	[64], 2013	Rat bone mesenchymal stromal cells	ELF-EMF
	[39], 2014	hBM–MSCs and mouse NSCs	ELF-EMF
	[70], 2016	Human dental pulp stem cells	PEMF
	[63], 2017	hBM–MSCs	ELF-EMF
	[71], 2017	hBM-MSCs and *in vivo* hBM-MSCs in mice	PEMF
	[62], 2019	Human neural progenitor cells	ELF-EMF
Osteogenesis	[73], 2008	hMSC	PEMF
	[72], 2009	hBM-MSC	PEMF
	[66], 2009	hBM-MSC	PEMF
	[57], 2009	Rat BM-MSC	ELF-EMF
	[67], 2013	BM-MSC, adipose tissue MSC	PEMF
	[58], 2013	Human adipose-derived SCs	ELF-EMF
	[68], 2014	hBM-MSC, adipose tissue MSC	PEMF
	[56], 2018	Rat BM-MSC	ELF-EMF
	[69], 2019	Osteoblast precursor cells	PEMF
Chondrogenesis	[74], 1987	Chondrocytes	PEMF
	[55], 2010	hMSC	ELF-EMF
	[75], 2017	MSC	PEMF
	[54], 2018	hMSC	ELF-EMF
	[56], 2018	Rat BM-MSC	ELF-EMF
Myogenesis	[76], 2019	Myoblasts	PEMF
Keratinizatio	[53], 2006	Human keratinocytes	ELF-EMF

Table 6.1: Representative studies in the field of cell differentiation with application of ELF-EMF or PEMF.

6.2 List of Tables

6.3 List of Figures

6.4 List of Abbreviations

AC	Alternating current
AuNP	Gold Nanoparticle
BEC	Biphasic electric current
DC	Direct current
DEP	Dielectrophoretic
DMEM	Dulbecco's Modified Eagle Medium
DNA	Deoxyribonucleic acid
ELF-EMF	Extremely low frequency EMF
EM	Electromagnetic
EMF	Electromagnetic Field
FCS	Fatal Calf Serum
FDTD	Finite difference time domain
hESC	Human embryonic stem cell
HIPEMS	High-intensity pulsed electromagnetic stimulation
iPSC	Induced pluripotent stem cell
mRNA	Messenger ribonucleic acid
MUT	Medium under test
NP	Nanoparticle
nsPEF	Nanosecond pulsed electric field
PC	Personal computer
PEG	Polyethylene glycol
PEMF	Pulsed EMF
PENG	Piezoelectric nanogenerator
PLA	Polylactic acid
TEM	Transversal electromagnetic
TMZ	Temozolomide
SPION	Superparamagnetic iron oxcide nanoparticle
TENG	Triboelectric nanogenerator
RMS	Root mean square
USB	Universal Serial Bus

6.5 List of Constants and Parameters

Constants with magnitude and unit

$\mathbf{e}_\mathrm{r}$	Unity vector in *r*-direction	1
$\mathbf{e}_\mathrm{x}$	Unity vector in *x*-direction	1
$\mathbf{e}_\mathrm{y}$	Unity vector in *y*-direction	1
$\mathbf{e}_\mathrm{z}$	Unity vector in *z*-direction	1
e	Euler number	2.718 28
$\mathrm{e_{charge}}$	Elementary charge	$1.602176634 \times 10^{-19}\,\mathrm{C}$
F	Faraday constant	$96485.33212\,\mathrm{C\,mol^{-1}}$
j	Imaginary unit	$\sqrt{-1}$
R	Gas constant	$8.314462618\,\mathrm{J\,mol^{-1}\,K^{-1}}$
z	Ion valence	± 1
μ_0	Vacuum permeability	$1.25663706212 \times 10^{-6}\,\mathrm{H\,m^{-1}}$
σ_Au	Specific conductivity of gold	$41\,\mathrm{MS\,m^{-1}}$
ε_0	Vacuum permittivity	$8.8541878128 \times 10^{-12}\,\mathrm{F\,m^{-1}}$
ξ	Constant for symmetric bilayers	1/18

Parameters and unit

α	Angle	°

α_e	Magnetic polarizability due to conductive and displacement currents	m^3
α_m	Magnetic polarizability due to magnetization	m^3
β	Angle	$^\circ$
χ	Magnetic susceptibility	1
$\chi_\perp$	Magnetic susceptibility normal to magnetic field	1
χ_p	Magnetic susceptibility of a particle	1
$\chi_\parallel$	Magnetic susceptibility parallel to magnetic field	1
ΔT	Increase in temperature	K
Δt	Time step	s
Δx	Discretization step in x-direction	m
Δy	Discretization step in y-direction	m
Δz	Discretization step in z-direction	m
$\Delta\chi$	Difference in magnetic susceptibility	1
$\mathbf{A}$	Area vector	m^2
$\mathbf{B}$	Magnetic flux density vector	T
$\mathbf{B}_\mathrm{inc}$	Incident magnetic flux density vector	T
$\mathbf{B}_\mathrm{mag}$	Magnetic flux density vector due to magnetization	T
$\mathbf{B}_\mathrm{tot}$	Total magnetic flux density vector	T
$\mathbf{C}$	Constant vector	1

$\mathbf{E}$	Electric field vector	$\mathrm{V\,m^{-1}}$
$\mathbf{E}_{\mathrm{cp}}$	Electric field vector within cytoplasm	$\mathrm{V\,m^{-1}}$
$\mathbf{E}_{\mathrm{inc}}$	Electric field vector of incident EMF	$\mathrm{V\,m^{-1}}$
$\mathbf{E}_{\mathrm{ind}}$	Induced electric field vector	$\mathrm{V\,m^{-1}}$
$\mathbf{E}_{\mathrm{np}}$	Electric field vector within nucleoplasm	$\mathrm{V\,m^{-1}}$
$\mathbf{E}_{\mathrm{pen}}$	Electric field vector of transmitted EMF	$\mathrm{V\,m^{-1}}$
$\mathbf{E}_{\mathrm{scat}}$	Electric field vector of scattered EMF	$\mathrm{V\,m^{-1}}$
$\mathbf{E}_{\mathrm{target}}$	Target electric field vector	$\mathrm{V\,m^{-1}}$
$\mathbf{E}_{\mathrm{tot}}$	Total electric field vector	$\mathrm{V\,m^{-1}}$
$\mathbf{F}_{\mathrm{mag}}$	Magnetophoretic force	N
$\mathbf{H}$	Magnetic field vector	$\mathrm{A\,m^{-1}}$
$\mathbf{H}_{\mathrm{inc}}$	Magnetic field vector of incident EMF	$\mathrm{A\,m^{-1}}$
$\mathbf{H}_{\mathrm{k}}$	Magnetic field vector of k-th particle	$\mathrm{A\,m^{-1}}$
$\mathbf{H}_{\mathrm{pen}}$	Magnetic field vector of transmitted EMF	$\mathrm{A\,m^{-1}}$
$\mathbf{H}_{\mathrm{scat}}$	Magnetic field vector of scattered EMF	$\mathrm{A\,m^{-1}}$
$\mathbf{H}_{\mathrm{tot}}$	Total magnetic field vector	$\mathrm{A\,m^{-1}}$
$\mathbf{J}$	Current density vector	$\mathrm{A\,m^{-2}}$
$\mathbf{J}_{\mathrm{ind}}$	Induced current density vector	$\mathrm{A\,m^{-2}}$
$\mathbf{k}_{\mathrm{inc}}$	Propagation constant vector of incident EMF	$\mathrm{m^{-1}}$

$\mathbf{k}_{\mathrm{pen}}$	Propagation constant vector of transmitted EMF	m^{-1}
$\mathbf{k}_{\mathrm{scat}}$	Propagation constant vector of scattered EMF	m^{-1}
$\mathbf{m}_{\mathrm{n}}$	Magnetic dipole moment vector of n-th particle	Am^2
$\mathbf{M}$	Magnetization vector	$\mathrm{N\,m}$
$\mathbf{M}$	Vector function	1
$\mathbf{m}$	Magnetic dipole moment vector	Am^2
$\mathbf{M}_{\mathrm{mag}}$	Magnetic torque force	$\mathrm{N\,m}$
$\mathbf{N}$	Vector function	1
$\mathbf{p}$	Magnetic dipole moment of an ion	Am^2
$\mathbf{R}'$	Position vector in spherical coordinates to region carrying charge	m
$\mathbf{R}$	Position vector in spherical coordinates	m
$\mathbf{r}$	Position vector	m
$\mathbf{r}_{\mathrm{k}}$	Position vector of k-th particle	m
$\mathbf{r}_{\mathrm{n}}$	Position vector of n-th particle	m
$\mathbf{S}$	Poynting vector	$\mathrm{W\,m}^{-2}$
$\mathbf{s}$	Line vector	m^2
$\mathbf{V}$	Vector function	1
μ	Total magnetic permeability	$\mathrm{H\,m}^{-1}$
μ_{r}	Relative magnetic permeability	$\mathrm{H\,m}^{-1}$

μ_S	Total magnetic permeability of a sphere	$\mathrm{H\,m^{-1}}$
ω	Angular frequency	Hz
$\Phi(\varphi)$	Separation function	1
ψ	Scalar function	1
ρ	Volumetric mass density	1
σ	Specific conductivity	$\mathrm{S\,m^{-1}}$
σ_0	Specific conductivity of zero	$\mathrm{S\,m^{-1}}$
σ_2	Specific conductivity in medium 2	$\mathrm{S\,m^{-1}}$
σ_{cp}	Specific conductivity of cytoplasm	$\mathrm{S\,m^{-1}}$
σ_{mt}	Specific conductivity of microtubule	$\mathrm{S\,m^{-1}}$
σ_{ne}	Specific conductivity of nuclear envelope	$\mathrm{S\,m^{-1}}$
σ_{np}	Specific conductivity of nucleoplasm	$\mathrm{S\,m^{-1}}$
σ_{pm}	Specific conductivity of plasma membrane	$\mathrm{S\,m^{-1}}$
σ_p	Specific conductivity of a particle	$\mathrm{S\,m^{-1}}$
$\Theta(\vartheta)$	Separation function	1
ε''	Imaginary part of complex total permittivity	$\mathrm{F\,m^{-1}}$
ε'	Real part of complex total permittivity	$\mathrm{F\,m^{-1}}$
ε	Total permittivity	$\mathrm{F\,m^{-1}}$
ε_1	Total permittivity in medium 1	$\mathrm{F\,m^{-1}}$

ε_2	Total permittivity in medium 2	$\mathrm{F\,m^{-1}}$
$\varepsilon_{\mathrm{ne}}$	Total permittivity of nuclear envelope	$\mathrm{F\,m^{-1}}$
$\varepsilon_{\mathrm{r,S}}$	Relative permittivity of a sphere	1
ε_{r}	Relative permittivity	1
ε_{S}	Total permittivity of a sphere	$\mathrm{F\,m^{-1}}$
$\varepsilon_{\mathrm{cp}}$	Total permittivity of cytoplasm	$\mathrm{F\,m^{-1}}$
$\varepsilon_{\mathrm{mp}}$	Total permittivity of microtubule	$\mathrm{F\,m^{-1}}$
$\varepsilon_{\mathrm{np}}$	Total permittivity of the nucleoplasm	$\mathrm{F\,m^{-1}}$
$\varepsilon_{\mathrm{r,cp}}$	Relative permittivity of the cytoplasm	1
$\varepsilon_{\mathrm{r,ne}}$	Relative permittivity of the nuclear envelope	1
$\varepsilon_{\mathrm{r,np}}$	Relative permittivity of the nucleoplasm	1
$\varepsilon_{\mathrm{r,pm}}$	Relative permittivity of the plasma membrane	1
$\varepsilon_{\mathrm{r,p}}$	Relative permittivity of a particle	1
$\varepsilon_{\mathrm{r,1}}$	Relative permittivity of medium 1	1
φ	Electric potential	V
φ_1	Electric potential	V
ξ	Cosine function of polar angle	1
$A(\vartheta,\varphi)$	Separation function	1
A	Area	$\mathrm{m^2}$

a	Length of one semi-axis of deformed liposome	m
a	Natural number	1
A_{cp}	Cross-sectional area of cytoplasm	m^2
A_{np}	Cross-sectional area of nucleoplasm	m^2
B	Magnetic flux density magnitude	T
B_0	Magnetic flux density magnitude of incident wave	T
$B_{//}$	Magnetic flux density magnitude parallel to magnetic moment	T
B_{ac}	Magnetic flux density magnitude accuracy	T
B_{th}	Magnetic flux density magnitude threshold	T
$C(\omega)$	Frequency-dependent capacitance	F
C	Capacitance	F
c	Length of one semi-axis of deformed liposome	m
c	Molar concentration	mol
C_0	Stray capacitance	F
C_1	Constant	1
C_2	Constant	1
c_{T}	Specific heat capacity	$\mathrm{J\,kg^{-1}\,K^{-1}}$
c_p	Expansion coefficient	1
C_{cp}	Capacitance of cytoplasm	F

C_{e}	Capacitance of ideal capacitor	F
C_{m}	Capacitance of plasma membrane	F
C_{ne}	Capacitance of nuclear envelope	F
$C_{\mathrm{PatchClamp}}$	Capacitance measured with patch clamp technique	F
C_{pm}	Capacitance of plasma membrane	F
C_{p}	Capacitance due to electrode polarization	F
$C_{\mathrm{tot},1}$	Total capacitance with material 1	F
$C_{\mathrm{tot},2}$	Total capacitance with material 2	F
C_{tot}	Total capacitance	F
d	Distance	m
d_1	Distance	m
d_2	Distance	m
d_p	Expansion coefficient	1
d_{Cell}	Diameter of a cell	m
E	Magnitude of electric field	$\mathrm{V\,m^{-1}}$
E_0	Electric field magnitude of incident wave	$\mathrm{V\,m^{-1}}$
$E_{\mathrm{r,inc}}$	Magnitude of electric field vector of scattered EMF in r-direction	$\mathrm{V\,m^{-1}}$
$E_{\mathrm{r,pen}}$	Magnitude of electric field vector of scattered EMF in r-direction	$\mathrm{V\,m^{-1}}$
$E_{\mathrm{r,scat}}$	Magnitude of electric field vector of scattered EMF in r-direction	$\mathrm{V\,m^{-1}}$

E_{th}	Magnitude of threshold electric field	$\mathrm{V\,m^{-1}}$
f	Frequency	Hz
F_1	Spectral amplitudes of function 1	1
f_1	Time-dependent function	1
F_2	Spectral amplitudes of function 2	1
f_2	Time-dependent function	1
$f_{0,1}$	Constant	1
$f_{0,2}$	Constant	1
f_{burst}	Burst repetition frequency	Hz
$f_{\mathrm{c}k,1}$	Coefficient function	1
$f_{\mathrm{c}n,2}$	Coefficient function	1
f_{c}	Cut-off frequency	Hz
F_{DEP}	Dielectrophoretic force	N
f_{PEMF}	Time-dependent PEMF function	1
f_{rep}	Repetition frequency	Hz
$f_{\mathrm{s}k,1}$	Coefficient function	1
$f_{\mathrm{s}n,2}$	Coefficient function	1
H_0	Magnetic field magnitude of incident wave	$\mathrm{A\,m^{-1}}$
$h_p^{(1)}$	Spherical Hankel function	1

$h_p^{(2)}$	Spherical Hankel function	1
H_{norm}	Normalized Magnetic field magnitude	1
I	Current	A
I_{cf}	Current in cleavage furrow	A
I_{cp}	Current within cytoplasm	A
I_{e}	Current in extracellular medium	A
I_{LE}	Current obtained with lumped element model	A
I_{Mie}	Current obtained with Mie Scattering calculations	A
I_{np}	Current within nucleoplasm	A
I_{tot}	Total current within a cell	A
I_{t}	Total current	A
j_p	Bessel function	1
$J_{p+\frac{1}{2}}$	Ordinary Bessel function	1
K	Capacitor constant	F
K	Scalar coefficient	1
k	Natural number	1
k	Wave number	m^{-1}
k_0	Wave number in vacuum	m^{-1}
k_{C}	Average elasticity modulus	J

L	Scalar coefficient	1
l_x	Length of semi-axis in x-direction	m
l_y	Length of semi-axis in y-direction	m
l_z	Length of semi-axis in z-direction	m
l_{mt}	Length of microtubule	m
L_{w}	Inductance of a wire	H
m_{NaCl}	Mass of NaCl	kg
M_{S}	Molar mass	$\mathrm{g\,mol^{-1}}$
M_{S}	Saturation magnetization	$\mathrm{A\,m^{-1}}$
N	Natural number	1
n	Natural number	1
n_{i}	Ion concentration inside a cell	$\mathrm{mol\,L^{-1}}$
n_{o}	Ion concentration outside a cell	$\mathrm{mol\,L^{-1}}$
n_{inc}	Wave impedance in the medium of incident wave	Ω
n_{pen}	Wave impedance in the medium of transmitted wave	Ω
o_p	Expansion coefficient	1
p	Degree of spherical harmonics	1
p	Ratio l_z/l_y	1
P_p^a	Legendre functions of first kind	1

P_{d}	Dissipative power	W
P_{r}	Reactive power	W
q_p	Expansion coefficient	1
$R(\omega)$	Frequency-dependent resistivity	Ω
$R(r)$	Separation function	1
R	Resistivity	Ω
r_0	Radius of liposome	m
r_{cell}	Radius of cell	m
R_{cf}	Resistivity of cleavage furrow	Ω
r_{Coil}	Radius of Helmholtz coils	m
R_{cp}	Resistivity of cytoplasm	Ω
r_{cp}	Radius of cytoplasm	m
R_{e}	Resistivity of extracellular medium or capacitor configuration	Ω
R_{i}	Resistivity of cell interior	Ω
r_{mt}	Radius of microtubule	m
R_{m}	Resistivity of plasma membrane	Ω
R_{ne}	Resistivity of nuclear envelope	Ω
r_{NP}	Radius of nanoparticle	m
r_{np}	Radius of nucleoplasm	m

$R_{\mathrm{PatchClamp}}$	Resistivity measured with patch clamp technique	Ω
R_{pm}	Resistivity of plasma membrane	Ω
R_{p}	Radius of a particle	m
R_{p}	Resistivity due to electrode polarization	Ω
R_{w}	Resistivity of a wire	Ω
SAR	Specific absorption rate	$\mathrm{W\,kg^{-1}}$
T	Temperature	K
t	time	s
T_1	Period time of function one	s
T_2	Period time of function two	s
t_{burst}	On-time of burst	s
t_{LF}	Pulse width	s
t_{ne}	Thickness of nuclear envelope	m
t_{pm}	Thickness of plasma membrane	m
U	Voltage	V
U_{out}	Output voltage	V
$V(\xi)$	Separation function	1
V	Volume	$\mathrm{m^3}$
v	Phase velocity	$\mathrm{m\,s^{-1}}$

V_e	Excitation voltage	V
V_m	Transmembrane voltage	V
v_tot	Total ion mobility	$\mathrm{m^2\,V^{-1}\,s^{-1}}$
$W(r)$	Separation function	1
y_p	Bessel function	1
$Y_{p+\frac{1}{2}}$	Ordinary Bessel function	1
z_p	Bessel function or Spherical Hankel function	1
Z_cap	Impedance of capacitor configuration	Ω
Z_cp	Impedance of cytoplasm	Ω
Z_measure	Measured impedance	Ω
Z_np	Impedance of nucleoplasm	Ω
Z_n	Total impedance of nucleus	Ω
M'	Magnitude of magnetization normalized to incident magnetic field	$\mathrm{Nm^2/A}$
M_i	Magnitude of magnetization in i-direction	$\mathrm{N\,m}$
N_i	Demagnetization factor in i-direction	1

7 Bibliography

[1] Lukas Berkelmann, Almke Bader, Saba Meshksar, Anne Dierks, Gökce Hatipoglu Majernik, Joachim K. Krauss, Kerstin Schwabe, Dirk Manteuffel, and Anaclet Ngezahayo. Tumour-treating fields (TTFields): Investigations on the mechanism of action by electromagnetic exposure of cells in telophase/cytokinesis. *Scientific Reports*, 9(1), may 2019. doi: 10.1038/s41598-019-43621-9.

[2] Saba Harke and Dirk Manteuffel. Lumped element model of spherical cells exposed to an external electric field. *IEEE Journal of Electromagnetics, RF and Microwaves in Medicine and Biology*, 5(4):355–361, dec 2021. doi: 10.1109/jerm.2021.3067596.

[3] Saba Meshksar, Lukas Berkelmann, and Dirk Manteuffel. Evaluation of bannisters subsurface-to-air model for implanted antennas. In *IEEE International Symposium on Antennas and Propagation and USNC-URSI Radio Science Meeting 2019*, 2019.

[4] Lukas Berkelmann, Almke Bader, Saba Meshksar, Anaclet Ngezahayo, and Dirk Manteuffel. In-vitro exposure system for tumor treating fields. In *IEEE International Engineering in Medicine and Biology Conference*, 2019.

[5] Saba Harke, Lukas Berkelmann, Anaclet Ngezahayo, and Dirk Manteuffel. In-vitro exposure setup for tumor treating fields. In *IEEE International Engineering in Medicine and Biology Conference*, 2020.

[6] Jan Hendrik Jäschke. Ermittlung und validierung messtechnischer möglichkeiten zur bestimmung dielektrischer materialparameter von flüssigkeiten im frequenzbereich von 100 khz bis 500 khz, 2019.

[7] Roya Trabelsi. Investigation of possible interaction mechanisms between electromagnetic fields and tumor cells in the frame of tumor treating fields, 2020.

[8] Saba Harke, Atefeh Habibpourmoghadam, Andrey B. Evlyukhin, Antonio Calà Lesina, and Boris N. Chichkov. Low-frequency magnetic response of gold nanoparticles. *Scientific Reports*, 2023.

[9] Saba Harke, Boris Chichkov, and Annette Hoffmeister. Theoretical analysis of classical pulsed electromagnetic field excitation in the frame of cell differentiation. In *BioEM International Conference on Bioelectromagnetics*, 2022.

[10] Richard H.W. Funk, Thomas Monsees, and Nurdan Özkucur. Electromagnetic effects – from cell biology to medicine. *Progress in Histochemistry and Cytochemistry*, 43(4): 177–264, feb 2009. doi: 10.1016/j.proghi.2008.07.001.

[11] Cristina Eguizabal, Nuria Montserrat, Anna Veiga, and Juan Belmonte. Dedifferentiation, transdifferentiation, and reprogramming: Future directions in regenerative medicine. *Seminars in Reproductive Medicine*, 31(01):082–094, jan 2013. doi: 10.1055/s-0032-1331802.

[12] Jodie H.K. Man, Lucianne Groenink, and Massimiliano Caiazzo. Cell reprogramming approaches in gene- and cell-based therapies for parkinson's disease. *Journal of Controlled Release*, 286:114–124, sep 2018. doi: 10.1016/j.jconrel.2018.07.017.

[13] Junsang Yoo, Euiyeon Lee, Hee Young Kim, Dong ho Youn, Junghyun Jung, Hongwon Kim, Yujung Chang, Wonwoong Lee, Jaein Shin, Soonbong Baek, Wonhee Jang, Won Jun, Soochan Kim, Jongki Hong, Hi-Joon Park, Christopher J. Lengner, Sang Hyun Moh, Youngeun Kwon, and Jongpil Kim. Electromagnetized gold nanoparticles mediate direct lineage reprogramming into induced dopamine neurons in vivo for parkinson's disease therapy. *nature nanotechnology*, 12:1006–1014, 2017. ISSN 1748-3387. doi: 10.1038/nnano.2017.133.

[14] Samantha Payne. Signals blog, it's electrifying! cell reprogramming using electromagnetic fields (blog article). URL `https://www.signalsblog.ca/its-electrifying-cell-reprogramming-using-electromagnetic-fields`.

[15] Yujung Chang, Byounggook Cho, Euiyeon Lee, Junyeop Kim, Junsang Yoo, Jung-Suk Sung, Youngeun Kwon, and Jongpil Kim. Electromagnetized gold nanoparticles improve neurogenesis and cognition in the aged brain. *Biomaterials*, 278:121157, nov 2021. doi: 10.1016/j.biomaterials.2021.121157.

[16] Yujung Chang, Junsang Yoo, Junyeop Kim, Yerim Hwang, Gayong Shim, Yu-Kyoung Oh, and Jongpil Kim. Electromagnetized graphene facilitates direct lineage reprogram-

ming into dopaminergic neurons. *Advanced Functional Materials*, 31(46):2105346, aug 2021. doi: 10.1002/adfm.202105346.

[17] Min-Ok Kim, Hyun Jung, Soo-Chan Kim, Jung-Keug Park, and Young-Kwon Seo. Electromagnetic fields and nanomagnetic particles increase the osteogenic differentiation of human bone marrow-derived mesenchymal stem cells. *International Journal of Molecular Medicine*, 35(1):153–160, oct 2014. doi: 10.3892/ijmm.2014.1978.

[18] Yun-Kyong Choi, Dong Heon Lee, Young-Kwon Seo, Hyun Jung, Jung-Keug Park, and Hyunjin Cho. Stimulation of neural differentiation in human bone marrow mesenchymal stem cells by extremely low-frequency electromagnetic fields incorporated with MNPs. *Applied Biochemistry and Biotechnology*, 174(4):1233–1245, aug 2014. doi: 10.1007/s12010-014-1091-z.

[19] Marie-Christine Daniel and Didier Astruc. Gold nanoparticles: assembly, supramolecular chemistry, quantum-size-related properties, and applications toward biology, catalysis, and nanotechnology. *Chemical Reviews*, 104(1):293–346, dec 2003. doi: 10.1021/cr030698+.

[20] Rua J. Kadhim, Esraa H. Karsh, Zainab J. Taqi, and Majid S. Jabir. Biocompatibility of gold nanoparticles: In-vitro and in-vivo study. *Materials Today: Proceedings*, 42: 3041–3045, 2021. doi: 10.1016/j.matpr.2020.12.826.

[21] Laura Benson. Tumor treating fields technology: Alternating electric field therapy for the treatment of solid tumors. *Seminars in Oncology Nursing*, 34(2):137–150, may 2018. doi: 10.1016/j.soncn.2018.03.005.

[22] Wolfgang Wick. TTFields: where does all the skepticism come from? *Neuro-Oncology*, 18(3):303–305, feb 2016. doi: 10.1093/neuonc/now012.

[23] Narasimha Kumar Karanam and Michael D. Story. An overview of potential novel mechanisms of action underlying tumor treating fields-induced cancer cell death and their clinical implications. *International Journal of Radiation Biology*, 97(8): 1044–1054, oct 2020. doi: 10.1080/09553002.2020.1837984.

[24] George Kolios and Yuben Moodley. Introduction to stem cells and regenerative medicine. *Respiration*, 85(1):3–10, dec 2012. doi: 10.1159/000345615.

[25] Seong Gyu Kwon, Yang Woo Kwon, Tae Wook Lee, Gyu Tae Park, and Jae Ho Kim. Recent advances in stem cell therapeutics and tissue engineering strategies. *Biomaterials Research*, 22(1), dec 2018. doi: 10.1186/s40824-018-0148-4.

[26] G. Filardo, M. Petretta, C. Cavallo, L. Roseti, S. Durante, U. Albisinni, and B. Grigolo. Patient-specific meniscus prototype based on 3d bioprinting of human cell-laden scaffold. *Bone &amp Joint Research*, 8(2):101–106, feb 2019. doi: 10.1302/2046-3758.82.bjr-2018-0134.r1.

[27] Soon Chul Heo, Won Chul Shin, Mi Jeong Lee, Ba Reun Kim, Il Ho Jang, Eun-Jung Choi, Jung Sub Lee, and Jae Ho Kim. Periostin accelerates bone healing mediated by human mesenchymal stem cell-embedded hydroxyapatite/tricalcium phosphate scaffold. *PLOS ONE*, 10(3):e0116698, mar 2015. doi: 10.1371/journal.pone.0116698.

[28] He Shenghui, Daisuke Nakada, and Sean J. Morrison. Mechanisms of stem cell self-renewal. *Annual Review of Cell and Developmental Biology*, 25(1):377–406, nov 2009. doi: 10.1146/annurev.cellbio.042308.113248.

[29] nature portfolio. Cell lineage, 2022. URL `https://www.nature.com/subjects/cell-lineage`.

[30] C.H. Waddington. *The Strategy of the Genes*. Routledge, apr 1957. doi: 10.4324/9781315765471.

[31] Ahmadreza Ghaffarizadeh, Gregory J. Podgorski, and Nicholas S. Flann. Modeling and visualizing cell type switching. *Computational and Mathematical Methods in Medicine*, 2014:1–10, 2014. doi: 10.1155/2014/293980.

[32] Konrad Hochedlinger and Kathrin Plath. Epigenetic reprogramming and induced pluripotency. *Development*, 136(4):509–523, feb 2009. doi: 10.1242/dev.020867.

[33] Siddharth Menon, Siny Shailendra, Andrea Renda, Michael Longaker, and Natalina Quarto. An overview of direct somatic reprogramming: The ins and outs of iPSCs. *International Journal of Molecular Sciences*, 17(1):141, jan 2016. doi: 10.3390/ijms17010141.

[34] Kaoru Sugimoto, Sean P. Gordon, and Elliot M. Meyerowitz. Regeneration in plants and animals: dedifferentiation, transdifferentiation, or just differentiation? *Trends in Cell Biology*, 21(4):212–218, apr 2011. doi: 10.1016/j.tcb.2010.12.004.

[35] Ernesto Lujan and Marius Wernig. An indirect approach to generating specific human cell types. *Nature Methods*, 10(1):44–45, jan 2013. doi: 10.1038/nmeth.2325.

[36] EuroStemCell. Regulation of stem cell research in germany. URL `https://www.eurostemcell.org/regulation-stem-cell-research-germany`.

[37] Harvard stem cell institute. Examining the ethics of embryonic stem cell research, 2007. URL `https://hsci.harvard.edu/examining-ethics-embryonic-stem-cell-research`.

[38] Yeju Seong, Jihye Moon, and Jongpil Kim. Egr1 mediated the neuronal differentiation induced by extremely low-frequency electromagnetic fields. *Life Sciences*, 102(1): 16–27, apr 2014. doi: 10.1016/j.lfs.2014.02.022.

[39] Martin L. Yarmush, Alexander Golberg, Gregor Serša, Tadej Kotnik, and Damijan Miklavcic. Electroporation-based technologies for medicine: Principles, applications, and challenges. *Annual Review of Biomedical Engineering*, 16(1):295–320, jul 2014. doi: 10.1146/annurev-bioeng-071813-104622.

[40] Tongxiang Lin and Shouhai Wu. Reprogramming with small molecules instead of exogenous transcription factors. *Stem Cells International*, 2015:1–11, 2015. doi: 10.1155/2015/794632.

[41] M. Masip, A. Veiga, J. C. Izpisua Belmonte, and C. Simon. Reprogramming with defined factors: from induced pluripotency to induced transdifferentiation. *Molecular Human Reproduction*, 16(11):856–868, jul 2010. doi: 10.1093/molehr/gaq059.

[42] Aleksandra Maziarz, Beata Kocan, Mariusz Bester, Sylwia Budzik, Marian Cholewa, Takahiro Ochiya, and Agnieszka Banas. How electromagnetic fields can influence adult stem cells: positive and negative impacts. *Stem Cell Research &amp Therapy*, 7 (1), apr 2016. doi: 10.1186/s13287-016-0312-5.

[43] Soonbong Baek, Xiaoyuan Quan, Soochan Kim, Christopher Lengner, Jung-Keug Park, and Jongpil Kim. Electromagnetic fields mediate efficient cell reprogramming into a pluripotent state. *ACS Nano*, 8(10):10125–10138, oct 2014. doi: 10.1021/nn502923s.

[44] Hyunjin Cho, Yun-Kyong Choi, Dong Heon Lee, Hee Jung Park, Young-Kwon Seo, Hyun Jung, Soo-Chan Kim, Sung-Min Kim, and Jung-Keug Park. Effects of magnetic nanoparticle-incorporated human bone marrow-derived mesenchymal stem cells exposed to pulsed electromagnetic fields on injured rat spinal cord. *Biotechnology and Applied Biochemistry*, 60(6):596–602, aug 2013. doi: 10.1002/bab.1109.

[45] Sina Habibi, Gholamreza khamisipour, Narges Obeidi, and Saeedeh Zare Jaliseh. Direct differentiation of human primary fibroblast into hematopoietic-like stem cells; a new way without viral transduction. *Cell Journal (Yakhteh)*, 22, 2020. doi: 10.22074/cellj.2020.6846.

[46] Shan Sun, Yaoming Liu, Samantha Lipsky, and Michael Cho†. Physical manipulation of calcium oscillations facilitates osteodifferentiation of human mesenchymal stem cells. *The FASEB Journal*, 21(7):1472–1480, jan 2007. doi: 10.1096/fj.06-7153com.

[47] Margherita Maioli, Salvatore Rinaldi, Sara Santaniello, Alessandro Castagna, Gianfranco Pigliaru, Sara Gualini, Vania Fontani, and Carlo Ventura. Radiofrequency energy loop primes cardiac, neuronal, and skeletal muscle differentiation in mouse embryonic stem cells: A new tool for improving tissue regeneration. *Cell Transplantation*, 21(6): 1225–1233, jun 2012. doi: 10.3727/096368911x600966.

[48] Margherita Maioli, Salvatore Rinaldi, Sara Santaniello, Alessandro Castagna, Gianfranco Pigliaru, Sara Gualini, Claudia Cavallini, Vania Fontani, and Carlo Ventura. Radio electric conveyed fields directly reprogram human dermal skin fibroblasts toward cardiac, neuronal, and skeletal muscle-like lineages. *Cell Transplantation*, 22(7): 1227–1235, jul 2013. doi: 10.3727/096368912x657297.

[49] Margherita Maioli, Salvatore Rinaldi, Sara Santaniello, Alessandro Castagna, Gianfranco Pigliaru, Alessandro Delitala, Francesca Bianchi, Carlo Tremolada, Vania Fontani, and Carlo Ventura. Radioelectric asymmetric conveyed fields and human adipose-derived stem cells obtained with a nonenzymatic method and device: A novel

approach to multipotency. *Cell Transplantation*, 23(12):1489–1500, dec 2014. doi: 10.3727/096368913x672037.

[50] Valentina Basoli, Sara Santaniello, Salvatore Rinaldi, Vania Fontani, Gianfranco Pigliaru, Matthias Wieser, Agata Strajeriu, Alessandro Castagna, Heinz Redl, Carlo Ventura, Regina Grillari, and Margherita Maioli. Physical stimulation by REAC and BMP4/WNT-1 inhibitor synergistically enhance cardiogenic commitment in iPSCs. *PLOS ONE*, 14(1):e0211188, jan 2019. doi: 10.1371/journal.pone.0211188.

[51] Sarah Sundelacruz, Michael Levin, and David L. Kaplan. Membrane potential controls adipogenic and osteogenic differentiation of mesenchymal stem cells. *PLoS ONE*, 3 (11):e3737, nov 2008. doi: 10.1371/journal.pone.0003737.

[52] Claudio Grassi, Marcello D'Ascenzo, Angela Torsello, Giovanni Martinotti, Federica Wolf, Achille Cittadini, and Gian Battista Azzena. Effects of 50hz electromagnetic fields on voltage-gated ca2 channels and their role in modulation of neuroendocrine cell proliferation and death. *Cell Calcium*, 35(4):307–315, apr 2004. doi: 10.1016/j.ceca.2003.09.001.

[53] Antonella Lisi, Alberto Foletti, Mario Ledda, Emanuela Rosola, Livio Giuliani, Enrico D' Emilia, and Settimio Grimaldi. Extremely low frequency 7 hz 100 μt electromagnetic radiation promotes differentiation in the human epithelial cell line HaCaT. *Electromagnetic Biology and Medicin*e, 25(4):269–280, jan 2006. doi: 10.1080/15368370601044184.

[54] Susanne Mayer-Wagner, Florian Hammerschmid, Helmut Blum, Stefan Krebs, Julia I. Redeker, Boris M. Holzapfel, Volkmar Jansson, and Peter E. Müller. Effects of single and combined low frequency electromagnetic fields and simulated microgravity on gene expression of human mesenchymal stem cells during chondrogenesis. *Archives of Medical Science*, 14(3):608–616, 2018. doi: 10.5114/aoms.2016.59894.

[55] Susanne Mayer-Wagner, Alice Passberger, Birte Sievers, Joachim Aigner, Burkhard Summer, Tobias S. Schiergens, Volkmar Jansson, and Peter E. Müller. Effects of low frequency electromagnetic fields on the chondrogenic differentiation of human mesenchymal stem cells. *Bioelectromagnetics*, 32(4):283–290, dec 2010. doi: 10.1002/bem.20633.

[56] Chang Tu, Yifan Xiao, Yongzhuang Ma, Hua Wu, and Mingyu Song. The legacy effects of electromagnetic fields on bone marrow mesenchymal stem cell self-renewal and multiple differentiation potential. *Stem Cell Research &amp Therapy*, 9(1), aug 2018. doi: 10.1186/s13287-018-0955-5.

[57] Yong Yang, Chaoxiong Tao, Dongming Zhao, Feng Li, Wenchun Zhao, and Hua Wu. EMF acts on rat bone marrow mesenchymal stem cells to promote differentiation to osteoblasts and to inhibit differentiation to adipocytes. *Bioelectromagnetics*, pages n/a–n/a, 2009. doi: 10.1002/bem.20560.

[58] Kyung Shin Kang, Jung Min Hong, Jo A Kang, Jong-Won Rhie, Young Hun Jeong, and Dong-Woo Cho. Regulation of osteogenic differentiation of human adipose-derived stem cells by controlling electromagnetic field conditions. *Experimental & Molecular Medicine*, 45(1):e6–e6, jan 2013. doi: 10.1038/emm.2013.11.

[59] Roberto Piacentini, Cristian Ripoli, Daniele Mezzogori, Gian Battista Azzena, and Claudio Grassi. Extremely low-frequency electromagnetic fields promote in vitro neurogenesis via upregulation of casubv/sub1-channel activity. *Journal of Cellular Physiology*, 215(1):129–139, apr 2008. doi: 10.1002/jcp.21293.

[60] Bruna Cuccurazzu, Lucia Leone, Maria Vittoria Podda, Roberto Piacentini, Elisa Riccardi, Cristian Ripoli, Gian Battista Azzena, and Claudio Grassi. Exposure to extremely low-frequency (50hz) electromagnetic fields enhances adult hippocampal neurogenesis in c57bl/6 mice. *Experimental Neurology*, 226(1):173–182, nov 2010. doi: 10.1016/j.expneurol.2010.08.022.

[61] Hyunjin Cho, Young-Kwon Seo, Hee-Hoon Yoon, Soo-Chan Kim, Sung-Min Kim, Kye-Yong Song, and Jung-Keug Park. Neural stimulation on human bone marrow-derived mesenchymal stem cells by extremely low frequency electromagnetic fields. *Biotechnology Progress*, 28(5):1329–1335, sep 2012. doi: 10.1002/btpr.1607.

[62] Alp Özgün, Ana Marote, Leo A. Behie, António Salgado, and Bora Garipcan. Extremely low frequency magnetic field induces human neuronal differentiation through NMDA receptor activation. *Journal of Neural Transmission*, 126(10):1281–1290, jul 2019. doi: 10.1007/s00702-019-02045-5.

[63] Anastasia Rosebud Aikins, Sung-Won Hong, Hyun-Jung Kim, Cheol-Ho Yoon, Joo-Hee Chung, MiJung Kim, and Chan-Wha Kim. Extremely low-frequency electromagnetic field induces neural differentiation of hBM-MSCs through regulation of (zn)-metallothionein-3. *Bioelectromagnetics*, 38(5):364–373, mar 2017. doi: 10.1002/bem.22046.

[64] Wen-Fang Bai, Wei-Cheng Xu, Yu Feng, Hong Huang, Xin-Ping Li, Chun-Yu Deng, and Ming-Sheng Zhang. Fifty-hertz electromagnetic fields facilitate the induction of rat bone mesenchymal stromal cells to differentiate into functional neurons. *Cytotherapy*, 15(8):961–970, aug 2013. doi: 10.1016/j.jcyt.2013.03.001.

[65] Consuelo Morgado-Valle, Leticia Verdugo-Díaz, David E. García, Christian Morales-Orozco, and R. Drucker-Colín. The role of voltage-gated ca 2 channels in neurite growth of cultured chromaffin cells induced by extremely low frequency (ELF) magnetic field stimulation. *Cell and Tissue Research*, 291(2):217–230, jan 1998. doi: 10.1007/s004410050992.

[66] Ming-Tzu Tsai, Wan-Ju Li, Rocky S. Tuan, and Walter H. Chang. Modulation of osteogenesis in human mesenchymal stem cells by specific pulsed electromagnetic field stimulation. *Journal of Orthopaedic Research*, 27(9):1169–1174, sep 2009. doi: 10.1002/jor.20862.

[67] Gabriele Ceccarelli, Nora Bloise, Melissa Mantelli, Giulia Gastaldi, Lorenzo Fassina, Maria Gabriella Cusella De Angelis, Davide Ferrari, Marcello Imbriani, and Livia Visai. A comparative analysis of theiin vitro/ieffects of pulsed electromagnetic field treatment on osteogenic differentiation of two different mesenchymal cell lineages. *BioResearch Open Access*, 2(4):283–294, aug 2013. doi: 10.1089/biores.2013.0016.

[68] Alessia Ongaro, Agnese Pellati, Leila Bagheri, Cinzia Fortini, Stefania Setti, and Monica De Mattei. Pulsed electromagnetic fields stimulate osteogenic differentiation in human bone marrow and adipose tissue derived mesenchymal stem cells. *Bioelectromagnetics*, 35(6):426–436, aug 2014. doi: 10.1002/bem.21862.

[69] Luvita Suryani, Jian Hui Too, Ammar Mansoor Hassanbhai, Feng Wen, Daryl Jimian Lin, Na Yu, and Swee-Hin Teoh. Effects of electromagnetic field on proliferation,

differentiation, and mineralization of MC3t3 cells. *Tissue Engineering Part C: Methods*, 25(2):114–125, feb 2019. doi: 10.1089/ten.tec.2018.0364.

[70] Wei-Hong Hei, Soochan Kim, Joo-Cheol Park, Young-Kwon Seo, Soung-Min Kim, Jeong Won Jahng, and Jong-Ho Lee. Schwann-like cells differentiated from human dental pulp stem cells combined with a pulsed electromagnetic field can improve peripheral nerve regeneration. *Bioelectromagnetics*, 37(3):163–174, mar 2016. doi: 10.1002/bem.21966.

[71] Yun-Kyong Choi, Enerelt Urnukhsaikhan, Hee-Hoon Yoon, Young-Kwon Seo, Hyunjin Cho, Jong-Seob Jeong, Soo-Chan Kim, and Jung-Keug Park. Combined effect of pulsed electromagnetic field and sound wave on in vitro and in vivo neural differentiation of human mesenchymal stem cells. *Biotechnology Progress*, 33(1):201–211, nov 2016. doi: 10.1002/btpr.2389.

[72] Li-Yi Sun, Dean-Kuo Hsieh, Tzai-Chiu Yu, Hsien-Tai Chiu, Sheng-Fen Lu, Geng-Hong Luo, Tom K. Kuo, Oscar K. Lee, and Tzyy-Wen Chiou. Effect of pulsed electromagnetic field on the proliferation and differentiation potential of human bone marrow mesenchymal stem cells. *Bioelectromagnetics*, 30(4):251–260, may 2009. doi: 10.1002/bem.20472.

[73] Z. Schwartz, B. J. Simon, M. A. Duran, G. Barabino, R. Chaudhri, and B. D. Boyan. Pulsed electromagnetic fields enhance BMP-2 dependent osteoblastic differentiation of human mesenchymal stem cells. *Journal of Orthopaedic Research*, 26(9):1250–1255, sep 2008. doi: 10.1002/jor.20591.

[74] Yuji Hiraki, Naoto Endo, Masaharu Takigawa, Akira Asada, Hideaki Takahashi, and Fujio Suzuki. Enhanced responsiveness to parathyroid hormone and induction of functional differentiation of cultured rabbit costal chondrocytes by a pulsed electromagnetic field. *Biochimica et Biophysica Acta (BBA) - Molecular Cell Research*, 931(1):94–100, oct 1987. doi: 10.1016/0167-4889(87)90054-1.

[75] Dinesh Parate, Alfredo Franco-Obregón, Jürg Fröhlich, Christian Beyer, Azlina A. Abbas, Tunku Kamarul, James H. P. Hui, and Zheng Yang. Enhancement of mesenchymal stem cell chondrogenesis with short-term low intensity pulsed electromagnetic fields. *Scientific Reports*, 7(1), aug 2017. doi: 10.1038/s41598-017-09892-w.

[76] Jasmine Lye Yee Yap, Yee Kit Tai, Jürg Fröhlich, Charlene Hui Hua Fong, Jocelyn Naixin Yin, Zi Ling Foo, Sharanya Ramanan, Christian Beyer, Shi Jie Toh, Marco Casarosa, Narendra Bharathy, Monica Palanichamy Kala, Marcel Egli, Reshma Taneja, Chuen Neng Lee, and Alfredo Franco-Obregón. Ambient and supplemental magnetic fields promote myogenesis ivia/i a TRPC1-mitochondrial axis: evidence of a magnetic mitohormetic mechanism. *The FASEB Journal*, 33(11):12853–12872, sep 2019. doi: 10.1096/fj.201900057r.

[77] Radio spectrum in wikipedia, 2022. URL `https://en.wikipedia.org/wiki/Radio_spectrum#ITU`.

[78] Depeng Meng, Tao Xu, Fengjin Guo, Weifeng Yin, and Tao Peng. The effects of high-intensity pulsed electromagnetic field on proliferation and differentiation of neural stem cells of neonatal rats in vitro. *Journal of Huazhong University of Science and Technology [Medical Sciences]*, 29(6):732–736, dec 2009. doi: 10.1007/s11596-009-0612-4.

[79] In Sook Kim, Jong Keun Song, Yu Lian Zhang, Tae Hyung Lee, Tae Hyung Cho, Yun Mi Song, Do Kyun Kim, Sung June Kim, and Soon Jung Hwang. Biphasic electric current stimulates proliferation and induces VEGF production in osteoblasts. *Biochimica et Biophysica Acta (BBA) - Molecular Cell Research*, 1763(9):907–916, sep 2006. doi: 10.1016/j.bbamcr.2006.06.007.

[80] In Sook Kim, Jong Keun Song, Yun Mi Song, Tae Hyung Lee, Tae Hyung Cho, Shin Saeng Lim, Hui Pan, Sung June Kim, and Soon Jung Hwang. Novel action of biphasic electric current in vitro osteogenesis of human bone marrow mesenchymal stromal cells coupled with VEGF production. *Bone*, 43:S43–S44, oct 2008. doi: 10.1016/j.bone.2008.08.019.

[81] In Sook Kim, Jong Keun Song, Yun Mi Song, Tae Hyung Cho, Tae Hyung Lee, Shin Saeng Lim, Sung June Kim, and Soon Jung Hwang. Novel effect of biphasic electric current on iin vitro/i osteogenesis and cytokine production in human mesenchymal stromal cells. *Tissue Engineering Part A*, 15(9):2411–2422, sep 2009. doi: 10.1089/ten.tea.2008.0554.

[82] Kejia Li, Tong Ning, Hao Wang, Yangzi Jiang, Jue Zhang, and Zigang Ge. Nanosecond pulsed electric fields enhance mesenchymal stem cells differentiation via DNMT1-regulated OCT4/NANOG gene expression. *Stem Cell Research &amp Therapy*, 11(1), jul 2020. doi: 10.1186/s13287-020-01821-5.

[83] Giulia Pinton, Angelo Ferraro, Massimo Balma, and Laura Moro. Specific low frequency electromagnetic fields induce epigenetic and functional changes in u937 cells, 2018.

[84] Giulia Pinton, Angelo Ferraro, Massimo Balma, and Laura Moro. Specific low-frequency electromagnetic fields induce expression of active KDM6b associated with functional changes in u937 cells. *Electromagnetic Biology and Medicine*, 39(2): 139–153, mar 2020. doi: 10.1080/15368378.2020.1737807.

[85] Yin Long, Hao Wei, Jun Li, Guang Yao, Bo Yu, Dalong Ni, Angela LF Gibson, Xiaoli Lan, Yadong Jiang, Weibo Cai, and Xudong Wang. Effective wound healing enabled by discrete alternative electric fields from wearable nanogenerators. *ACS Nano*, 12(12): 12533–12540, nov 2018. doi: 10.1021/acsnano.8b07038.

[86] Cheng Xu, Yunlong Zi, Aurelia Chi Wang, Haiyang Zou, Yejing Dai, Xu He, Peihong Wang, Yi-Cheng Wang, Peizhong Feng, Dawei Li, and Zhong Lin Wang. On the electron-transfer mechanism in the contact-electrification effect. *Advanced Materials*, 30(15):1706790, mar 2018. doi: 10.1002/adma.201706790.

[87] Zhong Lin Wang. From contact electrification to triboelectric nanogenerators. *Reports on Progress in Physics*, 84(9):096502, sep 2021. doi: 10.1088/1361-6633/ac0a50.

[88] Changsheng Wu, Aurelia C. Wang, Wenbo Ding, Hengyu Guo, and Zhong Lin Wang. Triboelectric nanogenerator: A foundation of the energy for the new era. *Advanced Energy Materials*, 9(1):1802906, nov 2018. doi: 10.1002/aenm.201802906.

[89] Enza Fazio, Bilal Gökce, Alessandro De Giacomo, Moreno Meneghetti, Giuseppe Compagnini, Matteo Tommasini, Friedrich Waag, Andrea Lucotti, Chiara Giuseppina Zanchi, Paolo Maria Ossi, Marcella Dell'Aglio, Luisa D'Urso, Marcello Condorelli, Vittorio Scardaci, Francesca Biscaglia, Lucio Litti, Marina Gobbo, Giovanni Gallo, Marco Santoro, Sebastiano Trusso, and Fortunato Neri. Nanoparticles engineering by pulsed laser ablation in liquids: Concepts and applications. *Nanomaterials*, 10(11):2317, nov 2020. doi: 10.3390/nano10112317.

[90] The european commission. Commission recommendation of 18 october 2011 on the definition of nanomaterial text with eea relevance, 2011. URL ELI:http://data.europa.eu/eli/reco/2011/696/oj.

[91] Wilfried Buchmüller and Cord Jakobeit, editors. *Erkenntnis, Wissenschaft und Gesellschaft*. Springer Berlin Heidelberg, 2016. doi: 10.1007/978-3-662-49912-2.

[92] H. Moshammer and P. Wallner. Gesundheitsrisiken durch nanopartikel? In *Nano*, pages 165–180. Springer Vienna, 2007. doi: 10.1007/978-3-211-49303-8_10.

[93] André Gazsó and Julia Haslinger, editors. *Nano Risiko Governance*. Springer Vienna, 2014. doi: 10.1007/978-3-7091-1405-6.

[94] Wolfgang R. Fahrner. Nanopartikel. In *Nanotechnologie und Nanoprozesse*, pages 123–139. Springer Berlin Heidelberg, may 2016. doi: 10.1007/978-3-662-48908-6_5.

[95] Myungjoon Kim, Saho Osone, Taesung Kim, Hidenori Higashi, and Takafumi Seto. Synthesis of nanoparticles by laser ablation: A review. *KONA Powder and Particle Journal*, 34(0):80–90, 2017. doi: 10.14356/kona.2017009.

[96] Xiangjun Han, Ke Xu, Olena Taratula, and Khashayar Farsad. Applications of nanoparticles in biomedical imaging. *Nanoscale*, 11(3):799–819, 2019. doi: 10.1039/c8nr07769j.

[97] Michael J. Mitchell, Margaret M. Billingsley, Rebecca M. Haley, Marissa E. Wechsler, Nicholas A. Peppas, and Robert Langer. Engineering precision nanoparticles for drug delivery. *Nature Reviews Drug Discovery*, 20(2):101–124, dec 2020. doi: 10.1038/s41573-020-0090-8.

[98] Muharrem Seleci, Didem Ag Seleci, Rebecca Joncyzk, Frank Stahl, Cornelia Blume, and Thomas Scheper. Smart multifunctional nanoparticles in nanomedicine. *BioNanoMaterials*, 17(1-2), jan 2016. doi: 10.1515/bnm-2015-0030.

[99] Hendrik Heinz, Chandrani Pramanik, Ozge Heinz, Yifu Ding, Ratan K. Mishra, Delphine Marchon, Robert J. Flatt, Irina Estrela-Lopis, Jordi Llop, Sergio Moya, and Ronald F. Ziolo. Nanoparticle decoration with surfactants: Molecular interactions, assembly, and applications. *Surface Science Reports*, 72(1):1–58, feb 2017. doi: 10.1016/j.surfrep.2017.02.001.

[100] Tianmeng Sun, Yu Shrike Zhang, Bo Pang, Dong Choon Hyun, Miaoxin Yang, and Younan Xia. Engineered nanoparticles for drug delivery in cancer therapy. *Angewandte Chemie International Edition*, pages n/a–n/a, oct 2014. doi: 10.1002/anie.201403036.

[101] Mauro Sousa de Almeida, Eva Susnik, Barbara Drasler, Patricia Taladriz-Blanco, Alke Petri-Fink, and Barbara Rothen-Rutishauser. Understanding nanoparticle endocytosis to improve targeting strategies in nanomedicine. *Chemical Society Reviews*, 50(9): 5397–5434, 2021. doi: 10.1039/d0cs01127d.

[102] Darío Manzanares and Valentín Ceña. Endocytosis: The nanoparticle and submicron nanocompounds gateway into the cell. *Pharmaceutics*, 12(4):371, apr 2020. doi: 10.3390/pharmaceutics12040371.

[103] Amir K. Varkouhi, Marije Scholte, Gert Storm, and Hidde J. Haisma. Endosomal escape pathways for delivery of biologicals. *Journal of Controlled Release*, 151(3):220–228, may 2011. doi: 10.1016/j.jconrel.2010.11.004.

[104] Vajihe Asgari, Amir Landarani-Isfahani, Hossein Salehi, Noushin Amirpour, Batool Hashemibeni, Saghar Rezaei, and Hamid Bahramian. The story of nanoparticles in differentiation of stem cells into neural cells. *Neurochemical Research*, 44(12): 2695–2707, nov 2019. doi: 10.1007/s11064-019-02900-7.

[105] Ahmed Abdal Dayem, Soo Lee, and Ssang-Goo Cho. The impact of metallic nanoparticles on stem cell proliferation and differentiation. *Nanomaterials*, 8(10):761, sep 2018. doi: 10.3390/nano8100761.

[106] Joseph Long, Hyejin Kim, Dajeong Kim, Jong Bum Lee, and Deok-Ho Kim. A biomaterial approach to cell reprogramming and differentiation. *Journal of Materials Chemistry B*, 5(13):2375–2389, 2017. doi: 10.1039/c6tb03130g.

[107] Dakrong Pissuwan, Sasiprapa Poomrattanangoon, and Porlin Chungchaiyart. Trends in using gold nanoparticles for inducing cell differentiation: A review. *ACS Applied Nano Materials*, 5(3):3110–3120, mar 2022. doi: 10.1021/acsanm.1c04173.

[108] Katharina Drews, Geertrui Tavernier, Joseph Demeester, Hans Lehrach, Stefaan C. De Smedt, Joanna Rejman, and James Adjaye. The cytotoxic and immunogenic hurdles

associated with non-viral mRNA-mediated reprogramming of human fibroblasts. *Biomaterials*, 33(16):4059–4068, jun 2012. doi: 10.1016/j.biomaterials.2012.02.025.

[109] Megan A. Yamoah, Phung N. Thai, and Xiao-Dong Zhang. Transgene delivery to human induced pluripotent stem cells using nanoparticles. *Pharmaceuticals*, 14(4):334, apr 2021. doi: 10.3390/ph14040334.

[110] Christian Plank, Franz Scherer, Ulrike Schillinger, Christian Bergemann, and Martina Anton. Magnetofection: Enhancing and targeting gene delivery with superparamagnetic nanoparticles and magnetic fields. *Journal of Liposome Research*, 13(1):29–32, jan 2003. doi: 10.1081/lpr-120017486.

[111] Krishna Kumar Haridhasapavalan, Manash P. Borgohain, Chandrima Dey, Bitan Saha, Gloria Narayan, Sachin Kumar, and Rajkumar P. Thummer. An insight into non-integrative gene delivery approaches to generate transgene-free induced pluripotent stem cells. *Gene*, 686:146–159, feb 2019. doi: 10.1016/j.gene.2018.11.069.

[112] Lara Prosen, Sara Prijic, Branka Music, Jaka Lavrencak, Maja Cemazar, and Gregor Sersa. Magnetofection: A reproducible method for gene delivery to melanoma cells. *BioMed Research International*, 2013:1–11, 2013. doi: 10.1155/2013/209452.

[113] Magda Lorena Arciniegas Vaca, Gustavo Alberto Pasquevich, Olga Mykhaylyk, Nicolás Germán Mele, Rodolfo Gustavo Goya, and Francisco Homero Sánchez. Physics of in vitro magnetofection. effect of magnetic transport and redistribution of nanoparticles. *Journal of Magnetism and Magnetic Materials*, 503:166606, jun 2020. doi: 10.1016/j.jmmm.2020.166606.

[114] Megan Yamoah, Maryam Moshref, Janhavi Sharma, Wei Chun Chen, Hannah Ledford, Jeong Han Lee, Karen Chavez, Wenying Wang, Javier López, Deborah Lieu, Padmini Sirish, and Xiao-Dong Zhang. Highly efficient transfection of human induced pluripotent stem cells using magnetic nanoparticles. *International Journal of Nanomedicine*, Volume 13:6073–6078, oct 2018. doi: 10.2147/ijn.s172254.

[115] Hyo Young Park, Eun Hyung Noh, Hyung-Min Chung, Man-Jong Kang, Eun Young Kim, and Se Pill Park. Efficient generation of virus-free iPS cells using liposomal magnetofection. *PLoS ONE*, 7(9):e45812, sep 2012. doi: 10.1371/journal.pone.0045812.

[116] Wahajuddin and Arora. Superparamagnetic iron oxide nanoparticles: magnetic nanoplatforms as drug carriers. *International Journal of Nanomedicine*, page 3445, jul 2012. doi: 10.2147/ijn.s30320.

[117] Murat Kaya Yapici, Ahmad Al Nabulsi, Nahla Rizk, Selwa Mokhtar Boularaoui, Nicolas Christoforou, and Sungmun Lee. Alternating magnetic field plate for enhanced magnetofection of iron oxide nanoparticle conjugated nucleic acids. *Journal of Magnetism and Magnetic Materials*, 469:598–605, jan 2019. doi: 10.1016/j.jmmm.2018.09.038.

[118] Chang Hyun Lee, Jung-Hyun Kim, Hyun Joo Lee, Kilsoo Jeon, HyeJin Lim, Hye yeon Choi, Eung-Ryoung Lee, Seung Hwa Park, Jae-Yong Park, Sunghoi Hong, Soonhag Kim, and Ssang-Goo Cho. The generation of iPS cells using non-viral magnetic nanoparticlebased transfection. *Biomaterials*, 32(28):6683–6691, oct 2011. doi: 10.1016/j.biomaterials.2011.05.070.

[119] Jingjiao Guan, Xiaogang Pan, L. James Lee, and Robert J. Lee. Viral, nonviral, and physical methods for gene delivery. In *Biopharmaceutical Drug Design and Development*, pages 141–173. Humana Press, 2008. doi: 10.1007/978-1-59745-532-9_8.

[120] Karrina McNamara and Syed A. M. Tofail. Nanoparticles in biomedical applications. *Advances in Physics: X*, 2(1):54–88, nov 2016. doi: 10.1080/23746149.2016.1254570.

[121] Ganesha Antarnusa and Edi Suharyadi. A synthesis of polyethylene glycol (PEG)-coated magnetite fesub3/subosub4/sub nanoparticles and their characteristics for enhancement of biosensor. *Materials Research Express*, 7(5):056103, may 2020. doi: 10.1088/2053-1591/ab8bef.

[122] A Barchanski, U Taylor, S Klein, S Petersen, D Rath, and S Barcikowski. Golden perspective: Application of laser-generated gold nanoparticle conjugates in reproductive biology. *Reproduction in Domestic Animals*, 46:42–52, aug 2011. doi: 10.1111/j.1439-0531.2011.01844.x.

[123] Annette Barchanski. *Laser-Generated Functional Nanoparticle Bioconjugates*. Springer Fachmedien Wiesbaden, June 2016. ISBN 365813514X. URL `https://www.ebook.de/de/product/25836723/annette_barchanski_laser_generated_functional_nanoparticle_bioconjugates.html`.

[124] Uri Weinberg. Novocure's tumortreating fields: Innovativebrain cancer therapy with-survival and safety benefits. URL https://www.nature.com/articles/d42473-018-00156-3.

[125] Ping Zhu and Jay-Jiguang Zhu. Tumor treating fields: a novel and effective therapy for glioblastoma: mechanism, efficacy, safety and future perspectives. *Chinese Clinical Oncology*, 6(4):41–41, aug 2017. doi: 10.21037/cco.2017.06.29.

[126] Stuart H. Burri, Vinai Gondi, Paul D. Brown, and Minesh P. Mehta. The evolving role of tumor treating fields in managing glioblastoma. *American Journal of Clinical Oncology*, 41(2):191–196, feb 2018. doi: 10.1097/coc.0000000000000395.

[127] O. Gallego. Nonsurgical treatment of recurrent glioblastoma. *Current Oncology*, 22 (4):273–281, aug 2015. doi: 10.3747/co.22.2436.

[128] Novocure. Novocure announces ce mark and first patient use of second generation optune system, 2015. URL https://www.novocure.com/novocure-announces-ce-mark-and-first-patient-use-of-second-generation-optune-system.

[129] Vikram S. Soni and Ted K. Yanagihara. Tumor treating fields in the management of glioblastoma: opportunities for advanced imaging. *Cancer Imaging*, 19(1), nov 2019. doi: 10.1186/s40644-019-0259-8.

[130] Charis-P. Segeritz and Ludovic Vallier. Cell culture. In *Basic Science Methods for Clinical Researchers*, pages 151–172. Elsevier, 2017. doi: 10.1016/b978-0-12-803077-6.00009-6.

[131] invitrogen. Cell culture basics. Online Handbook. URL https://www.vanderbilt.edu/viibre/CellCultureBasicsEU.pdf.

[132] K. Asami, Y. Takahashi, and S. Takashima. Dielectric properties of mouse lymphocytes and erythrocytes. *Biochimica et Biophysica Acta (BBA) - Molecular Cell Research*, 1010 (1):49–55, jan 1989. doi: 10.1016/0167-4889(89)90183-3.

[133] Debanjan Das, Farhan Ahmad Kamil, Karabi Biswas, and Soumen Das. Evaluation of single cell electrical parameters from bioimpedance of a cell suspension. *RSC Adv.*, 4 (35):18178–18185, 2014. doi: 10.1039/c4ra00400k.

[134] I. Ermolina, Yu. Polevaya, and Yu. Feldman. Analysis of dielectric spectra of eukaryotic cells by computer modeling. *European Biophysics Journal*, 29(2):141–145, may 2000. doi: 10.1007/s002490050259.

[135] Karl Schoenbach, Barbara Hargrave, Ravindra Joshi, Juergen Kolb, Richard Nuccitelli, Christopher Osgood, Andrei Pakhomov, Michael Stacey, R. Swanson, Jody White, Shu Xiao, Jue Zhang, Stephen Beebe, Peter Blackmore, and E. Buescher. Bioelectric effects of intense nanosecond pulses. *IEEE Transactions on Dielectrics and Electrical Insulation*, 14(5):1088–1109, oct 2007. doi: 10.1109/tdei.2007.4339468.

[136] Vijayanand Vajrala, James R. Claycomb, Hugo Sanabria, and John H. Miller. Effects of oscillatory electric fields on internal membranes: An analytical model. *Biophysical Journal*, 94(6):2043–2052, mar 2008. doi: 10.1529/biophysj.107.114611.

[137] Cornelia Wenger, Moshe Giladi, Ze'ev Bomzon, Ricardo Salvador, Peter J. Basser, and Pedro C. Miranda. Modeling tumor treating fields (TTFields) application in single cells during metaphase and telophase. In *2015 37th Annual International Conference of the IEEE Engineering in Medicine and Biology Society (EMBC)*. IEEE, aug 2015. doi: 10.1109/embc.2015.7319977.

[138] Yu Zhao and Guigen Zhang. Elucidating the mechanism of 200 kHz tumor treating fields with a modified DEP theory. In *2018 IEEE International Symposium on Signal Processing and Information Technology (ISSPIT)*. IEEE, dec 2018. doi: 10.1109/isspit.2018.8705145.

[139] Angus I Lamond and Judith E Sleeman. Nuclear substructure and dynamics. *Current Biology*, 13(21):R825–R828, oct 2003. doi: 10.1016/j.cub.2003.10.012.

[140] Ron Milo; Paul Jorgensen and Mike Springer. B10numb3r5 the database of useful biological numbers: Diameter of rat embryonic fibroblast nucleus, 2023. URL `https://bionumbers.hms.harvard.edu/bionumber.aspx?id=104145&ver=6&trm=fibroblastcellsize&org=`.

[141] Thomas Frisch and Olivier Thoumine. Predicting the kinetics of cell spreading. *Journal of Biomechanics*, 35(8):1137–1141, aug 2002. doi: 10.1016/s0021-9290(02)00075-1.

[142] Ron Milo; Paul Jorgensen and Mike Springer. B10numb3r5 the database of useful biological numbers: Relative static permittivity (dielectric constant) of membrane interior (lipids), 2023. URL https://bionumbers.hms.harvard.edu/bionumber.aspx?id=104080&ver=1&trm=cellmembranepermittivity&org=.

[143] Ana Valero, Thomas Braschler, and Philippe Renaud. A unified approach to dielectric single cell analysis: Impedance and dielectrophoretic force spectroscopy. *Lab on a Chip*, 10(17):2216, 2010. doi: 10.1039/c003982a.

[144] Jiafeng Yao, Li Wang, Kai Liu, Hongtao Wu, Hao Wang, Jingshi Huang, and Jianping Li. Evaluation of electrical characteristics of biological tissue with electrical impedance spectroscopy. *ELECTROPHORESIS*, 41(16-17):1425–1432, jan 2020. doi: 10.1002/elps.201900420.

[145] Premkumar Ellappan and Raji Sundararajan. A simulation study of the electrical model of a biological cell. *Journal of Electrostatics*, 63(3-4):297–307, mar 2005. doi: 10.1016/j.elstat.2004.11.007.

[146] Ahmet C. Sabuncu, Jie Zhuang, Juergen F. Kolb, and Ali Beskok. Microfluidic impedance spectroscopy as a tool for quantitative biology and biotechnology. *Biomicrofluidics*, 6(3):034103, sep 2012. doi: 10.1063/1.4737121.

[147] Xiao Ma, Xiaotian Du, Hang Li, Xuanhong Cheng, and James C. M. Hwang. Ultra-wideband impedance spectroscopy of a live biological cell. *IEEE Transactions on Microwave Theory and Techniques*, 66(8):3690–3696, aug 2018. doi: 10.1109/tmtt.2018.2851251.

[148] Agnese Denzi, Caterina Merla, Paola Camilleri, Alessandra Paffi, Guglielmo d'Inzeo, Francesca Apollonio, and Micaela Liberti. Microdosimetric study for nanosecond pulsed electric fields on a cell circuit model with nucleus. *The Journal of Membrane Biology*, 246(10):761–767, apr 2013. doi: 10.1007/s00232-013-9546-7.

[149] C. Merla, A. Denzi, A. Paffi, M. Casciola, G. d'Inzeo, F. Apollonio, and M. Liberti. Novel passive element circuits for microdosimetry of nanosecond pulsed electric fields. *IEEE Transactions on Biomedical Engineering*, 59(8):2302–2311, aug 2012. doi: 10.1109/tbme.2012.2203133.

[150] T.R. Gowrishankar, Donald A. Stewart, and James C. Weaver. Model of a confined spherical cell in uniform and heterogeneous applied electric fields. *Bioelectrochemistry*, 68(2):181–190, may 2006. doi: 10.1016/j.bioelechem.2005.07.002.

[151] Eilon D. Kirson, Vladimír Dbalý, František Tovaryš, Josef Vymazal, Jean F. Soustiel, Aviran Itzhaki, Daniel Mordechovich, Shirley Steinberg-Shapira, Zoya Gurvich, Rosa Schneiderman, Yoram Wasserman, Marc Salzberg, Bernhard Ryffel, Dorit Goldsher, Erez Dekel, and Yoram Palti. Alternating electric fields arrest cell proliferation in animal tumor models and human brain tumors. *Proceedings of the National Academy of Sciences*, 104(24):10152–10157, jun 2007. doi: 10.1073/pnas.0702916104.

[152] Jack Tuszynski, Cornelia Wenger, Douglas Friesen, and Jordane Preto. An overview of sub-cellular mechanisms involved in the action of TTFields. *International Journal of Environmental Research and Public Health*, 13(11):1128, nov 2016. doi: 10.3390/ijerph13111128.

[153] Cornelia Wenger, Pedro C. Miranda, Ricardo Salvador, Axel Thielscher, Zeev Bomzon, Moshe Giladi, Maciej M. Mrugala, and Anders R. Korshoej. A review on tumor-treating fields (TTFields): Clinical implications inferred from computational modeling. *IEEE Reviews in Biomedical Engineering*, 11:195–207, 2018. doi: 10.1109/rbme.2017.2765282.

[154] Theodoros T. Zygiridis and Nikolaos V. Kantartzis. Finite-difference modeling of nonlinear phenomena in time-domain electromagnetics: A review. In *Applications of Nonlinear Analysis*, pages 897–931. Springer International Publishing, 2018. doi: 10.1007/978-3-319-89815-5_29.

[155] *Sim4Life Manual*. URL `file:///C:/Users/Public/Documents/Sim4Life/6.2/Documentation/html/Manual/EM/EMLF_Theory.html`.

[156] Julius Adams Stratton. *Electromagnetic Theory*. McGraw-Hill Book Company, Inc., 1941. URL `https://archive.org/details/electromagnetict031016mbp/page/n647/mode/2up`.

[157] Jan-Patrick Schäfer. *Implementierung und Anwendung analytischer und numerischer Verfahren zur Lösung der Maxwellgleichungen für die Untersuchung der Lichtausbreitung in biologischem Gewebe*. PhD thesis, 2011.

[158] Gustav Mie. Beiträge zur optik trüber medien, speziell kolloidaler metallösungen. *Annalen der Physik*, 330(3):377–445, 1908. doi: 10.1002/andp.19083300302.

[159] Craig F. Bohren and Donald R. Huffman. *Absorption and Scattering of Light by Small Particles*. Wiley, apr 1998. doi: 10.1002/9783527618156.

[160] Klaus Jänich. *Analysis für Physiker und Ingenieure*. Springer Berlin Heidelberg, 2001. doi: 10.1007/978-3-662-05703-2.

[161] T. Prof. Dr.-Ing. Harriehausen. Gewöhnliche differentialgleichungen, lösungsansätze für einige praktisch wichtige fälle, 2004. URL `http://www.micbaum.y0w.de/uploads/LoesungsansaetzeDGLzweiterOrdnung.pdf`.

[162] Saint Petersburg ITMO University. Mie calculator, 2022. URL `https://physics.itmo.ru/ru/mie#/nearfield`.

[163] Jan-Patrick Schäfer. Matscat, 2012. URL `https://de.mathworks.com/matlabcentral/fileexchange/36831-matscat`.

[164] Milton Kerker. *The Scattering of Light and Other Electromagnetic Radiation*. Elsevier, 1969. doi: 10.1016/c2013-0-06195-6.

[165] Myrtill Simkó. Induction of cell activation processes by low frequency electromagnetic fields. *The Scientific World JOURNAL*, 4:4–22, 2004. doi: 10.1100/tsw.2004.174.

[166] T Ning, , K Zhang, B Chin Heng, and Z Ge. Diverse effects of pulsed electrical stimulation on cells - with a focus on chondrocytes and cartilage regeneration. *European Cells and Materials*, 38:79–93, sep 2019. doi: 10.22203/ecm.v038a07.

[167] Felix T. Hong. Magnetic field effects on biomolecules, cells, and living organisms. *Biosystems*, 36(3):187–229, jan 1995. doi: 10.1016/0303-2647(95)01555-y.

[168] Christina L. Ross, Mevan Siriwardane, Graça Almeida-Porada, Christopher D. Porada, Peter Brink, George J. Christ, and Benjamin S. Harrison. The effect of low-frequency electromagnetic field on human bone marrow stem/progenitor cell differentiation. *Stem Cell Research*, 15(1):96–108, jul 2015. doi: 10.1016/j.scr.2015.04.009.

[169] Constantine A. Balanis. *Advanced Engineering Electromagnetics*. John Wiley Sons, 1938. ISBN 0-471-62194-3.

[170] Permittivity in wikipedia, 2022. URL https://en.wikipedia.org/wiki/Permittivity#/media/File:Dielectric_responses.svg.

[171] R Pethig and D B Kell. The passive electrical properties of biological systems: their significance in physiology, biophysics and biotechnology. *Physics in Medicine and Biology*, 32(8):933–970, aug 1987. doi: 10.1088/0031-9155/32/8/001.

[172] T. Taghian, D. A. Narmoneva, and A. B. Kogan. Modulation of cell function by electric field: a high-resolution analysis. *Journal of The Royal Society Interface*, 12(107): 20150153, jun 2015. doi: 10.1098/rsif.2015.0153.

[173] T.B. Jones. Basic theory of dielectrophoresis and electrorotation. *IEEE Engineering in Medicine and Biology Magazine*, 22(6):33–42, nov 2003. doi: 10.1109/memb.2003.1304999.

[174] J. Bernhardt. Biologische wirkungen elektromagnetischer felder / biological effects of electromagnetic fields. *Zeitschrift für Naturforschung C*, 34(7-8):616–627, aug 1979. doi: 10.1515/znc-1979-7-821.

[175] IEEE recommended practice for determining the peak spatial-average specific absorption rate (SAR) in the human head from wireless communications devices: Measurement techniques.

[176] Maruti Uppalapati, Ying-Ming Huang, Thomas N. Jackson, and William O. Hancock. Microtubule alignment and manipulation using AC electrokinetics. *Small*, 4(9): 1371–1381, sep 2008. doi: 10.1002/smll.200701088.

[177] Ulrich Terpitz, Vladimir L. Sukhorukov, and Dirk Zimmermann. Prototype for automatable, dielectrophoretically-accessed intracellular membrane–potential measurements by metal electrodes. *ASSAY and Drug Development Technologies*, 11(1):9–16, feb 2013. doi: 10.1089/adt.2012.455.

[178] Thomas K. Monsees and Richard H. W. Funk. Wirkung von oberflächenladungen und elektro-magnetischen feldern auf zellen. *BIOmaterialien*, 6(2), jan 2005. doi: 10.1515/biomat.2005.6.2.67.

[179] N. Siauve, R. Scorretti, N. Burais, L. Nicolas, and A. Nicolas. Electromagnetic fields and human body: a new challenge for the electromagnetic field computation. *COMPEL -*

The international journal for computation and mathematics in electrical and electronic engineering, 22(3):457–469, sep 2003. doi: 10.1108/03321640310474868.

[180] Martha; Rafik M. Ghobrial; Uosef Ahmed; H. Miller Jr John; Kloc Malgorzata Wosik, Jarek; Villagran. Effects of magnetic fields and field gradients on living cells. *eMagRes*, mar 2007. doi: 10.1002/9780470034590. URL `https://onlinelibrary.wiley.com/doi/full/10.1002/9780470034590.emrstm1609`.

[181] Steven Hughes, Alicia J. El Haj, and Jon Dobson. Magnetic micro- and nanoparticle mediated activation of mechanosensitive ion channels. *Medical Engineering &amp Physics*, 27(9):754–762, nov 2005. doi: 10.1016/j.medengphy.2005.04.006.

[182] Wim Bras, James Torbet, Gregory P. Diakun, Geert L. J. A. Rikken, and J. Fernando Diaz. The diamagnetic susceptibility of the tubulin dimer. *Journal of Biophysics*, 2014:1–5, feb 2014. doi: 10.1155/2014/985082.

[183] W. Bras, G.P. Diakun, J.F. Díaz, G. Maret, H. Kramer, J. Bordas, and F.J. Medrano. The susceptibility of pure tubulin to high magnetic fields: A magnetic birefringence and x-ray fiber diffraction study. *Biophysical Journal*, 74(3):1509–1521, mar 1998. doi: 10.1016/s0006-3495(98)77863-4.

[184] S. Engstrom. Physical mechanisms of non-thermal extremely-low-frequency magnetic-field effects. *URSI Radio Science Bulletin, vol. 2004, no. 311, pp. 95-106*, 2004. doi: 10.23919/URSIRSB.2004.7909638. URL `https://ieeexplore.ieee.org/abstract/document/7909638`.

[185] Régine Dazzoni, Axelle Grélard, Estelle Morvan, Anthony Bouter, Christopher J. Applebee, Antoine Loquet, Banafshé Larijani, and Erick J. Dufourc. The unprecedented membrane deformation of the human nuclear envelope, in a magnetic field, indicates formation of nuclear membrane invaginations. *Scientific Reports*, 10(1), mar 2020. doi: 10.1038/s41598-020-61746-0.

[186] M. Iwasaka. Deformation of cellular components of bone forming cells when exposed to a magnetic field. *AIP Advances*, 9(3):035327, mar 2019. doi: 10.1063/1.5079635.

[187] W. Helfrich. Lipid bilayer spheres: Deformation and birefringence in magnetic fields. *Physics Letters A*, 43(5):409–410, apr 1973. doi: 10.1016/0375-9601(73)90396-4.

[188] Lellis F. Braganza, Barry H. Blott, Tessa J. Coe, and David Melville. The superdiamagnetic effect of magnetic fields on one and two component multilamellar liposomes. *Biochimica et Biophysica Acta (BBA) - General Subjects*, 801(1):66–75, sep 1984. doi: 10.1016/0304-4165(84)90213-7.

[189] W Helfrich. Elastic properties of lipid bilayers: Theory and possible experiments. *Zeitschrift für Naturforschung C*, 28(11-12):693–703, dec 1973. doi: 10.1515/znc-1973-11-1209.

[190] T.S. Tenforde and R.P. Liburdy. Magnetic deformation of phospholipid bilayers: Effects on liposome shape and solute permeability at prephase transition temperatures. *Journal of Theoretical Biology*, 133(3):385–396, aug 1988. doi: 10.1016/s0022-5193(88)80329-1.

[191] Bruno Pontes, Yareni Ayala, Anna Carolina C. Fonseca, Luciana F. Romão, Racкele F. Amaral, Leonardo T. Salgado, Flavia R. Lima, Marcos Farina, Nathan B. Viana, Vivaldo Moura-Neto, and H. Moysés Nussenzveig. Membrane elastic properties and cell function. *PLoS ONE*, 8(7):e67708, jul 2013. doi: 10.1371/journal.pone.0067708.

[192] Julien Aureille, Valentin Buffière-Ribot, Ben E Harvey, Cyril Boyault, Lydia Pernet, Tomas Andersen, Gregory Bacola, Martial Balland, Sandrine Fraboulet, Laurianne Van Landeghem, and Christophe Guilluy. Nuclear envelope deformation controls cell cycle progression in response to mechanical force. *EMBO reports*, 20(9), aug 2019. doi: 10.15252/embr.201948084.

[193] Y. Kinouchi, S. Tanimoto, T. Ushita, K. Sato, H. Yamaguchi, and H. Miyamoto. Effects of static magnetic fields on diffusion in solutions. *Bioelectromagnetics*, 9(2):159–166, 1988. doi: 10.1002/bem.2250090207.

[194] Vitalii Zablotskii, Tatyana Polyakova, Oleg Lunov, and Alexandr Dejneka. How a high-gradient magnetic field could affect cell life. *Scientific Reports*, 6(1), nov 2016. doi: 10.1038/srep37407.

[195] Tomasz Panczyk and Philip J. Camp. Lorentz forces induced by a static magnetic field have negligible effects on results from classical molecular dynamics simulations of aqueous solutions. *Journal of Molecular Liquids*, 330:115701, may 2021. doi: 10.1016/j.molliq.2021.115701.

[196] John F. Schenck. The role of magnetic susceptibility in magnetic resonance imaging: MRI magnetic compatibility of the first and second kinds. *Medical Physics*, 23(6): 815–850, jun 1996. doi: 10.1118/1.597854.

[197] Roger S. M. Rikken, Roeland J. M. Nolte, Jan C. Maan, Jan C. M. van Hest, Daniela A. Wilson, and Peter C. M. Christianen. Manipulation of micro- and nanostructure motion with magnetic fields. *Soft Matter*, 10(9):1295–1308, 2014. doi: 10.1039/c3sm52294f.

[198] J.M. Valles, K. Lin, J.M. Denegre, and K.L. Mowry. Stable magnetic field gradient levitation of xenopus laevis: toward low-gravity simulation. *Biophysical Journal*, 73(2): 1130–1133, aug 1997. doi: 10.1016/s0006-3495(97)78145-1.

[199] E. Beaugnon and R. Tournier. Levitation of water and organic substances in high static magnetic fields. *Journal de Physique III*, 1(8):1423–1428, aug 1991. doi: 10.1051/jp3:1991199.

[200] Qin Hu, Ravi P. Joshi, and Damijan Miklavcic. Calculations of cell transmembrane voltage induced by time-varying magnetic fields. *IEEE Transactions on Plasma Science*, 48(4):1088–1095, apr 2020. doi: 10.1109/tps.2020.2975421.

[201] J.C. Weaver. Electroporation of cells and tissues. *IEEE Transactions on Plasma Science*, 28(1):24–33, 2000. doi: 10.1109/27.842820.

[202] Vitalij Novickij, Janja Dermol, Audrius Grainys, Matej Kranjc, and Damijan Miklavc□ic□. Membrane permeabilization of mammalian cells using bursts of high magnetic field pulses. *PeerJ*, 5:e3267, apr 2017. doi: 10.7717/peerj.3267.

[203] Damijan Miklavcic, Vitalij Novickij, Matej Kranjc, Tamara Polajzer, Sasa Haberl Meglic, Tina Batista Napotnik, Rok Romih, and Darja Lisjak. Contactless electroporation induced by high intensity pulsed electromagnetic fields via distributed nanoelectrodes. *Bioelectrochemistry*, 132:107440, apr 2020. doi: 10.1016/j.bioelechem.2019.107440.

[204] V. Zablotskii, O. Lunov, B. Novotná, O. Churpita, P. Trošan, V. Holán□, E. Syková, A. Dejneka, and Š. Kubinová. Down-regulation of adipogenesis of mesenchymal stem cells by oscillating high-gradient magnetic fields and mechanical vibration. *Applied Physics Letters*, 105(10):103702, sep 2014. doi: 10.1063/1.4895459.

[205] Jingfan Chen, Muzhaozi Yuan, Caitlin A. Madison, Shoshana Eitan, and Ya Wang. Blood-brain barrier crossing using magnetic stimulated nanoparticles. *Journal of Controlled Release*, 345:557–571, may 2022. doi: 10.1016/j.jconrel.2022.03.007.

[206] Elias Georgas, Muzhaozi Yuan, Jingfan Chen, Ya Wang, and Yi-Xian Qin. Bioactive superparamagnetic iron oxide-gold nanoparticles regulated by a dynamic magnetic field induce neuronal ca2 influx and differentiation. *Bioactive Materials*, 26:478–489, aug 2023. doi: 10.1016/j.bioactmat.2023.01.007.

[207] Muzhaozi Yuan, Eric A. Bancroft, Jingfan Chen, Rahul Srinivasan, and Ya Wang. Magnetic fields and magnetically stimulated gold-coated superparamagnetic iron oxide nanoparticles differentially modulate l-type voltage-gated calcium channel activity in midbrain neurons. *ACS Applied Nano Materials*, 5(1):205–215, jan 2022. doi: 10.1021/acsanm.1c02665.

[208] L. León Félix, B. Sanz, V. Sebastián, T. E. Torres, M. H. Sousa, J. A. H. Coaquira, M. R. Ibarra, and G. F. Goya. Gold-decorated magnetic nanoparticles design for hyperthermia applications and as a potential platform for their surface-functionalization. *Scientific Reports*, 9(1), mar 2019. doi: 10.1038/s41598-019-40769-2.

[209] Peng Wang, Jianfei Sun, Zhichao Lou, Fengguo Fan, Ke Hu, Yi Sun, and Ning Gu. Assembly-induced thermogenesis of gold nanoparticles in the presence of alternating magnetic field for controllable drug release of hydrogel. *Advanced Materials*, 28(48): 10801–10808, oct 2016. doi: 10.1002/adma.201603632.

[210] Min Wei, Zhaofei Yang, Song Li, and Weidong Le. Nanotherapeutic and stem cell therapeutic strategies in neurodegenerative diseases: A promising therapeutic approach. *International Journal of Nanomedicine*, Volume 18:611–626, feb 2023. doi: 10.2147/ijn.s395010.

[211] Daniel N. Grant, Matthew J. Cozad, David A. Grant, Richard A. White, and Sheila A. Grant. iin vitro/ielectromagnetic stimulation to enhance cell proliferation in extracellular matrix constructs with and without metallic nanoparticles. *Journal of Biomedical Materials Research Part B: Applied Biomaterials*, 103(8):1532–1540, dec 2014. doi: 10.1002/jbm.b.33338.

[212] Inc Mathematica's ElementData function, Wolfram Research. Technical data for gold: https://periodictable.com/elements/079/data.html, 2023. URL `https://periodictable.com/Elements/079/data.html`.

[213] Vincenzo Amendola, Moreno Meneghetti, Mauro Stener, Yan Guo, Shaowei Chen, Patricia Crespo, Miguel Angel García, Antonio Hernando, Paolo Pengo, and Lucia Pasquato. Physico-chemical characteristics of gold nanoparticles. In *Gold Nanoparticles in Analytical Chemistry*, pages 81–152. Elsevier, 2014. doi: 10.1016/b978-0-444-63285-2.00003-1.

[214] Chi-Yen Li, Sunil Karna, Chin-Wei Wang, and Wen-Hsien Li. Spin polarization and quantum spins in au nanoparticles. *International Journal of Molecular Sciences*, 14 (9):17618–17642, aug 2013. doi: 10.3390/ijms140917618.

[215] A Ayuela, P Crespo, M A García, A Hernando, and P M Echenique. sp magnetism in clusters of gold thiolates. *New Journal of Physics*, 14(1):013064, jan 2012. doi: 10.1088/1367-2630/14/1/013064.

[216] P. G. van Rhee, P. Zijlstra, T. G. A. Verhagen, J. Aarts, M. I. Katsnelson, J. C. Maan, M. Orrit, and P. C. M. Christianen. Giant magnetic susceptibility of gold nanorods detected by magnetic alignment. *Physical Review Letters*, 111(12):127202, sep 2013. doi: 10.1103/physrevlett.111.127202.

[217] Simon Trudel. Unexpected magnetism in gold nanostructures: making gold even more attractive. *Gold Bulletin*, 44(1):3–13, feb 2011. doi: 10.1007/s13404-010-0002-5.

[218] Gareth L. Nealon, Bertrand Donnio, Romain Greget, Jean-Paul Kappler, Emmanuel Terazzi, and Jean-Louis Gallani. Magnetism in gold nanoparticles. *Nanoscale*, 4(17):5244, 2012. doi: 10.1039/c2nr30640a.

[219] Romain Gréget, Gareth L. Nealon, Bertrand Vileno, Philippe Turek, Christian Mény, Frédéric Ott, Alain Derory, Emilie Voirin, Eric Rivière, Andrei Rogalev, Fabrice Wilhelm, Loïc Joly, William Knafo, Géraldine Ballon, Emmanuel Terazzi, Jean-Paul Kappler, Bertrand Donnio, and Jean-Louis Gallani. Magnetic properties of gold nanoparticles: A room-temperature quantum effect. *ChemPhysChem*, 13(13):3092–3097, jun 2012. doi: 10.1002/cphc.201200394.

[220] E Guerrero, M A Muñoz-Márquez, M A García, P Crespo, E Fernández-Pinel, A Hernando, and A Fernández. Surface plasmon resonance and magnetism of thiol-capped gold nanoparticles. *Nanotechnology*, 19(17):175701, mar 2008. doi: 10.1088/0957-4484/19/17/175701.

[221] C.M. Hurd. The magnetic susceptibility of silver and gold in the range 6–300°k. *Journal of Physics and Chemistry of Solids*, 27(9):1371–1374, sep 1966. doi: 10.1016/0022-3697(66)90130-2.

[222] File:helmholtz coil.svg: Wikipedia, 2022. URL `https://commons.wikimedia.org/wiki/File:Helmholtz_coil.svg`.

[223] Atefeh Kordzadeh and Nicola De Zanche. Permittivity measurement of liquids, powders, and suspensions using a parallel-plate cell. *Concepts in Magnetic Resonance Part B: Magnetic Resonance Engineering*, 46(1):19–24, jan 2016. doi: 10.1002/cmr.b.21318.

[224] Eckard Gerlach and Peter Grosse. *Physik*. ViewegTeubner Verlag, 1999. doi: 10.1007/978-3-322-96803-6.

[225] Yuri Feldman, Raul Nigmatullin, Evgeny Polygalov, and John Texter. Fractal-polarization correction in time domain dielectric spectroscopy. *Physical Review E*, 58(6):7561–7565, dec 1998. doi: 10.1103/physreve.58.7561.

[226] Anna Norlin. *Investigation of electrochemical properties and performance of stimulation/sensing electrodes for pacemaker applications*. PhD thesis, KTH, Materials Science and Engineering, 2005. QC 20101014.

[227] Hermann Schwan. Elektrodenpolarisation und ihr einfluß auf die bestimmung dielektrischer eigenschaften von flüssigkeiten und biologischem material. *Zeitschrift für Naturforschung B*, 6(3):121–129, mar 1951. doi: 10.1515/znb-1951-0301.

[228] H. P. Schwan. Alternating current electrode polarization. *Biophysik*, 3(2):181–201, jun 1966. doi: 10.1007/bf01191612.

[229] H. P. Schwan. ELECTRODE POLARIZATION IMPEDANCE AND MEASUREMENTS IN BIOLOGICAL MATERIALS. *Annals of the New York Academy of Sciences*, 148(1 Bioelectrodes):191–209, feb 1968. doi: 10.1111/j.1749-6632.1968.tb20349.x.

[230] Paul Ben Ishai, Mark S Talary, Andreas Caduff, Evgeniya Levy, and Yuri Feldman. Electrode polarization in dielectric measurements: a review. *Measurement Science and Technology*, 24(10):102001, aug 2013. doi: 10.1088/0957-0233/24/10/102001.

[231] Carl A. Marrese. Preparation of strongly adherent platinum black coatings. *Analytical Chemistry*, 59(1):217–218, jan 1987. doi: 10.1021/ac00128a049.

[232] D. Malleo, J. T. Nevill, A. van Ooyen, U. Schnakenberg, L. P. Lee, and H. Morgan. Note: Characterization of electrode materials for dielectric spectroscopy. *Review of Scientific Instruments*, 81(1):016104, jan 2010. doi: 10.1063/1.3284516.

[233] Harke Saba, Boris Chichkov, and Annette Hoffmeister. Theoretical analysis of classical pulsed electromagnetic field excitation in the frame of cell differentiation. In *BioEM international conference on bioelectromagnetics*, 2022.

[234] Thomas Westermann. *Mathematik für Ingenieure*. Springer Berlin Heidelberg, 2020. doi: 10.1007/978-3-662-61323-8.

[235] Vitalii Zablotskii, Alexandr Dejneka, Šárka Kubinová, Damien Le-Roy, Frédéric Dumas-Bouchiat, Dominique Givord, Nora M. Dempsey, and Eva Syková. Life on magnets: Stem cell networking on micro-magnet arrays. *PLoS ONE*, 8(8):e70416, aug 2013. doi: 10.1371/journal.pone.0070416.

[236] Andrey B. Evlyukhin and Vladimir R. Tuz. Electromagnetic scattering by arbitrary-shaped magnetic particles and multipole decomposition: Analytical and numerical approaches. *Physical Review B*, 107(15):155425, apr 2023. doi: 10.1103/physrevb.107.155425.

[237] Rochester university lecture notes chapter 6. URL `http://teacher.pas.rochester.edu/PHY217/LectureNotes/Chapter6/LectureNotesChapter6.html`.

[238] V. Ya. Halchenko, D. L. Ostapushchenko, and M. A. Vorobyov. Mathematical simulation of magnetization processes of arbitrarily shaped ferromagnetic test objects in fields of given spatial configurations. *Russian Journal of Nondestructive Testing*, 44 (9):589–600, sep 2008. doi: 10.1134/s1061830908090015.

[239] M. Beleggia, M. De Graef, and Y. Millev. Demagnetization factors of the general ellipsoid: An alternative to the maxwell approach. *Philosophical Magazine*, 86(16): 2451–2466, jun 2006. doi: 10.1080/14786430600617161.

[240] J. A. Osborn. Demagnetizing factors of the general ellipsoid. *Physical Review*, 67 (11-12):351–357, jun 1945. doi: 10.1103/physrev.67.351.

[241] L. D. Landau and E.M. Lifshitz. *Electrodynamics of Continuous Media (Course of Theoretical Physics)*. 1984.

[242] Urs Zywietz, Andrey B. Evlyukhin, Carsten Reinhardt, and Boris N. Chichkov. Laser printing of silicon nanoparticles with resonant optical electric and magnetic responses. *Nature Communications*, 5(1), mar 2014. doi: 10.1038/ncomms4402.

[243] Di Du and Sibani Lisa Biswal. Micro-mutual-dipolar model for rapid calculation of forces between paramagnetic colloids. *Physical Review E*, 90(3):033310, sep 2014. doi: 10.1103/physreve.90.033310.

[244] Pooja Tiwari, Komal Vig, Vida Dennis, and Shree Singh. Functionalized gold nanoparticles and their biomedical applications. *Nanomaterials*, 1(1):31–63, jun 2011. doi: 10.3390/nano1010031.

[245] R. G. Sharma. The phenomenon of superconductivity. In *Superconductivity*, pages 13–48. Springer International Publishing, 2015. doi: 10.1007/978-3-319-13713-1_2.

[246] J. M. D. Coey. *Magnetism and Magnetic Materials*. Cambridge University Press, March 2010. ISBN 0521816149. URL `https://www.ebook.de/de/product/11264722/j_m_d_coey_magnetism_and_magnetic_materials.html`.

[247] Johannes B Erhardt, Erwin Fuhrer, Oliver G Gruschke, Jochen Leupold, Matthias C Wapler, Jürgen Hennig, Thomas Stieglitz, and Jan G Korvink. Should patients with brain implants undergo MRI? *Journal of Neural Engineering*, 15(4):041002, may 2018. doi: 10.1088/1741-2552/aab4e4.

[248] Keyang Huang, Huili Ma, Juan Liu, Shuaidong Huo, Anil Kumar, Tuo Wei, Xu Zhang, Shubin Jin, Yaling Gan, Paul C. Wang, Shengtai He, Xiaoning Zhang, and Xing-Jie Liang. Size-dependent localization and penetration of ultrasmall gold nanoparticles in

cancer cells, multicellular spheroids, and tumors iin vivo/i. *ACS Nano*, 6(5):4483–4493, may 2012. doi: 10.1021/nn301282m.

[249] Erik C. Dreaden, Alaaldin M. Alkilany, Xiaohua Huang, Catherine J. Murphy, and Mostafa A. El-Sayed. The golden age: gold nanoparticles for biomedicine. *Chem. Soc. Rev.*, 41(7):2740–2779, 2012. doi: 10.1039/c1cs15237h.

[250] Saba Harke, Lukas Berkelmann, Anaclet Ngezahayo, and Dirk Manteuffel. In-vitro exposure setup for tumor treating fields. In *IEEE International Engineering in Medicine and Biology Conference*, 2020.

[251] Jean-Luc Dellis. Zfit, 2022. URL `https://de.mathworks.com/matlabcentral/fileexchange/19460-zfit`.

[252] DDBST GmbH Dortmund Data Bank (DDB). Dielectric constant of 2-propanol, 2022. URL `http://www.ddbst.de/en/EED/PCP/DEC_C95.php`.

[253] INC. Trask Instrumentation. Conductivity chart of liquids, 2022. URL `https://www.traskinstrumentation.com/pdf/app_notes/Conductivity_Chart_of_Liquids.pdf`.

[254] Christian Schmidt. Vergleich der gemessenen elektrischen leitfähigkeit von wasser mit der berechnung der leitfähigkeit aus analytischen ergebnissen, 2013. URL `https://www.researchgate.net/publication/327869226_Vergleich_der_gemessenen_elektrischen_Leitfahigkeit_von_Wasser_mit_der_Berechnung_der_Leitfahigkeit_aus_analytischen_Ergebnissen`.

[255] Claus Czeslik, Heiko Seemann, and Roland Winter. *Basiswissen Physikalische Chemie*. ViewegTeubner, 2010. doi: 10.1007/978-3-8348-9359-8.

8 Scientific Path and Scientific Publications

8.1 Scientific Path

Saba Harke

- Birthname: Meshksar

Contact

saba.harke@icloud.com

Scientist and doctoral degree — Since 07/2018
Leibniz School of Optics, Department of Physics and Department of Electrical Engineering, Leibniz University Hannover

Research assistant and teaching activities — 10/2017 - 04/2018
Institute of Electrical Engineering and Measurement Technology, Leibniz University Hannover

Electrical Engineering and Information Technology (M.Sc.) — 04/2016 - 07/2018
Leibniz University Hannover

Internship — 04/2016 - 09/2016
T4i engineering
Loughborough, UK

Visiting Researcher — 09/2015 - 02/2016
Loughborough University (UK)

Research assistant — 09/2012 - 10/2015
Institute of Mechatronic Systems
Leibniz University Hannover

Research assistant — 01/2012 - 07/2012
Institute of Electrical Engineering and Measurement Technology, Leibniz University Hannover

Electrical Engineering and Information Technology (B.Sc.) — 09/2011 - 03/2016
Leibniz University Hannover

Hanover, 27th July 2023

8.2 Publications

Journal publications

1. Lukas Berkelmann, Almke Bader, Saba Meshksar, Anne Dierks, Gökce Hatipoglu Majernik, Joachim K. Krauss, Kerstin Schwabe, Dirk Manteuffel, and Anaclet Ngezahayo. Tumour-treating fields (TTFields): Investigations on the Mechanism of Action by Electromagnetic Exposure of Cells in Telophase/Cytokinesis. Scientific Reports, 9(1), may 2019. doi: 10.1038/s41598-019-43621-9

2. Saba Harke and Dirk Manteuffel. Lumped Element Model of Spherical Cells Exposed to an External Electric Field. IEEE Journal of Electromagnetics, RF and Microwaves in Medicine and Biology, 5(4):355–361, dec 2021. doi: 10.1109/jerm.2021.3067596

3. Saba Harke, Atefeh Habibpourmoghadam, Andrey B. Evlyukhin, Antonio Calà Lesina and Boris N. Chichkov. Low-Frequency Magnetic Response of Gold Nanoparticles. Scientific Reports, 2023.

Conference proceedings

1. Saba Meshksar, Lukas Berkelmann, Dirk Manteuffel. Evaluation of Bannisters Subsurface-to-Air Model for Implanted Antennas. In IEEE International Symposium on Antennas and Propagation and USNC-URSI Radio Science Meeting, 2019.

2. Lukas Berkelmann, Almke Bader, Saba Meshksar, Anaclet Ngezahayo and Dirk Manteuffel . In-Vitro Exposure System for Tumor Treating Fields. In IEEE International Engineering in Medicine and Biology Conference, 2019.

3. Saba Harke; Lukas Berkelmann; Anaclet Ngezahayo and Dirk Manteuffel. In-Vitro Exposure Setup for Tumor Treating Fields. In IEEE International Engineering in Medicine and Biology Conference, 2020.

4. Saba Harke, Boris Chichkov, and Annette Hoffmeister. Theoretical Analysis of Classical Pulsed Electromagnetic Field Excitation in the Frame of Cell Differentiation. In BioEM international conference on bioelectromagnetics, 2022.

Supervised Bachelor theses

1. Jan Hendrik Jäschke. Ermittlung und Validierung messtechnischer Möglichkeiten zur Bestimmung dielektrischer Materialparameter von Flüssigkeiten im Frequenzbereich von 100 khz bis 500 khz, 2019.

2. Roya Trabelsi. Investigation of Possible Interaction Mechanisms Between Electromagnetic Fields and Tumor Cells in the Frame of Tumor Treating Fields (TTFields), 2020.